



Cardiff
Catalysis Institute

Sefydliad Catalysis
Caerdydd



Continuous sugar upgrading using Lewis acid catalysts

Thesis submitted in accordance with the requirements of Cardiff University for the degree of Doctor of Philosophy by

Ricardo Navar

School of Chemistry

Cardiff University

2021

Supervisor

Ceri Hammond



Acknowledgements

Firstly, I would like to thank my supervisor, Dr. Ceri Hammond, for his immense support throughout these 3-4 years, as well as giving me the opportunity to undertake my Ph.D. with him. Even though on paper I did not necessarily fill the requirements, in my opinion, he placed faith in me, and with his advice and guidance, helped me grow as a researcher. Additionally, I would also like to thank everyone that was in Ceri Hammond's group, which also aided in my growth as a researcher as well as creating a welcoming and invigorating environment, both professionally and socially. I would also like to thank Dr. Andrew Logsdail, for being my interim supervisor when Ceri was transferring. He provided a sense of ease when things might have become hectic due to all the changes in the final year.

I would also like to thank my parents for their unconditional support throughout my academic journey. They are literally the reason I was able to undergo not only my Ph.D., but all of my studies, which I cannot thank them enough for placing this trust in me, sacrificing what little they had so that I can pursue this passion of mine.

Furthermore, I would like to thank my wife and my daughter for putting up with this bright idea of mine of going to the other side of the world so that I can pursue this aforesaid passion of mine. Without their blessing, I could (*literally*) not have gone here.

I also would like to thank Conacyt (Consejo Nacional de Ciencia y Tecnología) for funding my Ph.D. (472256).

Abstract

Sugar upgrading to commodity chemicals has become prevalent over the last decades, owing in part to the potential of Lewis acid catalysts, in particular Sn-Beta zeolites. Sn-Beta has shown to possess high activity for the conversion of glucose to fructose as well as smaller molecules such as α -hydroxy esters (methyl lactate and methyl vinyl glycolate) and trioses (dihydroxyacetone, glyceraldehyde, pyruvaldehyde). Despite its promising kinetic potential, drawbacks that hinder it from being an industrially-used catalyst include the relatively low amount of Sn capable of being incorporated and the requirement of fluoride media to successfully synthesise Sn-Beta. Thus, top-down methods such as solid-state incorporation (SSI) has been of great interest for hard-to-incorporate heteroatoms such as Sn at higher wt. %. With this in mind, this thesis begins with an in-depth mechanistic study in the SSI of Sn-Beta, observing the acetate-zeolite interaction/evolution from the initial mechanochemical step to the ramp rate, both in inert gas flow and air using *in situ* spectroscopic techniques (Chapter 3). Furthermore, an optimised protocol for the heat treatment is obtained, having no negative impact in the kinetic performance of the zeolite. Chapter 4 investigates the influence of using different initial precursor (B, Fe, Ga, Al) for the zeolites' subsequent SSI. Tests were done with glucose isomerisation as well as retro-aldol fragmentation in continuous flow. Following this, Chapter 5 demonstrates the application of a different type of Lewis acid catalyst: metal-organic frameworks (MOFs). The MOFs *i.e.*, UiO-66(Zr) were studied in different polar solvents under continuous flow to understand their stability and were subsequently tested for disaccharide (lactose) isomerisation, a substrate which would typically not be possible to upgrade using conventional zeolites. Lactose isomerisation was done using binary mixtures of alcohol/water to successfully carry out the reaction. Chapter 6 sets out to carry out the SSI protocol, conventionally done in hydroxide-assisted zeolites, in fluoride-assisted zeolites. Tests were conducted firstly in a commercial, hydroxide-assisted zeolite using an alkaline media along with a pore directing agent at various temperatures. Thereafter, SSI protocol was conducted for three fluoride zeolites (Hf-, Sn-, Zr-) using the same conditions. Lastly, Chapter 7 discusses the results acquired as well as any pertaining challenges which might have been left open due to aforementioned results.

TABLE OF CONTENTS

1. Introduction.....	1
1.1 The pursuit of chemical sustainability	1
1.2 Biomass as a precursor for commodity chemicals.....	4
1.3. Lignocellulosic biomass.....	6
1.3.1 Lignin.....	6
1.3.2 Hemicellulose	9
1.3.3 Cellulose	11
1.3.4. Glucose	12
1.3.5 Glucose upgrading to platform chemicals	14
1.4 Homogeneous and heterogeneous catalysis.....	15
1.4.1 Zeolites.....	17
1.4.2 Zeolite synthesis.....	18
1.4.2 Optimisation of zeolite synthesis	21
1.4.2.1 Addition of seeds	21
1.4.2.2. Microwave synthesis.....	22
1.4.2.3. Hydrothermal synthesis <i>via</i> tumbling	22
1.5 Catalyst deactivation.....	22
1.5.1 Fouling/Coking deactivation.....	23
1.5.2 Poisoning.....	24
1.5.3 Thermal degradation and sintering	25
1.5.4 Gas/vapour with solid interaction restructuring.....	26
1.5.5 Leaching.....	26
1.5.6 Hydrothermal dissolution.....	27
1.6. Structural modification of zeolites.....	28

1.6.1. Bottom-up zeolite synthesis	29
1.6.1.1 ‘Soft’ secondary template.	29
1.6.2 “Hard” secondary template	30
1.6.2.1 Carbon-based hard templates	30
1.6.2.2 Cellulose as a hard template	31
1.6.2.3 Other hard templates	31
1.7 Top-down approach	32
1.7.1 Desilication	32
1.7.2 Surfactants and amines for pore-size tuning	33
1.8 Sn-incorporated zeolites.....	35
1.8.1 Sn incorporation <i>via</i> demetallation	36
1.8.2. Synthesis of heteroatom-substituted zeolites	38
1.9 Sn-Beta for biomass valorisation	38
1.9.1 Baeyer-Villiger oxidation	38
1.9.2 Meerwein-Ponndorf-Verley-Oppenauer reduction.....	39
1.9.3 Sugar isomerisation.....	40
1.10 Metal-organic-frameworks.	43
1.11. Objectives of the thesis	44
1.12 References.....	46
Chapter 2. Experimental and methods	62
2.1 List of acronyms	62
2.2 Formulae and expressions.....	63
2.3 Catalyst synthesis.....	64
2.3.1 Hydrothermal Beta zeolite	64
2.3.2 Post-synthetic modification	64

2.3.2.1 Demetallation	64
2.3.2.2 Desilication	65
2.3.3 UiO-66-Zr-H and UiO-66-Zr-NH ₂ MOF synthesis	65
2.4 Kinetic evaluation	66
2.4.1 Batch glucose isomerisation (GI).....	66
2.4.2 Batch Meerwein-Ponndorf-Verley (MPV) reduction	67
2.4.3 Continuous GI reaction	67
2.4.4 Continuous lactose isomerisation	67
2.5 Analytical methods	68
2.5.1 Chromatography	68
2.5.1.1 Gas Chromatography – Flame Ionization Detector	69
2.5.1.2 High Performance Liquid Chromatography (HPLC)	70
2.5.2 Quantification of GC and LC products	72
2.5.2.1 GC quantification.....	72
2.5.2.2 GC quantification.....	75
2.6 Catalyst characterisation	77
2.6.1 Powder X-Ray Diffraction (pXRD).....	77
2.6.2 Physisorption for surface and porosimetry analysis	78
2.6.3 Infrared Spectroscopy – Diffuse Reflectance Infrared Fourier Transform Spectroscopy (DRIFTS)	81
2.6.4 Temperature Programmed Desorption (TPD) – Mass Spectroscopy (MS).....	83
2.6.5 Diffuse Reflectance Ultraviolet-visible (UV-vis) spectroscopy	84
2.6.6 Thermogravimetric analysis (TGA).....	84
2.6.7 Electron Microscopy (EM)	85
2.6.7.1 Scanning electron microscopy (SEM)	85

2.6.7.2. Transmission Electron Microscopy (TEM)	87
2.6.8 Nuclear Magnetic Resonance (NMR) spectroscopy	87
2.6.8.1 Magic angle spinning (MAS) NMR	89
2.6.9. Inductively Coupled Plasma – Mass Spectroscopy (ICP-MS)	91
2.6.10. Raman Spectroscopy.....	91
2.6.11 X-ray Absorption Spectroscopy (XAS).....	92
2.7 References.....	94
Chapter 4. A greener approach to solid-state incorporation: kinetic evaluation of different heteroatom-derived Sn-beta zeolites	135
4.1 Introduction.....	135
4.2 Results and discussion	137
4.2.1 Catalyst synthesis and characterisation.....	137
4.2.2 Kinetic evaluation of synthesised catalyst materials	144
4.2.2.1 Retro-aldol fragmentation.....	144
4.2.2.2 Effect of water and alkali on kinetic performance.....	151
4.2.2.3 Low temperature glucose isomerisation	154
4.3 Conclusions.....	159
4.4 References.....	160
Chapter 5. Tailoring of beta zeolites with post-synthetic modifications using pore-directing agents for sugar valorisation	164
5.1 Introduction.....	164
5.2. Results and discussion	168
5.2.1. Zeolite characterisation.....	168
5.2.2. Catalytic tests of the hierarchical Sn-Beta samples.....	171
5.2.3. Catalytic tests of the desilicated, fluoride-synthesised Hf-, Zr-, and Sn-Beta zeolites	175

5.3 Conclusion	178
5.4 References.....	179
Chapter 6. Polar solvent stability of UiO-66 metal organic framework and its application for lactose valorisation under continuous flow.....	184
6.1 Introduction.....	184
6.2 Results and discussion	186
6.2.1 MOF synthesis and characterisation	186
6.2.2 Solvothermal stability studies of UiO-66(Zr)-H.....	189
6.2.3. Kinetic studies of MOF for lactose isomerisation	192
6.3 Conclusions.....	201
6.4 References.....	203
Chapter 7. Conclusions and pertaining challenges	209
7.1 Final conclusions	209
7.2 Pertaining challenges	213
Appendix.....	216
Chapter 3 Appendix	216
Chapter 4 Appendix	219
Chapter 5 Appendix	222
Chapter 6 Appendix	224

1. Introduction

1.1 The pursuit of chemical sustainability

Over the last century, the exponential population growth along with changes in societal needs has propelled us in the search for alternatives in energy sources and chemical demands to supply our daily requirements. To date, fossil fuels are the primary resource for energy and chemical production. In particular, the main sources of energy have been coal, oil, and natural gas (Figure 1.1). Unfortunately, these sources are finite and take a toll on the environment, as they are some of the largest contributing sources of local air pollution and emitters of greenhouse gases (GHC) such as carbon dioxide, methane (CH_4), and nitrous oxide (N_2O). These gases have been linked to climate change, as well as other negative human health effects, such as asthma, cancer, and a wide array of neurological and cardiovascular diseases. Thus, it is of paramount importance to search for new energy sources to mitigate the use of non-renewable resources.

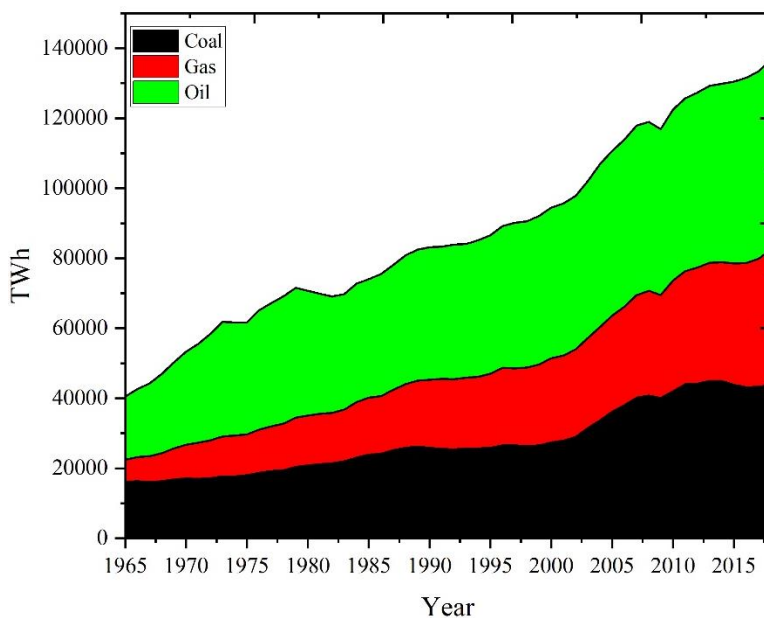


Figure 1.1. Fossil fuel consumption by fuel type in terawatt-hour equivalents (TWh), World, 1965 to 2018. Source: BP Statistical Review of Global Energy (2019).

While fossil fuel is critically important in our day to day lives and will remain so in the near future, there has been progress over the last two decades in regard to the use of renewable energy as

alternative sources for the use in the energy sector. It is predicted, according to the U.S. Energy Information Administration (EIA), that energy production from renewable resources will overtake other fossil fuel-derived resources as the main means of production by 2050, as represented in Figure 1.2.

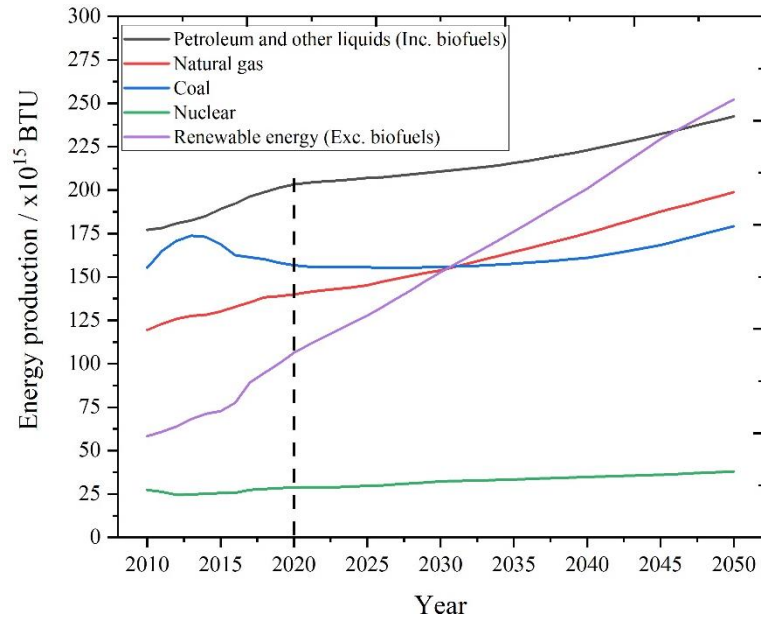


Figure 1.2. Primary energy consumption by energy source, world, 2010 to 2050. Source: International Energy Outlook 2019. U.S. Energy Information Administration.

Renewable energy comprises of a plethora of naturally occurring resources that are constantly replenished. Some sources include sunlight, wind, water (which includes rain, waves, or tides) and geothermal heat, stored in the Earth (Figure 1.3). These resources can be easily used for applications in the transportation, residential and commercial sectors. Other sources such as fuel cells, specifically a proton exchange membrane (PEM) cell is another alternative for the transportation sector, which has a substantial advantage over internal combustion engines, producing only water, heat, and electricity.

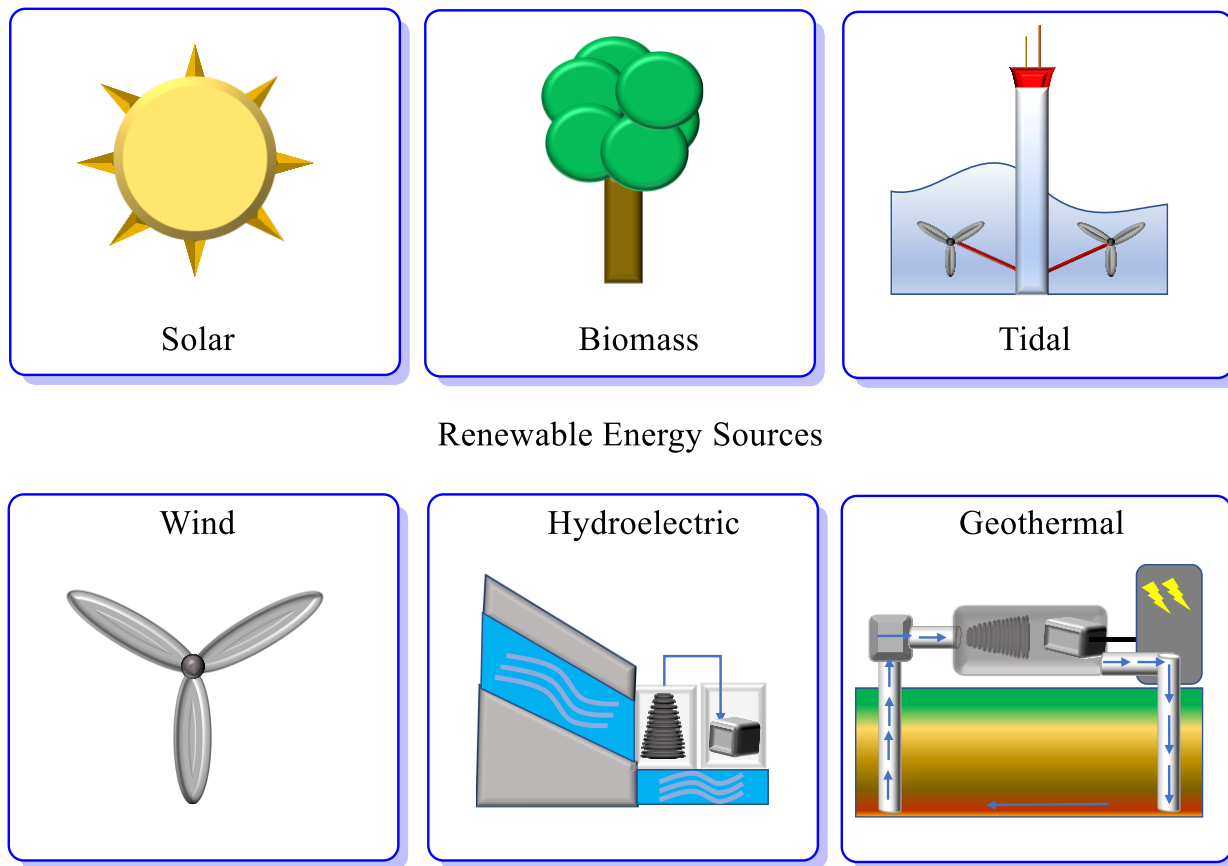


Figure 1.3. Sources of renewable energy.

Nevertheless, polymers and other commodity chemicals are still carbon-based resources. This makes biomass an intriguing source to produce said chemicals due to their flexibility to different end-products and relatively low cost, having shown to be more economically feasible for three agro-industrial processes^{1,2} Indeed, biomass has proven to have high potential for the sustainable processing of fuels and chemicals due to its renewable feedstock and worldwide availability.^{3,4}

The chemical industry encompasses the companies that produce end-product (or intermediate) chemicals with the conversion of raw materials (oil, water, metals, air), be it non-renewable or renewable. Chemical industries produce more than 50,000 chemicals, generating approximately three trillion US dollars per year, supplying a plethora of markets, such as chemical for agriculture, food, hygiene, environment, pharmaceutical, and many more.⁵ The chemical sector plays a critical role to the sustainable development of a nation's economy. Nearly all chemicals, both bulk and fine chemicals, are carbon-based, requiring the use of carbon-based precursors to generate these

new commodity chemicals. Unlike chemicals, energy production has alternative vectors to produce energy *via* different means.

1.2 Biomass as a precursor for commodity chemicals.

Biomass can be classified as all organic material that stems from plants or animals, such as algae, trees, agricultural crops and organic waste such as manure.^{6,7} Plant-derived biomass, for instance, essentially derives from the reaction between CO₂ in the air, water and sunlight *via* photosynthesis, to create the biomass building blocks. Of all types of biomasses, approximately 80 % of biomass is derived from plants, whilst the second most abundant is from bacteria, constituting *ca.* 15 %. The remaining 5 % is made up of animal, archaea and fungi biomass.⁸

Commodity chemicals are a sub-sector of the chemical industry which comprises to groups of chemicals that are made at large scale to accommodate the demands of the global market. Some known commodity chemicals that have been produced *via* biomass consist in 1,6-hexanediol for polyester and polyurethane production,⁹ caprolactone for nylon manufacturing,¹⁰ alcohols (methanol, ethanol) and alcohols (2-butanol, pentanol)⁶, and ethylene glycol.¹¹

Throughout history, society has taken advantage of the energy stored in the bonds of biomass by burning the biomass to produce heat as well as eating other types of biomass for their sugar and starch contents. Alternatively, biomass can also be used as feedstock for chemical or biochemical valorisation, producing highly sought-after chemicals which can be used for a vast array of applications.

Biochemical valorisation involves the use of enzymes or fermentative conversion. Enzymes are proteins that are biological catalysts, *i.e.*, they increase the reaction rate by lowering the activation energy, allowing reactions to occur several orders of magnitude faster.^{12,13} These processes involve anaerobic digestion, decomposing the biomass through bacterial activity which yields biogas, whereas alcoholic fermentation is used to produce ethanol from sugar and starch crops.

Chemical (or thermochemical) valorisation involves a more straightforward approach. Most thermochemical valorisations operate at high temperatures. The most used approaches are pyrolysis, liquefaction, and gasification.¹⁴ Pyrolysis consists of thermal decomposition in the absence of oxygen. Typical products obtained *via* pyrolysis are char, bio-oil (oxygen-containing compounds *i.e.* methanol, formaldehyde, phenol, acetic acid, 1-hydroxypropane), and various

gaseous products.^{15,16} Temperature plays an important role when undergoing pyrolysis, giving a distinct product distribution as well as yielding smaller molecules the higher the temperature, yielding more in the gaseous fraction.^{17,18}

Gasification is another thermochemical process that converts biomass into gas using a gasifying agent, such as air, oxygen, steam or CO₂.¹⁹ Although different, pyrolysis is the first step in gasification; pyrolysis is performed to separate organic liquids and non-condensable gases from the solid product (char). Overall product distribution differs from pyrolysis, with syngas, a gas mixture of carbon monoxide, hydrogen, methane, and carbon dioxide, is obtained. Other products obtainable can be light (ethane and propane) and heavy (tar) hydrocarbons.^{19,20} Temperatures and pressures can vary between 500 to 1400 °C, and from atmospheric to 33 bar.²¹

Unlike pyrolysis and gasification, hydrothermal liquefaction involves the use of low temperatures (250-350 °C) at high pressure (~5-20 MPa) for its reaction. This process is primarily suited for converting high moisture biomass (>80 % moisture); this is to abolish the need of drying, unlike other thermochemical processes.^{22,23} While it is initially intended to be used for wet biomass feedstock (microalgae: lipids, proteins/amino acids),²⁴⁻²⁶ it can also be applied for dry biomass, *e.g.*, lignin, cellulose, hemicellulose.²⁷ Product distribution can vary depending on initial feedstock, although the liquid portion is considered to be the main product obtained; this typically constitutes of biocrude oil (acetaldehyde, ethanol, acetone, 2-propanone, pyridine, benzoic acid, and other oxygenated, hydrocarbons, and nitrogenated compounds), a dark, viscous material with high energetic content (70-95 % of petroleum fuel).²⁸ Main gases produced are CO₂, H₂, and other short chain carbon compounds (C₂-C₄). Some solid residues can also be present, such as tar.

Over the last 2 decades, a lot of attention has been placed for the use of catalysts for lignin valorisation, such as the C-O dehydroaryloxylation using Ir catalysts or hydrogenation of aryl-ether bonds with Co-Zn catalysts.^{29,30} Other methods for breaking recalcitrant bonds consist in the use of ionic liquids and/or acids such as trifluoroacetic acid, which has shown promising results in the breakage of cellulose.^{31,32} However, the latter can suffer in applicability due to their toxicity, laborious preparation, and high-cost process in use. Therefore, heterogeneous catalysts, such as noble metals on supports (Pt/Al₂O₃, Ru/AC, Ni/ZSM-5), are considered a more feasible option for the saccharification of these complex hydrocarbons.³³

1.3. Lignocellulosic biomass

Out of the different types of biomass, lignocellulosic biomass is considered to be a favourable alternative to non-renewable fossil resources. In addition to being an abundant natural resource, it is the most economical type of biomass available as well as being a nonedible biomass,³⁴ having the potential to be converted into an assortment of platform chemicals as well as liquid fuel for transportation.^{35–37} Lignocellulosic biomass is made up of three polymers: lignin (*ca.* 10–25 % mass fraction), hemicellulose (20–35 %), and cellulose (35–50 %), which differ in mass fraction in accordance with the plant species and season (Figure 1.4).^{38,39} These feedstocks have multiple applications for a plethora of markets; some include: energy (biorefinery,⁴⁰ fuel pellets⁴¹), non-energy (paper,^{42,43} composite material,⁴⁴ mulch⁴⁵), industrial polymer (polyolefins,⁴⁶ polyesters,⁴⁷) and basic chemical (ethylene glycol⁴⁸, succinic acid,⁴⁹ propylene⁵⁰ production).

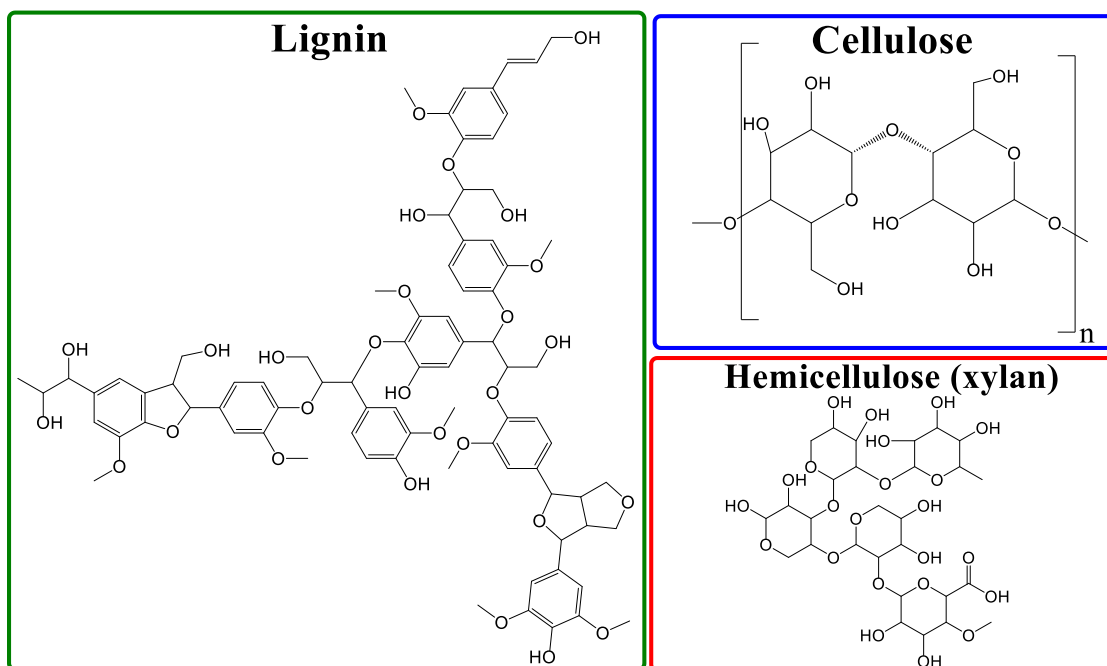


Figure 1.4. Three main lignocellulosic structures.

1.3.1 Lignin

Lignin is a complex three-dimensional aromatic polymer that provides rigidity to plants and trees. It is water-insoluble and composed mainly of three main lignin monolignols: caffeyl, sinapyl, p-coumaryl, coniferyl and 5-hydroxyconiferyl alcohol, as shown in Figure 1.5.^{51–54} These monolignols are derived from L-phenylalanine, where enzymes (such as L-phenylalanine-ammonia-

lyase) and other enzymatic steps convert this to the final monolignols. All these lignols are incorporated into lignin in the form of phenylpropanoids, *e.g.* guaiacyl (G), syringyl (S), p-coumaryl (also known as p-hydroxyphenyl, H).⁵⁵ These undergo a process called lignification, which links the phenylpropanoid units via radical coupling reactions.⁵⁶

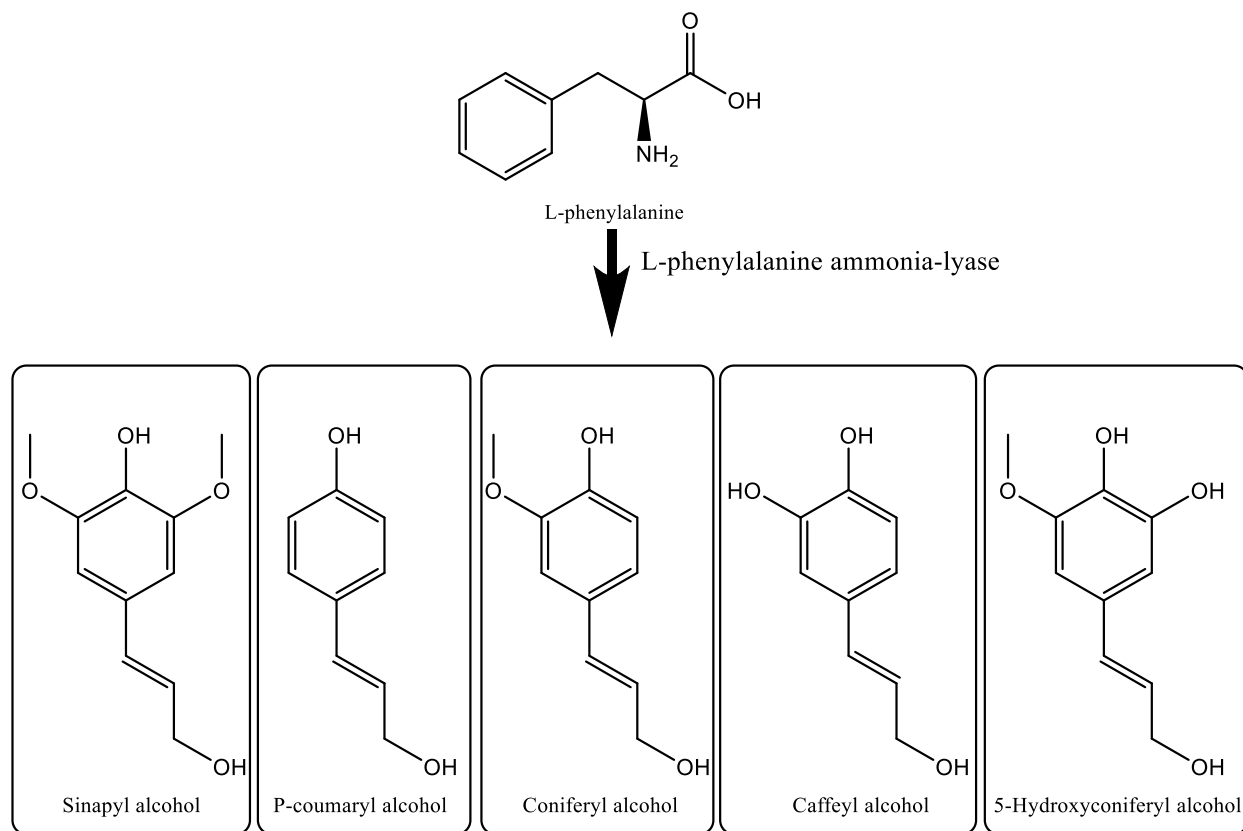


Figure 1.5. Main monolignol subunits of lignin.

Lignin valorisation continues to be a difficult task. This is due to the distribution of bond strengths in the C-O and C-C linkages and the tendency for low-molecular-weight species to recondense, unlike cellulose which is composed of purely $\beta(1-4)$ glycosidic bonds (bond between -OH group of C1 of monosaccharide and the -OH of C4 of another monosaccharide) and hemicellulose which has various glycosidic bonds in a random manner, hence, its relatively weak structure.⁵¹ Lignin depolymerization has been extensively studied via different routes, including: i) purely thermal degradation, yielding low molecular weight species in vapour phase which subsequently condense, creating oligomers;⁵⁷ ii) depolymerisation *via* catalytic oxidation⁵⁸⁻⁶⁰; iii) hydrodeoxygenation

with transition metal catalysts;⁶¹ iv) (electrocatalytic) hydrogenation;^{62–65} and v) catalytic cracking (Figure 1.6).⁶⁶

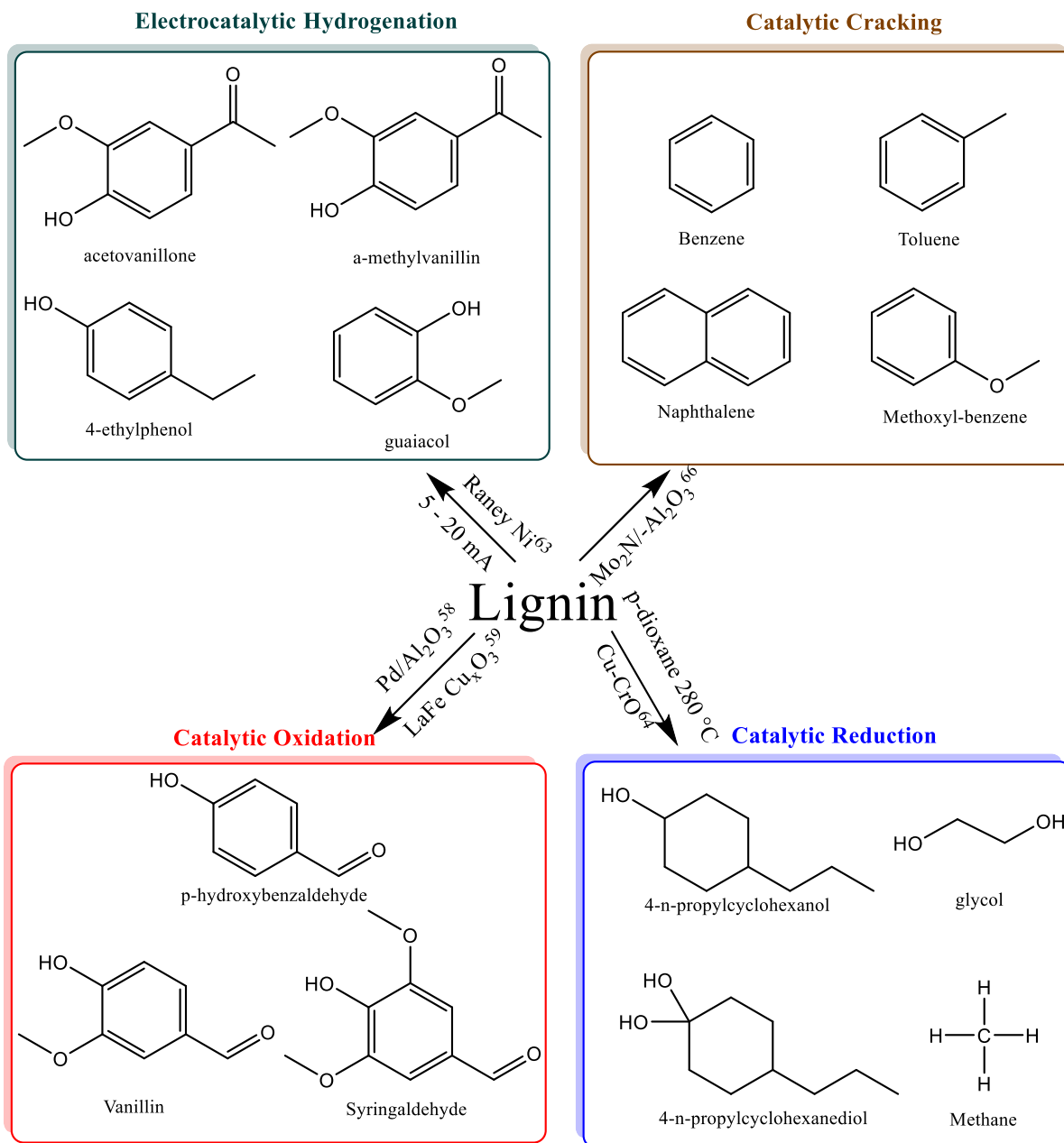


Figure 1.6. Lignin valorisation *via* different routes.

While there is considerable diversity towards product distribution depending on the route taken, valorisation can be troublesome due to the complexity of the polymer, particularly on a larger scale.

Challenges regarding the economic feasibility and the search for new catalysts have are currently being tackled to further obtain newer alternatives for the upgrading of this feedstock ^{51,52}

1.3.2 Hemicellulose

Hemicellulose, the second most abundant component of lignocellulosic biomass, is a heteropolymer comprised of short chains (500-3,000 units) made of different pentose (xylose, arabinose) and hexose (galactose, glucose) monosaccharides. All of the monosaccharides that comprise the hemicellulose are of the D configuration (-OH of the farthest chiral centre from the C=O to the right) with the exception of arabinose, which is L (-OH of the farthest chiral centre from the C=O to the left). Of the three polymers, it is the most labile as well as being water-soluble, and is able to undergo hydrolysis even without the use of a catalyst.⁶⁷ One of the first valorisations of this heteropolymer was for the production of furfural using a 15 % sulfuric acid solution at *ca.* 150 °C by Quaker Oats in 1921.^{68,69} Over time, valorisation of the hemicellulose monomers xylose and arabinose have awoken the interest of many researchers, being able to upgrade these sugars either by enzymatic or catalytic means, predominantly by the former, as can be seen in Figure 1.7.⁷⁰⁻⁷⁸

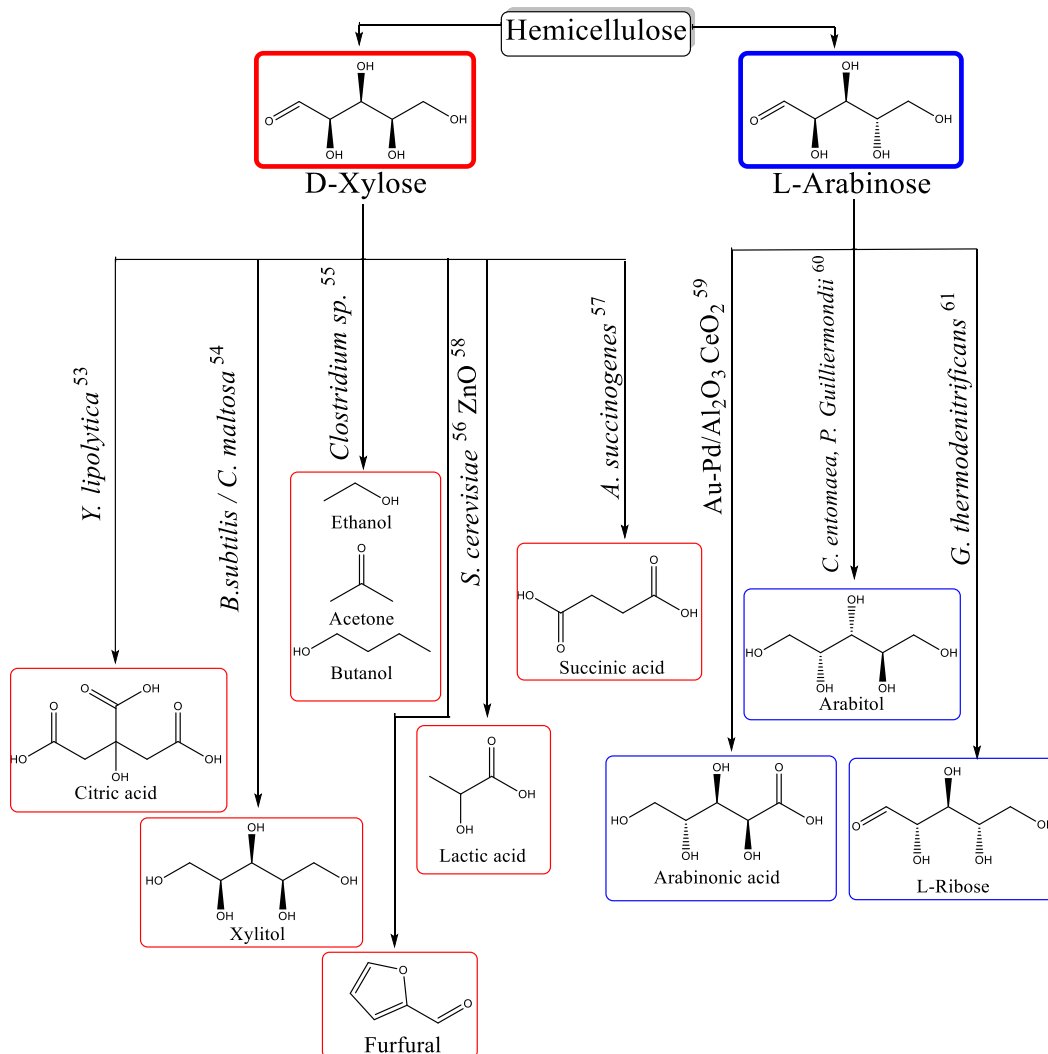


Figure 1.7. Summary of some of xylose and arabinose end products.

Of the aforementioned platform chemicals, furfural is considered to be one of the most highly sought-after commodity chemicals, having many potential industrial applications. Obtained *via* dehydration of xylose, furfural can be used as a nematocide and fungicide. Furthermore, it is well-known for being used as a solvent to extract unsaturated compounds from motor (or lubricating) oil (range of 18-24C hydrocarbons), refining it by removing mercaptans, polar, and aromatic compounds *via* furfural extraction.⁷⁹⁻⁸¹ Additionally, furfural can be further converted to other compounds, as shown in Figure 1.8, such as furfuryl alcohol, levulinic acid, among others.⁸²⁻⁸⁷

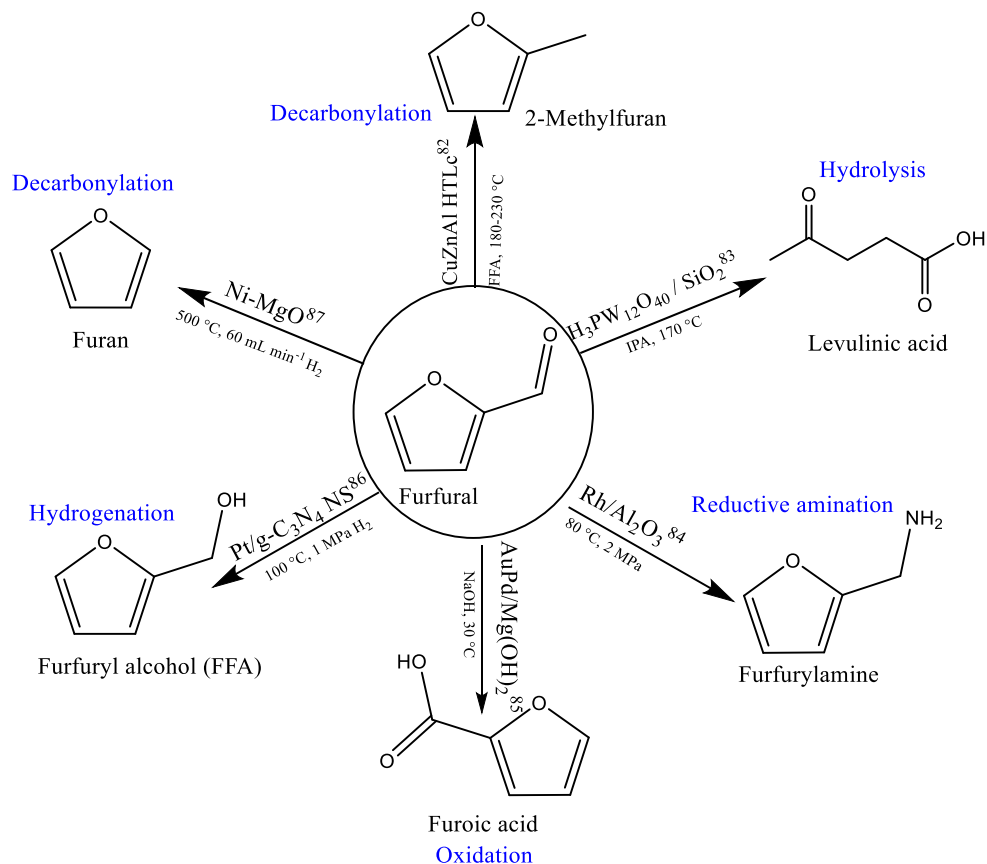


Figure 1.8. Furfural and its derivatives.

1.3.3 Cellulose

Cellulose is the most abundant polymer obtainable from lignocellulosic biomasses. It consists of hundreds to thousands of $\beta(1\rightarrow4)$ linked glucose monomers. The structure forms linear chains unlike hemicellulose, which can form branched chains; cellulose is also water insoluble like lignin. As it is solely composed of glucose subunits, cellulose can be hydrolysed enzymatically or chemically to create soluble oligosaccharides (cellobiose) and subsequently to the glucose monomer. The established method for cellulose hydrolysis is typically acid hydrolysis, using a strong acid such as sulphuric acid. This, however, has several drawbacks regarding the operational costs, catalyst recovery, neutralisation of the acid, and corrosion of reactors.⁸⁸ Consequently, the use of liquid acid transitioned into applications of various other acids (Figure 1.9), such as HCl and HF as well as organic acids (maleic and oxalic acid).^{89–91} Over time, the use of heterogeneous solid acids have been extensively researched to mitigate the use of liquids and reduce the potentially costly and unattractive downstream unit operations.⁹² These primarily consist of: i)

metal oxides, *i.e.*, catalysts with Lewis/Brønsted acid sites, such as Nb-W, ZrO₂ and (activated) carbon fibers (ACF), endowing the ACF solid acid properties *via* sulfonation and hydrothermal treatment;^{93–95} ii) sulfonated solid acids, *e.g.*, Amberlyst® and Nafion NR50®⁹⁶; iii) heteropoly acids (HPA) like dodecatungstophoric acid H₃PW₁₂O₄₀;⁹⁷ and iv) H-form catalysts, which can be a variety of zeolites, such as H-beta, H-mordenite, H-USY.^{92,98}

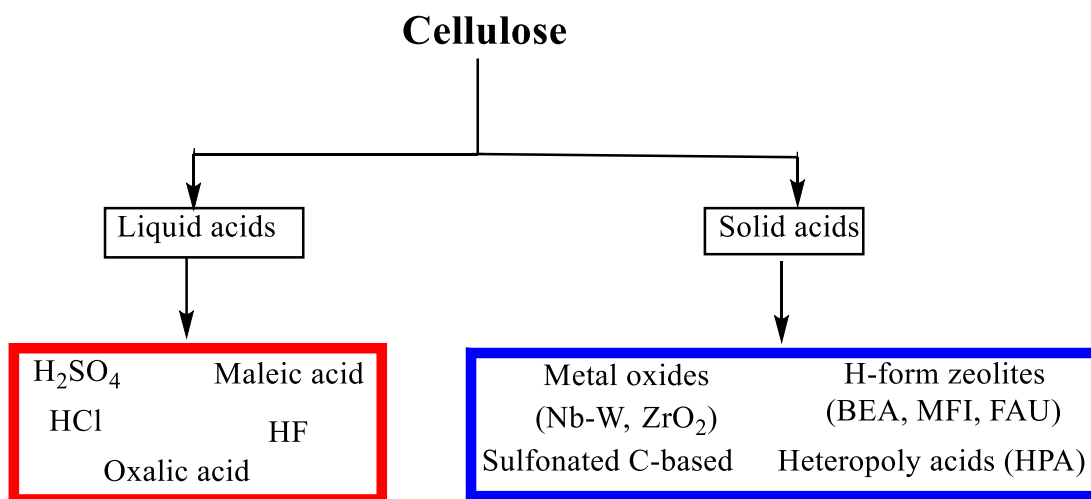


Figure 1.9. Summary of hydrolysis methods of cellulose *via* liquid acids and solid acids.

1.3.4. Glucose

The glucose monomer is considered a highly important precursor and has been extensively studied for valorisation due to its potential of producing a wide array of platform chemicals, as is shown in Figure 1.10.

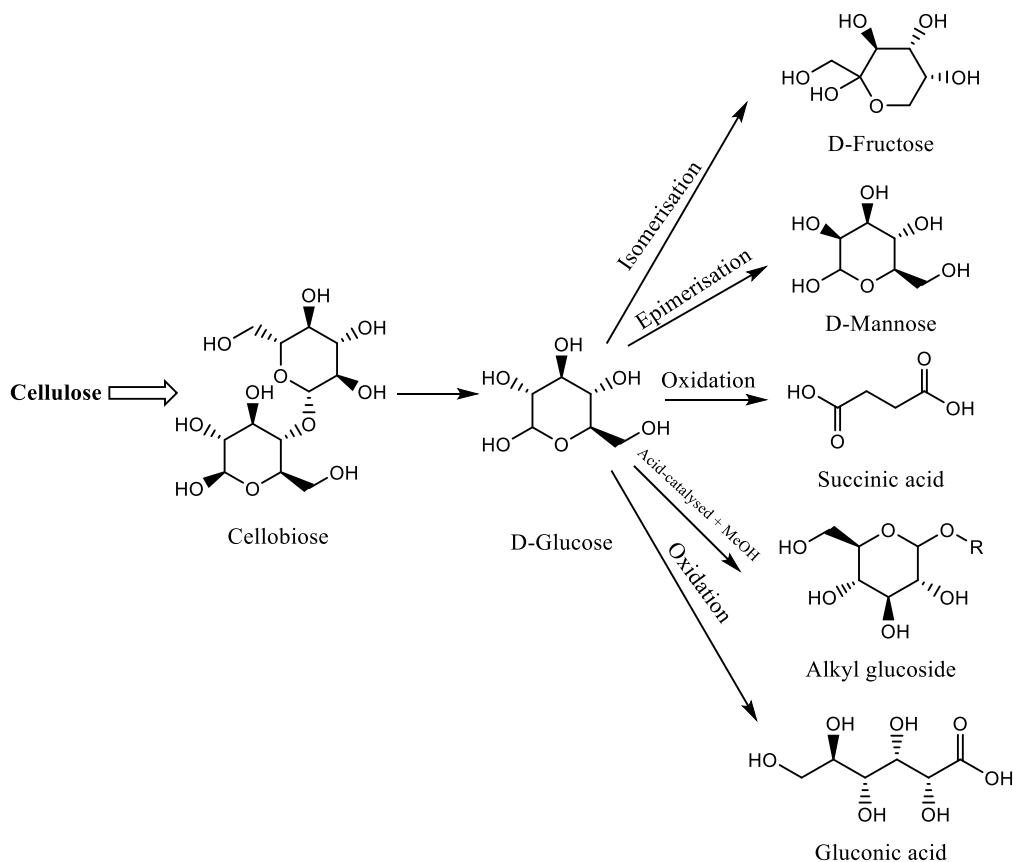


Figure 1.10. Schematic of different products obtainable from glucose.

One of the more prominent uses not mentioned in the previous figure involves the use of glucose to produce bio-ethanol *via* fermentation.⁹⁹ An additional process done at industrial scale is the production of fructose; this production entails the usage of enzymes such as α -amylase and glucoamylase for initial hydrolysis of the feedstock, and glucose isomerase to isomerise the glucose into fructose.

Fructose, along with glucose, is used to yield high fructose corn syrup (HFCS), a sweetener and an alternative to sucrose produced from corn starch.¹⁰⁰ Different ratios of HFCS can be classified according to their fructose content, the most common ones being HFCS-42, HFCS-55, and HFCS-90, which indicates 42, 55, and 90 % fructose content with the remainder being glucose and water.¹⁰¹

Advantages compared to sucrose is that it is relatively cheaper to produce than sucrose (32 ¢/lb for HFCS vs 52 ¢/lb for sucrose), due to HFCS main moieties being monosaccharides, they are easier

solubilised compared to sucrose, which is a disaccharide, thus, not crystallising under certain conditions.¹⁰¹ Furthermore, it is somewhat sweeter than sucrose.

Although valorisation of such compounds by enzymatic means has been prevalent, valorisation by chemical means has been thoroughly investigated and has increasingly become of interest. This primarily stems from the particular downfalls of using enzymes as catalysts. Whilst presenting an outstanding selectivity for the desired product, enzymes require strict operational conditions, which can make their utilisation laborious and expensive. Some enzymes, such as glucose isomerase, are expensive enzyme which requires immobilisation, adding to the labour required.¹⁰² Other limitations include enzyme stability at high temperatures or in turbulent flows, and their stability in the organic solvents.^{103–105} Thus, the use of heterogeneous catalysts provides an alternate route for the valorisation of virtually any sort of biomass-derived feedstock such as algae (transesterification to biodiesel),¹⁰⁶ municipal solid wastes (cardboard, paper, organic waste),^{107,108} chitin (production of N-acetylglucosamine and 5-HMF),^{109,110} corn stover (furfural production),¹¹¹ among others, while having an overall higher flexibility in terms of operational conditions.

1.3.5 Glucose upgrading to platform chemicals

Glucose can further be used as a feedstock to produce fine chemicals *via* retro-aldol fragmentation. This reaction consists of a β -hydroxy carbonyl compound decomposing into an aldehyde or ketone whilst forming another carbonyl with the remaining fragment. This provides other primary renewable building blocks that derive from glucose and/or fructose, such as methyl lactate (ML), a valuable building block which, after converting it to lactic acid, can be used to create polymers such as polylactic acid (PLA).^{112,113} Other compounds generated can be glycolaldehyde, or dihydroxyacetone, as can be seen in Figure 1.11.

5-Hydroxymethylfurfural (5-HMF) which is obtained *via* dehydration of fructose, for instance, is considered as a valuable intermediate to produce biofuels such as dimethylfuran (DMF), levulinic acid, a precursor for pharmaceuticals and additives, and dihydroxymethylfuran, a potential substitute in the production of polymers.^{114–116}

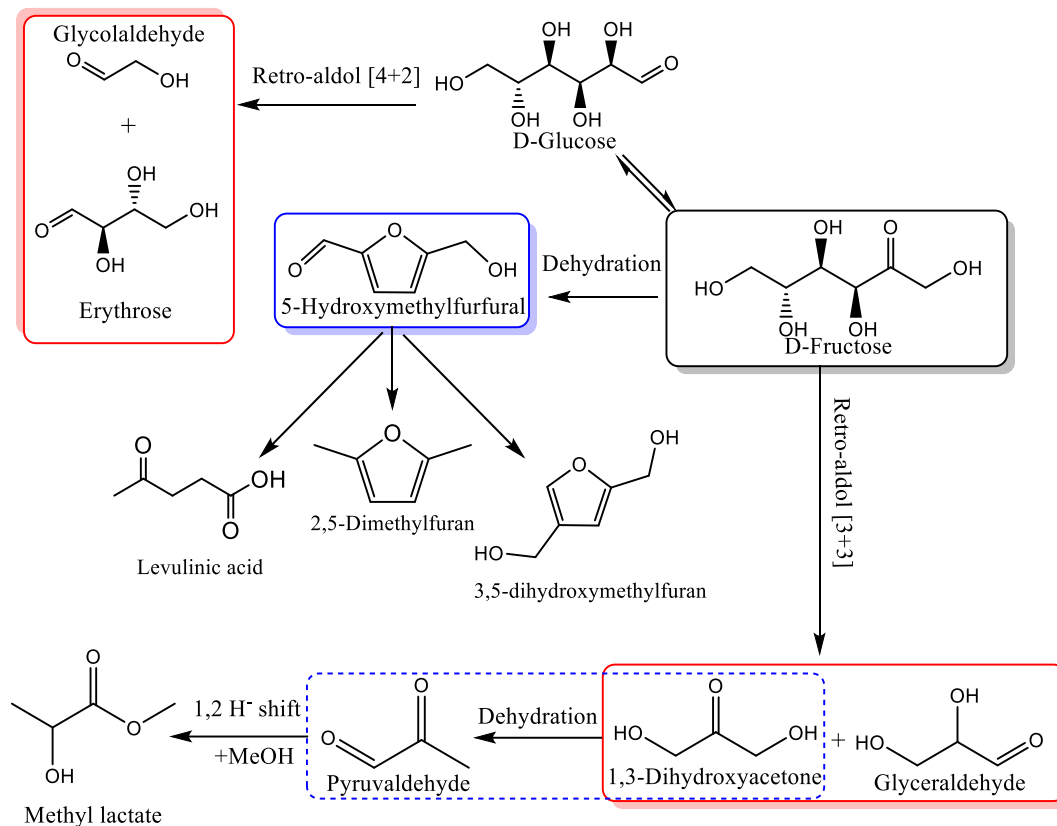


Figure 1.11. Additional pathways for creating chemical building blocks from glucose and fructose.

1.4 Homogeneous and heterogeneous catalysis.

Homogeneous catalysts are those where both the catalyst and reactants are in the same state (liquid or gas typically). Common examples of homogeneous catalysis include:¹¹⁷

- Lewis acids as catalysts (Diels-Alder reactions)
- General acid and base catalysis (ester hydrolysis)
- Enzymatic processes
- Co-ordination complexes (polyester condensations)
- Porphyrin complexes (epoxidations, hydroxylations)
- Ozone decomposition via chlorine atoms

Heterogeneous catalysts on the other hand, involve use of a solid-state catalyst with a liquid and/or gas reactant. Typically, reactions occur on the surface of the material. Most synthesized catalysts typically contain expensive metals such as platinum and palladium to promote reactions (catalytic hydrogenation),¹¹⁸ although others use rare-earth metals to provide stability and alternative reactions/products.¹¹⁹ Others as previously mentioned can contain a variety of transition metals which endow the catalyst with different acidic properties, giving them the potential to undergo reactions such as cracking, reduction, isomerisation, and many more. The main differences between homogeneous and heterogeneous catalysts can be seen in Table 1.1.

Table 1.1. Main characteristics of heterogeneous and homogeneous catalysis

Heterogeneous Catalysis	Homogeneous Catalysis
Variety of reaction phases Solid/Solid (S/S) <i>e.g.</i> alloys, Solid/Liquid, (S/L) and Solid/Gas (S/G)	Liquid phases are mostly used in comparison to gas phase reactions
High industrial application (over 85% of the processes)	Less preferred industrially; more complex reactions possible
Broader range of operating conditions	Generally milder reaction conditions than heterogeneous catalysts
Specialized set of analytic methods required (X-Ray methods, Operando spectroscopy)	Investigation of reactions by spectroscopic methods (NMR, MS, IR, UV-Vis) directly in solution possible.
Easy to separate	Difficult to separate

Heterogeneous catalysis plays a critical role in virtually all types of industrial processes for the production of base chemicals, and will continue to do so with the switch to more sustainable processes. By accelerating reactions by orders of magnitude, these materials enable us to obtain products in the thermodynamically most favourable regime, decreasing the use of high temperatures and/or pressures significantly. Approximately 90 % of products are obtained *via* the use of catalysts, testament to their importance in the chemical industry.¹²⁰ Some common examples include: i) production of ammonia (*via* Haber-Bosch process) using nitrogen and hydrogen;¹²¹ ii) Brønsted acid catalysts used for fluid catalytic cracking (FCC);^{122,123} iii) olefin polymerisation (*e.g.*, propylene, polypropylene) *via* Ziegler-Natta polymerisation;¹²⁴ and iv) production of nylon using noble metal catalysts (Pd, Pt).^{125,126} Of the wide array of heterogeneous catalysts, ones in

particular that stand out are the Brønsted and Lewis acid catalysts, *i.e.*, proton donors and electron acceptors, respectively. These catalysts have received much attention over the past decades for numerous processes and include a notable class of heterogeneous catalysts: zeolites.

1.4.1 Zeolites

The first zeolite minerals were discovered in 1765 by A.F. Cronstedt, a Swedish mineralogist; he discovered the mineral stilbite and described it as boiling stone due to the mineral seemingly emitting a vapour during heating, hence, the derivation of the name: ‘*zeo*’, to boil and lithos, ‘stone’.¹²⁷

Zeolites are natural or synthetic microporous crystalline aluminosilicates comprised of TO_4 ($\text{T} = \text{SiO}_4$ or AlO_4) structural units. These TO_4 units assemble into secondary building units (SBU) which can form different three-dimensional shapes (polyhedral, cubic, hexagonal) which subsequently join to create a three-dimensional framework.¹²⁸ These units, along with the primary building units (PBU), which are tetrahedra linked by oxygen bridges to form the aforementioned SBU, combine amongst each other to form a structure which is characterised by their different channels and chambers.¹²⁹ Zeolites can have more than one type of SBU, thus, they are typically classified according to this characteristic.

While zeolites are typically found in three dimensional structures, *i.e.*, three dimensional channels, other types of structures have been synthesised (Figure 1.12). For instance, one-dimensional zeolites which consist of unconnected, micropore networks,¹³⁰ and two-dimensional zeolites, where these typically derive from 3D zeolites and have a lamellar structure.^{131,132} This variety of structures provides zeolites with a variety of diffusional properties, which can impact selectivity towards products in different systems.

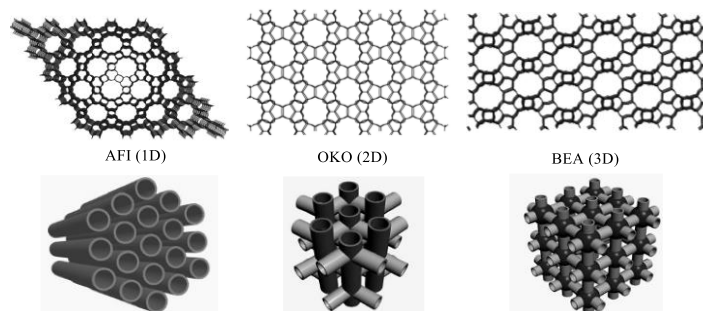


Figure 1.12 Framework examples of 1D, 2D and 3D zeolites (top) with their schematic topologies (bottom).

1.4.2 Zeolite synthesis

Zeolite synthesis typically involves in the hydrothermal treatment of an aqueous solution. A typical synthesis zeolite is carried out in the following manner (Figure 1.13):¹³³

- Amorphous reactants (usually Si and Al precursors) are mixed with a cation source (Na^+ , Ca^+) in a basic medium (primary amorphous phase). A structure directing agent (SDA) is typically used as well to obtain a homogeneous zeotype (*i.e.* same PBU and SBU).
- The homogeneous mixture is heated, typically in a sealed autoclave (for temperatures above 100 °C). Mixture undergoes changes due to the equilibration reactions which occur and is converted into a pseudo-steady-state intermediate (secondary amorphous phase)
- Reactants remain amorphous during the rise of the synthesis temperature (induction period).
- Crystalline zeolite can be detected after the induction period.
- Replacement of all amorphous material with highly crystalline zeolite after washing and drying.
- Removal of the organic template (SDA) *via* calcination.

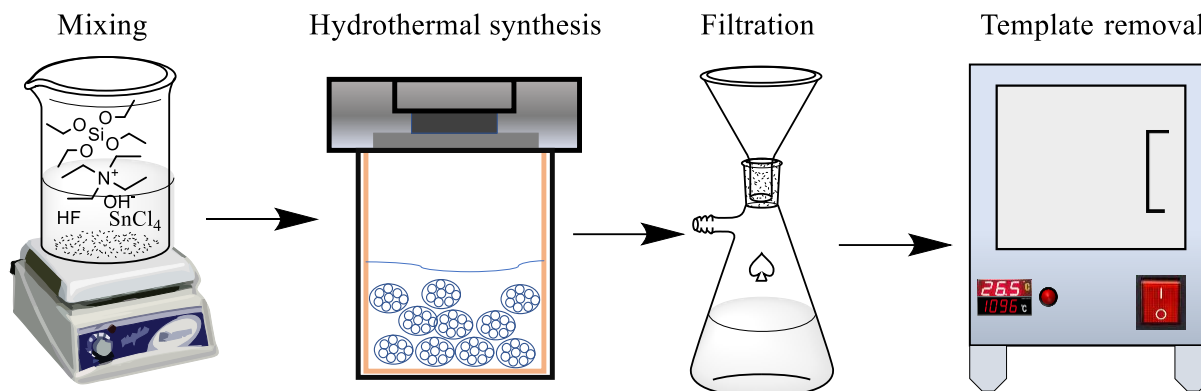


Figure 1.13. Typical procedure for hydrothermal synthesis of a catalyst.

When under hydrothermal synthesis, the particles undergo several phases of aggregation and densification; these occur when reaching primarily different size particles to create an energetically more favourable particle. Through various steps of aggregation and densification, the particles form the final crystal zeolite, as can be seen in Figure 1.14.¹³⁴

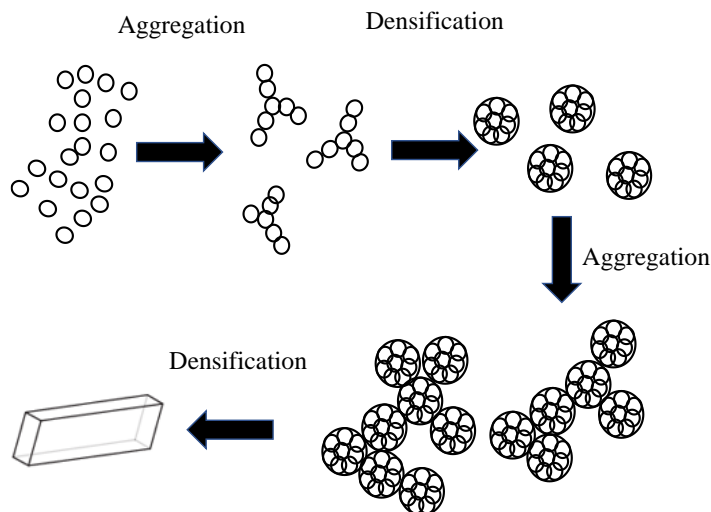


Figure 1.14. Aggregation model for the formation of zeolite crystals.

Another factor for the synthesis of a zeolite to be successful is the presence of a “mineralising” agent. This mineraliser has to carry out different functions, such as: i) it must convert the starting materials into mobile forms (i.e. taking them into solution or vapour phase); ii) carry out chemical reactivity so that the mobile units can react and form new chemical bonds and generate a framework, and; iii) de-complex from the mobile units during or after (ii) so it can exist as a stable solid phase.¹³³ Hydroxide ions are shown to be one of the most effective mineralisers.

Other than hydroxide ions, fluoride ions have also been shown to be highly effective as mineralisers for zeolites. In 1978, Flanigen showed the possibility of synthesising of a silica polymorphs using fluoride ions.¹³⁵ This new mineraliser opened up new possibilities of synthesis, primarily with incorporating different heteroatoms which would be relatively difficult and time-consuming when using hydroxide ions.

Aside from the incorporation of newer heteroatoms, the use of the fluoride and alkaline mineralisers provide substantially different sizes in regard to its crystallite.¹³⁶ Fluoride ions form larger, more well-defined crystals ($> 10\mu\text{m}$), as is shown in Figure 1.15 with fewer defects in comparison to the hydroxide.^{137,138}

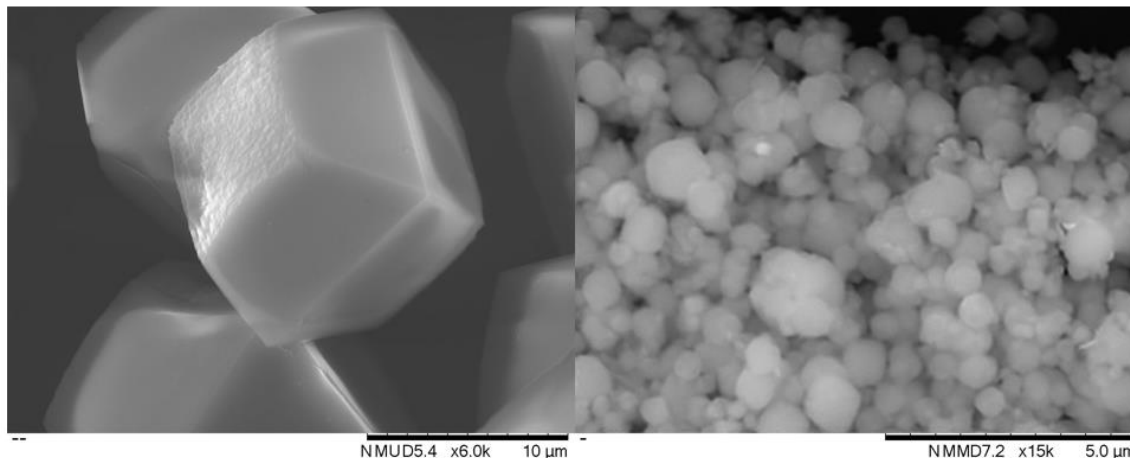


Figure 1.15. Zeolite images synthesised in fluoride media (left, 6x magnification) and hydroxide media (right, 15x magnification).

In aluminosilicates, upon condensation of these TO_4 units, the zeolite lattices are typically negatively charged due to the presence of trivalent Al^{3+} in the structure (*i.e.*, AlO_4^-). Accordingly, to maintain electroneutrality, cations from the group IA and IIA elements (sodium, potassium, calcium) are typically found to compensate the net negative charge of the framework (Figure 1.16).¹³⁹ The cation that is used to electronegatively compensates can also provide additional properties; for instance, Na^+ is used to soften ‘hard’ water, *i.e.*, water with high calcium ions, by ion exchange.^{140,141} When protons are present as charge compensating ions, zeolites are endowed with Brønsted acidity, which can be used to catalyse a plethora of reactions.

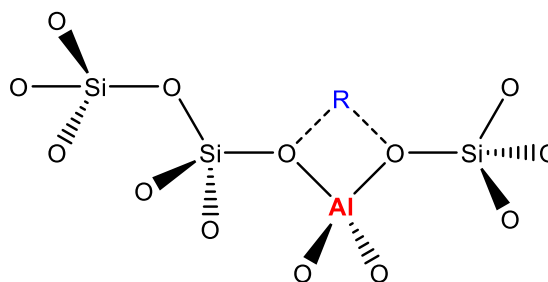


Figure 1.16. Aluminosilicate zeolite with charge-balancing cation ‘R’ to compensate the negative charge from the $[\text{AlO}_4]^-$ structural unit.

Similarly, encapsulated metals (*e.g.*, Sn, Zr, Hf) within the zeolitic structure exhibit various degrees of Lewis acidity, as shown in Figure 1.17. A Lewis acid is defined as an electron pair acceptor. A representative example of a Lewis acid consists in boron trifluoride (BF₃). BF₃ has an empty 2p orbital on the trivalent boron, which is able to accept electrons from a Lewis base. Acid strength can be tuned as well by changing the halides. For instance, BCl₃ is a stronger Lewis acid due to having a lower LUMO in comparison to BF₃.¹⁴² One of the first zeolites discovered with Lewis acidic properties was titanium silicalite-1 (TS-1) of the MFI framework. Discovered in 1983 by Eni S.p.A, the zeolite had the ability to activate peroxides, and activity for reactions such as alkylation, disproportion and isomerisation.¹⁴³ As a result, different heteroatoms have since been used to isomorphously substitute silicon atoms from the framework and tested for their activity, providing diversity in terms on Lewis acid strengths as well as product distribution.

M = Zr, Hf, Sn, Zn, Ti

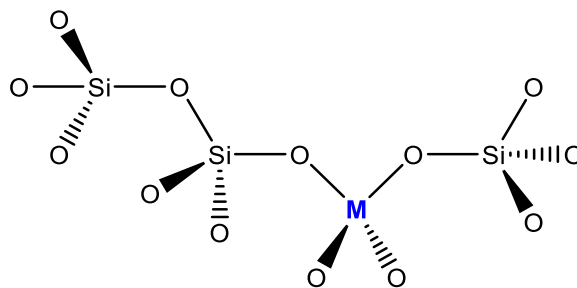


Figure 1.17. Schematic representation of a zeolite with ‘M’ metal isomorphously substituted to create Lewis acidity.

1.4.2 Optimisation of zeolite synthesis

1.4.2.1 Addition of seeds

Optimisation of the time profile of a synthesis is typically influenced by the reaction variables, such as temperature, reaction composition, and mass transfer effects. Some ways to accelerate the synthesis can be by reducing the induction period, moving a non-ideal system towards its optimum, or altering the balance between nucleation and growth.¹³³ Some ways that this has been achieved is by the addition of pre-synthesised crystal seeds to by-pass normal nucleation and to aid systems which would have trouble in the nucleation step, as well as to control their crystal size.^{144–146} Other benefits that seeds could provide is the synthesis in the absence of an organic structure directing agent (OSDA), providing a ‘greener’ synthesis of zeolites.^{147,148}

1.4.2.2. Microwave synthesis

Microwave synthesis has also shown to have significant improvements for various zeolite synthesis. This is due to the thermal gradient across the reaction volume that is presented in conventional vessels used for hydrothermal synthesis. The main advantage of microwave synthesis is the drastic shortening of reaction time required for the material to crystallise.¹⁴⁹ Furthermore, microwave synthesis can also modify the structural properties of a zeolite, i.e., producing smaller nanoparticles.¹⁵⁰

1.4.2.3. Hydrothermal synthesis *via* tumbling

Conventionally, hydrothermal synthesis involves the use of an autoclave and heating it statically. Hydrothermal synthesis under slow rotation has been shown to produce novel zeolitic frameworks, particularly nanosheets and other morphological variations of known zeolites (*i.e.*, multilamellar MFI).^{151–154} This could be due to agitation preventing excessive aggregation, hence, the smaller final crystal size.

1.5 Catalyst deactivation

One of the pertaining challenges that comes with using zeolites for biomass conversion is catalyst deactivation. Catalyst deactivation consists of the loss of the catalyst's selectivity or activity over time. Preventing this from occurring is a great challenge for research, given that large scale operations suffer greatly due to the cost of this problem. There are numerous ways these solid catalysts can be deactivated, the most common of which are summarised in Table 1.2 and are fully described in the following section.

Table 1.2. Types of catalyst deactivations.¹⁵⁵

Mechanism	Type	Description
Poisoning	Chemical	Chemisorption of species/compounds on the active sites of the catalysts
Fouling	Mechanical	Physical deposition of species from fluid phase onto the catalytic surface and in catalyst pores
Thermal degradation	Thermal	Thermally induces loss of catalytic surface area, support area and active phase-support reactions
Vapor formation	Chemical	Reaction of gas with catalyst phase to produce volatile compound
Vapor-solid and solid-solid reactions	Chemical	Reaction of fluid, support, or promoter with catalytic phase to produce inactive phase
Attrition/crushing	Mechanical	Loss of catalytic material due to abrasion, loss of internal surface area due to mechanical-induced crushing of the catalyst particle

1.5.1 Fouling/Coking deactivation

Fouling, more generally known as “coking”, is one of the most prominent forms of deactivation, particularly for porous catalyst such as zeolites. Deactivation in this case generally occurs through the accumulation of carbonaceous residue within, or on top of, the catalyst, blocking access of the reactants to the active sites which are embedded within the porous framework (Figure 1.18). One of the classical examples of coking is Fluid Catalytic Cracking (FCC), which involves in the use of acidic zeolites to catalytically crack heavy hydrocarbons (high molecular weight) into smaller carbon number compounds.¹⁵⁶ This fouling can arise from:

- Heavy components that are present in the feed
- Reactants that are not soluble in the solvent
- Unstable by-products that have been produced with the catalyst

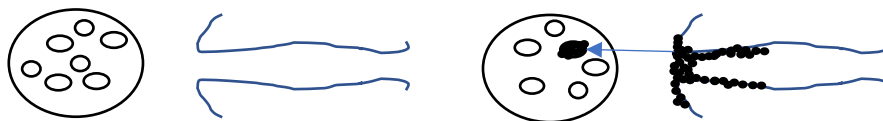


Figure 1.18. Visual representation of catalyst deactivation by fouling in the pore mouth.

This deactivation is primarily caused due to the zeolites' small pore size and structure, making these two parameters just as crucial as acid strength and density for a zeolite, depending on the type of process in which the zeolite is used, according to Guisnet *et al.*¹⁵⁷

Deactivation *via* coke deposition consist in two categories: reversible and irreversible. Figure 1.19 provides an illustration on four possible modes of deactivation by carbonaceous deposits with the ZSM-5 zeolite. Mode 1 depicts a reversible adsorption on acid sites; Mode 2 an irreversible adsorption on sites with partial blocking of pore intersections; Mode 3 shows a partial steric blocking of pores; Mode 4 illustrates an extensive steric blocking of pores by exterior deposits.^{155,158}

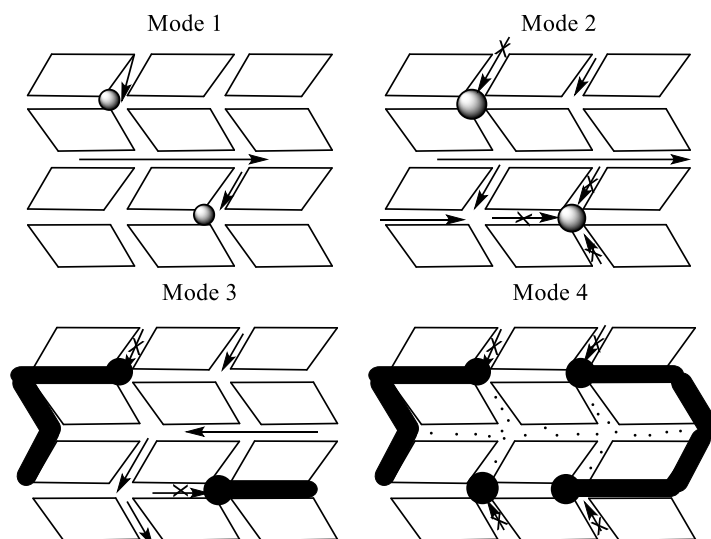


Figure 1.19. Possible methods of deactivation by coke deposition in ZSM-5 (adapted from Guisnet *et al.*).

1.5.2 Poisoning

Poisoning consists in the strong chemisorption of reactants, products, or impurities on the active site. This accumulation on the surface of active site inhibits it from carrying out any additional reactions, rendering it inactive, as shown in Figure 1.20. Mechanistically, poisoning is a complex process which can involve: i) physical blockage of one or more catalytic site; ii) electronic modification of the nearest neighbour atoms, or iii) hindering surface diffusion of adsorbed reactants.¹⁵⁵

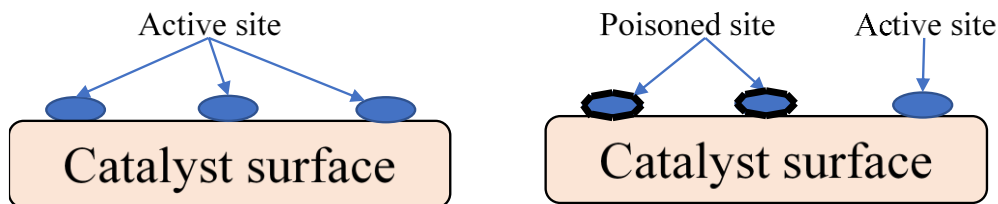


Figure 1.20. Catalyst deactivation by poisoning.

Some of the most well-known poisons are sulphur, which is especially problematic when catalytically upgrading bitumen-derived heavy oils. A high content of sulphur leads to the rapid deactivation of the catalyst in downstream refining but can also produce harmful SO_x emissions.^{159,160} For instance, poisoning by sulphur, lead, or arsenic can deactivate the catalyst irreversibly due to the strong interaction they have with the active sites.^{161,162} Thus, it is more convenient to purify the reactants originally, if possible, rather than removing the poison from the active site.

1.5.3 Thermal degradation and sintering

Thermally induced degradation of catalysts consists of deactivation due to use of elevated temperatures. This deactivation can occur through various means, such as: i) loss of surface area due to crystallite growth of the catalytic phase; ii) loss of support area due to collapsing of crystallites of the active phase; and iii) modifications of the catalytically active site. The first two mentioned fall under sintering (Figure 1.21), which is the process of forming a solid mass by heat (generally $>500\text{ }^\circ\text{C}$), and pressure, whilst the last one can occur *via* a solid-solid reaction.¹⁶³ This temperature is called Tamman temperature for lattice (bulk) recrystallisation for metal oxides, and Hüttig temperature, which is the temperature for surface recrystallisation for metal oxides.¹⁶⁴ These types of deactivation, just as poisoning, are typically irreversible or difficult to reverse.

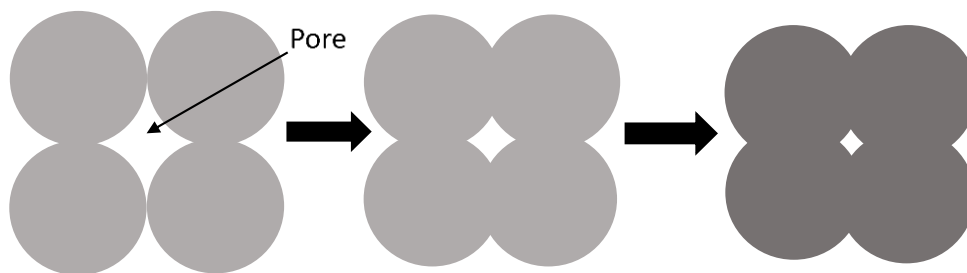


Figure 1.21. Modification of crystal and pore structure *via* sintering.

1.5.4 Gas/vapour with solid interaction restructuring

Restructuring gas/vapour-solid interactions are similar to the restructuring of surface caused by sintering, although below the Tamman and Hüttig temperatures. Some examples include the sintering of Ni/Al₂O₃ in methanation due to the formation of Ni(CO)₄ and its subsequent downstream decomposition to large Ni crystallites. This can lead to weakening metal-support interactions, resulting in sintering.^{165,166}

1.5.5 Leaching

Leaching results from a solvolysis of species of the catalyst into solution. There exist three different scenarios for heterogeneous catalysts in the liquid phase:¹⁶⁷

- 1) The metal does not leach, and catalysis is fully heterogeneous.
- 2) The metal leaches, but the leached component does not show any activity. This, nevertheless, is considered mainly heterogeneous catalysis.
- 3) The metal leaches and forms a homogeneous catalyst; this type of catalysis is considered homogeneous in nature.

Leaching is considered irreversible due to the active sites being flushed out of the reactor. Furthermore, it can have significant consequences for the process. Due to the solubilisation of the catalytic material with the feed, the final product can potentially be hazardous; additionally, it can decrease the economic potential.¹⁶⁸

Two forms to verify that leaching has not occurred involve analysing the of the liquid phase of the reaction or the heterogeneous catalysts. Inductively Coupled Plasma Mass Spectroscopy (ICP-MS) or Atomic Emission Spectroscopy (AES) can be used for the liquid phase, whereas X-ray Fluorescence (XRF) or Energy Dispersive X-Ray (EDX) can be applied to the solid catalyst. To

determine if the catalyst is leaching in the reactor, a hot filtration test can be applied (Figure 1.22). This involves removing the catalyst from the reactor mid-reaction, to determine if any ongoing catalytic activity following removal of the solid is present. Ideally, catalytic activity should cease from the moment the solid catalyst is removed from the reactor.¹⁶⁹

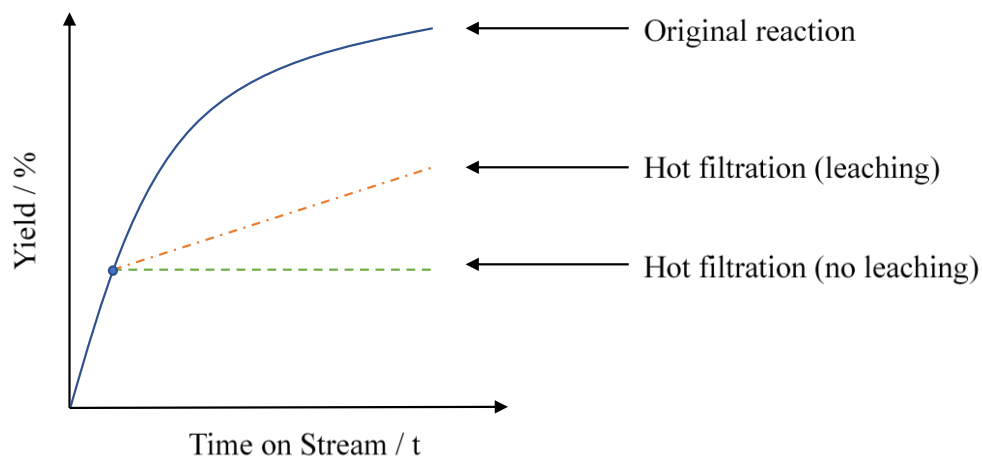


Figure 1.22. Schematic representation of a reaction in batch reactors demonstrating hot filtration tests with leaching and non-leaching.

1.5.6 Hydrothermal dissolution

Lastly, deactivation by hydrothermal dissolution entails the loss of zeolite crystallinity upon processing in hot water, as can be seen in Figure 1.23.¹⁷⁰ Just like most of the methods of deactivation, hydrothermal dissolution is irreversible due to the result of the dissolution producing new phases of metal and metal oxides, restructuring such as sintering, or partial/complete amorphization of the catalyst. For instance, when applying water to zeolite Beta in continuous flow, a high amount of amorphization can be observed by powder X-ray diffraction (XRD) and porosimetry.¹⁷¹ According to Ravenelle *et al.*, the hydrothermal dissolution of zeolites consists in the hydrolysis of the siloxane bonds; particularly, Si-O-Al hydrolysis is proton catalysed, whereas hydroxyl ions catalyse siloxane bond cleavage.¹⁷² When undergoing siloxane hydrolysis, a Si-O-Si bond is broken, forming two SiOH groups.¹⁷³ This reaction is further accelerated due to the strong interaction between the water molecules and hydroxyl ions, creating more defective groups within the framework.

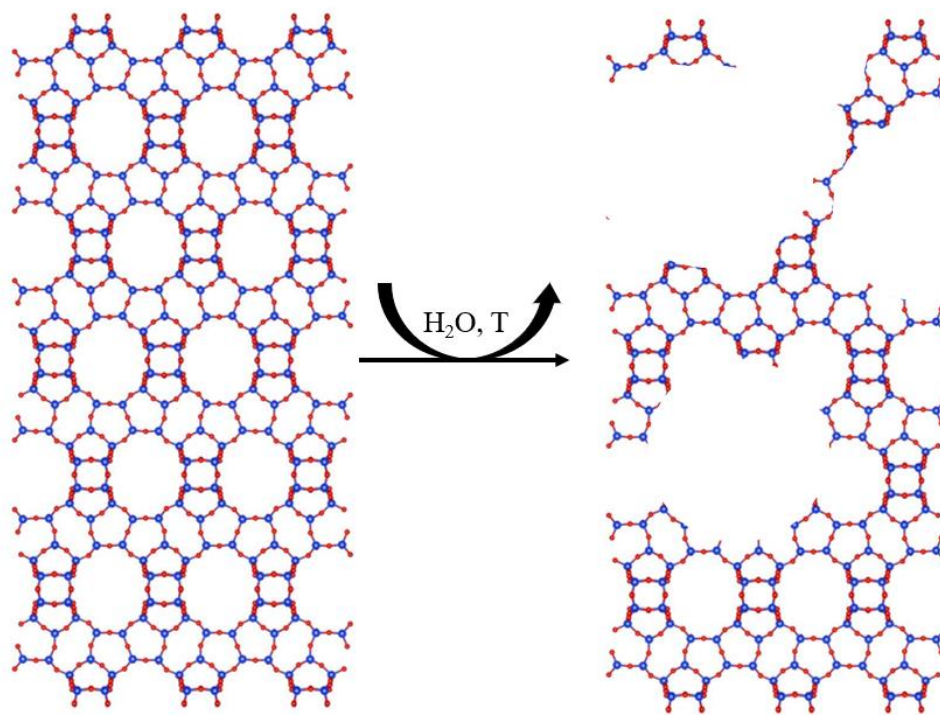


Figure 1.23. Hydrothermal dissolution of Beta zeolite.

Other types of deactivations attacking specifically the active metal site can occur. In the presence of steam, aluminium atoms can be removed from the zeolite lattice, resulting in the formation of extraframework aluminium (EFAI).^{174,175} These form a different alumina phase outside the framework, which has been associated as aluminium in the form of octahedrally coordinated aluminium.

1.6. Structural modification of zeolites

As previously mentioned, natural zeolites are inherently microporous (pore diameter – $d_p = < 2$ nm). Nevertheless, the creation of synthetic zeolites has allowed the creation of a plethora of zeolites with different porosity. Mesoporous ($d_p = 2-50$ nm) and macroporous ($d_p = >50$ nm) zeolites have been synthesised to combat steric hindrances, modification of selectivity or products, or to provide a higher lifetime for zeolite catalysts in certain processes.¹⁷⁶⁻¹⁷⁸ Furthermore, these pore channels can be combined to create micro-meso or micro-macro porosity. These zeolites are

known as hierarchically organized materials, or simply hierarchical zeolites. Because of this bimodal porosity, hierarchical zeolites can outperform purely microporous materials in certain applications.¹⁷⁹

While zeolites tend to deactivate through various means, modifications on the framework have been prepared to mitigate some of the effects of deactivation or provide enhanced properties in terms of activity, selectivity, or even the use of bulkier substrates. Generally, there are two approaches to modify and/or synthesise zeolites; these consist in ‘bottom-up’ and ‘top-down’ approaches.

1.6.1. Bottom-up zeolite synthesis

The bottom-up approach methods use the concepts of molecular self-assembly and/or molecular recognition, which was described in Section 1.4.2. This consists in the synthesis of zeolites primarily from a sol-gel precursor or a homogeneous mixture, and subsequently crystallising the zeolite from this gel hydrothermally under autogenous pressure.¹⁸⁰ All zeolites are typically synthesised by this method, using a specific Organic Structure Directing Agent (OSDA) to modify structure. However, within the realm of bottom-up approaches, modifications or more specifically, additions to the zeolite sol can be done. A great part of these modifications’ out-turn consists in creating mesoporosity. Some examples including the use dual templating, *i.e.*, addition of a second OSDA to the original OSDA to create the specific framework to create mesopores in the zeolitic framework,^{181,182} or using a multifunctional template, which has the function of two OSDA, forming a micro/meso zeolite or 2D zeolites^{153,183} These can further be divided by ‘soft’ and ‘hard’ secondary templates.

1.6.1.1 ‘Soft’ secondary template.

These templates are denominated soft due to their flexibility and versatility compared to their ‘hard’ template counterparts. These templates can act as a physical scaffold which can replace the OSDA or can have a certain chemical interaction with the zeolitic phase.¹⁸⁴ Some of these include the use of polymers and silylated surfactants such as trimethoxysilylpropyldimethyloctadecyl ammonium chloride.^{185,186} Some examples of polymers are the use of cationic polymers poly(diallyldimethylammonium) (PDDA) chloride and polyethyleneimine (PEI) for the functionalisation agents to create a zeolite membrane.¹⁸⁷ Moreover, PDDA can also be used in

addition to an OSDA to synthesis hierarchical (*i.e.*, micro-meso zeolite), showing the high versatility that can be obtained using the same polymers.¹⁸⁸

Crystal structure can also be controlled with the implementation of polymers.¹⁸⁹ Polyacrylamide (PAM), for instance, has been shown to form hollow ZSM-5 crystals *via* dissolution-recrystallisation method.¹⁹⁰ Polystyrene has a similar effect, as shown by Valtchev, creating Silicalite-1 hollow spheres (Figure 1.24).¹⁹¹



Figure 1.24. Application of polystyrene for Silicalite-1 hollow spheres.

1.6.2 “Hard” secondary template

Hard templates have been used for synthesis in a wide array of zeolites and metallophosphates; they generally consist in plant materials, aerogels, and more typically carbon compounds.¹⁸⁴ The function of these hard templates is to infiltrate the solution, planting itself within the zeolite precursors where it undergoes typical hydrothermal synthesis. Lastly, when calcining (to remove the template), the templates are combusted or undergo dissolution along with the conventional OSDA, creating additional cavities within the zeolitic framework.¹⁹² However, there may exist some drawbacks when it comes to destroying the hard template; this can be due to the conditions required to destroy which can have a detrimental effect on the zeolitic framework.

1.6.2.1 Carbon-based hard templates

Carbonaceous templating is one of the most common hard templates to create hierarchical zeolites. This involves the use of carbon nanostructures such as nanoparticles, nanowires or nanotubes, which are subsequently removed just like most hard templates (calcination, acid dissolution). Carbon templates have been applied in a variety of different topologies (LTA, BEA, FAU),

confining the zeolite in a three-dimensionally ordered mesoporous structure (3DOM) (Figure 1.25).¹⁹³ As demonstrated by Chen *et al.*, the confinement with 3DOM increased the overall surface area and created mesopores, and showed an increase in mesopore size with respect to the size of the 3DOM carbon.

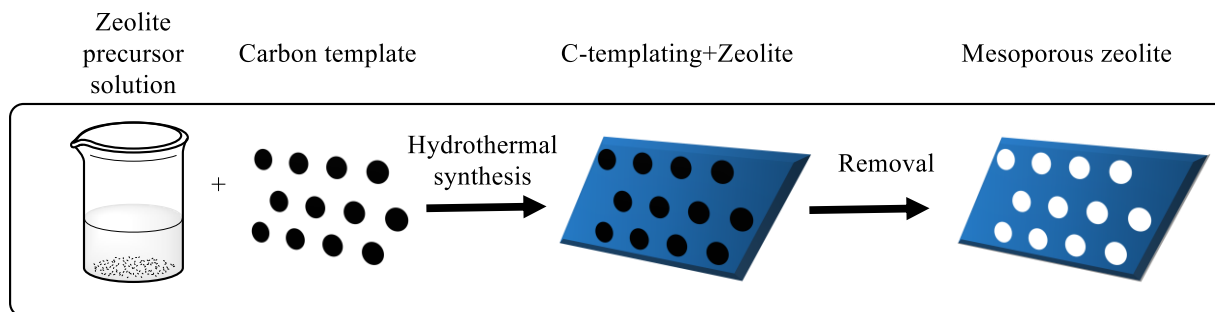


Figure 1.25. Implementation of carbonaceous template for mesopore creation in zeolites.

1.6.2.2 Cellulose as a hard template

Abdulridha *et al.* successfully synthesised Y zeolites (FAU) with cellulose nanocrystals, creating a highly mesoporous zeolite without any effects towards its crystallinity. Other than being relatively easy to remove (at 600 °C), the use of cellulose nanocrystals provides a more economic and sustainable way to synthesis mesoporous FAU zeolites which require typically toxic hard/soft templating.¹⁹⁴

1.6.2.3 Other hard templates

Nanosized calcium carbonate can also be applied to create mesopores in the range of 50-100 nm. These crystals follow the relatively same procedure in which they are trapped in the zeolitic framework, when the nanoparticles are removed *via* acid dissolution they give similar results to Figure 1.25.¹⁹⁵

Another interesting hard template that has been used for the preparation of nanoporous carbons, consists in MgO precursor (MgO, magnesium acetate, citrate, gluconate) templating. Along with a carbonaceous polymeric precursor (PVA, PET, HPC), this methodology can prepare various carbon precursors, such as activated carbon, without the need for stabilisation and activation processes. This template can be applicable to zeolites, where Linares synthesised a Silicalite-1

with intracrystalline mesoporosity using MgO, showing an effective synthesis and preserved crystallinity.¹⁹⁶

Advantages of the MgO precursors consist in: i) MgO being removable with a diluted non-corrosive acid; ii) recyclable; ii) the size of the mesopore is tuneable according to the MgO precursor used; iv) micropore size and volume are controllable by carbon precursor used.

1.7 Top-down approach

In contrast to the ‘bottom-up’ approach, where the material (*i.e.*, carbon, polymers, silylated surfactants) is added to the hydrothermal sol-gel from the start and assembled step by step to modify the zeolite, top-down synthesis consists of treating the finished zeolite to introduce the intracrystalline mesoporosity. Generally called post-synthetic treatment, this approach comprises of two distinctive treatments: demetallation and desilication. However, demetallation does not necessarily modify the overall structure of the catalysts so much rather that it endows it with different catalytic activity depending on the metal incorporated.

1.7.1 Desilication

Desilication, is an example of a top-down method used to leach out silicon atoms to create hierarchical zeolites. One of the first instances of desilication was reported by Cizmek *et al.*, where he showed the dissolution of high-silica zeolites under 5 M NaOH solution. Desilication according to this mechanism has been attributed to two reactions:¹⁹⁷

- 1) Breakage of Si-O-Si and/or Si-O-Al bonds through the OH⁻ of the solution.¹⁹⁸
- 2) Formation of solid phases caused by reactions of the soluble species and/or from the dissolved solids.¹⁹⁹

Ogura *et al.* thereafter carried out desilication under mild conditions (0.2 M NaOH) to create uniform mesopores (*ca.* 4 nm in diameter) on ZSM-5.²⁰⁰ This, however, diminished the micropore area by around 40 %. By analysing the parameters such as temperature, stirring speed, time and Si/Al ratio, it was found that framework aluminium plays a role in the post-treated zeolite, in which it was determined that aluminium has a crucial role for silicon extraction.²⁰¹ It was found that the

extraction of silicon could be suppressed by the presence of adjacent aluminium in the framework.²⁰² With a lower Si/Al (*i.e.*, more aluminium in the framework), silicon extraction is hindered due to the Si-O-Al bonds in the presence of hydroxide ions despite the relative ease of Si-O-Si extraction, as can be seen in Figure 1.26.

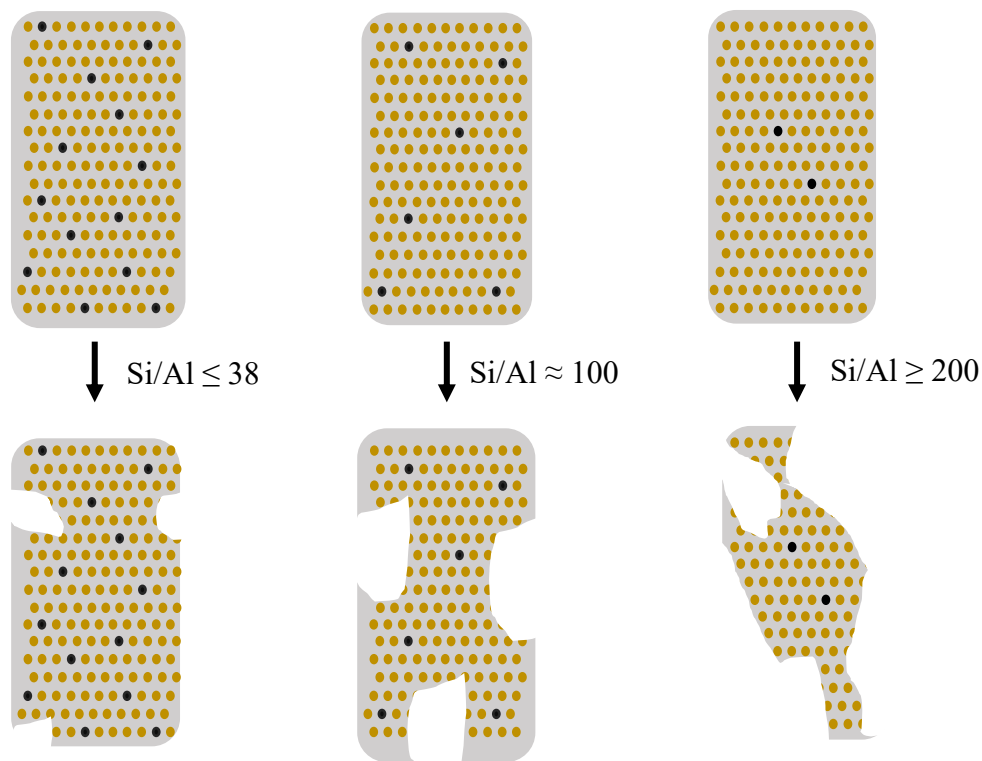


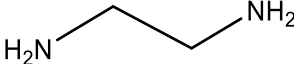
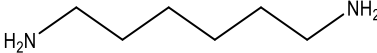
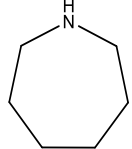
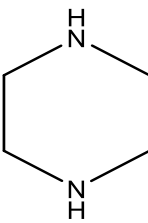
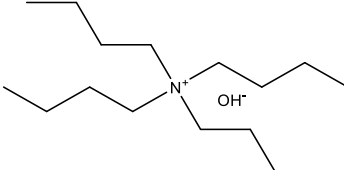
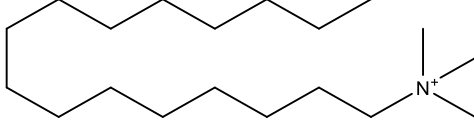
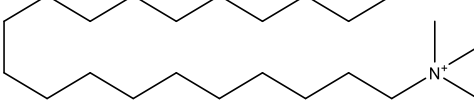
Figure 1.26. Desilication effect on different Si/Al ratios. Adapted from reference 187.

1.7.2 Surfactants and amines for pore-size tuning

The use of different pore-directing agents (PDAs) for pore size tuning can not only improve rates of deactivation but also allow other materials to catalyse bulkier substrates where it could not be possible if used in its innate form (*e.g.*, MFI with glucose isomerisation). Post-synthetic leaching can further be tuned with the use of quaternary ammonium cations along with the alkaline solution. The use of (PDA) also can also be essential to mitigating any amorphization that can occur when desilicating with alkaline media if the Si/Al ratio is high (> 200).

One of the most prominent examples is the use of cetyltrimethylammonium bromide (or chloride) (CTA^+). However, there are a multitude of PDA that can be used as mesoporegens, as can be seen in Table 1.3:

Table 1.3. Reactants used as PDA for mesopore creation.

Name	Structure	Ion	Method	Ref
Ethylenediamine		-	T-D	203,204
1,6-Diaminohexane		-	B-U	204,205
Hexamethyleneimine (Azepane)		-	B-U, T-D	206,207
Piperazine		-	T-D	207
Tetrabutylammonium		OH ⁻	T-D	208
Hexadecyl trimethylammonium		Br ⁻ , Cl ⁻ , OH ⁻	B-U, T-D	209,210
Octadecyl trimethylammonium		Br ⁻ , Cl ⁻	T-D	211

*T-D = Top-down approach

*B-U = Bottom-up approach

PDA's can be cationic tetraalkylammonium (TAA) surfactants or in non-ionic organic amines. These are effective in protecting the parent zeolitic framework and capable of directing mesopore formation when undergoing base leaching. Amines have also been shown to create larger mesopores ($d = 5-8$ nm) compared to those treated with TAA ($d = 2-6$ nm).²⁰⁴ This could be due to how the TAA can accommodate itself better within the channels of the framework and have a more favourable interaction, irrespective of their length (carbon atoms: 10-20), in contrast to the amines.

Since TAA are composed of an attractive segment long hydrophobic carbon chain (cetyl, octadecyl) and a repulsive segment which would be the cationic quaternary ammonium, these surfactants self-assemble to create micelles. A micelle consists of an aggregate of surfactants which arrange themselves in an aqueous solution; these act as templates and confine themselves into the zeolitic framework while leaching is carried out, where they can be subsequently calcined to release the space which would correspond to the mesopore, as is shown in Figure 1.27.

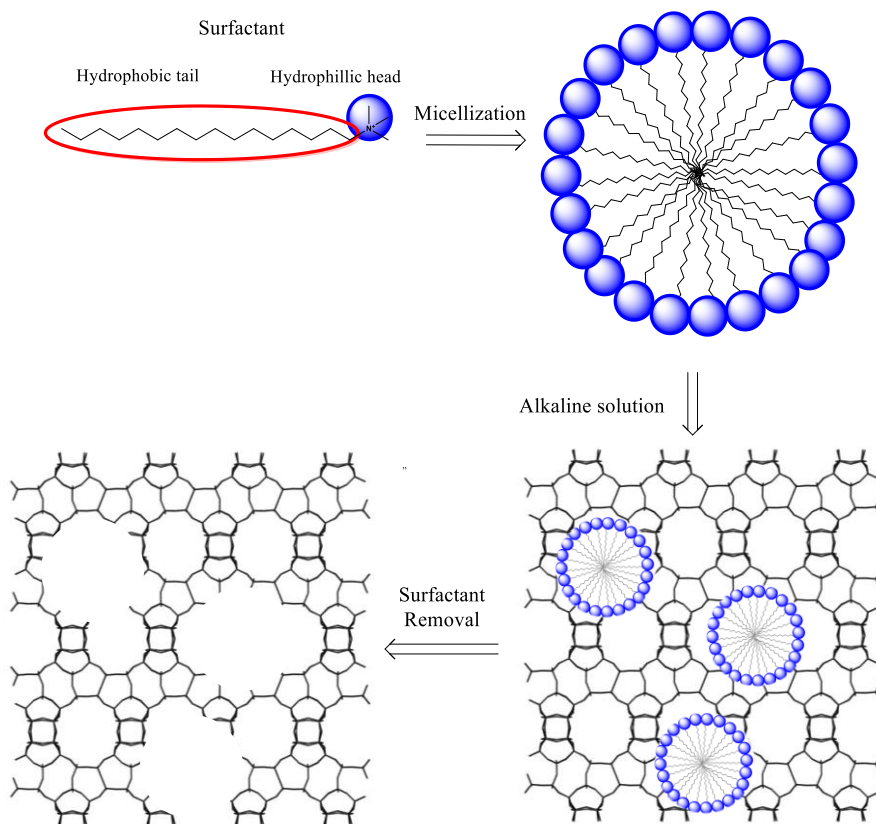


Figure 1.27. Formation of micelle from surfactants such as CTA^+ , and subsequent infiltration and removal of the micelle to form the mesopore.

1.8 Sn-incorporated zeolites

Of the previously mentioned Lewis acid zeolites, one that stands out for its activity is the Sn incorporated zeolites. One of the most common frameworks to isomorphously substitute this heteroatom is the beta zeolite, although there have been incorporation of Sn into other frameworks, such as Sn-TUD and Sn-MFI.^{212,213} First synthesised in 1997 by Mal and Ramaswamy,²¹⁴ Sn-Beta

was shown to be highly active and selective in the acetylation of trimethylstyrene (1,3,5-trimethylbenzene) to 2,4,6-trimethylacetophenone.

Beta zeolites are one of the few zeolites which are comprised of intergrown polymorphs, creating a disordered framework, as is shown in Figure 1.28. This disorder comes from the [001] plane from the two or three of these polymorphs (A, B, and C), which are all mutually intersected along the 12-ring channels.^{215,216}

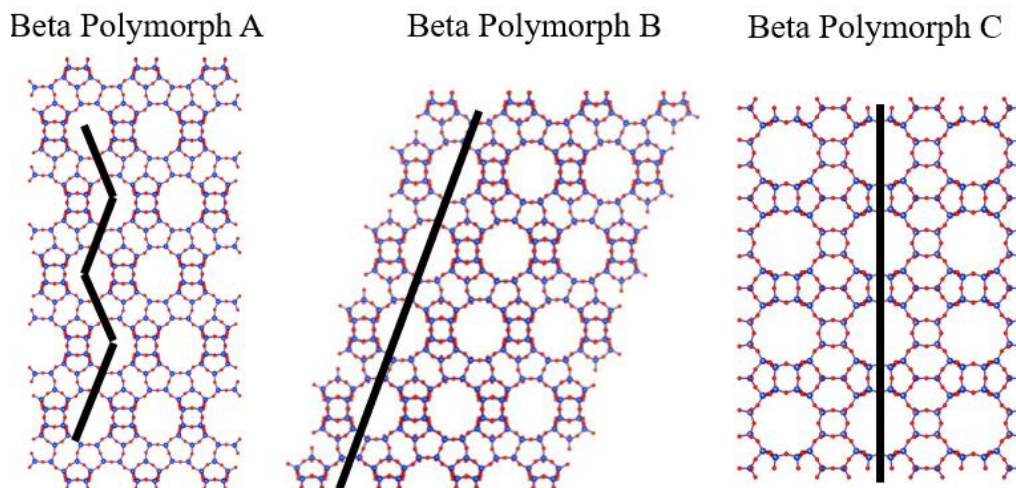


Figure 1.28. Polymorphs of beta framework. Lines indicating the location of the 12-membered rings.

For Sn-Beta synthesis, it is typical to use fluoride ions due to the relative difficulty of Sn incorporation caused by the increased atomic radius.²¹⁷ The use of this mineraliser along with a stoichiometric amount of SDA (tetraethylammonium hydroxide – TEOH) ensures the crystallisation of the zeolite. This also is particularly important to guarantee no other zeotypes are produced.²¹⁸

1.8.1 Sn incorporation *via* demetallation

Another method that does not require the use of fluoride as a mineraliser consists in demetallation. Demetallation, as the name says, is a top-down approach which consists of stripping framework heteroatom (not silicon) atoms. Due to the typically lower quantities of the heteroatom (high Si/M ratio), demetallation does not destroy the micropore structure. This is undoubtedly one of the most useful and widely used modifications due to the significant post-application that can be achieved with the post-treated zeolite. One of the most common framework atoms, aluminium, typically

uses a highly concentrated acid (e.g., HNO_3) at mild temperature ($100\text{ }^\circ\text{C}$). This creates silanol ‘nests’ where a variety of heteroatoms can be reinserted by different means, such as solid-state incorporation (Figure 1.29)^{171,219} and incipient wetness impregnation.²²⁰ This creates the possibility to incorporate different heteroatoms other than Sn,^{221,222} such as Hf,²²³ Zr,²¹⁹ Nb^{224,225} and many more. A higher degree of incorporation is possible in contrast to the bottom-up hydrothermally synthesized approach, which can only achieve relatively low percentages (*ca.* 1 wt %), whereas post-synthetic incorporation can achieve up to 5 wt % of the heteroatom.²²⁶ In addition, the use of demetallation also has shown to increase zeolite’s mesoporosity.

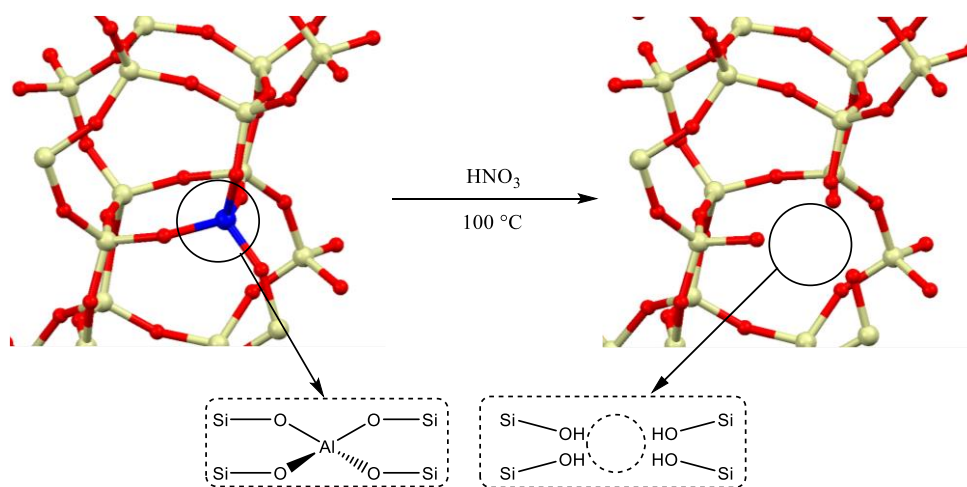


Figure 1.29. Schematic representation of demetallation of Beta zeolite.

Other than HNO_3 , other acids have been implemented and have shown good results when it comes to demetallating. Oxalic acid, for instance, can easily remove framework aluminium from the zeolite, reaching up to a Si/Al molar ratio of more than 100 at room temperature without any severe effect on the crystallinity and or textural properties. Silicon tetrachloride (SiCl_4) has also been shown to demetallated as well as occupy the silanol nests left by the aluminium atoms. This can potentially heal pre-existing defects the original material may have had. When used for demetallation, SiCl_4 can result in the formation of hydrochloric acid, which can subsequently cause further demetallation.²²⁷ The combined use of mild acids and calcination has also been tested by Müller *et al.*, using a mild concentration of oxalic acid along with calcination treatment.²²⁸ This resulted in a framework with higher flexibility which enabled interaction between Brønsted protons and oxygen atoms in the framework.

1.8.2. Synthesis of heteroatom-substituted zeolites

A major advantage with the use of demetallation is the creation of vacant sites (silanol nests, Figure 1.26) for another heteroatom to isomorphously substitute itself and endow a zeolite with diverse catalytic properties. One method consists in the solid-state ion-exchange or incorporation (SSI) of a zeolite whose aluminium atoms have been stripped by a highly concentrated acid (*e. g.*, HNO₃).¹⁶⁹ This involves in the mechanochemical grinding of the desired metal precursor into the dealuminated zeolite. Subsequently, the sample is calcined and the resulting zeolite with a new heteroatom is successfully substituted. Various elements have been incorporated in different frameworks, for instance: Cu,²²⁹ Mn,²³⁰ Ti, Sn, and Zr.^{219,231} Other than mechanochemical grinding, post-synthetic impregnation has been carried out by liquid-phase grafting, reflux, or by passing a vapourised metal precursor through the sample.^{232,233}

SSI, unlike traditional bottom-up synthesis, have the ease of incorporating a more-than-usual quantity of heteroatoms. In particular Lewis acid zeolites such as Sn, Ti, Zr, Nb, and Hf in the zeolite (1 wt. % bottom-up vs. up to 5 wt. % top-down) if provided with the adequate number of vacant sites.²²⁶ Incorporation of these heteroatoms at higher than 1 wt. % (in a bottom-up approach) would lead to a drastic retardation of zeolite nucleation (*ca.* 40 days) needed for the amorphous sol-gel to crystallise and create the zeolite crystals.¹⁶⁹

1.9 Sn-Beta for biomass valorisation

1.9.1 Baeyer-Villiger oxidation

Over time, a variety of reactions have been shown to be effectively catalysed by use of Sn-incorporated (Beta) zeolites. The Baeyer-Villiger oxidation (BVO) is used to convert ketones and aldehydes into more valuable esters and lactones. Traditionally performed with use of peracids, the implementation of Sn-Beta zeolites and hydrogen peroxide (Figure 1.30), discovered by Corma *et al.*, in 2001, results in a less polluting and cheaper oxidation taking place.^{234,235} Furthermore, Hammond *et al.* have reported the upgrading of 4-substituted cycloketones (4-isopropyl cyclohexanone) using Sn-Beta (normal and hierarchical) under continuous flow, showing the potential for these catalysts to achieve a sustainable production of renewable lactone monomers.²³⁶

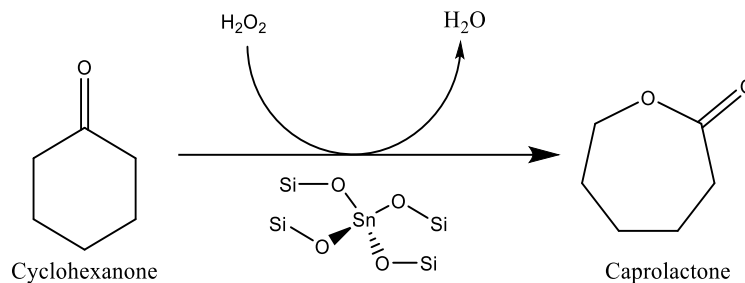


Figure 1.30. Baeyer-Villiger oxidation using Sn-Beta and hydrogen peroxide as catalyst and oxidant, respectively.

Due to the bifunctional nature of the Sn sites, the Lewis acidic tin atom can activate the carbonyl group whilst the adjacent basic oxygen atom of the Sn-OH can form a hydrogen bond with H_2O_2 .²³⁷ This discovery allowed more studies to come for Sn-Beta in oxidation reactions.^{238–240} Although Ti-containing zeolites have a well-established application in this area, it has been shown that Sn-Beta to be an alternative to Ti-containing zeolites, particularly as they both exhibit different types of performance. For instance, with the reactant dihydrocarvone, Sn-Beta is capable of being fully selective for the lactone whereas Ti-Beta showed selectivity towards the epoxide and diols.²⁴¹

1.9.2 Meerwein-Ponndorf-Verley-Oppenauer reduction.

The Meerwein-Ponndorf-Verley (MPV) reduction of ketones and aldehydes along with the complementary Oppenauer oxidation (MPVO) have been shown to be particularly useful reactions due to their highly chemoselective nature (*e.g.*, C=C bonds are not attacked) and mild conditions it requires to undergo reaction.^{237,242} MPV involves the use of secondary alcohols as hydrogen donors whereas in MPVO the ketone is the oxidant. The reaction begins with a cyclic six-membered transition state where the oxidant and reductant (ketone and secondary alcohol, respectively) are coordinated with the metal centre, and undergo an intermolecular hydride transfer from the alcohol to the carbonyl, as shown in Figure 1.31.^{243,244}

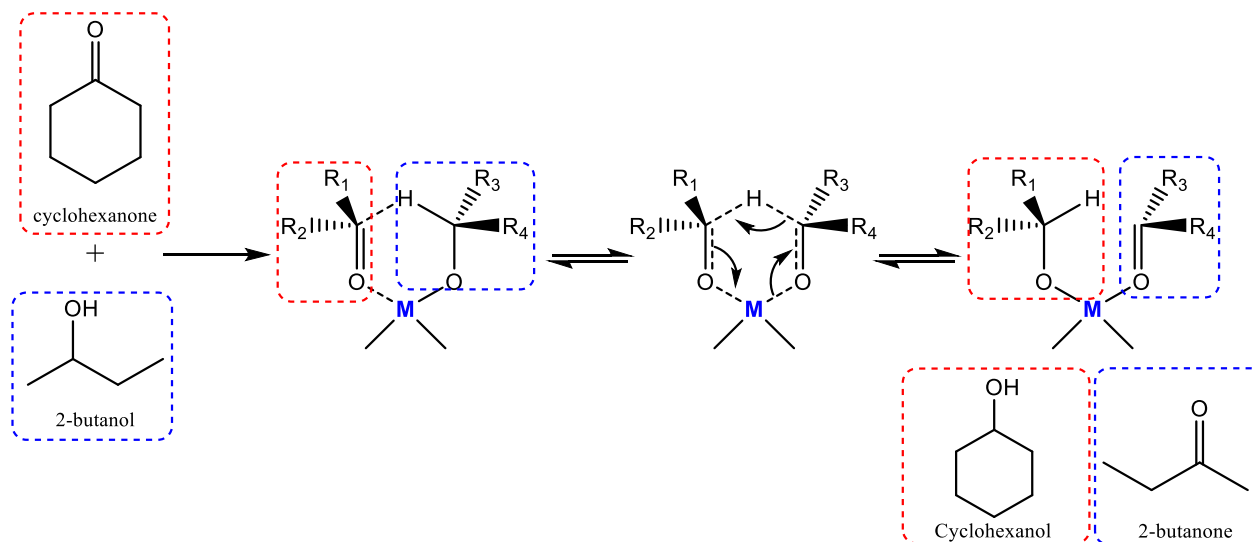


Figure 1.31. General mechanism of MPVO reaction using a Lewis acid metal centre.

While the MPV reaction may differ from BVO, they share a lot of similarities as to how they are catalysed. Both reportedly use the same partially hydrolysed Sn-OH groups that were found active for BVO reactions which can form a hydrogen bond with H₂O₂. The steps using Sn-Beta are essentially the same as with using other metal centres, such as Zr-Beta or aluminium alkoxides. Firstly, adsorption of ketone and alcohol on the Lewis acid centre is required. Subsequently, deprotonation of the alcohol occurs, followed by C-C hydride transfer, proton transfer from the catalyst, and lastly product desorption.²³⁷

1.9.3 Sugar isomerisation

As mentioned previously, glucose and xylose are the main basic units of cellulose and hemicellulose, respectively. Glucose, as the only monomer in cellulose, which is the most abundant lignocellulosic biomass, has been extensively studied to show the potential of valorisation using heterogeneous catalysts. It was not until 2009 that Moliner *et al.* demonstrated the potential of Sn-Beta to isomerise glucose to fructose, showing as well the ability to catalyse this reaction in water.²⁴⁵ Prior to this, Holm *et al.* also showed the ability for sucrose, glucose and fructose dissolved in methanol to be converted into racemic methyl lactate in yields up to 68%.²⁴⁶ This can potentially provide advantages through valorisation by chemical means with respect to

the enzymatic route due to the strict conditions needed to be applied for the enzymes to take activity. Given the resilient properties of zeolites, reactions can take place at elevated temperatures, exceeding the maximum conversion obtainable governed by the thermodynamic equilibrium by the enzyme glucose isomerase, which is done industrially at 333 K (*ca.* 50 % wt/wt glucose and 42 % wt/wt fructose).²⁴⁷

While glucose and fructose are normally present in cyclic six-membered (aldopyranose and ketopyranose) and five-membered (aldofuranose and ketofuranose) forms,²⁴⁸ it has been shown by Roman-Leshkov *et al.* that the sugar is adsorbed on Sn-Beta in their open-chained form, without exhibiting any apparent reaction barriers when ring-opening and ring-closing occurs (Figure 1.32).²⁴⁹ Their proposed mechanism consists of: i) coordination of glucose to active site; ii) intramolecular hydride transfer, and; iii) desorption of fructose from zeolite. Just like previous reactions (BVO and MPV), it is suggested that glucose isomerisation activity is more in open sites than closed sites.

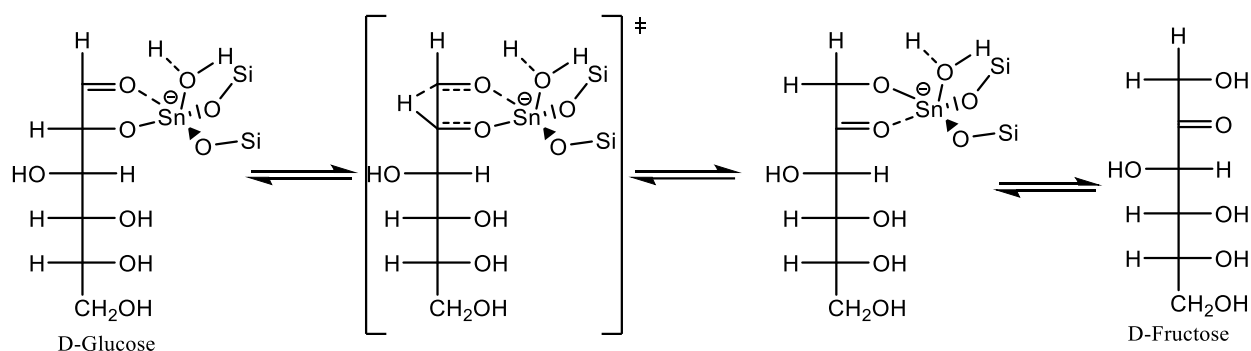


Figure 1.32. Glucose to fructose isomerisation mechanism proposed by Roman-Leshkov *et al.*²⁴⁹

As mentioned previously, reactions for BVO require the use of Sn-OH to form a hydrogen bond with H₂O₂. These two types of tin sites (Figure 1.33) were studied by Boronat *et al.*, which showed *via* ONIOM and Density Functional Theory (DFT) that the partially hydrolysed framework Sn, *i.e.*, Sn-OH was much more active than the fully closed Sn species.²⁵⁰ Furthermore, Hammond *et al.* showed the importance of hydration in Sn-Beta species for glucose isomerisation in continuous flow. Using a small quantity of water with a MeOH/glucose reaction feed, the rate of deactivation was minimised significantly.²⁵¹

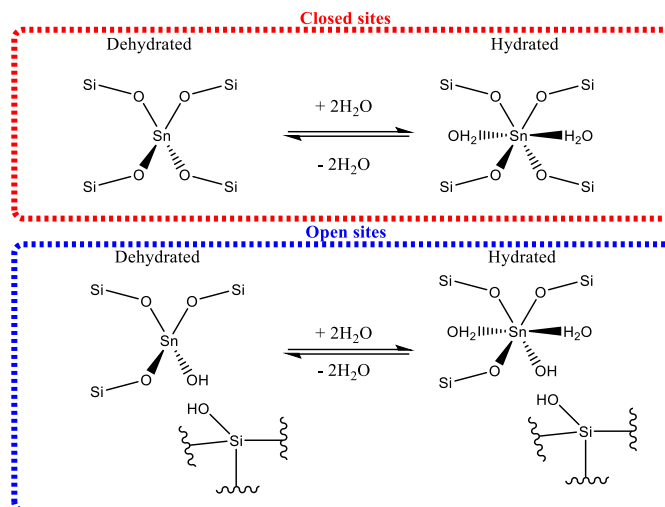


Figure 1.33. Closed and open sites for different Sn species, dehydrated and hydrated.

Other than the highly sought-after reaction of glucose to fructose isomerisation, Sn-Beta has been shown to isomerise and epimerise (C-C shift) different monosaccharides (Figure 1.34) with the addition of borate salts, or with ion exchanging the Sn-Beta with Na^+ cations to shift the reaction pathway.^{252–256}

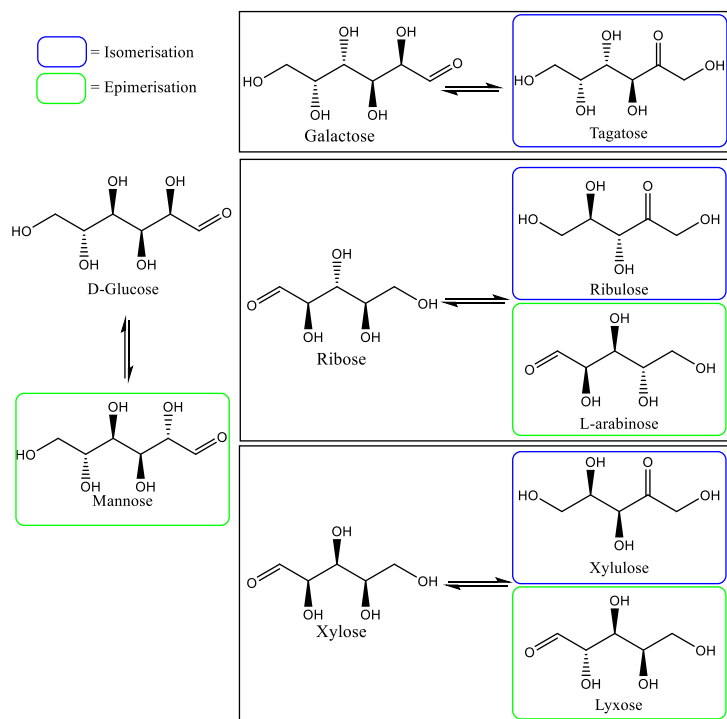


Figure 1.34. Schematic of isomerisation (blue squares) and epimerization (green squares) reactions of different monosaccharides.

1.10 Metal-organic-frameworks.

Another interesting class of material that has been gaining attention for the use of biomass valorisation is metal-organic-frameworks (MOFs). MOFs are an organic-inorganic hybrid crystalline material which consists of a (organic) polymer and metal centres which are formed by reticular synthesis. This synthesis is based on the understanding of the structure coordination compounds which was established by Werner, which essentially consist of the linking between organic and inorganic units by strong bonds, as shown in Figure 1.36.²⁵⁷ The first known MOFs were published by Tomic in 1965, where the chelation of different aromatic polymers and a metal ion, such as Zn, Al, Ni and Fe, was demonstrated. These original MOFs showed high thermal stability, the level of which was a function of the metal involved in the incorporation.²⁵⁸

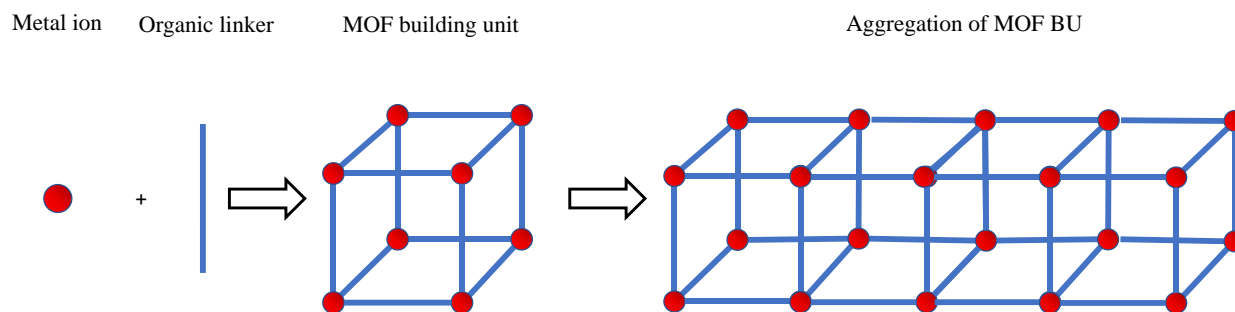


Figure 1.36. Representation of metal-organic-framework synthesis.

Over the last 2 decades, the synthesis of new MOFs (along with other structures) has been exponential, according to the Cambridge Structure Database (CSD) (Figure 1.37), due to the great flexibility they have when it comes to metal centre and polymer linkers. This endows them with potential for a plethora of applications, in particular for fuel cells,²⁵⁹ supercapacitors,²⁶⁰ and gas storage/separation.²⁶¹

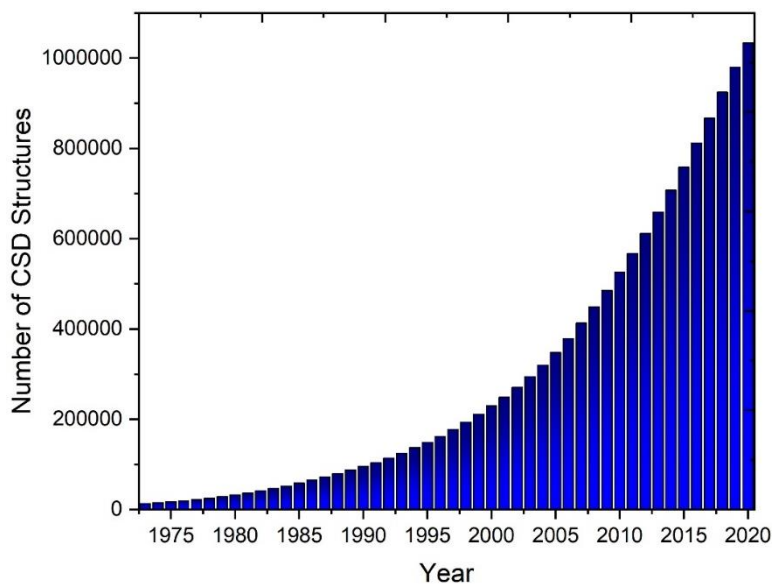


Figure 1.37. Number of structures reported in the CSD. Structures include zeolites, covalent-, and metal-organic structures.

While thousands of MOFs have been created, only a small fraction are used as catalysts.^{262–264} The most prominent examples that have been used widely as catalysts are UiO-66/67, MOF-808 and NU-1000. Furthermore, these MOFs, along with their active metal centre, can also have functional groups such as $-\text{NO}_3$, $-\text{NH}_2$, $-\text{OH}$, and SO_3H , providing additional functionality.^{265,266} Although the application is still relatively new, these have the potential to be used under continuous operational conditions.

1.11. Objectives of the thesis

The overall objective will focus on the modification of zeolites to see the potential of enhanced kinetic performance in a variety of reactions such as glucose isomerisation and its subsequent retro-aldol fragmentation, alongside MPV.

In Chapter III, a study involving the mechanism of solid-state incorporation (SSI) of Sn (II) acetate and dealuminated beta zeolite using various spectroscopic techniques is investigated. Furthermore, an optimisation for the calcination step is also investigated, and zeolites are tested to observe if the choice of synthesis technology resulted in any substantial effects on the final kinetic parameters.

Chapter IV presents the influence of different precursor M-Beta (M = Fe, B, Ga, Al) zeolites for their subsequent SSI. Zeolites are demetallated and Sn is incorporated to be tested for both glucose isomerisation (low temperature) and retro-aldol fragmentation (high temperature) to observe any differences in their kinetic activity. SSI's major disadvantage consists in the use of highly concentrated acid to remove the aluminium to create the vacant sites. Application of other metals could potentially remove this drawback and make way for demetallation under milder conditions a possibility, making SSI more industrially and economically feasible.

Chapter V involves the use of hierarchical zeolites. Different metal zeolites (Sn, Hf, Zr) are synthesised and subsequently desilicated to observe if there are any improvements when it comes to its performance or rate of deactivation for glucose isomerisation and/or retro-aldol fragmentation. The use of surfactants will also be implemented in desilication to determine if pore tuning using a PDA shows a more beneficial effect than with solely alkaline solution.

For Chapter VI, the MOFs UiO-Zr-66-H and its amino-functionalized analogue UiO-Zr-66-NH₂ are tested under continuous flow conditions to determine their activity as catalysts for the bulkier lactose isomerisation in continuous flow. These tests are done with the most stable polar solvents and with different mixtures to determine the effect the solvents.

1.12 References

1. Deng, J., Li, M. & Wang, Y. Biomass-derived carbon: Synthesis and applications in energy storage and conversion. *Green Chem.* **18**, 4824–4854 (2016).
2. Martinez-Hernandez, E., Amezcua-Allieri, M. A. & Aburto, J. Assessing the cost of biomass and bioenergy production in agroindustrial processes. *Energies* **14**, (2021).
3. Somerville, C., Youngs, H., Taylor, C., Davis, S. C. & Long, S. P. Feedstocks for lignocellulosic biofuels. *Science (80-.)*. **329**, 790–792 (2010).
4. Isikgor, F. H. & Becer, C. R. Lignocellulosic biomass: a sustainable platform for the production of bio-based chemicals and polymers. *Polym. Chem.* **6**, 4497–4559 (2015).
5. Wilkins, M. & Tennant, M. Advances in Procedural Automation in the Chemical Industry. *Comput. Aided Chem. Eng.* **31**, 1115–1119 (2012).
6. Straathof, A. J. J. Transformation of biomass into commodity chemicals using enzymes or cells. *Chem. Rev.* **114**, 1871–1908 (2014).
7. McKendry, P. Energy production from biomass (part 1): Overview of biomass. *Bioresour. Technol.* **83**, 37–46 (2002).
8. Bar-On, Y. M., Phillips, R. & Milo, R. The biomass distribution on Earth. *Proc. Natl. Acad. Sci. U. S. A.* **115**, 6506–6511 (2018).
9. Kim, H., Lee, S. & Won, W. System-level analyses for the production of 1,6-hexanediol from cellulose. *Energy* **214**, 118974 (2021).
10. Thaore, V., Chadwick, D. & Shah, N. Sustainable production of chemical intermediates for nylon manufacture: A techno-economic analysis for renewable production of caprolactone. *Chem. Eng. Res. Des.* **135**, 140–152 (2018).
11. Pang, J., Zheng, M., Sun, R., Song, L., Wang, A., Wang, X. & Zhang, T. Catalytic conversion of cellulosic biomass to ethylene glycol: Effects of inorganic impurities in biomass. *Bioresour. Technol.* **175**, 424–429 (2015).
12. Radzicka, A. & Wolfenden, R. A proficient enzyme. *Science (80-.)*. **267**, 90–93 (1995).
13. Callahan, B. P. & Miller, B. G. OMP decarboxylase—An enigma persists. *Bioorg. Chem.* **35**, 465–469 (2007).
14. Wang, A. G., Austin, D. & Song, H. Catalytic Biomass Valorization. in *Biomass Volume Estimation and Valorization for Energy* vol. 395 116–124 (InTech, 2017).
15. Balat, M., Balat, M., Kirtay, E. & Balat, H. Main routes for the thermo-conversion of biomass into fuels and chemicals. Part 1: Pyrolysis systems. *Energy Convers. Manag.* **50**, 3147–3157 (2009).
16. Yaman, S. Pyrolysis of biomass to produce fuels and chemical feedstocks. *Energy Convers. Manag.* **45**, 651–671 (2004).
17. Maschio, G., Koufopoulos, C. & Lucchesi, A. Pyrolysis, a promising route for biomass utilization. *Bioresour. Technol.* **42**, 219–231 (1992).
18. Demiral, I. & Ayan, E. A. Pyrolysis of grape bagasse: Effect of pyrolysis conditions on the product yields and characterization of the liquid product. *Bioresour. Technol.* **102**, 3946–3951 (2011).
19. Molino, A., Chianese, S. & Musmarra, D. Biomass gasification technology: The state of the art overview. *J. Energy Chem.* **25**, 10–25 (2016).
20. Ruiz, J. A., Juárez, M. C., Morales, M. P., Muñoz, P. & Mendivil, M. A. Biomass gasification for electricity generation: Review of current technology barriers. *Renew. Sustain. Energy Rev.* **18**, 174–183 (2013).

21. Morrin, S., Lettieri, P., Chapman, C. & Mazzei, L. Two stage fluid bed-plasma gasification process for solid waste valorisation: Technical review and preliminary thermodynamic modelling of sulphur emissions. *Waste Manag.* **32**, 676–684 (2012).
22. Balat, M. Mechanisms of thermochemical biomass conversion processes. Part 3: Reactions of liquefaction. *Energy Sources, Part A Recover. Util. Environ. Eff.* **30**, 649–659 (2008).
23. Demirbas, A. Mechanisms of liquefaction and pyrolysis reactions of biomass. *Energy Convers. Manag.* **41**, 633–646 (2000).
24. Vardon, D. R., Sharma, B. K., Scott, J., Yu, G., Wang, Z., Schideman, L., Zhang, Y. & Strathmann, T. J. Chemical properties of biocrude oil from the hydrothermal liquefaction of *Spirulina* algae, swine manure, and digested anaerobic sludge. *Bioresour. Technol.* **102**, 8295–8303 (2011).
25. Lavanya, M., Meenakshisundaram, A., Renganathan, S., Chinnasamy, S., Lewis, D. M., Nallasivam, J. & Bhaskar, S. Hydrothermal liquefaction of freshwater and marine algal biomass: A novel approach to produce distillate fuel fractions through blending and co-processing of biocrude with petrocrude. *Bioresour. Technol.* **203**, 228–235 (2016).
26. Mahmood, A. S. N., Brammer, J. G., Hornung, A., Steele, A. & Poulston, S. The intermediate pyrolysis and catalytic steam reforming of Brewers spent grain. *J. Anal. Appl. Pyrolysis* **103**, 328–342 (2013).
27. Gollakota, A. R. K., Kishore, N. & Gu, S. A review on hydrothermal liquefaction of biomass. *Renew. Sustain. Energy Rev.* **81**, 1378–1392 (2018).
28. Brown, T. M., Duan, P. & Savage, P. E. Hydrothermal liquefaction and gasification of *Nannochloropsis* sp. *Energy and Fuels* **24**, 3639–3646 (2010).
29. Deuss, P. J. & Barta, K. From models to lignin: Transition metal catalysis for selective bond cleavage reactions. *Coord. Chem. Rev.* **306**, 510–532 (2016).
30. Dou, X., Li, W., Zhu, C., Jiang, X., Chang, H. M. & Jameel, H. Cleavage of aryl-ether bonds in lignin model compounds using a Co-Zn-beta catalyst. *RSC Adv.* **10**, 43599–43606 (2020).
31. Xu, C., Arancon, R. A. D., Labidi, J. & Luque, R. Lignin depolymerisation strategies: Towards valuable chemicals and fuels. *Chem. Soc. Rev.* **43**, 7485–7500 (2014).
32. Shiga, T. M., Xiao, W., Yang, H., Zhang, X., Olek, A. T., Donohoe, B. S., Liu, J., Makowski, L., Hou, T., McCann, M. C., Carpita, N. C. & Mosier, N. S. Enhanced rates of enzymatic saccharification and catalytic synthesis of biofuel substrates in gelatinized cellulose generated by trifluoroacetic acid. *Biotechnol. Biofuels* **10**, 1–15 (2017).
33. Shrotri, A., Kobayashi, H. & Fukuoka, A. Cellulose Depolymerization over Heterogeneous Catalysts. *Acc. Chem. Res.* **51**, 761–768 (2018).
34. Qian, E. W. *Pretreatment and Saccharification of Lignocellulosic Biomass. Research Approaches to Sustainable Biomass Systems* (Elsevier, 2013). doi:10.1016/B978-0-12-404609-2.00007-6.
35. Cateto, C. A., Barreiro, M. F., Rodrigues, A. E. & Belgacem, M. N. Optimization study of lignin oxypropylation in view of the preparation of polyurethane rigid foams. *Ind. Eng. Chem. Res.* **48**, 2583–2589 (2009).
36. Mosier, N. S., Hendrickson, R., Brewer, M., Ho, N., Sedlak, M., Dreshel, R., Welch, G., Dien, B. S., Aden, A. & Ladisch, M. R. Industrial scale-up of pH-controlled liquid hot water pretreatment of corn fiber for fuel ethanol production. *Appl. Biochem. Biotechnol. - Part A Enzym. Eng. Biotechnol.* **125**, 77–97 (2005).
37. Park, Y. C., Oh, E. J., Jo, J. H., Jin, Y. S. & Seo, J. H. Recent advances in biological production of sugar alcohols. *Curr. Opin. Biotechnol.* **37**, 105–113 (2016).

38. Ge, X., Chang, C., Zhang, L., Cui, S., Luo, X., Hu, S., Qin, Y. & Li, Y. *Conversion of Lignocellulosic Biomass Into Platform Chemicals for Biobased Polyurethane Application. Advances in Bioenergy* vol. 3 (Elsevier Inc., 2018).
39. Donaldson, L. A. Seasonal changes in lignin distribution during tracheid development in *Pinus radiata* D. Don. *Wood Sci. Technol.* **25**, 15–24 (1991).
40. Konwar, L. J., Mikkola, J. P., Bordoloi, N., Saikia, R., Chutia, R. S. & Katak, R. *Sidestreams from bioenergy and biorefinery complexes as a resource for circular bioeconomy. Waste Biorefinery: Potential and Perspectives* (Elsevier B.V., 2018). doi:10.1016/B978-0-444-63992-9.00003-3.
41. Pradhan, P., Mahajani, S. M. & Arora, A. Production and utilization of fuel pellets from biomass: A review. *Fuel Process. Technol.* **181**, 215–232 (2018).
42. Blanco, A., Negro, C., Monte, C., Fuente, E. & Tijero, J. The challenges of sustainable papermaking. *Environ. Sci. Technol.* **38**, (2004).
43. Marinova, M., Mateos-Espejel, E., Jemaa, N. & Paris, J. Addressing the increased energy demand of a Kraft mill biorefinery: The hemicellulose extraction case. *Chem. Eng. Res. Des.* **87**, 1269–1275 (2009).
44. Karumuri, S., Hiziroglu, S. & Kalkan, A. K. Thermoset-cross-linked lignocellulose: A moldable plant biomass. *ACS Appl. Mater. Interfaces* **7**, 6596–6604 (2015).
45. Shulga, G., Betkers, T., Shakels, V., Neiberte, B., Verovkins, A., Brovkina, J., Belous, O., Ambrazaitene, D. & Žukauskaite, A. Effect of the modification of lignocellulosic materials with a lignin-polymer complex on their mulching properties. *BioResources* **2**, 572–582 (2007).
46. Ten, E. & Vermerris, W. Functionalized polymers from lignocellulosic biomass: State of the art. *Polymers (Basel)*. **5**, 600–642 (2013).
47. Zhang, J., Li, J., Tang, Y., Lin, L. & Long, M. Advances in catalytic production of bio-based polyester monomer 2,5-furandicarboxylic acid derived from lignocellulosic biomass. *Carbohydr. Polym.* **130**, 420–428 (2015).
48. Pang, J., Zheng, M., Li, X., Sebastian, J., Jiang, Y., Zhao, Y., Wang, A. & Zhang, T. Unlock the Compact Structure of Lignocellulosic Biomass by Mild Ball Milling for Ethylene Glycol Production. *ACS Sustain. Chem. Eng.* **7**, 679–687 (2019).
49. Liu, R., Liang, L., Li, F., Wu, M., Chen, K., Ma, J., Jiang, M., Wei, P. & Ouyang, P. Efficient succinic acid production from lignocellulosic biomass by simultaneous utilization of glucose and xylose in engineered *Escherichia coli*. *Bioresour. Technol.* **149**, 84–91 (2013).
50. Vasiliadou, E. S. & Lemonidou, A. A. Production of Biopropylene Using Biomass-Derived Sources. *Encycl. Inorg. Bioinorg. Chem.* 1–12 (2016) doi:10.1002/9781119951438.eibc2454.
51. Ragauskas, A. J., Beckham, G. T., Bidy, M. J., Chandra, R., Chen, F., Davis, M. F., Davison, B. H., Dixon, R. A., Gilna, P., Keller, M., Langan, P., Naskar, A. K., Saddler, J. N., Tschaplinski, T. J., Tuskan, G. A. & Wyman, C. E. Lignin valorization: Improving lignin processing in the biorefinery. *Science (80-.)*. **344**, 1246843 1-10(2014).
52. Strassberger, Z., Tanase, S. & Rothenberg, G. The pros and cons of lignin valorisation in an integrated biorefinery. *RSC Adv.* **4**, 25310–25318 (2014).
53. Vanholme, R. *et al.* Caffeoyl shikimate esterase (CSE) is an enzyme in the lignin biosynthetic pathway in *Arabidopsis*. *Science (80-.)*. **341**, 1103–1106 (2013).
54. Bonawitz, N. D., Kim, J. I., Tobimatsu, Y., Ciesielski, P. N., Anderson, N. A., Ximenes, E.,

- Maeda, J., Ralph, J., Donohoe, B. S., Ladisch, M. & Chapple, C. Disruption of Mediator rescues the stunted growth of a lignin-deficient Arabidopsis mutant. *Nature* **509**, 376–380 (2014).
55. Boerjan, W., Ralph, J. & Baucher, M. Lignin Biosynthesis. *Annu. Rev. Plant Biol.* **54**, 519–546 (2003).
56. Erdtman, H. Lignins: Occurrence, formation, structure and reactions. *J. Polym. Sci. Part B Polym. Lett.* **10**, 228–230 (1972).
57. Patwardhan, P. R., Brown, R. C. & Shanks, B. H. Understanding the fast pyrolysis of lignin. *ChemSusChem* **4**, 1629–1636 (2011).
58. Behling, R., Valange, S. & Chatel, G. Heterogeneous catalytic oxidation for lignin valorization into valuable chemicals: What results? What limitations? What trends? *Green Chem.* **18**, 1839–1854 (2016).
59. Zhang, J., Deng, H. & Lin, L. Wet aerobic oxidation of lignin into aromatic aldehydes catalysed by a perovskite-type oxide: LaFe_{1-x}Cu_xO₃ (x=0, 0.1, 0.2). *Molecules* **14**, 2747–2757 (2009).
60. Sales, F. G., Maranhão, L. C. A., Filho, N. M. L. & Abreu, C. A. M. Experimental evaluation and continuous catalytic process for fine aldehyde production from lignin. *Chem. Eng. Sci.* **62**, 5386–5391 (2007).
61. Harris, E. E., D'Ianni, J. & Adkins, H. Reaction of Hardwood Lignin with Hydrogen. *J. Am. Chem. Soc.* **60**, 1467–1470 (1938).
62. Cantu, D. C., Padmaperuma, A. B., Nguyen, M. T., Akhade, S. A., Yoon, Y., Wang, Y. G., Lee, M. S., Glezakou, V. A., Rousseau, R. & Lilga, M. A. A Combined Experimental and Theoretical Study on the Activity and Selectivity of the Electrocatalytic Hydrogenation of Aldehydes. *ACS Catal.* **8**, 7645–7658 (2018).
63. Cyr, A., Chiltz, F., Jeanson, P., Martel, A., Brossard, L., Lessard, J. & Ménard, H. Electrocatalytic hydrogenation of lignin models at Raney nickel and palladium-based electrodes. *Can. J. Chem.* **78**, 307–315 (2000).
64. Godard, H. P., McCarthy, J. L. & Hibbert, H. Hydrogenation of Wood. *J. Am. Chem. Soc.* **62**, 988 (1940).
65. Rao, R., Dandekar, A., Baker, R. T. K. & Vannice, M. A. Properties of copper chromite catalysts in hydrogenation reactions. *J. Catal.* **171**, 406–419 (1997).
66. Zheng, Y., Chen, D. & Zhu, X. Aromatic hydrocarbon production by the online catalytic cracking of lignin fast pyrolysis vapors using Mo₂N/γ-Al₂O₃. *J. Anal. Appl. Pyrolysis* **104**, 514–520 (2013).
67. Yoon, S., Macewan, K. & Heiningen, A. Van. Forest Products Biorefinery. *Tappi J.* 27–31 (2008).
68. Brownlee, H. J. & Miner, C. S. Industrial Development of Furfural. *Ind. Eng. Chem.* **40**, 201–204 (1948).
69. Peters, F. N. The Furans Fifteen Years of Progress. *Ind. Eng. Chem.* **28**, 755–759 (1936).
70. Ledesma-Amaro, R., Lazar, Z., Rakicka, M., Guo, Z., Fouchard, F., Coq, A. M. C. Le & Nicaud, J. M. Metabolic engineering of *Yarrowia lipolytica* to produce chemicals and fuels from xylose. *Metab. Eng.* **38**, 115–124 (2016).
71. Cheng, H., Wang, B., Lv, J., Jiang, M., Lin, S. & Deng, Z. Xylitol production from xylose mother liquor: A novel strategy that combines the use of recombinant *Bacillus subtilis* and *Candida maltosa*. *Microb. Cell Fact.* **10**, 1–12 (2011).
72. Xin, F., Wu, Y. R. & He, J. Simultaneous fermentation of glucose and xylose to butanol by

- Clostridium sp. strain BOH3. *Appl. Environ. Microbiol.* **80**, 4771–4778 (2014).
73. Novy, V., Brunner, B. & Nidetzky, B. l-Lactic acid production from glucose and xylose with engineered strains of *Saccharomyces cerevisiae*: Aeration and carbon source influence yields and productivities. *Microb. Cell Fact.* **17**, 1–11 (2018).
 74. Salvachúa, D., Mohagheghi, A., Smith, H., Bradfield, M. F. A., Nicol, W., Black, B. A., Bidy, M. J., Dowe, N. & Beckham, G. T. Succinic acid production on xylose-enriched biorefinery streams by *Actinobacillus succinogenes* in batch fermentation. *Biotechnol. Biofuels* **9**, 1–15 (2016).
 75. Paulino, P. N., Reis, O. C., Licea, Y. E., Albuquerque, E. M. & Fraga, M. A. Valorisation of xylose to lactic acid on morphology-controlled ZnO catalysts. *Catal. Sci. Technol.* **8**, 4945–4956 (2018).
 76. Smolentseva, E., Kusema, B. T., Beloshapkin, S., Estrada, M., Vargas, E., Murzin, D. Y., Castillon, F., Fuentes, S. & Simakov, A. Selective oxidation of arabinose to arabinonic acid over Pd-Au catalysts supported on alumina and ceria. *Appl. Catal. A Gen.* **392**, 69–79 (2011).
 77. Saha, B. C. & Bothast, R. J. Production of L-arabitol from L-arabinose by *Candida entomaea* and *Pichia guilliermondii*. *Appl. Microbiol. Biotechnol.* **45**, 299–306 (1996).
 78. Yeom, S. J., Kim, N. H., Park, C. S. & Oh, D. K. L-ribose production from L-arabinose by using purified L-arabinose isomerase and mannose-6-phosphate isomerase from *Geobacillus thermodenitrificans*. *Appl. Environ. Microbiol.* **75**, 6941–6943 (2009).
 79. Hoydonckx, H. E., Van Rhijn, W. M., Van Rhijn, W., De Vos, D. E. & Jacobs, P. A. Furfural and Derivatives. *Ullmann's Encyclopedia of Industrial Chemistry* (2007) doi:doi:10.1002/14356007.a12_119.pub2.
 80. Dulie, N. W., Woldeyes, B., Demsash, H. D. & Jabasingh, A. S. An Insight into the Valorization of Hemicellulose Fraction of Biomass into Furfural: Catalytic Conversion and Product Separation. *Waste and Biomass Valorization* (2020) doi:10.1007/s12649-020-00946-1.
 81. Fakhr Hoseini, S. M., Tavakkoli, T. & Hatamipour, M. S. Extraction of aromatic hydrocarbons from lube oil using n-hexane as a co-solvent. *Sep. Purif. Technol.* **66**, 167–170 (2009).
 82. Niu, H., Luo, J., Li, C., Wang, B. & Liang, C. Transfer Hydrogenation of Biomass-Derived Furfural to 2-Methylfuran over CuZnAl Catalysts. *Ind. Eng. Chem. Res.* **58**, 6298–6308 (2019).
 83. Nandiwale, K. Y., Vishwakarma, M., Rathod, S., Simakova, I. & Bokade, V. V. One-Pot Cascade Conversion of Renewable Furfural to Levulinic Acid over a Bifunctional H3PW12O40/SiO2Catalyst in the Absence of External H2. *Energy and Fuels* **35**, 539–545 (2021).
 84. Chatterjee, M., Ishizaka, T. & Kawanami, H. Reductive amination of furfural to furfurylamine using aqueous ammonia solution and molecular hydrogen: An environmentally friendly approach. *Green Chem.* **18**, 487–496 (2016).
 85. Douthwaite, M., Huang, X., Iqbal, S., Miedziak, P. J., Brett, G. L., Kondrat, S. A., Edwards, J. K., Sankar, M., Knight, D. W., Bethell, D. & Hutchings, G. J. The controlled catalytic oxidation of furfural to furoic acid using AuPd/Mg(OH)2. *Catal. Sci. Technol.* **7**, 5284–5293 (2017).
 86. Chen, X., Zhang, L., Zhang, B., Guo, X. & Mu, X. Highly selective hydrogenation of furfural to furfuryl alcohol over Pt nanoparticles supported on g-C 3 N 4 nanosheets catalysts in water. *Nat. Publ. Gr.* 1–13 (2016) doi:10.1038/srep28558.

87. Cecilia, J. A., Garc, C. & Maireles-torres, P. Selective Production of Furan from Gas-Phase Furfural Decarbonylation on Ni-MgO Catalysts'. (2019) doi:10.1021/acssuschemeng.8b06155.
88. Torget, R. W., Kim, J. S. & Lee, Y. Y. Fundamental aspects of dilute acid hydrolysis/fractionation kinetics of hardwood carbohydrates. 1. Cellulose hydrolysis. *Ind. Eng. Chem. Res.* **39**, 2817–2825 (2000).
89. Xu, W., Grénman, H., Liu, J., Kronlund, D., Li, B., Backman, P., Peltonen, J., Willför, S., Sundberg, A. & Xu, C. Mild Oxalic-Acid-Catalyzed Hydrolysis as a Novel Approach to Prepare Cellulose Nanocrystals. *ChemNanoMat* **3**, 109–119 (2017).
90. Yeganeh, F., Behrooz, R. & Rahimi, M. The effect of Sulfuric acid and Maleic acid on characteristics of nano-cellulose produced from waste office paper. *Int. J. Nano Dimens.* **8**, 206–215 (2017).
91. Rorrer, G. L., Ashour, S. S., Hawley, M. C. & Lamport, D. T. A. Solvolysis of wood and pure cellulose by anhydrous hydrogen fluoride vapor. *Biomass* **12**, 227–246 (1987).
92. Huang, Y. B. & Fu, Y. Hydrolysis of cellulose to glucose by solid acid catalysts. *Green Chem.* **15**, 1095–1111 (2013).
93. Tagusagawa, C., Takagaki, A., Iguchi, A., Takanabe, K., Kondo, J. N., Ebitani, K., Hayashi, S., Tatsumi, T. & Domen, K. Highly active mesoporous Nb-W oxide solid-acid catalyst. *Angew. Chemie - Int. Ed.* **49**, 1128–1132 (2010).
94. Wattanapaphawong, P., Reubroycharoen, P. & Yamaguchi, A. Conversion of cellulose into lactic acid using zirconium oxide catalysts. *RSC Adv.* **7**, 18561–18568 (2017).
95. Hu, S., Jiang, F. & Hsieh, Y. Lo. 1D lignin-based solid acid catalysts for cellulose hydrolysis to glucose and nanocellulose. *ACS Sustain. Chem. Eng.* **3**, 2566–2574 (2015).
96. Xu, Y., Liu, G., Fu, J., Kang, S., Xiao, Y., Yang, P. & Liao, W. Catalytic hydrolysis of cellulose to levulinic acid by partly replacing sulfuric acid with Nafion® NR50 catalyst. *Biomass Convers. Biorefinery* **9**, 609–616 (2019).
97. Tian, J., Wang, J., Zhao, S., Jiang, C., Zhang, X. & Wang, X. Hydrolysis of cellulose by the heteropoly acid H3PW12O40. *Cellulose* **17**, 587–594 (2010).
98. Onda, A., Ochi, T. & Yanagisawa, K. Selective hydrolysis of cellulose into glucose over solid acid catalysts. *Green Chem.* **10**, 1033–1037 (2008).
99. Mohd Azhar, S. H., Abdulla, R., Jambo, S. A., Marbawi, H., Gansau, J. A., Mohd Faik, A. A. & Rodrigues, K. F. Yeasts in sustainable bioethanol production: A review. *Biochem. Biophys. Reports* **10**, 52–61 (2017).
100. White, J. S. Straight talk about high-fructose corn syrup: what it is and what it ain't. *Am J Clin Nutr* **2008** **88**, 1716–1721 (2008).
101. Parker, K., Salas, M. & Nwosu, V. C. High fructose corn syrup: Production, uses and public health concerns. *Biotechnol. Mol. Biol. Rev.* **5(5)**, 71–78 (2010).
102. Chapman, J., Ismail, A. E. & Dinu, C. Z. Industrial applications of enzymes: Recent advances, techniques, and outlooks. *Catalysts* **8**, 20–29 (2018).
103. Grigoras, A. G. Catalase immobilization—A review. *Biochem. Eng. J.* **117**, 1–20 (2017).
104. Griebenow, K. & Klibanov, A. M. Can conformational changes be responsible for solvent and excipient effects on the catalytic behavior of subtilisin Carlsberg in organic solvents? *Biotechnol. Bioeng.* **53**, 351–362 (1997).
105. Sheldon, R. A. Enzyme immobilization: The quest for optimum performance. *Adv. Synth. Catal.* **349**, 1289–1307 (2007).
106. Galadima, A. & Muraza, O. Biodiesel production from algae by using heterogeneous

- catalysts : A critical review. *Energy* **78**, 72–83 (2014).
107. Ding, K., Zhong, Z., Wang, J., Zhang, B., Addy, M. & Ruan, R. Effects of alkali-treated hierarchical HZSM-5 zeolites on the production of aromatic hydrocarbons from catalytic fast pyrolysis of waste cardboard. *J. Anal. Appl. Pyrolysis* **125**, 153–161 (2017).
 108. Ateş, F., Miskolczi, N. & Borsodi, N. Comparison of real waste (MSW and MPW) pyrolysis in batch reactor over different catalysts. Part I: Product yields, gas and pyrolysis oil properties. *Bioresour. Technol.* **133**, 443–454 (2013).
 109. Zang, H., Yu, S., Yu, P., Ding, H., Du, Y., Yang, Y. & Zhang, Y. Hydrothermal conversion of N-acetyl-D-glucosamine to 5-hydroxymethylfurfural using ionic liquid as a recycled catalyst in a water-dimethyl sulfoxide mixture. *Carbohydr. Res.* **442**, 1–8 (2017).
 110. Wang, Y., Pedersen, C. M., Deng, T., Qiao, Y. & Hou, X. Direct conversion of chitin biomass to 5-hydroxymethylfurfural in concentrated ZnCl₂ aqueous solution. *Bioresour. Technol.* **143**, 384–390 (2013).
 111. Lai, F., Yan, F., Wang, P., Li, C. & Shen, X. Efficient conversion of carbohydrates and biomass into furan compounds by chitin / Ag co-modified H 3 PW 12 O 40 catalysts. *J. Clean. Prod.* **316**, 128243 (2021).
 112. Román-Ramírez, L. A., McKeown, P., Shah, C., Abraham, J., Jones, M. D. & Wood, J. Chemical Degradation of End-of-Life Poly(lactic acid) into Methyl Lactate by a Zn(II) Complex. *Ind. Eng. Chem. Res.* **59**, 11149–11156 (2020).
 113. Gupta, A. P. & Kumar, V. New emerging trends in synthetic biodegradable polymers - Polylactide: A critique. *Eur. Polym. J.* **43**, 4053–4074 (2007).
 114. Rosatella, A. A., Simeonov, S. P., Frade, R. F. M. & Afonso, C. A. M. 5-Hydroxymethylfurfural (HMF) as a building block platform: Biological properties, synthesis and synthetic applications. *Green Chem.* **13**, 754–793 (2011).
 115. Van Putten, R. J., Van Der Waal, J. C., De Jong, E., Rasrendra, C. B., Heeres, H. J. & De Vries, J. G. Hydroxymethylfurfural, a versatile platform chemical made from renewable resources. *Chem. Rev.* **113**, 1499–1597 (2013).
 116. Gandini, A. & Belgacem, M. N. Furans in polymer chemistry. *Prog. Polym. Sci.* **22**, 1203–1379 (1997).
 117. van Leeuwen, P. *Homogeneous Catalysis – Understanding the Art*. (2004). doi:10.1007/1-4020-2000-7.
 118. Zhu, J., Wood, J., Deplanche, K., Mikheenko, I. & Macaskie, L. E. Selective hydrogenation using palladium bioinorganic catalyst. *Appl. Catal. B Environ.* **199**, 108–122 (2016).
 119. Arun, N., Sharma, R. V. & Dalai, A. K. Green diesel synthesis by hydrodeoxygenation of bio-based feedstocks: Strategies for catalyst design and development. *Renew. Sustain. Energy Rev.* **48**, 240–255 (2015).
 120. Chorkendorff, I. & Niemantsverdriet, J. W. *Concepts of Modern Catalysis and Kinetics. Concepts of Modern Physics: The Haifa Lectures* (Wiley-VCH, 2007). doi:10.1142/P510.
 121. Liu, H. Ammonia synthesis catalyst 100 years: Practice, enlightenment and challenge. *Cuihua Xuebao/Chinese J. Catal.* **35**, 1619–1640 (2014).
 122. Vogt, E. T. C. & Weckhuysen, B. M. Fluid catalytic cracking: recent developments on the grand old lady of zeolite catalysis. *Chem. Soc. Rev.* **44**, 7342–7370 (2015).
 123. Contrella, N. D., Sampson, J. R. & Jordan, R. F. Copolymerization of ethylene and methyl acrylate by cationic palladium catalysts that contain phosphine-diethyl phosphonate ancillary ligands. *Organometallics* **33**, 3546–3555 (2014).
 124. Chikkali, S. H. Ziegler–Natta polymerization and the remaining challenges. *Resonance* **22**,

- 1039–1060 (2017).
125. Klein, J. P. Compounds and methods for producing nylon 6. (2018).
 126. Zong, B., Sun, B., Cheng, S., Mu, X., Yang, K., Zhao, J., Zhang, X. & Wu, W. Green Production Technology of the Monomer of Nylon-6: Caprolactam. *Engineering* **3**, 379–384 (2017).
 127. Zimmermann, N. E. R. & Haranczyk, M. History and Utility of Zeolite Framework-Type Discovery from a Data-Science Perspective. *Cryst. Growth Des.* **16**, 3043–3048 (2016).
 128. Flanigen, E. M., Broach, R. W. & Wilson, S. T. Introduction. *Zeolites Ind. Sep. Catal.* 1–26 (2010) doi:10.1002/9783527629565.ch1.
 129. Mozgawa, W., Król, M. & Barczyk, K. FT-IR studies of zeolites from different structural groups. *Chemik* **65**, 671–674 (2011).
 130. Coulomb, J. P. & Floquet, N. Determination of zeolite closed porosity in (1D) channel systems (AFI and MTW types). *Stud. Surf. Sci. Catal.* **174**, 913–916 (2008).
 131. Roth, W. J. & Ejkka, J. Two-dimensional zeolites: Dream or reality? *Catal. Sci. Technol.* **1**, 43–53 (2011).
 132. Roth, W. J., Nachtigall, P., Morris, R. E. & Čejka, J. Two-dimensional zeolites: Current status and perspectives. *Chem. Rev.* **114**, 4807–4837 (2014).
 133. Cundy, C. S. & Cox, P. A. The hydrothermal synthesis of zeolites: Precursors, intermediates and reaction mechanism. *Microporous Mesoporous Mater.* **82**, 1–78 (2005).
 134. Dokter, W. H., van Garderen, H. F., Beelen, T. P. M., van Santen, R. A. & Bras, W. Homogeneous versus Heterogeneous Zeolite Nucleation. *Angew. Chemie Int. Ed. English* **34**, 73–75 (1995).
 135. Flanigen, E. M. & Patton, R. L. Silica polymorph and process for preparing same. 7 (1978).
 136. Louis, B. & Kiwi-Minsker, L. Synthesis of ZSM-5 zeolite in fluoride media: An innovative approach to tailor both crystal size and acidity. *Microporous Mesoporous Mater.* **74**, 171–178 (2004).
 137. Schüth, F. & Schmidt, W. Microporous and Mesoporous Materials. *Microporous Mesoporous Mater.* **4**, 269–279 (2002).
 138. Larlus, O. & Valtchev, V. P. Control of the morphology of all-silica BEA-type zeolite synthesized in basic media. *Chem. Mater.* **17**, 881–886 (2005).
 139. Wright, P. A. Acid Catalysts. *Encycl. Mater. Sci. Technol.* 1–6 (2001) doi:10.1016/b0-08-043152-6/00001-2.
 140. Ghadamnan, E., Nabavi, S. R. & Abbasi, M. Nano LTA Zeolite in Water Softening Process : Synthesis , Characterization , Kinetic studies and process optimization by Response Surface Methodology (RSM). *J. Water Environ. Nanotechnol.* **4**, 119–138 (2019).
 141. Xue, Z., Li, Z., Ma, J., Bai, X., Kang, Y., Hao, W. & Li, R. Effective removal of Mg²⁺ and Ca²⁺ ions by mesoporous LTA zeolite. *Desalination* **341**, 10–18 (2014).
 142. Luo, H. Y., Lewis, J. D. & Román-Leshkov, Y. Lewis Acid Zeolites for Biomass Conversion: Perspectives and Challenges on Reactivity, Synthesis, and Stability. *Annu. Rev. Chem. Biomol. Eng.* **7**, 663–692 (2016).
 143. Taramasso, M., Milanese, S., Perego, G., Milan & Notari, B. Preparation of Porous Crystalline Synthetic Material Comprised of Silicon and Titanium Oxides. *United States Pat.* 1–8 (1983).
 144. Ji, Y., Wang, Y., Xie, B. & Xiao, F. S. Zeolite Seeds: Third Type of Structure Directing Agents in the Synthesis of Zeolites. *Comments Inorg. Chem.* **36**, 1–16 (2016).
 145. Ren, N., Yang, Z. J., Lv, X. C., Shi, J., Zhang, Y. H. & Tang, Y. A seed surface

- crystallization approach for rapid synthesis of submicron ZSM-5 zeolite with controllable crystal size and morphology. *Microporous Mesoporous Mater.* **131**, 103–114 (2010).
146. Xue, T., Wang, Y. M. & He, M. Y. Synthesis of ultra-high-silica ZSM-5 zeolites with tunable crystal sizes. *Solid State Sci.* **14**, 409–418 (2012).
 147. Kamimura, Y., Tanahashi, S., Itabashi, K., Sugawara, A., Wakihara, T., Shimojima, A. & Okubo, T. Crystallization behavior of zeolite beta in OSDA-free, seed-assisted synthesis. *J. Phys. Chem. C* **115**, 744–750 (2011).
 148. Honda, K., Yashiki, A., Sadakane, M. & Sano, T. Hydrothermal conversion of FAU and *BEA-type zeolites into MAZ-type zeolites in the presence of non-calcined seed crystals. *Microporous Mesoporous Mater.* **196**, 254–260 (2014).
 149. Zhou, R., Zhong, S., Lin, X. & Xu, N. Synthesis of zeolite T by microwave and conventional heating. *Microporous Mesoporous Mater.* **124**, 117–122 (2009).
 150. Ansari, M., Aroujalian, A., Raisi, A., Dabir, B. & Fathizadeh, M. Preparation and characterization of nano-NaX zeolite by microwave assisted hydrothermal method. *Adv. Powder Technol.* **25**, 722–727 (2014).
 151. Gu, I., Warzywoda, J. & Bac, N. Synthesis of zeolite MCM-22 under rotating and static conditions. **31**, 241–251 (1999).
 152. Smeets, S., Koch, L., Mascello, N., Sesseg, J., McCusker, L. B., Hernández-Rodríguez, M., Mitchell, S. & Pérez-Ramírez, J. Structure analysis of a BEC-type germanosilicate zeolite including the location of the flexible organic cations in the channels. *CrystEngComm* **17**, 4865–4870 (2015).
 153. Choi, M., Na, K., Kim, J., Sakamoto, Y., Terasaki, O. & Ryoo, R. Stable single-unit-cell nanosheets of zeolite MFI as active and long-lived catalysts. *Nature* **461**, 246–249 (2009).
 154. Kasian, N., Tuel, A., Verheyen, E., Kirschhock, C. E. A., Taulelle, F. & Martens, J. A. NMR evidence for specific germanium siting in IM-12 zeolite. *Chem. Mater.* **26**, 5556–5565 (2014).
 155. Bartholomew, C. H. Mechanisms of catalyst deactivation. *Appl. Catal. A Gen.* **212**, 17–60 (2001).
 156. Sadeghbeigi, R. *Fluid Catalytic Cracking Handbook: Design, Operation, and Troubleshooting of FCC Facilities.* (2000).
 157. Guisnet, M., Magnoux, P. & Martin, D. Roles of acidity and pore structure in the deactivation of zeolites by carbonaceous deposits. *Catal. Deactiv.* **111**, 1–19 (1997).
 158. Guisnet, M. & Magnoux, P. Coking and deactivation of zeolites. Influence of the Pore Structure. *Appl. Catal.* **54**, 1–27 (1989).
 159. Primo, A. & Garcia, H. Zeolites as catalysts in oil refining. *Chem. Soc. Rev.* **43**, 7548–7561 (2014).
 160. Harrhy, J. H., Wang, A., Jarvis, J. S., He, P., Meng, S., Yung, M., Liu, L. & Song, H. Understanding zeolite deactivation by sulfur poisoning during direct olefin upgrading. *Commun. Chem.* **2**, 1–13 (2019).
 161. Li, X., Li, J., Peng, Y., Chang, H., Zhang, T., Zhao, S., Si, W. & Hao, J. Environmental Mechanism of arsenic poisoning on SCR catalyst of CeW/Ti and its novel efficient regeneration method with hydrogen. **184**, 246–257 (2016).
 162. Dong-jie, Y. A. N., Tong, G. U. O., Ya, Y. U. & Zhao-hui, C. Lead poisoning and regeneration of Mn-Ce/TiO₂ catalysts for NH₃-SCR of NO_x at low temperature. **49**, 0–7 (2021).
 163. Argyle, M. D. & Bartholomew, C. H. Heterogeneous catalyst deactivation and regeneration:

- A review. *Catalysts* **5**, 145–269 (2015).
164. Dai, Y., Lu, P., Cao, Z., Campbell, C. T. & Xia, Y. The physical chemistry and materials science behind sinter-resistant catalysts. *Chem. Soc. Rev.* **47**, 4314–4331 (2018).
 165. Liang, C., Tian, H., Gao, G., Zhang, S., Liu, Q., Dong, D. & Hu, X. Methanation of CO₂ over alumina supported nickel or cobalt catalysts: Effects of the coordination between metal and support on formation of the reaction intermediates. *Int. J. Hydrogen Energy* **45**, 531–543 (2020).
 166. Gao, J., Liu, Q., Gu, F., Liu, B., Zhong, Z. & Su, F. Recent advances in methanation catalysts for the production of synthetic natural gas. *RSC Adv.* **5**, 22759–22776 (2015).
 167. Arends, I. W. C. E. & Sheldon, R. A. Activities and stabilities of heterogeneous catalysts in selective liquid phase oxidations: Recent developments. *Appl. Catal. A Gen.* **212**, 175–187 (2001).
 168. Hammond, C. Intensification studies of heterogeneous catalysts: Probing and overcoming catalyst deactivation during liquid phase operation. *Green Chem.* **19**, 2711–2728 (2017).
 169. Hammond, C., Conrad, S. & Hermans, I. Simple and scalable preparation of highly active lewis acidic Sn-β. *Angew. Chemie - Int. Ed.* **51**, 11736–11739 (2012).
 170. Stefanidis, S. D., Kalogiannis, K. G., Pilavachi, P. A., Fougret, C. M., Jordan, E. & Lappas, A. A. Catalyst hydrothermal deactivation and metal contamination during the in situ catalytic pyrolysis of biomass. *Catal. Sci. Technol.* **6**, 2807–2819 (2016).
 171. Padovan, D., Parsons, C., Simplicio Grasina, M. & Hammond, C. Intensification and deactivation of Sn-beta investigated in the continuous regime. *Green Chem.* **18**, 5041–5049 (2016).
 172. Ravenelle, R. M., Schübler, F., Damico, A., Danilina, N., Van Bokhoven, J. A., Lercher, J. A., Jones, C. W. & Sievers, C. Stability of zeolites in hot liquid water. *J. Phys. Chem. C* **114**, 19582–19595 (2010).
 173. Kim, J. M. & Ryoo, R. Disintegration of mesoporous structures of MCM-41 and MCM-48 in water. *Bulletin of the Korean Chemical Society* vol. 17 66–68 (1996).
 174. Triantafyllidis, C. S., Vlessidis, A. G. & Evmiridis, N. P. Dealuminated H-Y zeolites: Influence of the degree and the type of dealumination method on the structural and acidic characteristics of H-Y zeolites. *Ind. Eng. Chem. Res.* **39**, 307–319 (2000).
 175. Gusev, A. A., Psarras, A. C., Triantafyllidis, K. S., Lappas, A. A. & Diddams, P. A. Effect of steam deactivation severity of ZSM-5 additives on LPG olefins production in the FCC process. *Molecules* **22**, (2017).
 176. Ding, L., Zheng, Y., Hong, Y. & Ring, Z. Effect of particle size on the hydrothermal stability of zeolite beta. *Microporous Mesoporous Mater.* **101**, 432–439 (2007).
 177. Garcia-Martinez, J., Xiao, C., Cychosz, K. A., Li, K., Wan, W., Zou, X. & Thommes, M. Evidence of intracrystalline mesostructured porosity in zeolites by advanced gas sorption, electron tomography and rotation electron diffraction. *ChemCatChem* **6**, 3110–3115 (2014).
 178. Van De Water, L. G. A., Bulcock, S., Masters, A. F. & Maschmeyer, T. Ce-TUD-1: Synthesis, characterization, and testing of a versatile heterogeneous oxidation catalyst. *Ind. Eng. Chem. Res.* **46**, 4221–4225 (2007).
 179. García-Martínez, J. & Li, K. *Mesoporous Zeolites. Mesoporous Zeolites: Preparation, Characterization and Applications* (Wiley-VCH Verlag GmbH & Co. KGaA, 2015). doi:10.1002/9783527673957.
 180. Pareek, V., Bhargava, A., Gupta, R., Jain, N. & Panwar, J. Synthesis and Applications of Noble Metal Nanoparticles: A Review. *Adv. Sci. Eng. Med.* **9**, 527–544 (2017).

181. Emdadi, L., Wu, Y., Zhu, G., Chang, C. C., Fan, W., Pham, T., Lobo, R. F. & Liu, D. Dual template synthesis of meso- and microporous MFI zeolite nanosheet assemblies with tailored activity in catalytic reactions. *Chem. Mater.* **26**, 1345–1355 (2014).
182. Wu, L., Degirmenci, V., Magusin, P. C. M. M., Szyja, B. M. & Hensen, E. J. M. Dual template synthesis of a highly mesoporous SSZ-13 zeolite with improved stability in the methanol-to-olefins reaction. *Chem. Commun.* **48**, 9492–9494 (2012).
183. Willhammar, T., Sun, J., Wan, W., Oleynikov, P., Zhang, D., Zou, X., Moliner, M., Gonzalez, J., Martínez, C., Rey, F. & Corma, A. Structure and catalytic properties of the most complex intergrown zeolite ITQ-39 determined by electron crystallography. *Nat. Chem.* **4**, 188–194 (2012).
184. Möller, K. & Bein, T. Mesoporosity – a new dimension for zeolites. *Chem. Soc. Rev.* **42**, 3689–3707 (2013).
185. Vu, H. T., Harth, F. M. & Wilde, N. Silylated zeolites with enhanced hydrothermal stability for the aqueous-phase hydrogenation of levulinic acid to γ -Valerolactone. *Front. Chem.* **6**, 1–9 (2018).
186. Shirani Lapari, S., Ramli, Z. & Triwahyono, S. Effect of Different Templates on the Synthesis of Mesoporous Sodalite. *J. Chem.* **2015**, 1–6 (2015).
187. Medina-Ramírez, A., Flores-Díaz, A. A., Ruiz Camacho, B. & García-Ruiz, G. Synthesis of zeolite membranes on calcium silicate support and their bioactive response. *Prog. Biomater.* **7**, 61–71 (2018).
188. Xiao, F. S., Wang, L., Yin, C., Lin, K., Di, Y., Li, J., Xu, R., Su, D. S., Schlögl, R., Yokoi, T. & Tatsumi, T. Catalytic properties of hierarchical mesoporous zeolites templated with a mixture of small organic ammonium salts and mesoscale cationic polymers. *Angew. Chemie - Int. Ed.* **45**, 3090–3093 (2006).
189. Yao, J., Huang, Y. & Wang, H. Controlling zeolite structures and morphologies using polymer networks. *J. Mater. Chem.* **20**, 9827–9831 (2010).
190. Jiang, J., Yang, Y., Duanmu, C., Xu, Y., Feng, L., Gu, X. & Chen, J. Preparation of hollow ZSM-5 crystals in the presence of polyacrylamide. *Microporous Mesoporous Mater.* **163**, 11–20 (2012).
191. Valtchev, V. Silicalite-1 hollow spheres and bodies with a regular system of macrocavities. *Chem. Mater.* **14**, 4371–4377 (2002).
192. Serrano, D. P., Escola, J. M. & Pizarro, P. Synthesis strategies in the search for hierarchical zeolites. *Chem. Soc. Rev.* **42**, 4004–4035 (2013).
193. Chen, H., Wydra, J., Zhang, X., Lee, P. S., Wang, Z., Fan, W. & Tsapatsis, M. Hydrothermal synthesis of zeolites with three-dimensionally ordered mesoporous-imprinted structure. *J. Am. Chem. Soc.* **133**, 12390–12393 (2011).
194. Abdulridha, S., Jiang, J., Xu, S., Zhou, Z., Liang, H., Mao, B., Zhou, Y., Garforth, A., Jiao, Y. & Fan, X. Cellulose Nanocrystals (CNCs) as Hard Templates for Preparing Mesoporous Zeolite Y Assemblies with High Catalytic Activity. *Green Chem.* 5115–5122 (2020) doi:10.1039/d0gc01070g.
195. Zhu, H., Liu, Z., Wang, Y., Kong, D., Yuan, X. & Xie, Z. Nanosized CaCO₃ as hard template for creation of intracrystal pores within silicalite-1 crystal. *Chem. Mater.* **20**, 1134–1139 (2008).
196. Carrillo, A. I., Linares, N. & Martínez, J. G. Introduction of mesoporosity in zeolites using nanoparticles as hard templates. *Tech. Proc. 2008 NSTI Nanotechnol. Conf. Trade Show, NSTI-Nanotech, Nanotechnol. 2008* **1**, 638–641 (2008).

197. Čižmek, A., Subotić, B., Šmit, I., Tonejc, A., Aiello, R., Crea, F. & Nastro, A. Dissolution of high-silica zeolites in alkaline solutions II. Dissolution of 'activated' silicalite-1 and ZSM-5 with different aluminum content. *Microporous Mater.* **8**, 159–169 (1997).
198. Čimek, A., Komunjer, L., Subotić, B., Široki, M. & Rončević, S. Kinetics of zeolite dissolution: Part 1. Dissolution of zeolite A in hot sodium hydroxide. *Zeolites* **11**, 258–264 (1991).
199. Čižmek, A., Komunjer, L., Subotić, B., Široki, M. & Rončević, S. Kinetics of zeolite dissolution: Part 3. Dissolution of synthetic mordenite in hot sodium hydroxide solutions. *Zeolites* **12**, 190–196 (1992).
200. Ogura, M., Shinomiya, S. Y., Tateno, J., Nara, Y., Kikuchi, E. & Matsukata, M. Formation of uniform mesopores in ZSM-5 zeolite through treatment in alkaline solution. *Chem. Lett.* 882–883 (2000) doi:10.1246/cl.2000.882.
201. Groen, J. C., Bach, T., Ziese, U., Paulaime-Van Donk, A. M., De Jong, K. P., Moulijn, J. A. & Pérez-Ramírez, J. Creation of hollow zeolite architectures by controlled desilication of Al-zoned ZSM-5 crystals. *J. Am. Chem. Soc.* **127**, 10792–10793 (2005).
202. Groen, J. C., Jansen, J. C., Moulijn, J. A. & Pérez-Ramírez, J. Optimal aluminum-assisted mesoporosity development in MFI zeolites by desilication. *J. Phys. Chem. B* **108**, 13062–13065 (2004).
203. Hasan, Z., Jun, J. W., Kim, C. U., Jeong, K. E., Jeong, S. Y. & Jung, S. H. Desilication of ZSM-5 zeolites for mesoporosity development using microwave irradiation. *Mater. Res. Bull.* **61**, 469–474 (2015).
204. Fernandez, S., Ostraat, M. L., Lawrence, J. A. & Zhang, K. Tailoring the hierarchical architecture of beta zeolites using base leaching and pore-directing agents. *Microporous Mesoporous Mater.* **263**, 201–209 (2018).
205. Inaba, M., Hamada, H., Kiricsi, I. & Nagy, J. B. Zeolite synthesis using 1,6-diaminohexane-based organic diammonium salts as templates. in *Porous materials in environmentally friendly processes* (eds. Kiricsi, I., Pál-Borbély, G., Nagy, J. B. & Karge, H. G. B. T.-S. in S. S. and C.) vol. 125 125–132 (Elsevier, 1999).
206. Wang, D., Zhang, L., Chen, L., Wu, H. & Wu, P. Postsynthesis of mesoporous ZSM-5 zeolite by piperidine-assisted desilication and its superior catalytic properties in hydrocarbon cracking. *J. Mater. Chem. A* **3**, 3511–3521 (2015).
207. Ji, Y. J., Xu, H., Wang, D. R., Xu, L., Ji, P., Wu, H. & Wu, P. Mesoporous MCM-22 zeolites prepared through organic amine-assisted reversible structural change and protective desilication for catalysis of bulky molecules. *ACS Catal.* **3**, 1892–1901 (2013).
208. Abelló, S., Bonilla, A. & Pérez-Ramírez, J. Mesoporous ZSM-5 zeolite catalysts prepared by desilication with organic hydroxides and comparison with NaOH leaching. *Appl. Catal. A Gen.* **364**, 191–198 (2009).
209. Fu, P., Yang, T., Feng, J. & Yang, H. Synthesis of mesoporous silica MCM-41 using sodium silicate derived from copper ore tailings with an alkaline molted-salt method. *J. Ind. Eng. Chem.* **29**, 338–343 (2015).
210. Meng, L., Mezari, B., Goesten, M. G. & Hensen, E. J. M. One-Step Synthesis of Hierarchical ZSM-5 Using Cetyltrimethylammonium as Mesopore-directing Agent. *Chem. Mater.* **29**, 4091–4096 (2017).
211. Warchoń, J., Misaelides, P., Petrus, R. & Zamboulis, D. Preparation and application of organo-modified zeolitic material in the removal of chromates and iodides. *J. Hazard. Mater.* **137**, 1410–1416 (2006).

212. Pachamuthu, M. P., Shanthi, K., Luque, R. & Ramanathan, A. SnTUD-1: A solid acid catalyst for three component coupling reactions at room temperature. *Green Chem.* **15**, 2158–2166 (2013).
213. Dapsens, P. Y., Mondelli, C., Jagielski, J., Hauert, R. & Pérez-Ramírez, J. Hierarchical Sn-MFI zeolites prepared by facile top-down methods for sugar isomerisation. *Catal. Sci. Technol.* **4**, 2302–2311 (2014).
214. Mal, N. K. & Ramaswamy, A. V. Synthesis and catalytic properties of large-pore Sn- β and Al-free Sn- β molecular sieves. *Chem. Commun.* **8**, 425–426 (1997).
215. Newsam, J. M., Treacy, M. M. J., Koetsier, W. T. & De Gruyter, C. B. Structural characterization of zeolite beta. *Proc. R. Soc. London, Ser. A Math. Phys. Sci.* **420**, 375–405 (1988).
216. Higgins, J. B., LaPierre, R. B., Schlenker, J. L., Rohrman, A. C., Wood, J. D., Kerr, G. T. & Rohrbach, W. J. The framework topology of zeolite beta. *Zeolites* **8**, 446–452 (1988).
217. Xu, H., Wang, X., Ji, P., Wu, H., Guan, Y. & Wu, P. Hydrothermal synthesis of Sn-Beta zeolites in F⁻-free medium. *Inorg. Chem. Front.* **5**, 2763–2771 (2018).
218. Casci, J. L. Zeolite Synthesis Using Catalytic Amounts of Template: Structure Blocking Effects and Stoichiometric Syntheses. *Stud. Surf. Sci. Catal.* **84**, 133–140 (1994).
219. Wolf, P., Hammond, C., Conrad, S. & Hermans, I. Post-synthetic preparation of Sn-, Ti- and Zr-beta: A facile route to water tolerant, highly active Lewis acidic zeolites. *Dalt. Trans.* **43**, 4514–4519 (2014).
220. Li, E. & Rudolph, V. Transesterification of vegetable oil to biodiesel over MgO-functionalized mesoporous catalysts. *Energy and Fuels* **22**, 145–149 (2008).
221. Harris, J. W., Cordon, M. J., Di Iorio, J. R., Vega-Vila, J. C., Ribeiro, F. H. & Gounder, R. Titration and quantification of open and closed Lewis acid sites in Sn-Beta zeolites that catalyze glucose isomerization. *J. Catal.* **335**, 141–154 (2016).
222. Al-Nayili, A., Yakabi, K. & Hammond, C. Hierarchically porous BEA stannosilicates as unique catalysts for bulky ketone conversion and continuous operation. *J. Mater. Chem. A* **4**, 1373–1382 (2016).
223. Iida, T., Ohara, K., Román-Leshkov, Y. & Wakihara, T. Zeolites with isolated-framework and oligomeric-extraframework hafnium species characterized with pair distribution function analysis. *Phys. Chem. Chem. Phys.* **20**, 7914–7919 (2018).
224. El Fergani, M., Candu, N., Coman, S. M. & Parvulescu, V. I. Nb-based zeolites: Efficient bi-functional catalysts for the one-pot synthesis of succinic acid from glucose. *Molecules* **22**, (2017).
225. Candu, N., El Fergani, M., Verziu, M., Cojocaru, B., Jurca, B., Apostol, N., Teodorescu, C., Parvulescu, V. I. & Coman, S. M. Efficient glucose dehydration to HMF onto Nb-BEA catalysts. *Catal. Today* **325**, 109–116 (2019).
226. Botti, L., Navar, R., Tolborg, S., Martinez-Espin, J. S., Padovan, D., Taarning, E. & Hammond, C. Influence of Composition and Preparation Method on the Continuous Performance of Sn-Beta for Glucose-Fructose Isomerisation. *Top. Catal.* **0**, 0 (2018).
227. Jia, X., Khan, W., Wu, Z., Choi, J. & Yip, A. C. K. Modern synthesis strategies for hierarchical zeolites: Bottom-up versus top-down strategies. *Adv. Powder Technol.* **30**, 467–484 (2019).
228. Müller, M., Harvey, G. & Prins, R. Comparison of the dealumination of zeolites beta, mordenite, ZSM-5 and ferrierite by thermal treatment, leaching with oxalic acid and treatment with SiCl₄ by ¹H, ²⁹Si and ²⁷Al MAS NMR. *Microporous Mesoporous Mater.*

- 34**, 135–147 (2000).
229. Shwan, S., Skoglundh, M., Lundegaard, L. F., Tiruvalam, R. R., Janssens, T. V. W., Carlsson, A. & Vennestrøm, P. N. R. Solid-State Ion-Exchange of Copper into Zeolites Facilitated by Ammonia at Low Temperature. *ACS Catal.* **5**, 16–19 (2015).
230. Beran, S., Wichterlová, B. & Karge, H. G. Solid-state incorporation of Mn 2+ ions in H-ZSM-5 zeolite. *J. Chem. Soc., Faraday Trans.* **86**, 3033–3037 (1990).
231. Ouyang, X., Hwang, S. J., Xie, D., Rea, T., Zones, S. I. & Katz, A. Heteroatom-substituted delaminated zeolites as solid lewis acid catalysts. *ACS Catal.* **5**, 3108–3119 (2015).
232. Rigutto, M. S., de Ruitter, R., Niederer, J. P. M. & van Bekkum, H. Titanium-Containing Large Pore Molecular Sieves from Boron-Beta: Preparation, Characterization and Catalysis. *Stud. Surf. Sci. Catal.* **84**, 2245–2252 (1994).
233. Bregante, D. T., Tan, J. Z., Sutrisno, A. & Flaherty, D. W. Heteroatom substituted zeolite FAU with ultralow Al contents for liquid-phase oxidation catalysis. *Catal. Sci. Technol.* **10**, 635–647 (2020).
234. Corma, A., Nemeth, L. T., Renz, M. & Valencia, S. Sn-zeolite beta as a heterogeneous chemoselective catalyst for Baeyer-Villiger oxidations. *Nature* **412**, 423–425 (2001).
235. Corma, A., Fornés, V., Iborra, S., Mifsud, M. & Renz, M. One-pot synthesis of phenols from aromatic aldehydes by Baeyer-Villiger oxidation with H₂O₂ using water-tolerant Lewis acids in molecular sieves. *J. Catal.* **221**, 67–76 (2004).
236. Yakabi, K., Mathieux, T., Milne, K., López-Vidal, E. M., Buchard, A. & Hammond, C. Continuous Production of Biorenewable, Polymer-Grade Lactone Monomers through Sn-β-Catalyzed Baeyer–Villiger Oxidation with H₂O₂. *ChemSusChem* **10**, 3652–3659 (2017).
237. Boronat, M., Corma, A. & Renz, M. Mechanism of the Meerwein - Ponndorf - Verley - Oppenauer (MPVO) redox equilibrium on Sn- and Zr - Beta zeolite catalysts. *J. Phys. Chem. B* **110**, 21168–21174 (2006).
238. Guan, F. F., Ma, T. T., Yuan, X., Zeng, H. Y. & Wu, J. Sn-Modified NaY Zeolite Catalysts Prepared by Post-Synthesis Methods for Baeyer–Villiger Oxidation. *Catal. Letters* **148**, 443–453 (2018).
239. Li, P., Liu, G., Wu, H., Liu, Y., Jiang, J. G. & Wu, P. Postsynthesis and selective oxidation properties of nanosized Sn-beta zeolite. *J. Phys. Chem. C* **115**, 3663–3670 (2011).
240. Jennings, J. A., Parkin, S., Munson, E., Delaney, S. P., Calahan, J. L., Isaacs, M., Hong, K. & Crocker, M. Regioselective Baeyer-Villiger oxidation of lignin model compounds with tin beta zeolite catalyst and hydrogen peroxide. *RSC Adv.* **7**, 25987–25997 (2017).
241. Renz, M., Blasco, T., Corma, A., Fornés, V., Jensen, R. & Nemeth, L. Selective and Shape-Selective Baeyer–Villiger Oxidations of Aromatic Aldehydes and Cyclic Ketones with Sn-Beta Zeolites and H₂O₂. *Chem. – A Eur. J.* **8**, 4708–4717 (2002).
242. Corma, A., Domine, M. E., Nemeth, L. & Valencia, S. Al-free Sn-Beta zeolite as a catalyst for the selective reduction of carbonyl compounds (Meerwein-Ponndorf-Verley Reaction). *J. Am. Chem. Soc.* **124**, 3194–3195 (2002).
243. Creighton, E. J., Huskens, J., Van Der Waal, J. C. & Van Bekkum, H. Meerwein-Ponndorf-Verley and Oppenauer reactions catalysed by heterogeneous catalysts. *Stud. Surf. Sci. Catal.* **108**, 531–537 (1997).
244. Van Der Waal, J. C., Kunkeler, P. J., Tan, K. & Van Bekkum, H. Zeolite titanium beta: A selective catalyst in the Meerwein-Ponndorf-Verley-Oppenauer reactions. *Stud. Surf. Sci. Catal.* **110**, 1015–1024 (1997).
245. Moliner, M., Roman-Leshkov, Y. & Davis, M. E. Tin-containing zeolites are highly active

- catalysts for the isomerization of glucose in water. *Proc. Natl. Acad. Sci.* **107**, 6164–6168 (2010).
246. Holm, M. S., Saravanamurugan, S. & Taarning, E. Conversion of Sugars to Lactic Acid Derivatives Using Heterogeneous Zeotype Catalysts. *Science (80-.)*. **328**, 602–605 (2010).
247. Tewari, Y. B. Thermodynamics of industrially-important, enzyme-catalyzed reactions. *Appl. Biochem. Biotechnol. Part A Enzym. Eng. Biotechnol.* **23**, 187–203 (1990).
248. Lambert, J. B., Lu, G., Singer, S. R. & Kolb, V. M. Silicate complexes of sugars in aqueous solution. *J. Am. Chem. Soc.* **126**, 9611–9625 (2004).
249. Román-Leshkov, Y., Moliner, M., Labinger, J. A. & Davis, M. E. Mechanism of glucose isomerization using a solid lewis acid catalyst in water. *Angew. Chemie - Int. Ed.* **49**, 8954–8957 (2010).
250. Boronat, M., Concepción, P., Corma, A., Renz, M. & Valencia, S. Determination of the catalytically active oxidation Lewis acid sites in Sn-beta zeolites, and their optimisation by the combination of theoretical and experimental studies. *J. Catal.* **234**, 111–118 (2005).
251. Padovan, D., Botti, L. & Hammond, C. Active Site Hydration Governs the Stability of Sn-Beta during Continuous Glucose Conversion. *ACS Catal.* **8**, 7131–7140 (2018).
252. Gunther, W. R., Wang, Y., Ji, Y., Michaelis, V. K., Hunt, S. T., Griffin, R. G. & Román-Leshkov, Y. Sn-Beta zeolites with borate salts catalyse the epimerization of carbohydrates via an intramolecular carbon shift. *Nat. Commun.* **3**, (2012).
253. Drabo, P. & Delidovich, I. Catalytic isomerization of galactose into tagatose in the presence of bases and Lewis acids. *Catal. Commun.* **107**, 24–28 (2018).
254. Bermejo-Deval, R., Gounder, R. & Davis, M. E. Framework and extraframework tin sites in zeolite beta react glucose differently. *ACS Catal.* **2**, 2705–2713 (2012).
255. Gunther, W. R., Duong, Q. & Román-Leshkov, Y. Catalytic consequences of borate complexation and pH on the epimerization of l-arabinose to l-ribose in water catalyzed by Sn-Beta zeolite with borate salts. *J. Mol. Catal. A Chem.* **379**, 294–302 (2013).
256. Bermejo-Deval, R., Orazov, M., Gounder, R., Hwang, S. J. & Davis, M. E. Active sites in Sn-beta for glucose isomerization to fructose and epimerization to mannose. *ACS Catal.* **4**, 2288–2297 (2014).
257. Diercks, C. S., Kalmutzki, M. J., Diercks, N. J. & Yaghi, O. M. Conceptual Advances from Werner Complexes to Metal-Organic Frameworks. *ACS Cent. Sci.* **4**, 1457–1464 (2018).
258. Tomic, E. A. Thermal stability of coordination polymers. *J. Appl. Polym. Sci.* **9**, 3745–3752 (1965).
259. Wen, X., Zhang, Q. & Guan, J. Applications of metal–organic framework-derived materials in fuel cells and metal-air batteries. *Coord. Chem. Rev.* **409**, 213214 (2020).
260. Mehtab, T., Yasin, G., Arif, M., Shakeel, M., Korai, R. M., Nadeem, M., Muhammad, N. & Lu, X. Metal-organic frameworks for energy storage devices: Batteries and supercapacitors. *J. Energy Storage* **21**, 632–646 (2019).
261. Li, H., Wang, K., Sun, Y., Lollar, C. T., Li, J. & Zhou, H. C. Recent advances in gas storage and separation using metal–organic frameworks. *Mater. Today* **21**, 108–121 (2018).
262. Xu, W., Dong, M., Di, L. & Zhang, X. A facile method for preparing uiO-66 encapsulated ru catalyst and its application in plasma-assisted co2 methanation. *Nanomaterials* **9**, 10–13 (2019).
263. Oozeerally, R., Burnett, D. L., Chamberlain, T. W., Walton, R. I. & Degirmenci, V. Exceptionally Efficient and Recyclable Heterogeneous Metal–Organic Framework Catalyst for Glucose Isomerization in Water. *ChemCatChem* **10**, 706–709 (2018).

264. Zhou, F., Lu, N., Fan, B., Wang, H. & Li, R. Zirconium-containing UiO-66 as an efficient and reusable catalyst for transesterification of triglyceride with methanol. *J. Energy Chem.* **25**, 874–879 (2016).
265. Ye, G., Qi, H., Zhou, W., Xu, W. & Sun, Y. Green and scalable synthesis of nitro- and amino-functionalized UiO-66(Zr) and the effect of functional groups on the oxidative desulfurization performance. *Inorg. Chem. Front.* **6**, 1267–1274 (2019).
266. Devarajan, N. & Suresh, P. MIL-101-SO₃H metal-organic framework as a Brønsted acid catalyst in Hantzsch reaction: An efficient and sustainable methodology for one-pot synthesis of 1,4-dihydropyridine. *New J. Chem.* **43**, 6806–6814 (2019).

Chapter 2. Experimental and methods

2.1 List of acronyms

Solid state incorporation:	SSI
Glucose Isomerisation:	GI
Meerwein-Ponndorf-Verley:	MPV
Tin Beta zeolite:	Sn-Beta
X-Ray Diffraction:	XRD
Scanning Electron Microscopy:	SEM
Transmission Electron Microscopy:	TEM
Diffuse Reflectance Infrared Fourier Transform Spectroscopy:	DRIFTS
Magic Angle Spinning Nuclear Magnetic Resonance:	MAS NMR
Carr-Purcell-Meiboom-Gill:	CPMG
High Performance Liquid Chromatography:	HPLC
Evaporative Light-Scattering Detector:	ELSD
Gas Chromatography:	GC
Flame Ionization Detector:	FID
Inductively Coupled Plasma Mass Spectroscopy:	ICP-MS
X-Ray Absorption Spectroscopy	XAS
Extended X-ray absorption fine structure	EXAFS
X-ray Absorption Near Edge Structure	XANES
Plug Flow Reactor:	PFR
Brunauer-Emmett-Teller surface area:	S _{BET}
Non-Local Density Functional Theory:	NLDFT
Pore-directing agent	PDA
Cetyltrimethylammonium	CTA ⁺
Chemical Shift Anisotropy	CSA

2.2 Formulae and expressions

Substrate conversion

$$X(\%) = \frac{\text{mol}_{\text{Substrate}} - \text{mol}_{\text{Substrate}_t}}{\text{mol}_{\text{Substrate}_0}} * 100$$

Product yield

$$Y(\%) = \frac{\text{mol}_{\text{Product}_t}}{\text{mol}_{\text{Substrate}_0}} * 100_{\text{Hexoses or } 50_{\text{ML and MVG}}}$$

Product selectivity

$$S(\%) = \frac{\text{Product } Y(\%)}{\text{Conversion } X(\%)} * 100$$

Carbon Balance

$$C(\%) = \frac{\sum \text{Carbon}_t}{\sum \text{Carbon}_0} * 100$$

Levenspiel rate of deactivation

$$k_d (h^{-1}) = \ln \left[\ln \left(\frac{1}{1 - \frac{X(\%)}{100}} \right) \right]$$

Turnover frequency

$$TOF_{\text{product}} (h^{-1}) = \frac{\text{mol}_{\text{Product}_t}}{\text{time}(h) * \text{mol}_{\text{Sn}}}$$

Productivity

$$\text{Productivity } (h^{-1}) = \frac{Q * \rho_{\text{Sol}} * \frac{\text{Product}_{\text{wt.}\%}}{100}}{m_{\text{catalyst}}}$$

2.3 Catalyst synthesis

2.3.1 Hydrothermal Beta zeolite

Beta zeolites with different metals were synthesized using fluoride ions as a mineralizer. In a typical synthesis, 30.6 g of tetraethylorthosilicate (TEOS) was added to 33.37 g of tetraethylammonium hydroxide (TEAOH) under constant stirring. After TEOS was hydrolysed (*i.e.*, homogenization of both liquids was achieved), a metal precursor (FeCl₃, AlCl₃, GaCl₃, SnCl₄, HfCl₄, ZrCl₄, HBO₃) was added and left stirring until the adequate water ratio (1:SiO₂:8.5H₂O) was reached. Water ratio was calculated by weighing the weight of the flask (taking into consideration the ethanol evaporation as well). Afterwards, HF was added to form a solid gel. Final molar ratios of the gel were 0.005-0.01M:1SiO₂:0.54TEAOH:0.54HF:8.5H₂O, where *M* corresponds the indicated metal. The gels were transferred into a stainless-steel autoclave with PTFE liners and placed in an oven set to a temperature of 140 °C and held isothermally under static conditions for 7 days.

The crystallised zeolites were subsequently filtered with copious amounts (~ 2 L) of water and dried at 110 °C overnight. Calcination of the organic template was achieved by heating the powder to 550 °C for 6 h at 2 °C/min in static air.

2.3.2 Post-synthetic modification

2.3.2.1 Demetallation

All metal Betas and commercial Beta (PS Sn-Beta, 1Sn-Beta_{COM19}) underwent demetallation using 20 mL g⁻¹ (zeolite) of a 13 M HNO₃ solution at 100 °C for 20 h. The dealuminated samples were filtered with copious amounts (~ 2 L) of water and left to dry at 110 °C overnight. Subsequently, SSI was carried out to fill the silanol nests of the metal-stripped zeolites with the desired metal; this was done by grinding the demetallated zeolite with a required amount (1 wt.%) of Sn(II) acetate with the sample for *ca.* 10 minutes. For instance, to create 1 g of 1 wt. % Sn-Beta, 0.02 g of Sn(II) acetate was mixed with 0.99 g of dealuminated Beta zeolite. Other Sn-Beta SSI materials containing different Sn loading were prepared by the same method, but with the mass of Sn-Beta adjusted appropriately. Thereafter, the demetallated/Sn acetate mixtures were heated in a combustion furnace (Carbolite MTF12/38/400) to 550 °C (10 °C min⁻¹ ramp rate) in nitrogen flow

(60 mL min⁻¹). After reaching set temperature, it was left isothermally for 3 hours and subsequently changed to air flow (60 mL min⁻¹) for 3 more hours.

$$m_{Sn(OAc)_2} = \frac{m_{cat} * Sn_{wt\%} * M_{Sn(OAc)_2}}{M_{Sn}}$$

$$m_{DeAl} = m_{cat} - (m_{cat} * Sn_{wt\%})$$

Where:

- $m_{Sn(OAc)_2}$ = Mass of Sn(II) acetate required
- m_{DeAl} = Mass of dealuminated Beta required
- m_{cat} = Desired mass of the final catalyst
- $Sn_{wt\%}$ = Desired wt. % of Sn of the final catalyst
- $M_{Sn(OAc)_2}$ = Molar mass of Sn(II) acetate
- M_{Sn} = Molar mass of Sn

2.3.2.2 Desilication

In the event of creating a hierarchical structure, desilication was carried out prior to dealumination. For commercial zeolites, they were first converted to their protonic form by calcining in static air at 550 °C at 5 °C min⁻¹ for 5 h. The H-form zeolite was thereafter suspended in a 0.2 M NaOH solution and was heated at the indicated temperature (0.5 h, 30 mL g⁻¹ of zeolite). The solid product was quenched in an ice bath, filtered with deionised water until reaching neutral pH, and dried at 110 °C overnight. Zeolites were converted back to NH₄-form by ion exchange using an aqueous solution of NH₄NO₃ (1 M, 2 h, 85 °C).

When a PDA was employed, 1:1 mixture of 0.2 M NaOH (or otherwise stated) and 0.2 CTA⁺ was first stirred and heated at temperatures ranging from 45-85 °C before the zeolite is added. As was undertaken for the initial desilication, the samples were left for 0.5 h and were subsequently quenched, filtered, and dried. Calcination for the removal of the PDA was carried out at 550 °C at a heating rate of 2 °C min⁻¹ for 6 h.

2.3.3 UiO-66-Zr-H and UiO-66-Zr-NH₂ MOF synthesis

Synthesis of UiO-66(Zr)-H was adapted from a published paper by Ma *et al.*¹ In a typical synthesis, 444 mg of ZrCl₄ and 316.5 mg of terephthalic acid (H₂BDC) were dissolved in 50 mL of

dimethylformamide (DMF) and stirred. 5.55 mL of acetic acid (glacial, $\geq 99\%$) was subsequently added to the solution and was left stirring for another 30 minutes. Afterwards, the solution was transferred to a stainless-steel autoclave with a PTFE liner and placed in an oven and heated statically at a temperature of 120 °C for 48 h. The samples were centrifuged for 10 minutes and washed with ethanol after every centrifugation thrice, and finally were statically dried in an oven at 100 °C overnight.

2.4 Kinetic evaluation

2.4.1 Batch glucose isomerisation (GI)

D-glucose ($\geq 99\%$) isomerisation batch experiments were performed in a pressurized 15 mL thick-walled Ace tubular glass reactor, which was heated in a temperature-controlled oil bath at 110 °C. The reactor was charged with 5 mL of a glucose/methanol (1:99 wt/wt) solution and an appropriate amount of catalyst which corresponded to Sn:glucose molar ratio of 1:50. The solution was stirred vigorously (800 rpm) and periodic aliquots of the samples were taken by quenching the reactor in an ice bath, followed by centrifugation to separate the solid (catalyst) phase. Sample preparation for analysis consisted of mixing 0.1 mL of the separated solution with 0.1 mL of 5 wt. % of sorbitol as the external standard, diluting the mixture with 0.4 mL of deionized water. GC-FID had a starting temperature of 50 °C and was heated to 180 °C at 15 °C min⁻¹. This was maintained for 3 minutes and was thereafter heated to 230 °C at the same heating rate. H₂ flow for the flame was 30 mL min⁻¹ and 300 ml min⁻¹ for air which was used as the carrier.

Samples were subsequently analysed by HPLC (Agilent 1260 infinity II). Compounds were separated with a Ca Hi-Plex column (6.5 x 300 mm, 8 µm particle size, Agilent) held at 80 °C. Ultrapure HPLC water was used as the mobile phase using a flow rate of 0.75 mL min⁻¹. An Evaporative Light Scattering Detector (ELSD Agilent 1200) was used to detect the sugars. ELSD was used with an evaporative and nebulizing temperature at 30 °C and a N₂ flow at 1 mL min for all analysis.

2.4.2 Batch Meerwein-Ponndorf-Verley (MPV) reduction

Batch reactions for the MPV reduction using cyclohexanone as reactant and 2-butanol as the secondary alcohol (hydride donor) were performed in a 50 mL round bottom flask equipped with a reflux condenser, controlled thermostatically by immersion in a silicon oil bath. The vessel was charged with a 10 mL solution of cyclohexanone in 2-butanol (0.2 M) with biphenyl (0.01 M) as the internal standard. The flask was subsequently heated to the desired temperature (100 °C internal temperature). An aliquot prior to the addition of the catalyst was obtained and analysed to obtain the initial point (T_0) by immersing and letting the vessel reach internal temperature. The reaction started when Sn-Beta catalyst (1 mol% of Sn relative to cyclohexanone) was added to the flask, being stirred at ± 750 rpm. Aliquots were taken periodically from the flask, centrifuged and subsequently analyzed in a GC-FID (Agilent 7820, 25m CP-Wax 52 CB).

2.4.3 Continuous GI reaction

D-glucose (Sigma-Aldrich ≥ 99 %) isomerisation (GI) and its consecutive retro-aldol fragmentation of fructose to methyl lactate (ML) production experiments were performed under continuous flow in a plug flow, tubular ($\frac{1}{4}$ ", 4.1 mm ID) stainless-steel reactor. The reactor was connected to an HPLC pump to regulate the reactant flow and be able to operate at high pressures. Catalysts (100 mg) were placed between two plugs of quartz wool and packed in the reactor with a 0.5 μm frit in the reactor's outlet. The reactor was then immersed in a thermostatted oil bath at the desired temperature (110 °C for GI and 160 °C for ML) at a flow of 0.65 mL min^{-1} for GI and 1 mL min^{-1} for ML. Glucose was solubilised in the chosen solvent at a concentration of 1 wt. %, and the solvent used was either pure methanol, or a mixture of ethanol and water (e.g. 99:1 v/v ratio). Pressure in the system was controlled using a backpressure regulator, set at desired pressure depending on the undergoing experiment (10 bar GI, 20 bar ML). Periodic aliquots were taken with a Vici Valco 10 position microelectric valve actuator placed at the outlet and analyzed by an Agilent 1260 Infinity HPLC coupled with a Hi-Plex Ca column and an ELS detector where sorbitol was used as an external standard.

2.4.4 Continuous lactose isomerisation

Lactose (Sigma-Aldrich ≥ 98 %) isomerisation experiments were performed under continuous flow in a plug flow, tubular ($\frac{1}{4}$ ", 4.1 mm ID) stainless-steel reactor. The reactor was connected to an HPLC pump to regulate the reactant flow and be able to operate in high pressures. A 1 wt. %

solution of lactose using various ratios of EtOH/H₂O (*e.g.*, 50:50, 75:25, 99:1 v/v) or purely H₂O. The chosen MOF or zeolite catalyst (100 mg) was placed between two plugs of quartz wool and packed in the reactor with a 0.5 μm frit in the reactor's outlet. The reactor was then immersed in a thermostatted oil bath at the desired temperature (160 °C) in a flow of 0.4 mL min⁻¹. Pressure in the system was controlled using a backpressure regulator, set at 20 bar. Periodic aliquots were taken with a Vici Valco 10 position microelectric valve actuator placed at the outlet and analyzed by an Agilent 1260 Infinity HPLC coupled with a Hi-Plex Ca column and an ELS detector where sorbitol was used as an external standard.

2.5 Analytical methods

2.5.1 Chromatography

Chromatography involves in the separation of a mixture of chemical substances into their individual constituents. Each type of interaction chromatography requires a mobile phase that carries it through a second substance called the stationary phase. This mobile phase can either be a liquid or a gas, depending on the system being used, while the stationary phase can be a solid or a liquid. The use of specific mobile and stationary phases determines how fast or slow the substances travel; this is termed as retention time. Originally employed by Mikhail Tsvet in 1900, it was used to separate plant pigments (chlorophyll, carotenes, etc).² Separation was done in a chromatographic setup similar to Figure 2.1. Over the years, this technique has advanced into more complex and automated systems capable of separating a wider array of compounds.

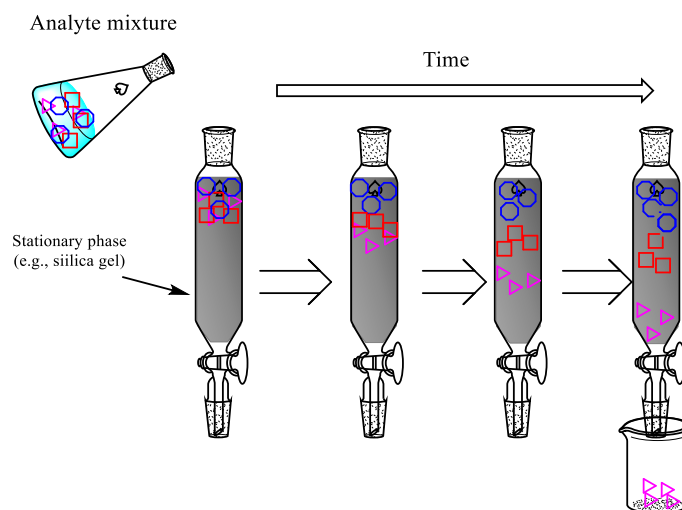


Figure 2.1. Chromatographic column setup for separating analytes.

2.5.1.1 Gas Chromatography – Flame Ionization Detector

Gas chromatography, also known as gas-liquid chromatography, is one of the most common analytical techniques used. In GC, the mixture being analysed is vaporised and is carried through the stationary phase, which is typically a metal or glass separation column using an inert gas (N_2 or He). Due to GC being gas-based separation, it is limited to components that have sufficient volatility and thermal stability to be volatilised into the gaseous phase. Therefore, GC is best used for analysing small to medium-sized molecules that are thermally stable. Operational temperatures are normally between 150 – 300 °C.

GC follows the same principle when it comes to separation; the compounds being analysed interact with the walls of the column which is coated with a stationary phase, eluting at different times (Figure 2.2) depending on their degree of interaction with the stationary phase.

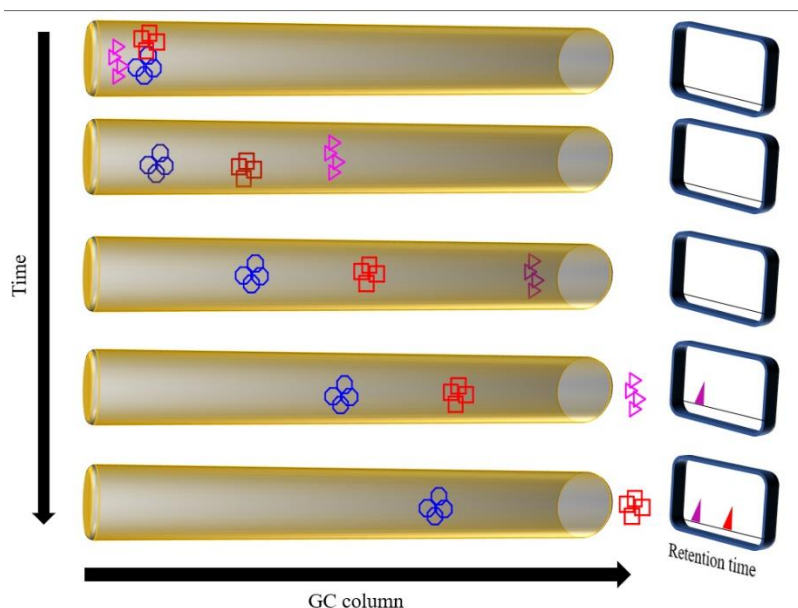


Figure 2.2. Schematic of compounds separation in a GC column.

The flame ionization detector (FID) is a standard instrument used for measuring hydrocarbon gas concentration. The FID is based on the detection of ions formed during combustion when exposed to a hydrogen flame. Since it is mass sensitive and not concentration sensitive, the carrier gas flow rate has minor effects on the detector response.

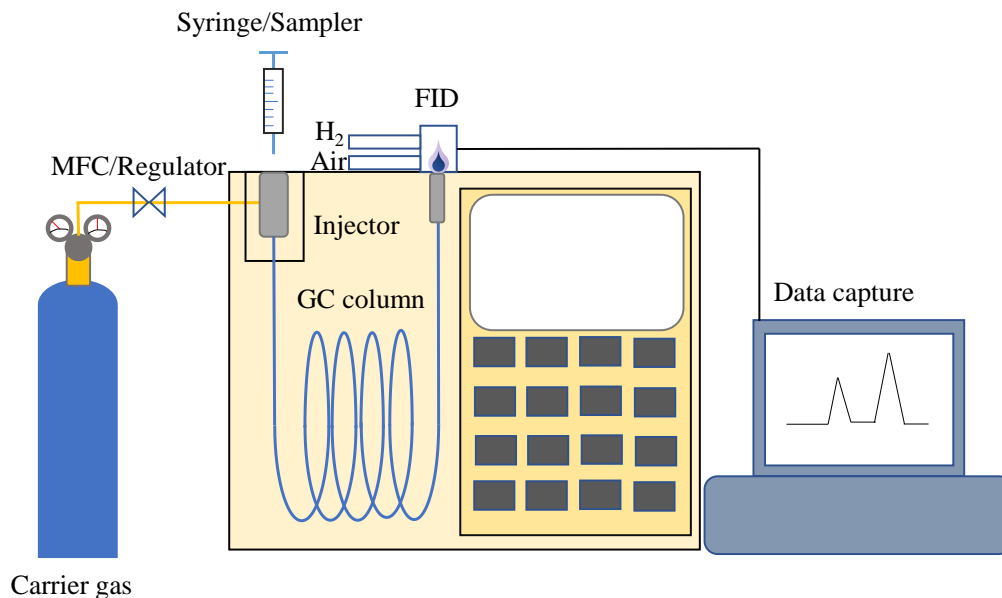


Figure 2.3. Schematic of GC-FID system.

2.5.1.2 High Performance Liquid Chromatography (HPLC)

HPLC is another alternative for samples analysis, consisting of relatively the same elements with different functionalities: it is a form of column chromatography which pumps an analyte or mixture in a solvent (mobile phase) at high pressure (up to 400 bar) through a column with a chromatographic pumping material (stationary phase). Just as the GC, the analytes are retained while traversing through the stationary phase. Unlike the GC however, this chromatographic technique is preferable when the analytes are not able to be vaporised or they are easily prone to decomposition (low thermal stability).

The HPLC has more flexibility when it comes to applying different methods to analyse the samples. Most HPLC are modular, *i.e.*, they are individual parts prefabricated offsite which can be easily assembled, as can be seen in Figure 2.4.

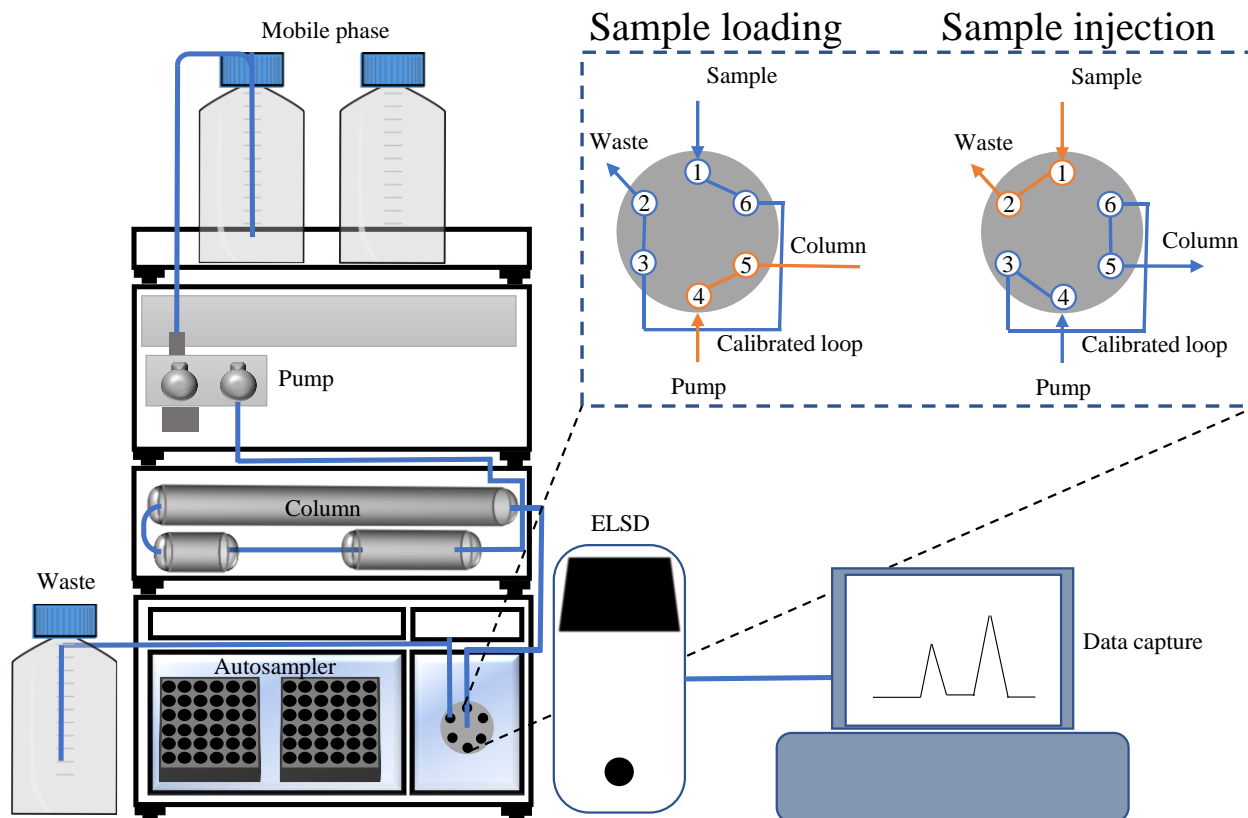


Figure 2.4. Schematic of HPLC modular system with pump, column oven, autosampler and an ELSD. Inset: sampling switching valve when loading a sample and its subsequent injection.

The switching valve, as can be seen in the figure, is a six-port two-position valve where the where in the load position, the sample loop or calibrated loop is filled with the sample while the system is equilibrating. When switching to the injection position, the calibrated loop is switched to the high-pressure part of the system, feeding the sample in the loop onto the column.

Common mobile phases include ultrapure HPLC grade water along with various organic solvents (acetonitrile or methanol). Acids such as formic acid or phosphoric can also be applied to aid in the separation process. For the analysis of sugars, a sulfonated polystyrene column with Ca^{2+} ions exchanged to H^+ ions to provide a good separation of the sugars (*e.g.*, Hi-Plex Ca).

Another important factor is the choice of detectors for the analysis, which is generally dependent on the analyte being analysed. One of the most commonly used detectors for the analysis of carbohydrates such as sugars is the Evaporative Light-Scattering Detector (ELSD) (Figure 2.5) This detector is suitable for non-volatile samples in a volatile eluent. The eluent is mixed with an

inert gas, typically nitrogen, passing through a nebulizer to create a fine spray. This spray is composed of droplets of the mobile phase containing the analyte of interest. The nebulized eluent goes through a heated tube to evaporate the mobile phase to subsequently detect the solid particles entering by a light source and a photodiode.

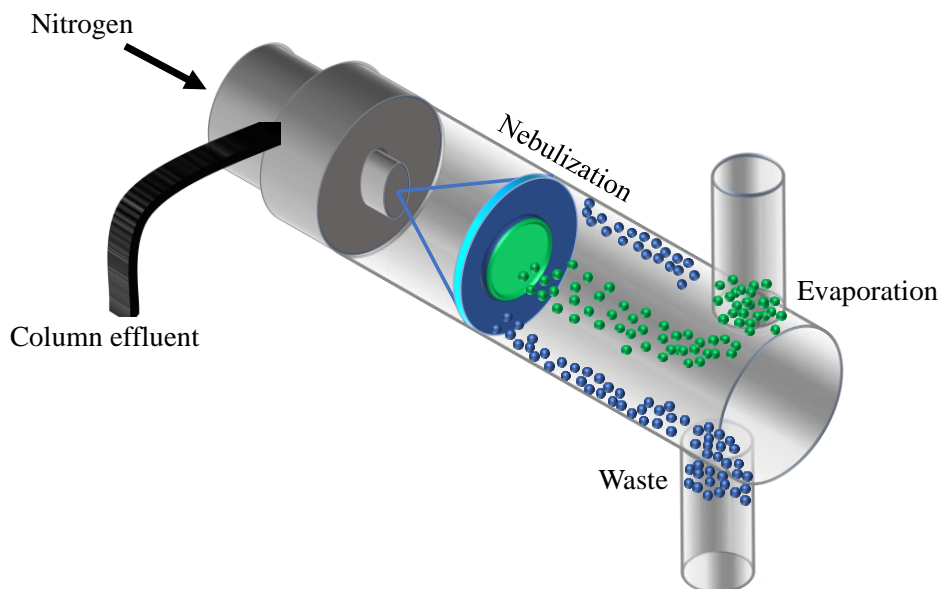


Figure 2.5. Schematic of Evaporative Light-Scattering Detector.

2.5.2 Quantification of GC and LC products

2.5.2.1 GC quantification

For HPLC analysis, an Agilent 1260 Infinity HPLC coupled with a Hi-Plex Ca column and an ELSD was used. A flow rate of 0.75 mL min^{-1} with a temperature of $80 \text{ }^\circ\text{C}$ was used for all analytes. The external calibration standard employed was sorbitol at 0.5 wt. % before dilution, using 0.1 g, 0.1 g, and 0.4 g of solution, external standard, and deionised water, respectively. Calibration curves were performed with varying degrees of wt. % of the analyte of interest, within the ranges of 0.1-1 wt.% in water which can be seen in Table 2.1. Samples of the analysed sample were done with the corresponding weights of analyte, sorbitol, and water mentioned in section 2.4.

Table 2.1. Concentration and areas obtained from HPLC of glucose and external standard sorbitol

Sample / wt. %	Glucose		Sorbitol	
	Area	Concentration / Moles	Area	Concentration / Moles
1 %	26898	5.5896E-06	9771	2.77608E-06
0.75 %	16600	4.12377E-06	9627	2.73757E-06
0.5 %	8638	2.72654E-06	9703	2.74307E-06
0.25 %	2972	1.40337E-06	9538	2.72381E-06
0.1 %	655	5.47301E-07	9743	2.73481E-06

Products were monitored by a GC-FID Agilent 7820, using a 25 m * 0.53 mm * 2 um CP-Wax 52 CB. A power equation ($y = ax^b$) was used to obtain the best fit due to the ELSD response, as can be seen in Figure 2.6.

To generate the calibration curve, the ratio of concentration of analyte and sorbitol was plotted against the ratio of their corresponding areas which were obtained by the HPLC:

$$Ratio_{Area} = \frac{Area_{Analyte}}{Area_{Standard}}$$

$$Ratio_{Concentration} = \frac{Concentration_{Analyte}}{Concentration_{Standard}}$$

The ratios were plotted and were fitted using the power trendline to find the corresponding calibration factors (CF), as shown in Figure 2.6.

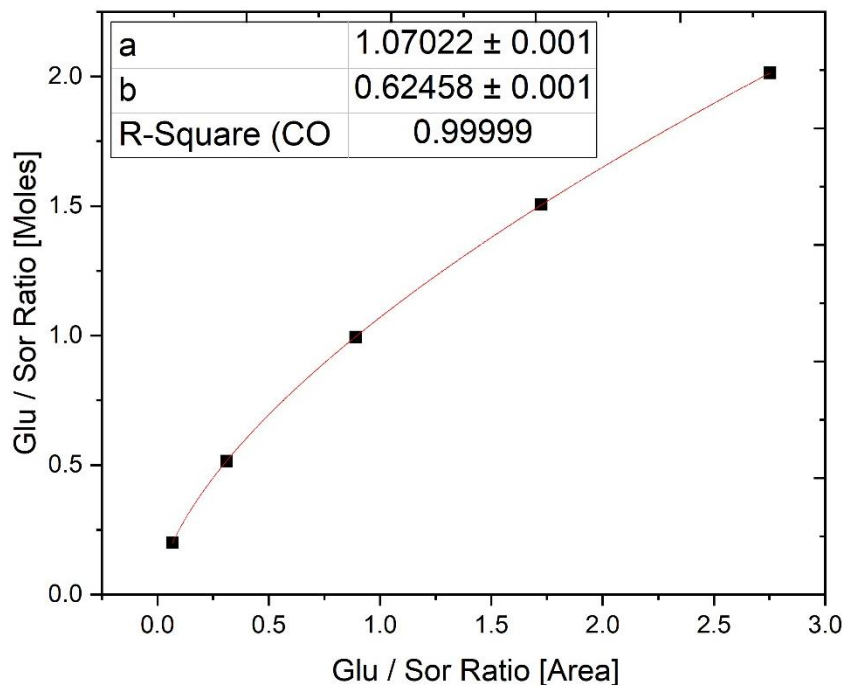


Figure 2.6. HPLC-ELSD-obtained calibration curve to obtain the response factor of glucose using sorbitol as an external standard.

With the adequate CFs, the unknown amount of analyte can be determined using the following formula:

$$\text{Analyte} = CF_a * \left(\frac{\text{Area}_{\text{Analyte}}^{CF_b}}{\text{Area}_{\text{Standard}}} \right) * \left(\frac{\text{Wt. \%}_{\text{Standard}}}{\text{Mass}_{\text{Standard}} * \text{MM}_{\text{Standard}}} \right)$$

*MW: Molar mass

This was done with the other analytes of interest, which are shown in Table 2.2.

Table 2.2. Calibration factors for the compounds analysed in the HPLC.

Analyte	R.T.	CF _a	CF _b
Lactose	9.6	0.5252	0.61
Lactulose	9.8	0.474	0.6169
Glucose	10.5	1.0705	0.6225
Mannose	11.6	0.9743	0.7227
Fructose	13.6	1.1536	0.6101
Sorbitol	21.5	-	-

*R.T. Retention time.

2.5.2.2 GC quantification

GC quantification was carried out with an Agilent 7820A (G4350A) GC with FID using a CP-Wax 52 CB column. Given that the work (using cyclohexanone – MPV) would be conducted within a range of 0.2 M, the range opted for calibration was within the range of 0.05 – 0.3 M (Table 2.3). The analytes were made and subsequently quantified by use of biphenyl (1 wt.%) as the standard.

Table 2.3. Area, mass, and concentration of cyclohexanone obtained in the GC-FID.

Molarity	Cyclohexanone			Biphenyl		
	Mass	Area	Moles	Mass	Area	Moles
0.3	0.3172	1629	0.003231788	109.9	109.9	1.0180922E-04
0.2	0.1999	1017.4	0.002036679	101.2	101.2	9.4676091E-05
0.1	0.1007	482.2	0.001025981	93.6	93.6	1.0375462E-04
0.05	0.0539	488.7	0.000549159	0.0162	181.1	1.0505155E-04

For the GC-FID, the trendline was linear, as can be seen in Figure 2.7. Thus, to calculate the analytes concentration, the following formula was used:

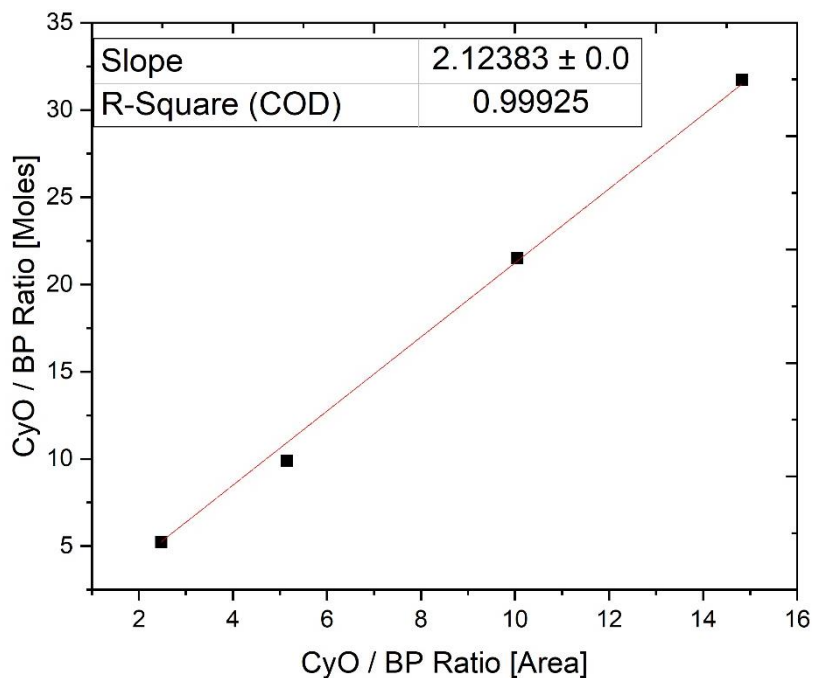


Figure 2.7. GC-FID-obtained calibration curve to obtain the response factor of cyclohexanone using biphenyl as an internal standard.

$$Analyte = CF * \left(\frac{Area_{Analyte}}{Area_{Standard}} \right) [Standard]$$

This was done with the other analytes of interest, which are shown in Table 2.4.

Table 2.4. Calibration factors for the compounds analysed using the GC-FID.

Analyte	R.T.	CF
Methyl lactate	14.12	6.459
Methyl vinyl glycolate	15.43	4.27
Cyclohexanone	14.74	2.2087
Cyclohexanol	16.02	2.19
Biphenyl	21.12	-

2.6 Catalyst characterisation

2.6.1 Powder X-Ray Diffraction (pXRD)

XRD is one of the most common characterisation techniques used for crystalline materials. It is a non-destructive technique that provides information on the materials structure, phases, as well as crystallinity (degree of structural order), grain size, and if the material presents crystal defects. The diffraction pattern is obtained when an incident beam of monochromatic X-rays is collimated to target the sample of interest. Due to the crystal being an array of atoms, X-ray waves are diffracted. As the sample and detector are rotated by a goniometer, the diffracted X-rays are being recorded. This interaction of the rays with the sample creates a constructive interference, as well as a diffracted ray, when conditions satisfy Bragg's Law:³

$$n\lambda = 2d \sin \theta$$

where:

n = Positive integer

λ = Wavelength of incident wave

d = Interplanar distance

θ = Angle of incidence

Bragg's Law indicates that when the X-ray beams are scattered from the planes in the crystal, it will travel distances differing by exactly one wavelength, given that $n = 1$. A schematic which shows the diffraction of X-rays from the sample can be seen in Figure 2.8.

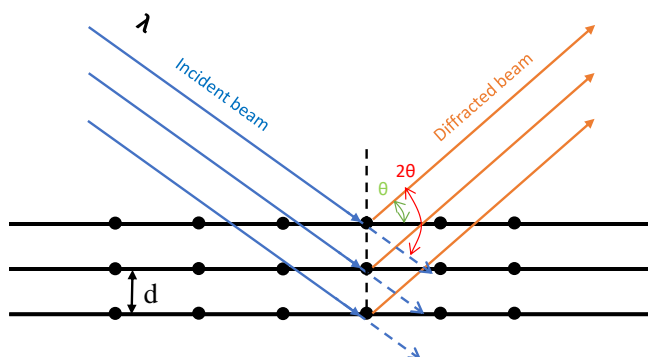


Figure 2.8. Schematic of diffraction of the incident beam into a crystalline sample according to Bragg's Law.

To obtain a diffraction (or spectra), there must be a constructive interference, as mentioned previously. This comes from two waves that are in phase with each other, creating a diffraction pattern. However, when deconstructive interference exists, the waves are out of phase, resulting in no diffraction pattern, as can be seen in Figure 2.9.

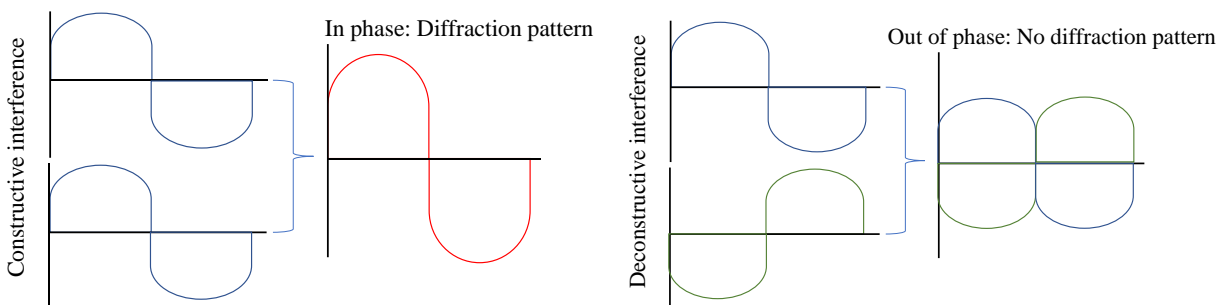


Figure 2.9. Schematic of constructive (left) and deconstructive (right) interference in XRD.

For this work, XRD patterns were recorded on an X'PertPRO diffractometer equipped with a $\text{CuK}\alpha$ radiation source (40 kV and 40 mA) and were recorded between $5\text{--}80^\circ 2\theta$ (step size 0.0167° , time/step 150 s, total time ≈ 1.5 h). XRD was used to verify crystallinity after synthesis and following various post-synthetic treatments (*i.e.*, desilication/dealumination), as well as to identify potential presence of extra-lattice phases such as SnO_2 .

2.6.2 Physisorption for surface and porosimetry analysis

Physisorption consists in the adsorption of gaseous molecules (adsorptive) onto the surface of the solid material (adsorbent). The gases typically used are nitrogen or argon, due to their inert nature, preventing them from interacting chemically with the solid.

The surface of the solid and how the adsorbate interacts with the adsorptive can be divided into three levels (Figure 2.10):⁴

- Van der Waals surface, which consists in the outer part of the van der Waals spheres of the surface atoms.
- Connolly surface, also known as the solvent-excluded surface, which is imagined as a cavity in bulk solvent, which encompasses the van der Waals surface.
- Lastly is the pore-accessible surface, which is the surface at r distance from the Connolly surface.

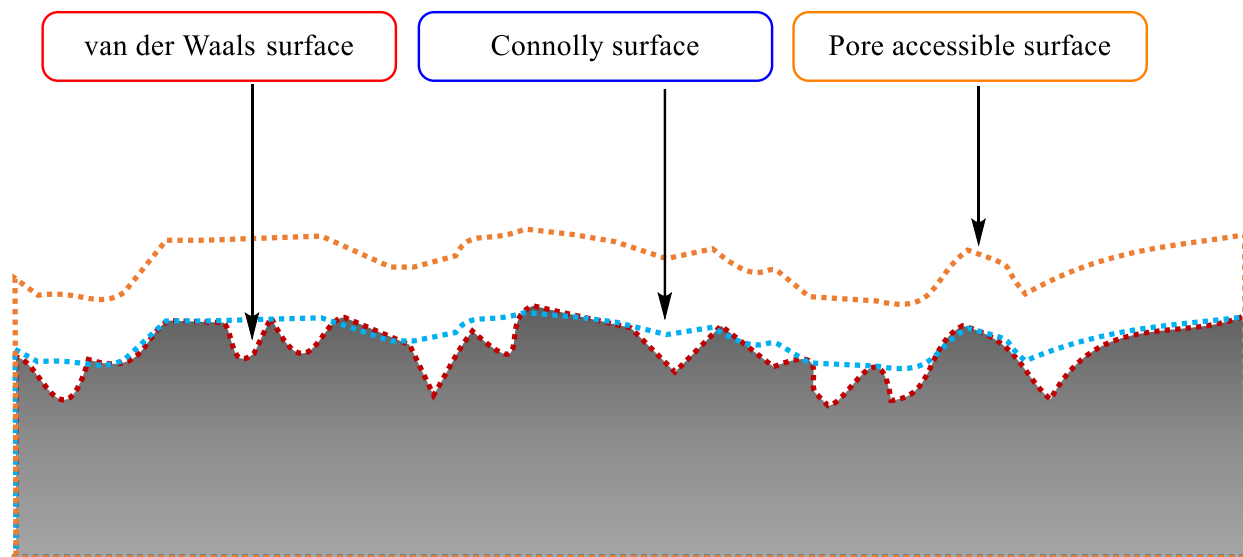


Figure 2.10. Schematic representation of possible surfaces of an adsorbent.

Physisorption can take place in various stages, particularly if mesopores are present (Figure 2.11). If micropores exist within the solid, an adsorption process denominated micropore filling also occurs. Mesopore physisorption, for instance, takes place in three stages. The first consists in monolayer adsorption, where all adsorbed molecules are in contact with the surface. Next is multilayer adsorption, in which the adsorbate forms more than one layer which is not in contact with the solid. Lastly, capillary (pore) condensation takes place, where this consists in condensation to a liquid-like phase in a pore at a pressure, P , less than the saturation pressure, P_0 , of the bulk liquid, which is used to maintain condensation.

The best known model of multilayer adsorption is that developed by Brunauer, Emmet, and Teller.⁵ It still continues to be the most used procedure to calculate the surface area of the material:

$$\frac{1}{v \left[\left(\frac{P_0}{P} \right) - 1 \right]} = \frac{c - 1}{v_m c} * \left(\frac{P}{P_0} \right) + \frac{1}{v_m c}$$

Where P and P_0 are the equilibrium and saturation pressure of the adsorbates at the temperature of adsorption, 'v' is the adsorbed gas quantity (cm^3 , mL), and v_m is the adsorbed gas on the surface or monolayer. The parameter C is related to the energy of the monolayer adsorption and can be an indicator of the shape of the isotherm.

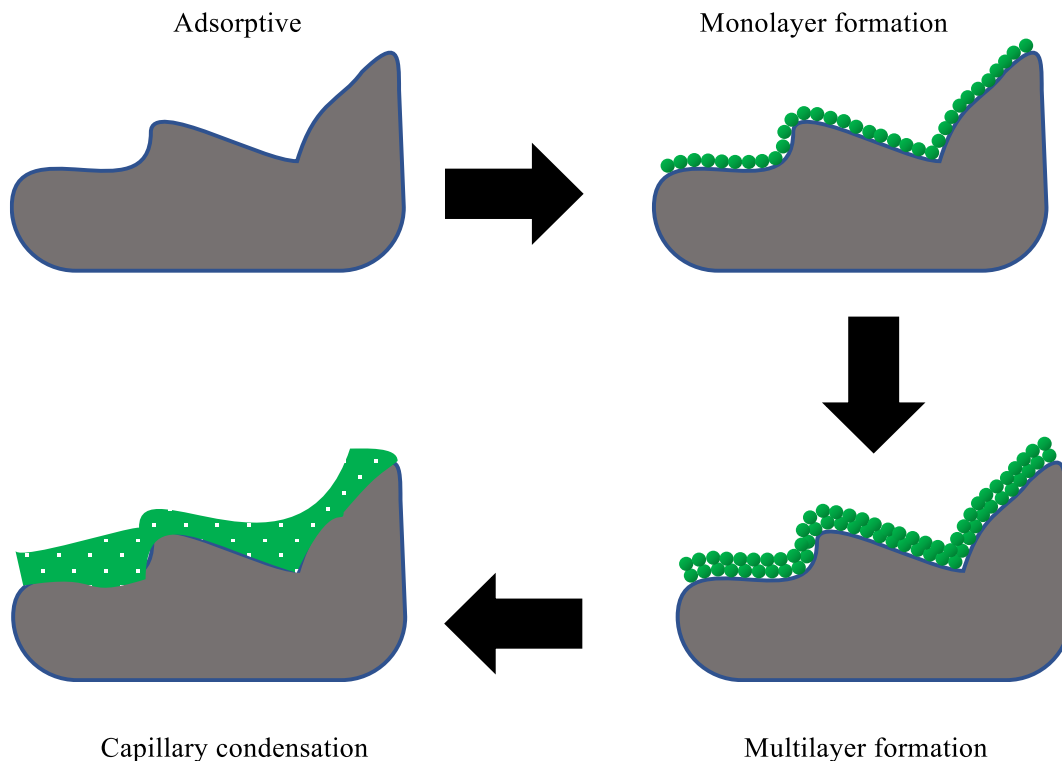


Figure 2.11. Schematic of different stages of adsorbate formation.

Although the use of BET is commonly used for surface analysis, more detailed information can be obtained when implementing Non-local density functional theory (NLDFT) based methods, particularly for pore size distribution (PSD), whereas with the other methods such as Barrett-Joyner-Halenda (BJH), which assumed capillary condensation of the adsorbate. NLDFT uses a classical fluid DFT to construct the adsorption isotherms in ideal pore geometries and conditions. For porosity, NLDFT is applied to create a series of theoretical isotherms, called kernels, from various values and are used with an appropriate physical representation (model) of the pore structure, such as slits (typically for carbonaceous species) or cylindrical pores alongside the adsorbate used (N_2 or Ar). The main benefit of NLDFT is the wide applicability it has, extending from micropores to macropores, and from a plethora of materials.

Other useful methods to use for micropore analysis is the t-plot method, which determines both the micro and/or mesopore volumes along with the surface area and external surface area. To correctly ascertain a value, the relative saturation pressure for the t-plot method should be assigned between 0.2-0.5 (P/P_0).

For this study, nitrogen adsorption isotherms were determined on a Quantachrome autosorb iQ at -196 °C. Prior to analysis, samples were degassed at 300 °C (for zeolites) or 120 °C (for MOFs) for 6 h. Specific surface area and total pore and micropore volume were determined from the DFT method using the NLDFT N₂ - silica equilibrium transition kernel at -196 °C based on a cylindrical pore model. Water sorption analysis was also conducted in the same porosimeter, using water as the solvent, within P/P₀ ranges of 0-0.7. External surface area was obtained with the t-plot method using a P/P₀ range from 0.2-0.5. Total pore volume was obtained at the P/P₀ of 0.99.

2.6.3 Infrared Spectroscopy – Diffuse Reflectance Infrared Fourier Transform Spectroscopy (DRIFTS)

Infrared spectroscopy is one of the most common and widely used spectroscopic techniques; it consists in the analysis of infrared light interacting with a molecule, and its main use is to determine functional groups in molecules. Infrared spectroscopy can be divided into three regions: the near infrared (NIR), which is approximately 14,000-4,000 cm⁻¹, and is mainly used to observe overtones (harmonics) and combination bands,⁶ far infrared (FIR), within the range of 400-10 cm⁻¹, primarily used to study lattice vibrations of crystals and rotational spectra, and lastly, the mid-range infrared (MIR) which is used for the identification of chemicals based on the interaction of molecules with electromagnetic radiation (EMR). This last region is the most commonly used for the analysis of both organic and inorganic samples.

IR spectroscopy involves in using energy to excite the bonds from a molecule. This can be presented in various types of vibrations and rotations in the molecule. These vibrations can be presented in different modes such as: bending, stretching, twisting, wagging, scissoring, and rocking. However, for the molecule to be IR active, a net dipole moment should result of the vibration when IR radiation occurs. This can be obtained through the equation:

$$\vec{\mu} = \sum_i Q_i \vec{r}_i$$

Where

- $\vec{\mu}$ is the dipole moment vector
- Q_i is the charge at the ith position

- \vec{r}_i is the distance (vector) which represents the charge at the i^{th} position.

Due to the dipole moment being a vector quantity, it can be broken down into horizon and vertical components to obtain the net dipole moment from a compound. One example to elucidate on net dipole moment consists in (E) and (Z) configurations of a haloalkene (Figure 2.12), where (E) configuration of a compound, *e.g.*, (E)-1,2-dibromoethene's C-Br vibrations would cancel each other out, showing no symmetric vibration, whereas (Z)-1,2-dibromoethene creates a net dipole moment from both vectors, resulting in a net dipole moment. Furthermore, this also influences properties of the reactants, where intermolecular dipole moment is shown to increase the boiling point of the reactant.

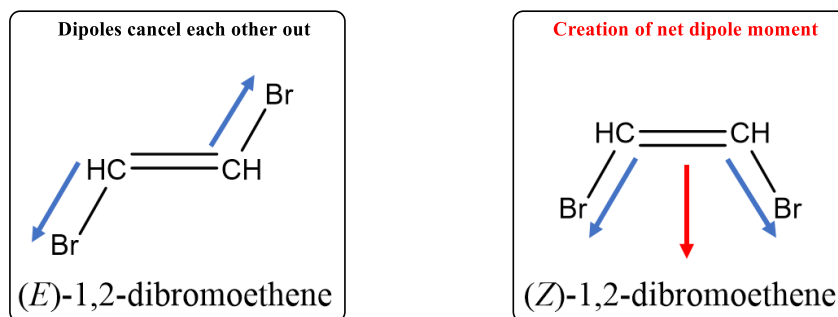


Figure 2.12. Example of net dipole moment of a chemical with E and Z configurations.

DRIFTS is an infrared spectroscopy sampling technique that collects and analyses scattered IR irradiation. It is applied to analyse powders and rough surface solids due to the technique relying upon scattering of radiation within the sample⁷. Unlike other sampling techniques which require pelletization and/or mixture with a reference (such as KBr), little to no sample preparation is required for DRIFTS.

DRIFT spectra for this work were recorded on a Bruker Tensor II spectrometer, using a Harrick praying mantis cell over a range of 4000-650 cm^{-1} at a resolution of 2 cm^{-1} . Silicon carbide was used as an IR source with ZnSe as beamsplitters. *In-situ* DRIFT spectroscopy was also performed with the same conditions under flow (Figure 2.13); calcination of the post-synthetic zeolite mixtures (demetallated - section 2.3.2.1) was analysed. The samples were heated at a ramp rate of 10 $^{\circ}\text{C min}^{-1}$ to set temperature 550 $^{\circ}\text{C}$ under nitrogen flow, switched to air (20 mL min^{-1}) after reaching set temperature and maintained under isotherm for 1h.

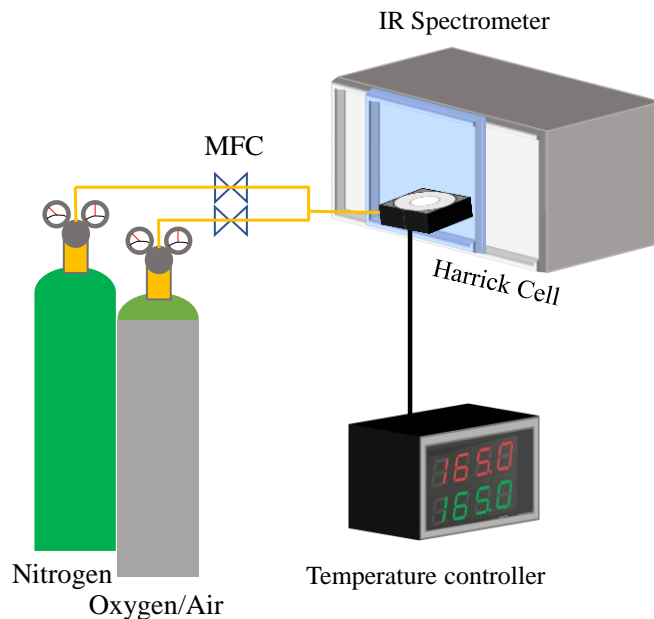


Figure 2.13. Schematic of *in-situ* DRIFTS for analysis of the calcination step of post-synthetically modified zeolites.

2.6.4 Temperature Programmed Desorption (TPD) – Mass Spectroscopy (MS)

TPD is highly useful technique, particularly in catalysis. It allows one to elucidate and study the interaction of gases with the solid surfaces or the use of probe molecules to measure the amount of acid or basic sites as well as their strength. The application of this technique involves the use of probe molecules, such as NH_3 , CO , or CO_2 , and saturating a solid catalyst after an earlier pretreatment to remove any physisorbed molecules on the surface (*e.g.*, H_2O). Using a designated ramp rate, the gaseous molecules are desorbed at different temperatures according to their relative strength of interaction with the material, which can be attributed to a higher desorption temperature. The signal of the desorbed molecules is typically recorded using a thermal conductivity detector (TCD) due to its lower sensitivity for the detection of organic compounds in comparison with other detectors (FID).⁸

In this thesis, the use of TPD was implemented for the analysis of gas evolutions obtained through post-synthetic calcination of demetallated beta and Sn(II) acetate; a schematic illustrating the setup can be seen in Figure 2.14. TPD-MS measurements were performed on a homemade system formed by mass flow controllers (MFC) equipped with a horizontal tube furnace where the sample is placed, connected with a Hiden QGA Mass Spectrometer. A weighed amount of catalyst was placed inside a calcination boat and placed in the horizontal furnace and compound evolutions

were monitored by the aforementioned spectrometer. The furnace was heated from 30 to 550 °C (ramp rate 10 °C/min) and a constant flow of nitrogen or helium was used throughout the experiment (20 mL min⁻¹). Nitrogen or helium flow was switched to air after reaching set temperature and continued for 1h.

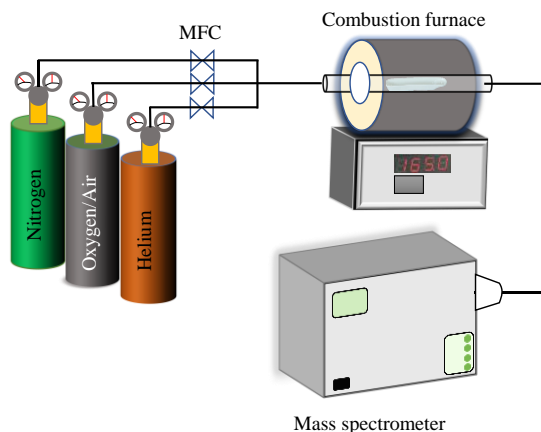


Figure 2.14. Schematic of *in-situ* TPD-MS for analysis of gas evolutions of post-synthetic zeolites under calcination.

2.6.5 Diffuse Reflectance Ultraviolet-visible (UV-vis) spectroscopy

DRUV-Vis technique consists in how much a chemical substance absorbs light; it works within the ranges of the ultraviolet (10-400 nm) and visible region (400-700 nm). Within these regions, molecules undergo electronic transitions and can be useful for the investigation of the electronic structure of materials. The radiation source is typically a tungsten (300-2500 nm), a deuterium arc lamp (190-400 nm) or light-emitting diodes for use in the visible region (400-700 nm). In the thesis, UV-Vis analysis was performed using a Cary 4000 UV-vis spectrophotometer. A scanning range between 200-800 nm was undertaken, at a scan rate of 200 nm min⁻¹.

2.6.6 Thermogravimetric analysis (TGA)

TGA is a useful analytical tool which measures the changes of the samples mass as a function of temperature and/or time. These measurements provide insight on of the materials thermal decomposition patterns. One of the main uses it has for zeolites or MOFs is to evaluate the thermal stability of the material. TGA can also be combined with other characterisation techniques, for instance a TGA-MS or TGA-IR, to further compliment analysis of the thermal decomposition.

For the analysis of post-synthetic zeolites, TGA tests were done to observe thermal decomposition changes when applying Sn(II) acetate on a demetallated zeolite, a defect-free zeolite (Beta silicalite), and the acetate by itself. TGA analysis was performed on a PerkinElmer TGA 4000 system. Samples were held isothermally at 30 °C for 30 min before being heated to 550 °C (10 °C min⁻¹ ramp rate) in nitrogen (30 mL min⁻¹). For MOFs, TGA analysis was performed the same system, and was done in the range of room temperature to 800 °C at a rate of 10 °C min⁻¹ under a constant flow of nitrogen (30 mL min⁻¹).

2.6.7 Electron Microscopy (EM)

Electron Microscopy is a tool used to obtain high resolution images of organic and inorganic samples. This is possible due to the usage of accelerated electrons as the source of illuminating radiation. It is helpful in catalysis to observe the morphology of the catalysts crystallites as well as their size.

2.6.7.1 Scanning electron microscopy (SEM)

SEM consists in scanning a focused electron beam over a surface to create an image; this allows the observation of surface morphology as well as homogeneity/uniformity of zeolites and MOFs, as well as the dispersion when using nanoparticles. The main components of the SEM are the source of electrons, EM lenses to focus the electrons, electron detectors, which can charge or amplify the charge from the incident electron beam, scanning coils that are used to deflect the beam in the X and Y axes so that it scans the sample in a raster fashion and the sample chamber, as shown in Figure 2.15.

SEM can use two types of detectors for imaging, which consist of:

Backscatter electron detector (BSE): Detects elastically scattered electrons; the electron beams ricochet from the when colliding with the atoms. Upon colliding with larger atoms (greater atomic number, Z), higher the chances of producing an elastic collision due to the greater cross-sectional area. Thus, with a higher Z, the more intense (brighter) the image will show.

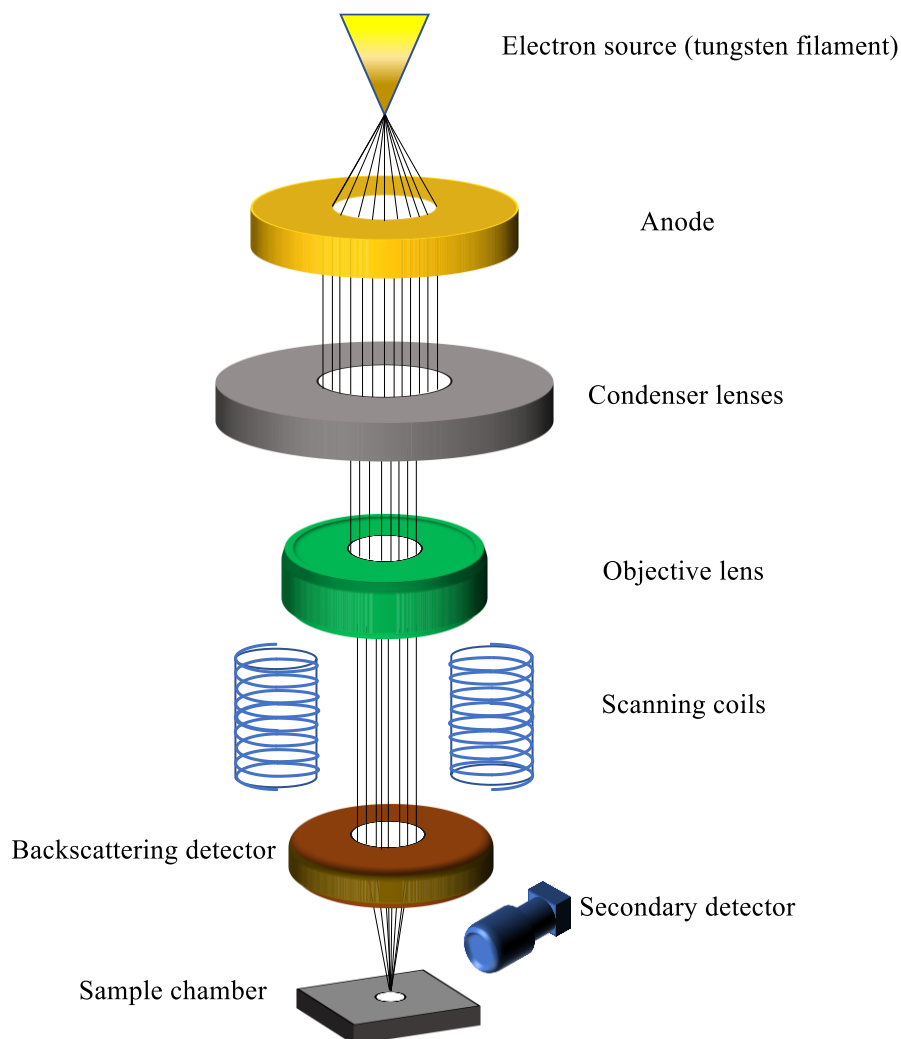


Figure 2.15. Schematic of a standard SEM system with BSE and SE detectors.

Secondary electron detectors (SE): these electrons originate from the surface regions of the sample. Unlike BSE, which occur due to elastic interactions, these occur from inelastic scattered interactions between the primary beam and the sample, containing lower energy. While BSE can show information regarding the Z from nanoparticles for instance, SED is more useful for the inspection of topography of the sample.

For this work, SEM images were obtained in a Hitachi TM3030 electron microscope using an accelerating voltage of 15 kV, using a secondary detector for imaging.

2.6.7.2. Transmission Electron Microscopy (TEM)

TEM is a technique that uses a particle beam of electrons to observe biological and non-biological samples. Whilst similar to SEM, the main difference comprises in how the images are produced. SEM images are created by the detection of reflected (Backscattering) or knocked-off electrons, whereas in TEM, the electron pass (transmitted) through the samples. These electrons make an image and are focused on an imaging device, typically a fluorescent screen. Normally, to obtain higher contrast image, the TEM can be defocused. This aids in obtaining lattice or structure images, important for the bulk characterisation of zeolites.

TEM images were recorded with a JEOL JEM 2100 operating at 200 kV. Zeolites were dispersed in a 300 mesh Cu grid and were recorded at various magnitudes (8,000 – 120,000X).

2.6.8 Nuclear Magnetic Resonance (NMR) spectroscopy

NMR is an essential tool for the elucidation of the molecular structure of organic and inorganic compounds. Like most spectroscopic techniques, it is non-destructive. Furthermore, it is the only one that is able to provide a complete analysis and interpretation regarding the structure.

The basic principle of NMR spectroscopy involves in the application of an EM radiation (radiofrequency – RF pulse) to a certain nucleus to subsequently measure the amount of energy required to put various nuclei in resonance. Some nuclei such as ^1H , ^{13}C , ^{27}Al , and ^{29}Si , have inherent spin properties, letting them behave like magnets. Spin is an important property which can determine whether a nucleus is NMR active or not. The nucleus, which consists of protons and neutrons, are made up of subatomic particles known as quarks and gluons. Quarks for protons and neutrons differ, where the former has two $+2e/3$ (u, d) and one $-e/3$ (u) charge quarks, resulting in a charge of $+1$ while the latter has two $-e/3$ (u, d) and one $+2e/3$ (d) charge quarks, resulting in the latter a net charge of 0 . This gives both the proton and neutron with a spin of $1/2$.

When the sum of the protons and neutrons is an odd number, they have fractional spins, such as ^1H and ^{19}F ($I= 1/2$), ^{11}B ($I= 3/2$), or ^{17}O ($I = 5/2$). When the number of protons and neutrons are odd numbers and add to an even mass nucleus, they will have integral spins, such as ^2H , and ^{14}N ($I = 1$). However, when both protons and neutrons are of even number and result in an even nuclei mass, they have zero spin ($I = 0$), making the nuclei NMR inactive (*e.g.*, ^{12}C and ^{16}O). Due to this, all these isotopes which contain odd number of protons and/or neutrons have an intrinsic nuclear

magnetic moment and angular momentum. In the absence of an external field, these are randomly oriented.

Quantum mechanics tells us that with a nucleus of spin I , it will have $2I+1$ possible orientations. For instance, a nucleus with spin $1/2$ will have two orientations (Figure 2.16). Without any external magnetic field, these orientations are of equal energy. Each of these orientations and/or different energy levels is a magnetic quantum number, defined as m .

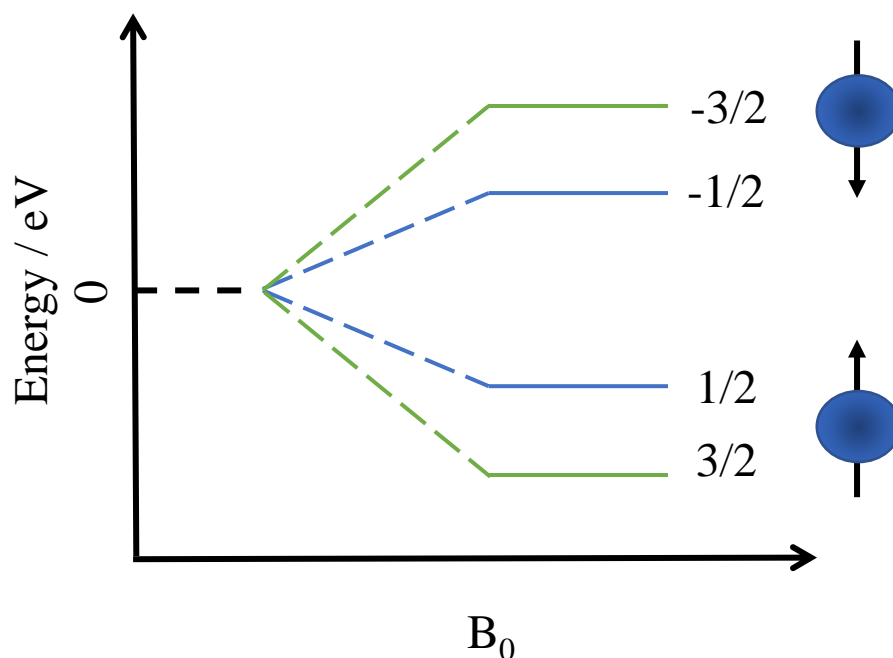


Figure 2.16. Energy levels of $1/2$ and $3/2$ spin nuclei. When a nucleus is in a higher energy state, the spin is aligned against the magnetic field whereas with a lower energy state, it becomes aligned.

When such compounds are placed in a magnetic field, these nuclei spin in the direction of the magnetic field (ground state). When the RF pulse is applied, the nuclei become excited and changes their magnetic moments opposed to the applied magnetic field (from longitudinal to transverse plane), as shown in Figure 2.17. The nuclei then undergo precession, more specifically, Larmor precession. Larmor precession is the change in orientation (or precession) of the magnetic moment when an external magnetic field is applied. This external magnetic field exerts a torque (τ), which is influenced by the number of spins and the gyromagnetic ratio (*i.e.*, magnetic moment/angular momentum ratio, γ) of the nuclei.

$$\tau = \mu * B$$

Where μ is the magnetic moment and B is the magnetic field.

Further into the RF pulse, when precession occurs, a free induction decay (FID) is observed. This is a signal generated by non-equilibrium nuclear spin magnetization precessing, and is created when the RF pulse is close to the Larmor frequency of the nuclei,

$$\omega = -\gamma * B$$

where ω is the Larmor frequency or angular frequency.

This FID signal is digitised and subsequently Fourier Transformed to obtain a frequency spectrum of the NMR. The units are called chemical shift (in ppm), which is the resonant frequency of a nucleus relative to a standard in a magnetic field.

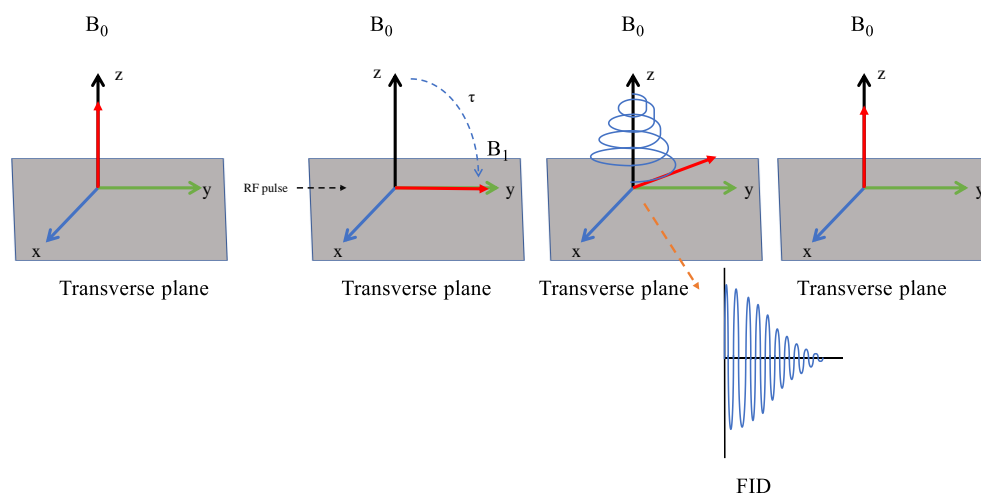


Figure 2.17. Schematic representation of nuclei precession using an RF pulse to obtain FID signal used to generate the spectra.

2.6.8.1 Magic angle spinning (MAS) NMR

Whilst being a versatile tool with a plethora of applications, there exist drawbacks when analysing solid samples. For instance, one of them include the relatively low sensitivity, requiring at least micromolar quantities of the material. When solid samples are analysed with NMR, the spectra tend to be very broad due to the crystallites' multiple orientations and interactions (chemical shift

anisotropy – CSA, quadrupolar, dipolar) in the magnetic field. These broad lines, referred to as ‘powder patterns’, can be highly informative when it comes to the local geometry of the solid and electronic structure, but they come with a complete loss of resolution.⁹

An approach used to eliminate or mitigate the effects of chemical shift anisotropy but not of the chemical shift dispersion is the implementation of Magic Angle Spinning (MAS).¹⁰ In MAS, the rotor is rotated around an axis of 54.74° with respect to the direction of the magnetic field (B_0) (Figure 2.18). These interactions in solids are orientation-dependent and can be averaged by MAS either partially or totally, depending on the MAS frequency.

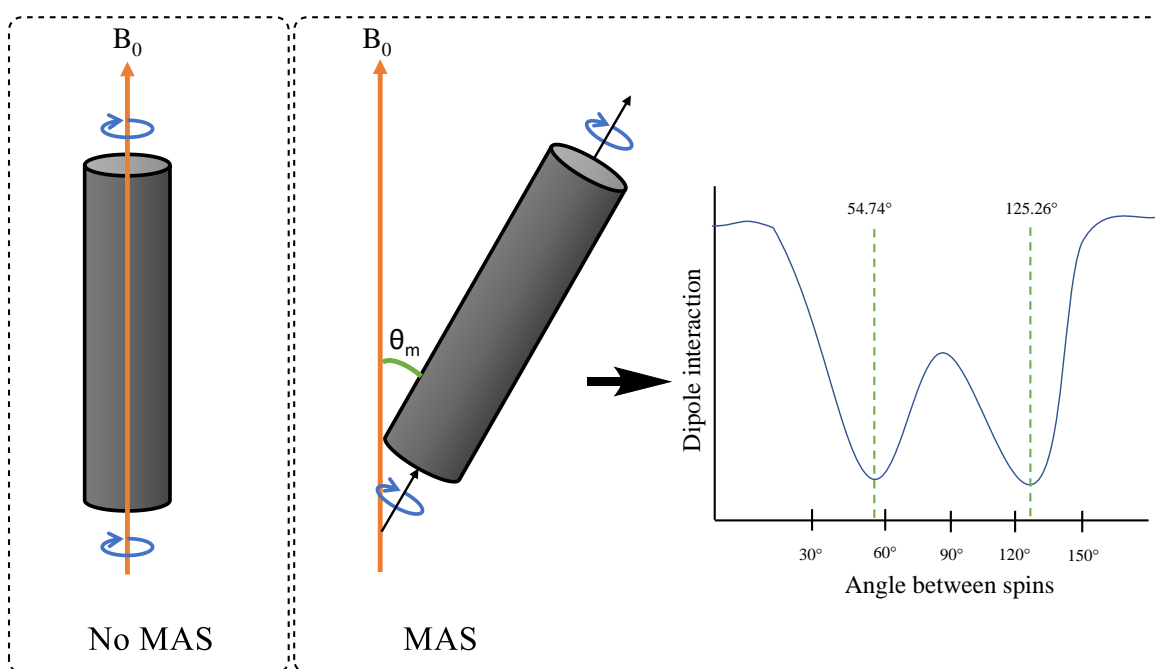


Figure 2.18. Diagram of a rotor with no MAS and MAS, showing how the dipole interaction averages to zero when applying the angle to the rotor.

Other implementations that have been shown to improve overall signal generation is the Carr-Purcell-Meiboom-Gill (CPMG) echo train acquisition. CPMG allows one to measure the transverse (x,y) or spin-spin T_2 relaxation times of the nucleus. The pulse sequence is similar to the Hahn echo, which uses π (180°) pulses to refocus inhomogeneous broadening of the nuclear spins; the only difference is that it uses an ‘n’ amount of spin echoes with delays (delay – pulse – delay). The application of CPMG acquisition along with MAS for NMR analysis on catalysts with low sensitivity such as Sn-Beta has proven to increase drastically the signal-to-noise ratio.¹¹

Nuclear Magnetic Resonance (NMR) was carried out in a Bruker Avance III HD 400 MHz NMR spectrometer. ^{119}Sn , ^1H , ^{13}C and ^{29}Si NMR were carried out at operating frequencies of 149.23, 400.20, 188.41 and 79.508 MHz, respectively. All analysis were run with a 10 kHz spin rate packed in ZrO_2 rotors. ^{119}Sn MAS DE CPMG NMR experiments were performed with the CPMG echo-train acquisition as described in references 12 and 13.^{12, 13} Spectra were measured by applying 100 echoes, using a $2.5\ \mu\text{s}$ 90° -pulse with a 180° proton decoupling. Two relaxation delays (t_1) were used: t_1 with 5 s and 2048-10480 scans, depending on the wt. % of tin, and a longer $t_1 = 135$ s with 512 scans. Tin chemical shifts were calibrated using tin (IV) oxide as reference. ^{29}Si MAS NMR were obtained by one-pulse experiment with a $4\ \mu\text{s}$ 45° -pulse with a 20 second recycle delay and 128 scans. Chemical shifts were calibrated using a pure siliceous beta silicate. ^1H MAS NMR were obtained by a one-pulse experiment with a $2.5\ \mu\text{s}$ pulse with a 3 second recycle delay. ^{13}C CP MAS were acquired with a relaxation delay of $t_1=5$ s, using 2048 scans NMR. Adamantane was used for calibration of the ^1H chemical shifts.

2.6.9. Inductively Coupled Plasma – Mass Spectroscopy (ICP-MS)

ICP-MS is an analytical technique used for elemental analysis, which can detect and measure elements at trace levels (ppb to ppt). Elements are led through a plasma source where they are ionised, which can be identified with respect to their mass.

In the thesis, metal concentrations of the zeolites were determined by ICP-MS using an Agilent 7900 ICP-MS using a mixture of ultrapure HNO_3 (2.5 mL) and HF (0.75 mL).

2.6.10. Raman Spectroscopy

Raman spectroscopy is an important tool to complement FTIR. These differ from one another in which FTIR is based on absorption, creating a change in the net dipole moment, whereas Raman spectroscopy is based on the inelastic scattering.

Inelastic scattering occurs from interactions with the incident electrons and the electrons of the sample, *i.e.*, the kinetic energy of the incident electron is not conserved. In Raman spectroscopy, the three most common inelastic scattering phenomena are the i) Rayleigh scattering, which indicates no change in energy; ii) Stokes Raman scattering, in which the atom or molecule absorbs energy (emitted radiation is of lower frequency than incident radiation); and iii) Anti-stokes Raman

scattering, attributed to an atom or molecule losing energy (emitted radiation is of higher frequency), as can be depicted in Figure 2.19. This energy difference provides information about the vibrational energy and frequencies. As they are also molecule-specific, they can be used for imaging.

For these experiments, Raman spectra were obtained with a Renishaw inVia spectrometer equipped with a laser line at 266 nm.

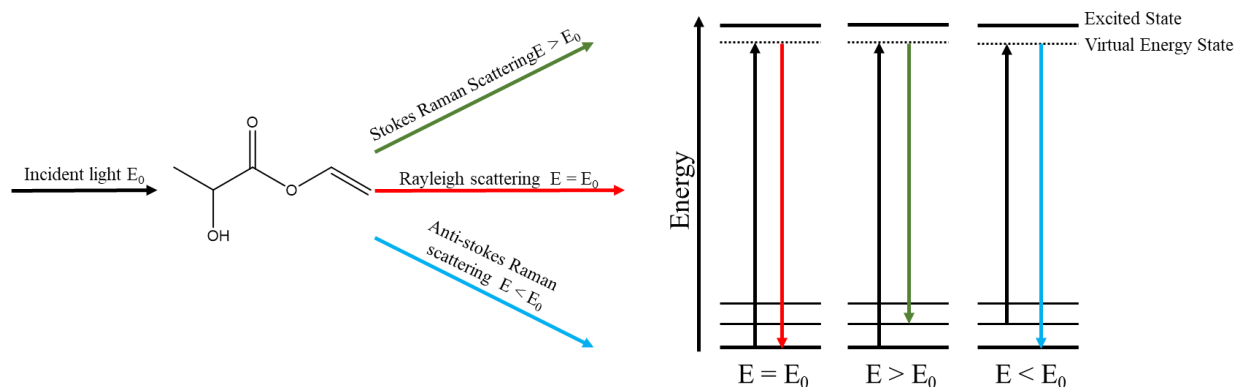


Figure 2.19. Different types of scattering that can undergo a sample in Raman spectroscopy, depicting the differences in energy transitions (E).

2.6.11 X-ray Absorption Spectroscopy (XAS)

XAS is a technique that characterises the chemical nature and environment of atoms in molecules. It can provide bulk measurements of the elemental, chemical composition, along with radial distances of neighbouring atoms. Normally, XAS is carried out in a synchrotron due to it requiring a high-intensity, coherent X-ray beam that is tuneable to be able to apply in a wide energy range. This is due to each element having their own set of characteristic absorption edges which correspond to different binding energies.¹⁴

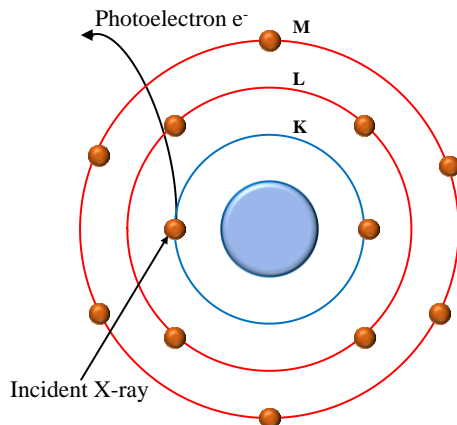


Figure 2.20. Graphical representation of an incident X-ray creating a photoelectron on the innermost shell (K-edge).

XAS can be divided into X-ray Absorption Near Edge Structure (XANES), and Extended X-ray Absorption Fine Structure (EXAFS). XANES consists in the scattering of multiple-scattering resonance of the low kinetic energy photoelectrons (around 10 below and 20 above the absorption edge). It can provide information of the oxidation states of the specimen.¹⁵

EXAFS is presented at higher energies (up to 500 eV), which originates from the scattering of the ejected photoelectron to its surrounding, giving data, such as the neighbouring atoms of the studied element.¹⁶

For this work, Sn K-edge XAFS measurements were carried out by a supervisor Dr. Ceri Hammond, along with various collaborators: Dr. Daniele Padovan, Dr. P. P. Wells and Dr. E. K. Gibson. XAS spectra were obtained on the B18 beamline at Diamond Light Source, Didcot, UK, using a Si(111) double crystal monochromator and were measured in transmission mode.

2.7 References

1. Ma, D.; Han, G.; Peh, S. B. & Chen, S. B., Water-Stable Metal-Organic Framework UiO-66 for Performance Enhancement of Forward Osmosis Membranes. *Industrial and Engineering Chemistry Research* **56**, 12773-12782 (2017).
2. Ettre, L. S.; Sakodinskii, K. I., M. S. Tswett and the discovery of chromatography II: Completion of the development of chromatography (1903–1910). *Chromatographia*, **35**, 329-338 **1993**
3. Bragg, W. H.; Bragg, W. L., The reflection of X-rays by crystals. *Proceedings of the Royal Society of London. Series A, Containing Papers of a Mathematical and Physical Character* **88**, 428-438 (1913)
4. Thommes, M.; Kaneko, K.; Neimark, A. V.; Olivier, J. P.; Rodriguez-Reinoso, F.; Rouquerol, J.; Sing, K. S. W., Physisorption of gases, with special reference to the evaluation of surface area and pore size distribution (IUPAC Technical Report). *Pure and Applied Chemistry* **87**, 1051-1069 (2015)
5. Brunauer, S.; Emmett, P. H.; Teller, E., Adsorption of Gases in Multimolecular Layers. *Journal of the American Chemical Society* **60**, 309-319 (1938)
6. Ozaki, Y.; Genkawa, T.; Futami, Y., Near-Infrared Spectroscopy. In *Encyclopedia of Spectroscopy and Spectrometry*; pp 40-49 (2017)
7. Larkin, P., Instrumentation and Sampling Methods. In *Infrared and Raman Spectroscopy* pp 27-54 (2011)
8. Budiman, H.; Nuryatini; Zuas, O., Comparison between GC-TCD and GC-FID for the determination of propane in gas mixture. *Procedia Chemistry* **16**, 465-472 (2015)
9. Polenova, T.; Gupta, R.; Goldbourt, A., Magic angle spinning NMR spectroscopy: a versatile technique for structural and dynamic analysis of solid-phase systems. *Anal Chem* **87**, 5458-5469 (2015)
10. Lowe, I. J., Free Induction Decays of Rotating Solids. *Physical Review Letters* **2**, 285-287 (1959)
11. Kolyagin, Y. G.; Yakimov, A. V.; Tolborg, S.; Vennestrøm, P. N. R.; Ivanova, I. I., Application of ^{119}Sn CPMG MAS NMR for Fast Characterization of Sn Sites in Zeolites with Natural ^{119}Sn Isotope Abundance. *Journal of Physical Chemistry Letters* **7**, 1249-1253 (2016)
12. Kolyagin, Y. G.; Yakimov, A. V.; Tolborg, S.; Vennestrøm, P. N. R.; Ivanova, I. I., Direct Observation of Tin in Different T-Sites of Sn-BEA by One- and Two-Dimensional ^{119}Sn MAS NMR Spectroscopy. *The Journal of Physical Chemistry Letters* **9**, 3738-3743 (2018)
13. Corma, A.; Nemeth, L. T.; Renz, M.; Valencia, S., Sn-zeolite beta as a heterogeneous chemoselective catalyst for Baeyer-Villiger oxidations. *Nature* **412**, 423-425 (2001)
14. Abraham, J.; Jose, B.; Jose, A.; Thomas, S., Chapter 2 - Characterization of green nanoparticles from plants. In *Phytonanotechnology*, Thajuddin, N.; Mathew, S., Eds. Elsevier: pp 21-39 (2020)
15. de Groot, F., High-Resolution X-ray Emission and X-ray Absorption Spectroscopy. *Chemical Reviews* **101**, 1779-1808 (2001)

16. Holbrook, R. D.; Galyean, A. A.; Gorham, J. M.; Herzing, A.; Pettibone, J., Chapter 2 - Overview of Nanomaterial Characterization and Metrology. In *Frontiers of Nanoscience*, Baalousha, M.; Lead, J. R., Eds. Elsevier: 2015; Vol. 8, pp 47-87.

Chapter 3. Tracking the solid-state incorporation of Sn into the framework of dealuminated zeolite beta, and consequences for catalyst design

3.1. Introduction

Isomorphously-substituted zeolites such as TS-1, Sn-Beta and Fe-ZSM-5, have emerged in recent decades as state of the art catalysts for a variety of sustainable chemical transformations.¹⁻³ Out of these catalysts, of particular interest amongst these Lewis acidic metallosilicates is Sn-containing zeolite Beta (Sn-Beta). Over recent years, this catalyst has emerged as one of the most promising in the area of green chemistry, due to its ability to catalyse reactions such as the Baeyer–Villiger oxidation of (renewable) ketones with H₂O₂, glucose isomerisation along with the conversion of hexoses to α -hydroxyester compounds including methyl lactate and methyl vinyl glycolate at high temperatures, various C-C bond forming reactions, and the catalytic transfer hydrogenation of carbonyl compounds.⁴⁻⁶

Sn-Beta is classically prepared by hydrothermal synthesis using fluoride as a mineraliser, where an aqueous sol-gel containing the metal precursors and an appropriate Structure Directing Agent (SDA) is crystallised at elevated temperature (140 °C) and pressures (autogenous).⁷⁻⁹ Whilst this results in the formation of highly active and selective catalysts, there are several drawbacks to this method of preparation, such as: the need for long crystallisation times,¹⁰ the requirement of fluoride as the mineraliser instead of using hydroxide, inhibited crystallisation of the material at higher loadings of Sn, therefore limiting catalyst productivity, and the creation of large crystallites due to suppression of the nucleation,¹¹⁻¹⁴ and hence, possessing less than ideal mass transfer properties.^{12,15} Thus, large scale utilisation of these catalysts which hold promising activity are not favourable.

With these disadvantages being the main obstacle for industrial scale utilization, the development of alternative preparation methodologies for Sn-Beta has received substantial attention.^{7,9,16-20} Top-down approaches have been garnering much attention, which consists in preparing the

stannosilicate zeolite from a prior, readily prepared aluminosilicate zeolite. Top-down synthesis is classically achieved by “demetallation-remetallation”. Demetallation consists in stripping Al from a commercially available aluminosilicate using typically a concentrated acid (*e.g.* HNO₃), resulting in the formation of silanol nests (*i.e.* vacant “T” sites). Remetallation can comprise of incorporating the desired metal (in this case, Sn) to the structure through various approaches.^{12,16,21,22} Amongst top-down approaches, solid-state methods of incorporation are particularly suitable for the preparation of Sn-Beta, as has been demonstrated.^{23–25} Here, a mechanochemically mixture of metal precursor (Sn(OAc)₂) and dealuminated Beta zeolite are heat treated in a two-step process which includes initially an inert atmosphere and subsequent change to air, leading to incorporation of Sn⁴⁺ into the framework of the zeolite. This approach, which has been termed Solid-State Incorporation (SSI), provides several advantages over other top-down methods, including fast synthesis timescales, the absence of solvents and wet chemicals in the remetallation stage, and the ability to incorporate higher loadings of metal than conventional hydrothermal synthesis due to its time-consuming nucleation step (> 2 wt. % Sn).^{25,26} Notably, the procedure can also be tuned to allow inclusion of other metal centres, such as Fe³⁺, Ti⁴⁺ and Zr⁴⁺, when desired.^{27,28}

SSI-prepared catalysts have been shown to exhibit comparable performance to classical Sn-Beta at lower loadings. Nevertheless, extra-framework SnO_x species are shown to form at higher loadings, particularly when the loading is increased above 5 wt. %.²⁵ Despite being inactive for the catalytic reactions of interest *i.e.* SnO_x species are spectator species, the co-presence of these species at higher loadings results in a drop in the intrinsic activity of the catalyst (turnover frequency, TOF). Consequently, these inactive sites limit opportunities to improve the productivity of the catalyst on a per gram basis, which is an important parameter for intensification purposes.²⁵ As such, elucidating the mechanism of heteroatom incorporation during SSI, and hence being able to scientifically improve the synthesis protocol either from a practicality (time, temperature) or a performance perspective (more uniform incorporation regardless of metal loading) is a challenge of practical importance and scientific interest.

However, this goal has been thwarted by the fact that limited knowledge exists regarding which parameters influence the incorporation mechanism(s). Furthermore, whilst some spectroscopic studies have recently focused on identifying the mechanism of heteroatom incorporation,^{16,29} these studies are emphasised in the influence of the heat treatment atmosphere and/or have variations in

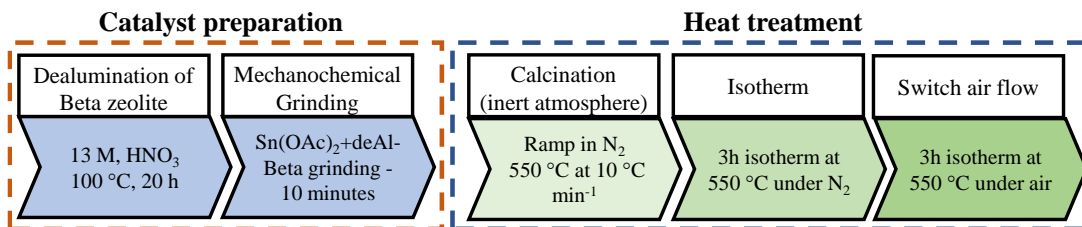
their post-synthetic modification (*i.e.* different Sn precursor, synthesis conditions), which does not provide information on the direct process of heteroatom incorporation at real operational conditions, *i.e.* during the critical heat treatment procedure.

By employing state-of-the-art spectroscopic methods, including ^{119}Sn Carr-Purcell-Meiboom-Gill (CPMG) Magic Angle Spinning (MAS) Nuclear Magnetic Resonance (NMR), *in situ* X-ray Absorption Spectroscopy (XAS), *in situ* Diffuse Reflectance Infrared Fourier Transform Spectroscopy (DRIFTS), *in situ* Temperature Programmed Desorption-Mass Spectrometry (TPD-MS), Raman, and Diffuse Reflectance UV-Vis (DRUV-Vis) Spectroscopy, alongside complimentary kinetic studies, a detailed study focused upon the chemistry occurring during SSI is hereby presented. In addition to providing unique molecular level insight into the preparation procedure, these studies also reveal which parameters influence successful synthesis of the catalyst, and thereby reveal how the synthesis protocol can be tailored to maximise the rapidity of the synthesis procedure. The catalytic performances of these materials were also evaluated for the Meerwein-Ponndorf-Verley transfer hydrogenation reaction and glucose isomerisation, both in batch and continuous flow, demonstrating that similar catalytic activity can be achieved even with a *ca.* 90 % faster calcination rate.

3.2. Results and discussion

3.2.1 Effect of physical grinding

SSI is a two-step procedure (Scheme 3.1), where dealuminated Beta zeolite (ZeolystTM, Si/M ratio = 19) and Sn(II) acetate (denoted as deAl-Beta and Sn(OAc)₂, respectively) are first treated mechanochemically (grinding) for 10 minutes prior to heat treatment of the solid mixture at elevated temperature (550 °C, 3 h N₂ and 3 h air, ramp rate 10 °C min⁻¹).²³ Elucidation of the changes that occurred to Sn(OAc)₂ after being grinded with the deAl-Beta was first studied. For all these studies, a 10 wt. % Sn-Beta zeolite (denoted 10Sn-Beta post-calcination), a wt. % which is theoretically capable of isomorphously incorporating itself to this Si/M zeolite, was used due to its ease of characterising given its high loading.



Scheme 3.1. Schematic of conventional solid-state incorporation process.

FTIR analysis of a physically mixed sample of Sn(OAc)₂/deAl-Beta revealed the formation of a new vibration at 1297 cm⁻¹ upon grinding, and that the so-called Δ value of Sn(OAc)₂ [$\nu\text{CO}_{\text{asym}} - \nu\text{CO}_{\text{sym}}$]³⁰ shifted from 137 cm⁻¹ in pure Sn(OAc)₂ alone (1404 cm⁻¹ and 1541 cm⁻¹), to 310 cm⁻¹ (1404 cm⁻¹ and 1714 cm⁻¹) subsequent to grinding with the dealuminated zeolite (Figure 3.1, Left). Alongside this shift in the vibrational spectra was the disappearance of the 245 nm band observed by DRUV-Vis, indicative of the Ligand-to-Metal Charge Transfer (LMCT) bands of the Sn(II) precursor (Figure 3.1, Right), losing the lower energy signal which is associated with pure Sn(OAc)₂. Additionally, a grinded Sn(OAc)₂ without deAl-Beta was carried out and the same tests were conducted, showing no changes to the Δ value or the absence LMCT bands unlike with the mixture, as observed in Figures 3.2 and 3.3.

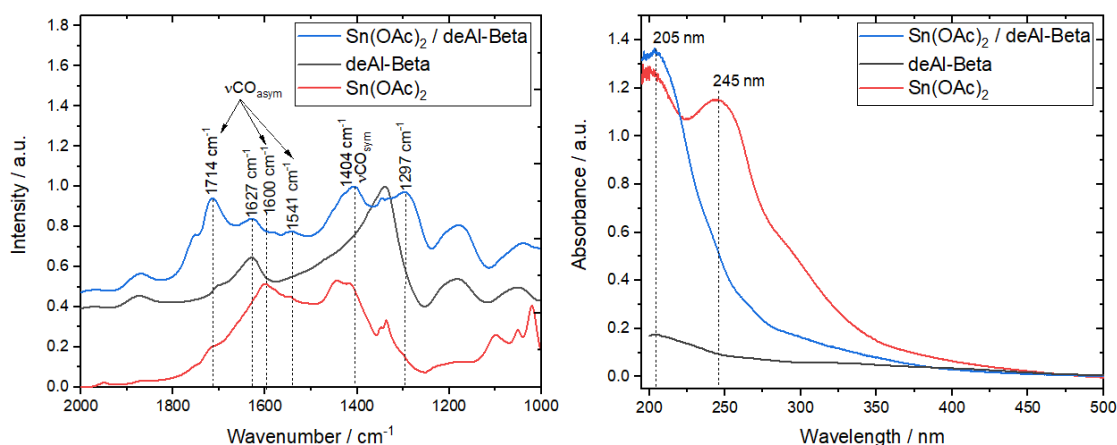


Figure 3.1. (Left) DRIFTS comparison of deAl-Beta, Sn(OAc)₂ (grinded), and physical mixture Sn(OAc)₂/deAl-Beta. (Right) DRUV-vis spectra of deAl-Beta, Sn(OAc)₂ (grinded), and physical mixture Sn(OAc)₂/deAl-Beta.

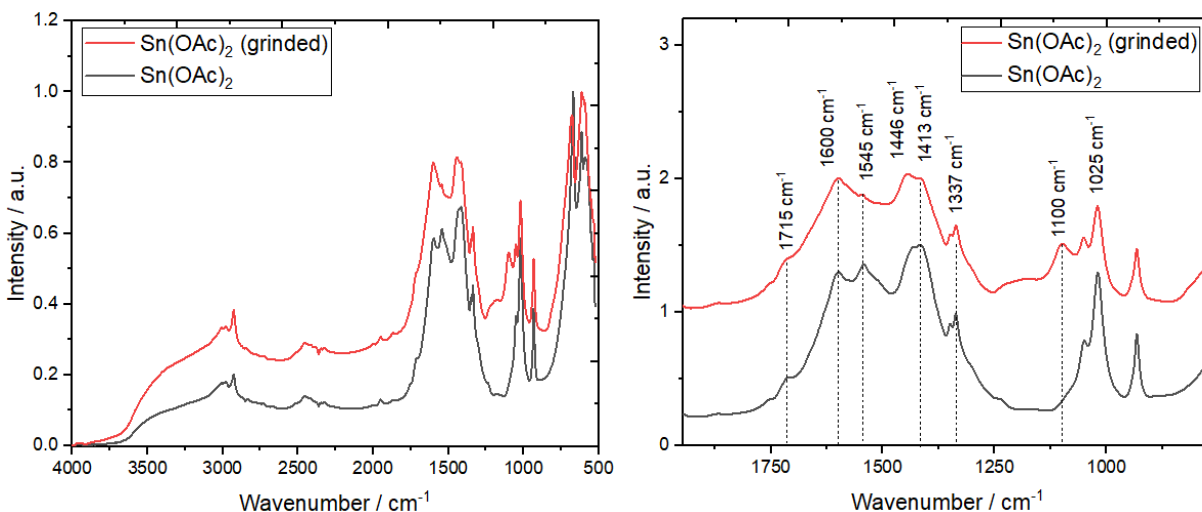


Figure 3.2. FTIR on grinded and pure $\text{Sn}(\text{OAc})_2$.

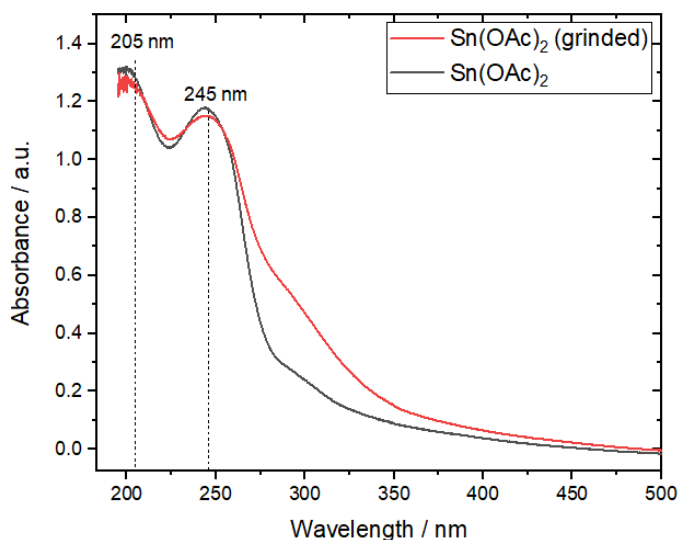


Figure 3.3. DRUV-Vis comparison of grinded and pure $\text{Sn}(\text{OAc})_2$.

The loss of one charge transfer band, coupled to the increase in the Δ value to $\pm 310 \text{ cm}^{-1}$, strongly indicates that upon grinding, the acetate ligands become more monodentate in nature, resulting in the formation of more inequivalent acetate oxygen atoms than those found in the original metal acetate complex.^{31,32} A shift towards monodentate coordination is supported by the new vibrational feature at 1297 cm^{-1} , which has been attributed to monodentate acetate groups.³³ An additional test using Si-Beta (*i.e.* zeolite with no vacancies and no dealumination) was carried out as an alternative zeolite for the mixture to observe the importance of the vacancies for SSI. Despite having no

vacancies, an increase in the Δ value and the emergence of the feature at 1297 cm^{-1} was observed (Figure 3.4). Nevertheless, the final product ($\text{Sn}(\text{OAc})_2/\text{Si-Beta}$) was shown to not be an active catalyst, implicating the need for vacant sites for the metal to incorporate itself.

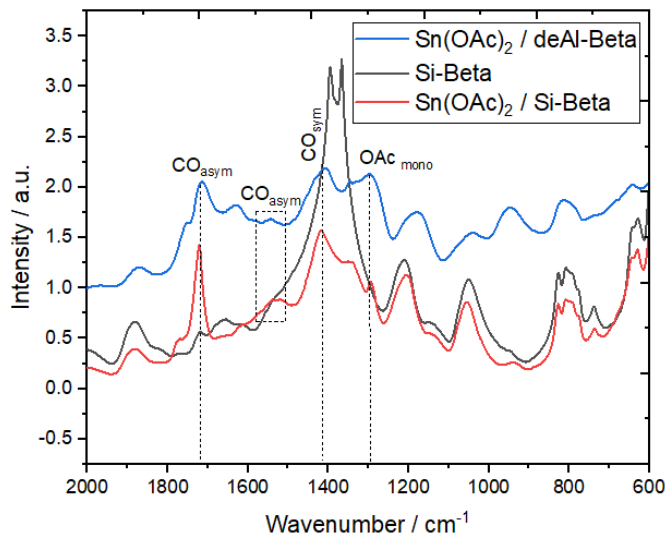


Figure 3.4. DRIFT spectra of i) Si-Beta, ii) $\text{Sn}(\text{OAc})_2/\text{Si-Beta}$, and iii) $\text{Sn}(\text{OAc})_2/\text{deAl-Beta}$.

However, although comparable on first glance, a more detailed analysis revealed that the presence of silanol nests led to differences in the vibrational bands related to asymmetric CO vibrations and monodentate acetate groups (Figure 3.5). This effect may be caused by formation of hydrogen bonds between silanol nests and the oxygens of the acetate groups, which are exclusively present in $\text{Sn}(\text{OAc})_2/\text{deAl-Beta}$.

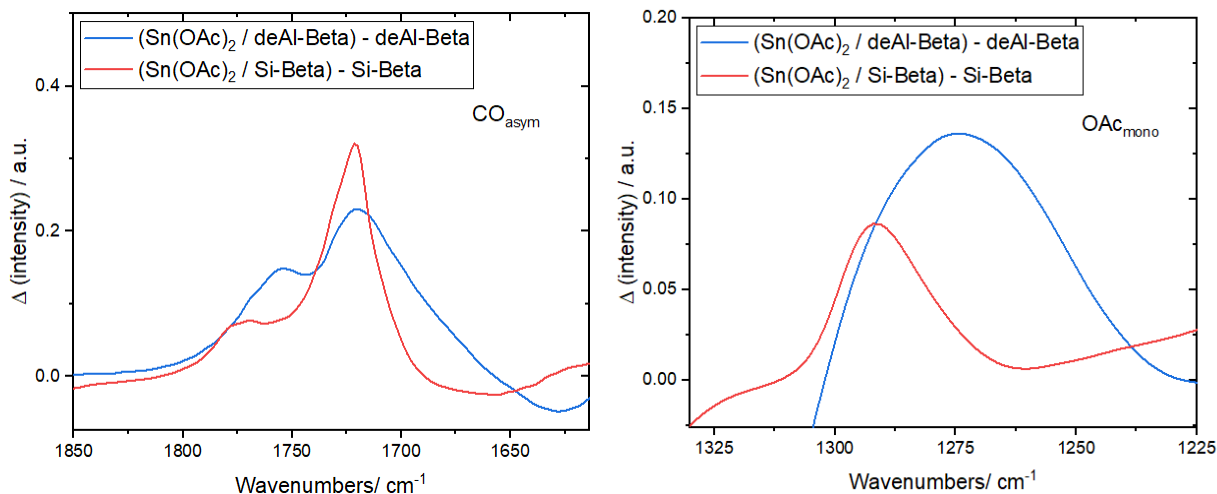


Figure 3.5. Differential FTIR spectra obtained through subtraction of (Left) Sn(OAc)₂/deAl-Beta mixture and deAl-Beta alone (blue line) and (Right) Sn(OAc)₂/Si-Beta mixture and Si-Beta alone (red line).

Further evidence of a shift towards a monodentate coordination upon grinding was also obtained by ¹³C MAS NMR. As can be seen (Figure 3.6), the ¹³C MAS NMR spectrum of Sn(OAc)₂ exhibited two symmetric doublets at -25.6 and -26.7 ppm, and -181.3 and -184.1 ppm. These doublets correspond to [CH₃-] and to [C=O], respectively, likely found in two separate crystal environments.³⁴ Similar to previous data obtained, no changes were observed following grinding of the acetate alone. However, when Sn(OAc)₂ was physically mixed with deAl-Beta, the doublets disappeared and only one intense peak for the methyl group, as well as a single broad carbonyl resonance were observed. This change indicates that after mixing Sn(OAc)₂ with the zeolite, the initial polymeric structure of Sn(OAc)₂ changes/collapses, having similar environments for the [CH₃-] groups, indicated by the single peak observed.

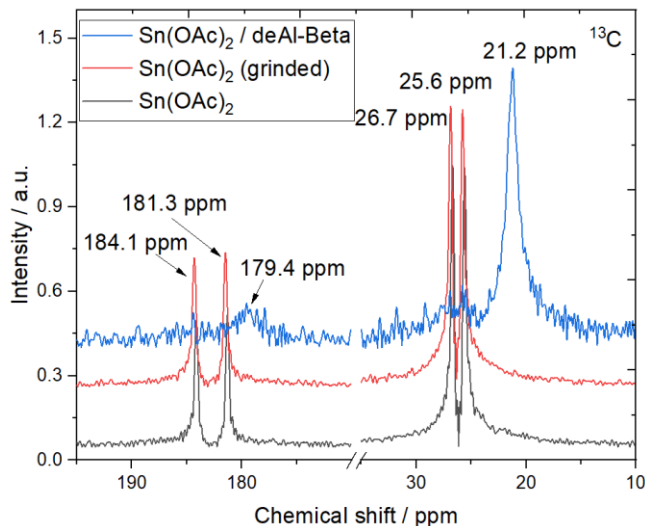


Figure 3.6. ^{13}C MAS NMR of normal and grinded $\text{Sn}(\text{OAc})_2$, and $\text{Sn}(\text{OAc})_2/\text{deAl-Beta}$.

To elucidate the impact of the grinding step on the Sn centres, ^{119}Sn Carr-Purcell-Meiboom-Gill (CPMG) MAS NMR measurements in Direct Excitation (DE) mode, in addition to preliminary XAS measurements, were performed on the $\text{Sn}(\text{OAc})_2/\text{deAl-Beta}$ grinded mixture (Figures 3.7). In spite of the changes to the acetate ligands, Sn was still found in a tetrahedral geometry and oxidation state +2, indicating that the overall speciation of the metal did not change throughout this process. This suggests that, upon grinding, partial coordination of Sn to the zeolite occurred, with the lattice providing two of the bonds required to maintain tetrahedral geometry after the change in acetate coordination from bidentate to monodentate.

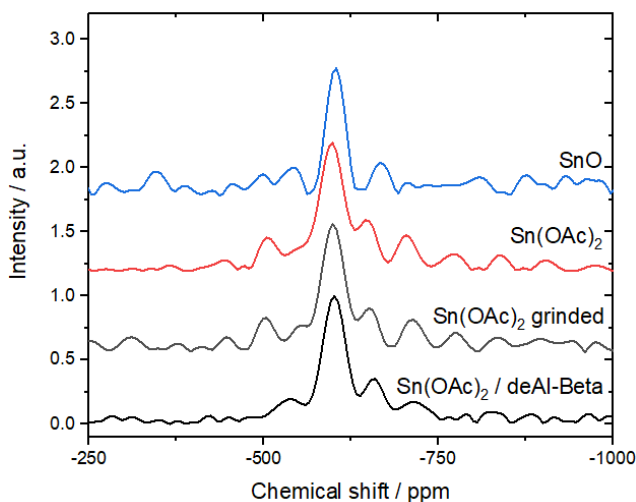


Figure 3.7. ^{119}Sn DE CPMG MAS NMR of pure $\text{Sn}(\text{OAc})_2$, $\text{Sn}(\text{OAc})_2/\text{deAl-Beta}$, $\text{Sn}(\text{OAc})_2/\text{Si-Beta}$, and SnO .

Complimentary data of the metal-zeolite interaction was provided by Raman analysis, gathered by Dr. Giulia Tarantino, a collaborator in the project. Upon grinding, new bands in the region 550-650 cm^{-1} were formed (Figure 3.8). Although absent in pure $\text{Sn}(\text{OAc})_2$, the intensity of these bands strongly depended on the relative amount of Sn, *i.e.*, the intensity of the new bands increased going from 2 wt. % of Sn to 10 wt. %. Notably, other works have reported Sn-O vibrational bands in such spectral region (550-650 cm^{-1}).³⁵ Therefore, the broad peak around 585 cm^{-1} , especially broad for the sample containing 10 wt. % Sn, may be reasonably assigned to Sn-O bonds in a range of different configurations as a result of interactions between $\text{Sn}(\text{OAc})_2$ and the zeolite.³⁵

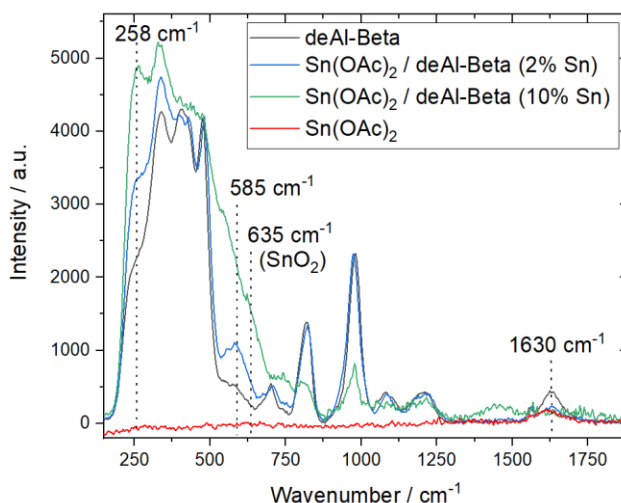


Figure 3.8. Raman spectra obtained using a 266 nm excitation wavelength of i) deAl-Beta (black line), ii) pure $\text{Sn}(\text{OAc})_2$ (red line), and $\text{Sn}(\text{OAc})_2/\text{deAl-Beta}$ mixture with iii) 2 wt. % of Sn (blue line), and iv) 10 wt. % of Sn (green line).

In summary, spectroscopic study of the first step of the SSI procedure revealed that upon grinding the metal precursor with deAl-Beta, several changes occurred to the acetate ligands, which moved from a bridged coordination to a more monodentate one. This did not occur when trying to grind $\text{Sn}(\text{OAc})_2$ alone, which showed no changes to its denticity or vibrational spectra. Si-Beta was shown to have some changes as well, showing shifts in the vibrational spectra. Nevertheless, the need for vacant sites for subsequent Sn incorporation was required for there to be an active catalyst. This indicated the presence of a zeolite is vital for $\text{Sn}(\text{OAc})_2$ to undergo changes in its coordination, regardless of vacancies. However, these changes were not accompanied by changes to the Sn centres, which remained in the +2 oxidation state and in a tetrahedral geometry, due to partial

coordination to the zeolite. These findings contrast to those recently reported by Schüth *et al*, which indicated formation of Sn(IV) via mechanochemical grinding using a ball mill in the absence of heat treatment.¹⁶ Sels *et al* demonstrated via Mössbauer spectroscopy the oxidation ratio of Sn(II)/Sn(IV) under both inert atmosphere and air. Under air it was shown to present a full oxidation to Sn(IV) whereas under inert atmosphere, the oxidation was shown to be much less (18 % Sn(IV)).²⁹ Comparison with control samples also showed different Sn(OAc)₂-zeolite interaction occur in the presence of silanol nests (i.e. substituting Si-Beta with deAl-Beta). Nevertheless, none of these samples (including Sn(OAc)₂ and SnO₂) exhibited catalytic activity prior to heat treatment, and only Sn(OAc)₂/deAl-Beta gained substantial activity following heat treatment. Thus, it is clear that only those spectral changes uniquely observed for the Sn(OAc)₂/deAl-Beta physical mixture are particularly relevant to the formation of an active catalyst following heat treatment.

3.2.2 Evolution of Sn during heat treatment of Sn(OAc)₂/deAl-Beta

Despite the changes that occur to Sn(OAc)₂ during the grinding stage, no catalytic activity was observed for the Sn(OAc)₂/deAl-Beta grinded mixture. Thus, to obtain catalytic activity by SSI, heat-treatment of Sn(OAc)₂/deAl-Beta was required. During previous research, this has been achieved by heating the sample to 550 °C (10 °C min⁻¹), first in a flow of N₂ (ramp and 3 h isotherm), and subsequently in a flow of air (3 h), at gas flow rates of 60 mL min⁻¹ throughout for 1.5 g of catalyst (WHSV= ~2400 h⁻¹) of catalyst.²⁶ Accordingly, to understand how the physically grinded ‘pre-catalyst’ gains catalytic activity, the evolution of the metal precursor in the mixture during heat treatment was followed at real conditions with a variety of *in situ* spectroscopic techniques, including TPD-MS, DRIFTS and XAS. Control experiments were also performed on grinded samples of Sn(OAc)₂ alone, deAl-Beta alone, and a physical mixture of Sn(OAc)₂/Si-Beta, where required.

First, to better understand the nature of the interactions between Sn(OAc)₂ and the zeolite, the gaseous effluent generated during calcination was monitored by Mass Spectrometry (TPD-MS). To maximise rigour, the MS system was connected directly to the calcination furnace employed for conventional catalyst synthesis and identical conditions (mass of catalyst, gas flow rates) were used to the standard protocol. Notably, CaCO₃ decomposition was conducted in the TPD-MS to

determine the delay between the evolution of the compound and the detection of the MS (Figure 3.9) to subsequently offset all MS spectra.

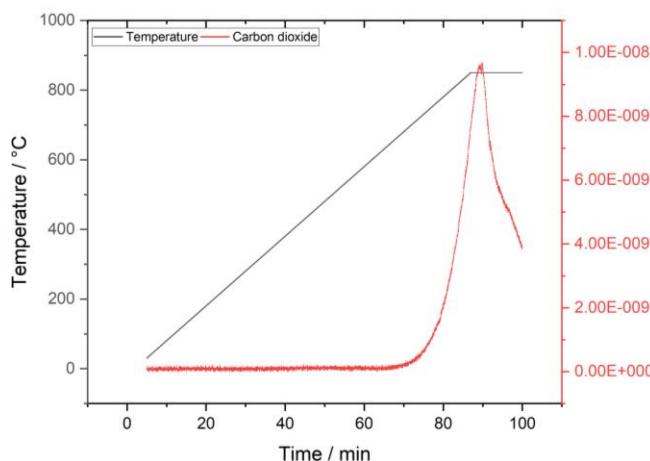


Figure 3.9. TPD-MS of CaCO_3 decomposition.

TPD-MS experiments of $\text{Sn}(\text{OAc})_2/\text{deAl-Beta}$ calcination detected a number of compounds, such as hydrogen, carbon monoxide, carbon dioxide, acetone, and acetic acid. The overwhelming majority of these compounds were detected during the ramping stage of the heat treatment, in particular at a temperature range 300-550 °C, and only a small percentage of such compounds were detected throughout the isotherm stages. To determine the relevance of these evolutions with respect to formation of an active catalyst, control experiments were performed by measuring the gaseous effluent generated from $\text{Sn}(\text{OAc})_2$ alone, and a $\text{Sn}(\text{OAc})_2/\text{Si-Beta}$ mixture, which did not result in the production of an active catalyst. To better observe the changes in compound evolution in the N_2/air switch part of the heat treatment, this switch can be observed in Figure 3.10 (Right), given that there was no evolution or any changes throughout isotherms, . As can be seen (Figure 3.10, Left), $\text{Sn}(\text{OAc})_2$ alone decomposes at much lower temperature when compared to $\text{Sn}(\text{OAc})_2/\text{deAl-Beta}$. In particular, all the volatile decomposition products were detected within the first 30 minutes of the ramp stage for $\text{Sn}(\text{OAc})_2$ and $\text{Sn}(\text{OAc})_2/\text{Si-Beta}$, at temperatures of < 280 °C and 350 °C, respectively. Typically, $\text{Sn}(\text{OAc})_2$ hydrolyses at temperatures ≤ 280 °C to form acetic acid and SnO , as can be seen for both $\text{Sn}(\text{OAc})_2/\text{Si-Beta}$ and $\text{Sn}(\text{OAc})_2$.^{29,36} At temperatures ≥ 295 °C, acetone was shown to be one of the main evolution gases, which is in line with the former two TPD tests.³⁷ However, $\text{Sn}(\text{OAc})_2/\text{deAl-Beta}$ presented all acetic acid and acetone evolutions at much elevated temperatures. Interestingly, acetone was shown to first evolve (*ca.*

435 °C) while acetic acid gradually decomposed throughout the ramp rate. This can be an important factor to create an active catalyst, requiring a gradual compound evolution, which is aided by the silanol nests of the deAl-Beta zeolite.

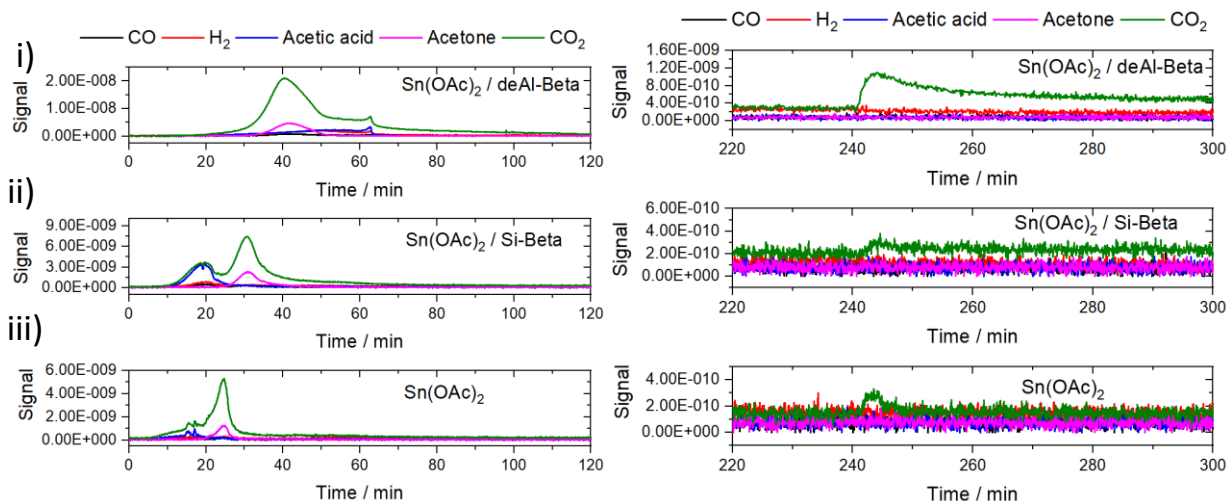


Figure 3.10. TPD-MS during calcination of (from top to bottom) i) $\text{Sn}(\text{OAc})_2/\text{deAl-Beta}$, ii) $\text{Sn}(\text{OAc})_2/\text{Si-Beta}$, and iii) pure $\text{Sn}(\text{OAc})_2$. Left plots consist of the first 2 hours which include the ramp and part of the N_2 isotherm. Right plots consist of the N_2/air switch step. Full TPD-MS profiles are presented in Annex 3.1-3.3.

Replacing N_2 flow with air flow (minute 232.5) (Figure 3.10, Right), an additional amount of carbon dioxide (CO_2) was released from $\text{Sn}(\text{OAc})_2/\text{deAl-Beta}$. This may suggest that despite most of the acetate being released during the first stage of the calcination, a particular amount of carbon was still retained in the mixture despite being subjected to very high temperature, suggesting that it remained present as a coordinated carbon compound. Further control experiments were achieved by performing TPD-MS analysis of deAl-Beta (Figure 3.11-12).

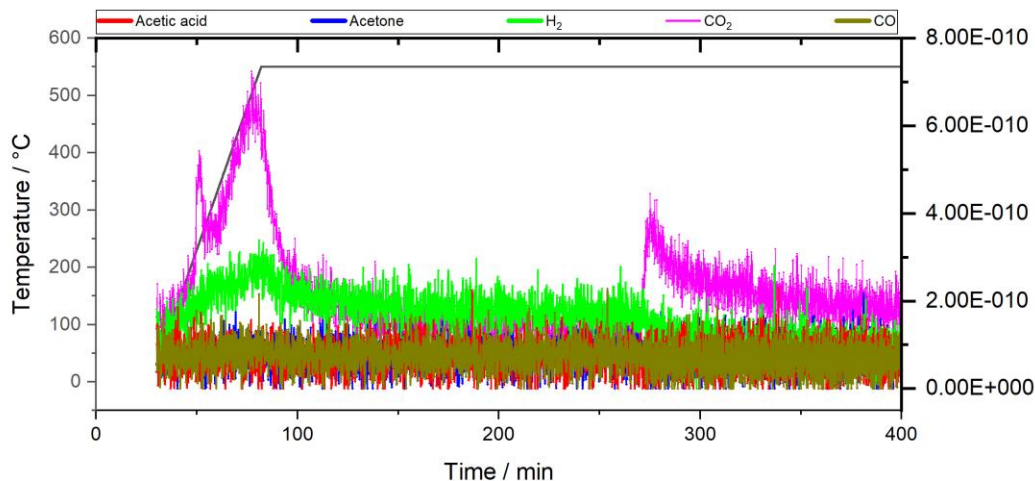


Figure 3.11. TPD-MS of deAl-Beta.

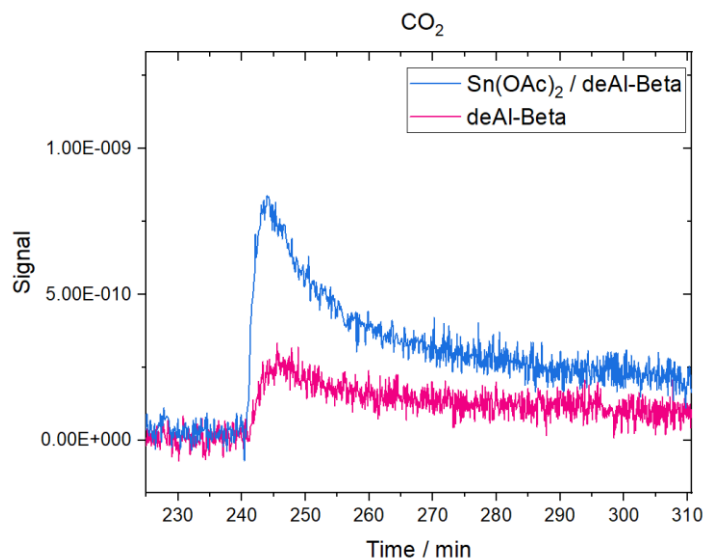


Figure 3.12. Comparison amount of CO_2 detected via TPD-MS for deAl-Beta and $\text{Sn}(\text{OAc})_2/\text{deAl-Beta}$ after switching from nitrogen to air flow.

These confirmed that, although some CO_2 was released from deAl-Beta alone, most of the observed CO_2 in Figure 3.10 (Right) arose mainly from residual carbon of the $\text{Sn}(\text{OAc})_2$. Therefore, additional CO_2 evolution may be related to established interactions between silanols and $\text{Sn}(\text{OAc})_2$. Interestingly, the TPD-MS profile of a deAl-Beta sample previously impregnated with acetic acid revealed similar product evolution to $\text{Sn}(\text{OAc})_2/\text{deAl-Beta}$ (Figure 3.13), suggesting that primary interconversion of the acetates into acetic acid, prior to further

decomposition into CO_2 as main product, may be a key step towards the synthesis of an active catalyst.

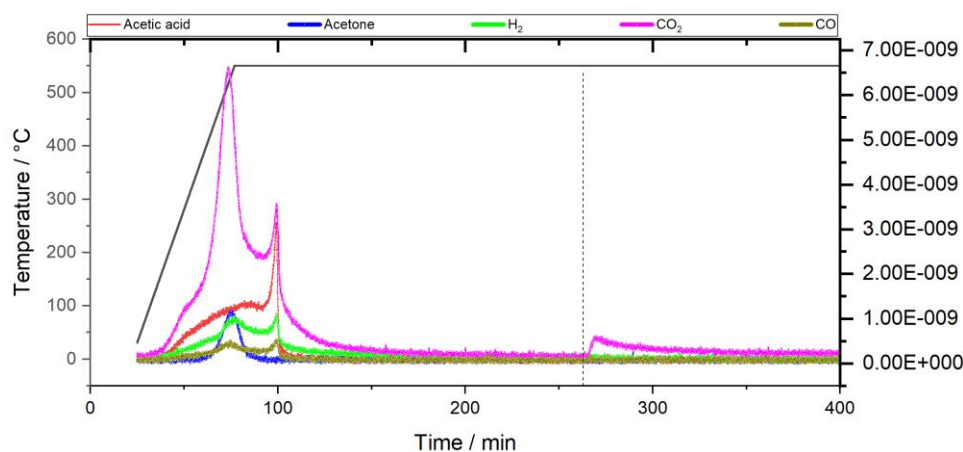


Figure 3.13. TPD-MS of 1wt. % $\text{Sn}(\text{OAc})_2/\text{deAl-Beta}$ impregnated with 9 wt. % acetic acid.

Complementing the TPD-MS data, the mass loss profiles of these samples were also measured by TGA (and DTG) during the initial ramping stage. As can be seen (Figure 3.14), the mass loss profiles of both $\text{Sn}(\text{OAc})_2$ and $\text{Sn}(\text{OAc})_2/\text{Si-Beta}$ are in excellent agreement to the TPD-MS data, exhibiting one major mass loss between 100-300 °C. Interestingly, the total mass lost during treatment of pure $\text{Sn}(\text{OAc})_2$ does not fully account for all the acetate present in the sample which accounts to 50 % of mass of the acetate in $\text{Sn}(\text{OAc})_2$ in contrast to the experimental mass loss of 40 %. This could either be due to the formation of a solid product of higher mass than elemental Sn, such as an oxide, carbonate, or oxycarbonate product, or due to the fact a small amount of acetate is lost during the isotherm and was not detected with the TPD-MS. In contrast, the mass loss profile of $\text{Sn}(\text{OAc})_2/\text{deAl-Beta}$ is more complex than its accompanying TPD-MS profile. Most notably, whereas no volatile compounds were observed in the effluent at low temperature, mass losses at low temperatures (< 200 °C) were observed. These can be attributed to (partial) dehydration of deAl-Beta, the product of which (water) could not reliably be monitored by MS, and hence, was omitted from the TPD-MS patterns for clarity (*vide supra*).

Data obtained from TPD-MS and TGA clearly indicated that the rate and mechanism of acetate decomposition is strongly influenced when a zeolite is present, modifying also the order of evolution of compounds. Also, these changes were not solely due to additional hydrolysis

processes caused by the presence of water present in the hydrated zeolite, since the pathway of acetate decomposition is different for $\text{Sn}(\text{OAc})_2/\text{Si-Beta}$ and $\text{Sn}(\text{OAc})_2/\text{deAl-Beta}$. Hence, the mechanism is particularly modified when the zeolite also possesses silanol nests. These findings are in good agreement with the FTIR spectra reported in Figures 3.4 and 3.5, which revealed different interactions occurring between $\text{Sn}(\text{OAc})_2/\text{deAl-Beta}$ and $\text{Sn}(\text{OAc})_2/\text{Si-Beta}$.

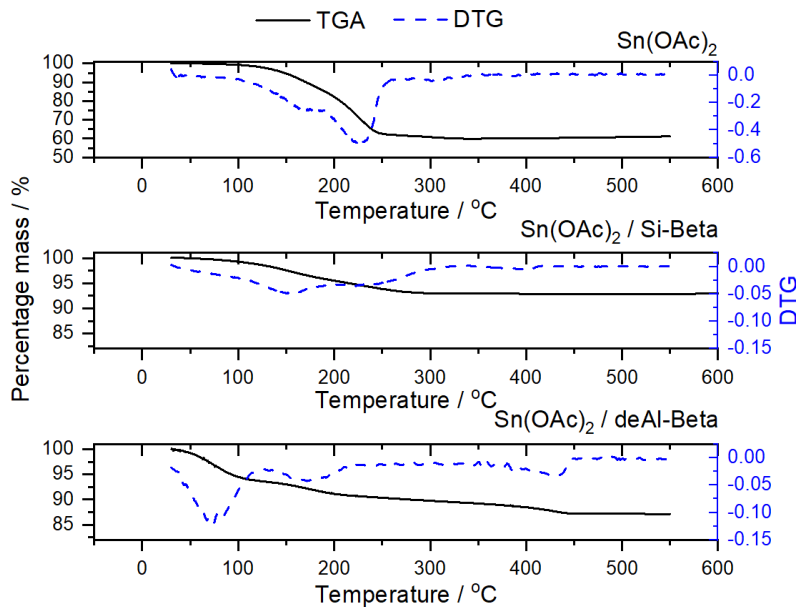


Figure 3.14. TGA profiles and derivatives of (from top to bottom) i) pure $\text{Sn}(\text{OAc})_2$, ii) $\text{Sn}(\text{OAc})_2/\text{Si-Beta}$, and iii) $\text{Sn}(\text{OAc})_2/\text{deAl-Beta}$.

To investigate the evolution of the silanol sites during heat treatment, ^{29}Si MAS NMR analysis was performed on samples of $\text{Sn}(\text{OAc})_2/\text{deAl-Beta}$ removed from the furnace after different periods of time during the ramping stage. As shown in Figure 3.15, ^{29}Si MAS NMR analysis revealed that the signal at -98 ppm, assigned to isolated $(\text{Si}(-\text{OSi-})_3\text{OH})$ groups (Q^3),³⁸ strongly decreased in the temperature range 300-550 °C, similar temperature where the major mass loss was observed in the TGA profile of $\text{Sn}(\text{OAc})_2/\text{deAl-Beta}$, and the evolution of most of the acetate in its decomposed forms from the sample was observed by TPD-MS. The simultaneous loss of both silanol sites and the organic molecules from the $\text{Sn}(\text{OAc})_2/\text{deAl-Beta}$ mixture further suggests that interactions between them are essential to achieve synthesis of an active Sn-Beta catalyst.

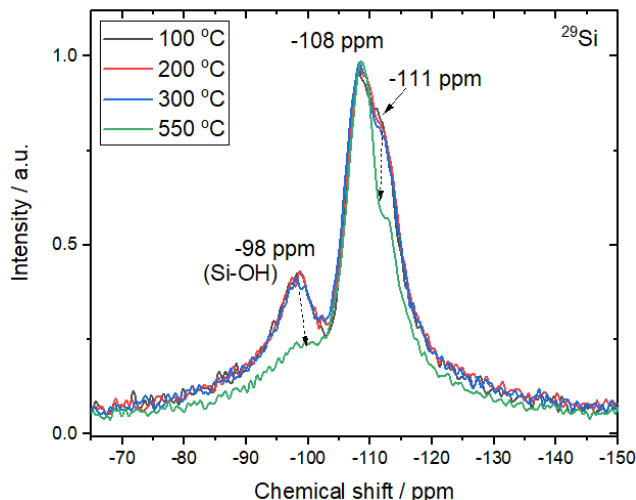


Figure 3.15. ^{29}Si MAS NMR of $\text{Sn}(\text{OAc})_2/\text{deAl-Beta}$ heated at different temperatures (stepwise ramping stage).

To gain further insights into the changes occurring from the modified $[\text{C}=\text{O}]$ groups during heat treatment, *in situ* DRIFTS measurements were subsequently performed. DRIFTS analysis of $\text{Sn}(\text{OAc})_2/\text{deAl-Beta}$ (Figure 3.16) revealed various changes to the $1750 - 1200 \text{ cm}^{-1}$ region at $325 \text{ }^\circ\text{C}$, which may be related to both (partial) dehydration of the zeolite and changes to the acetate coordination. A control experiment on $\text{Sn}(\text{OAc})_2$ alone revealed that these changes did not occur in the absence of the zeolite (Figure 3.17). However, despite some shifts which may indicate changes in coordination, some of the $\text{C}=\text{O}$ stretching modes of acetate were still present at $325 \text{ }^\circ\text{C}$. Indeed, it is only when CO_2 started to be detected in the effluent at approximately $400 \text{ }^\circ\text{C}$ did further decomposition of the acetate occur, eliminating both CO asymmetric and CO symmetric stretching signals (1541 , and 1413 cm^{-1} , respectively), which is in line with the *in situ* TPD-MS analysis and TGA. Alongside the loss of features related to the removal of the acetate, DRIFT spectra recorded at the end of the ramp revealed the 950 cm^{-1} band gradually fading which has been attributed to framework defects such as surface silanol sites, typically present in zeolites synthesised in OH^- media.^{39–41}

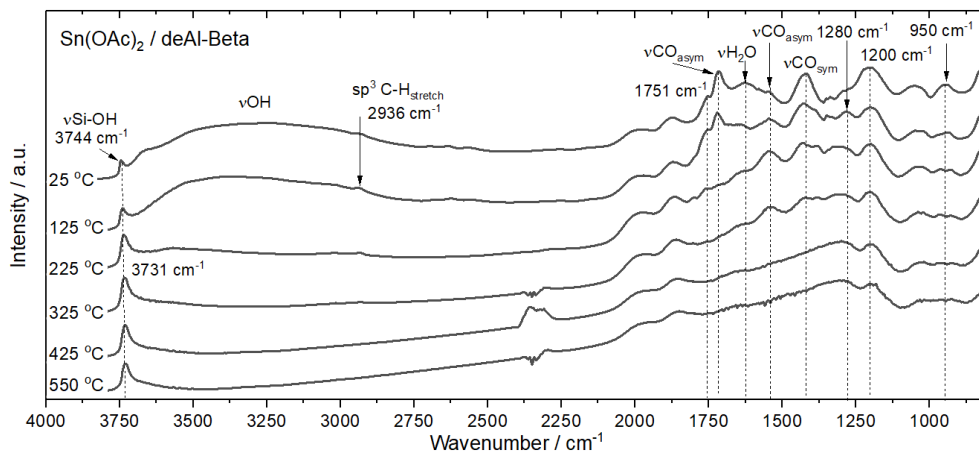


Figure 3.16. In situ DRIFTS for calcination of $\text{Sn}(\text{OAc})_2/\text{deAl-Beta}$ during the ramping stage.

In situ DRIFT analysis of the following stages of the heat treatment was also performed, indicating only minor changes occurring throughout the three hours isotherm in N_2 and the three hours isotherm in air, whilst re-hydration of the material with restoral of the 950 cm^{-1} band was clearly observed at the end of the calcination (Figure 3.18). Given the defective nature of the zeolite used, reappearance of the 950 cm^{-1} band at atmospheric is possible, where the zeolites undergo hydroxylation at relatively low temperature.⁴² The appearance of the 950 cm^{-1} does, however, have a relation with metal centres; higher metal content such as Sn is shown to create more defects attributed to this wavenumber, which can be result of the high intensity of 950 cm^{-1} observed for $\text{Sn}(\text{OAc})_2/\text{deAl-Beta}$ catalyst.

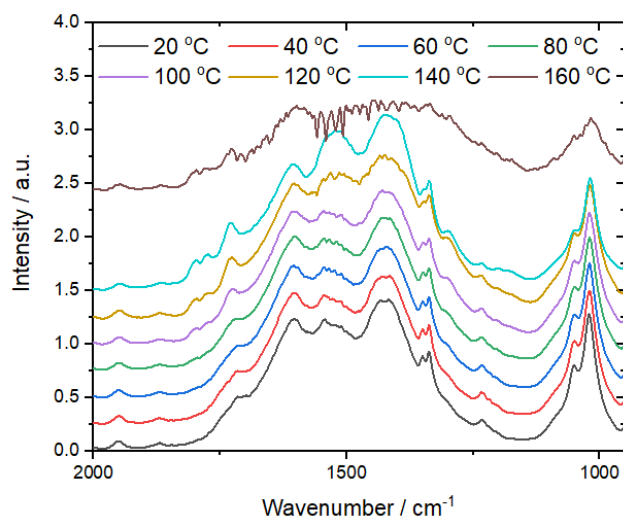


Figure 3.17. *In situ* DRIFTS of the calcination of $\text{Sn}(\text{OAc})_2$; range $2000\text{--}900\text{ cm}^{-1}$.

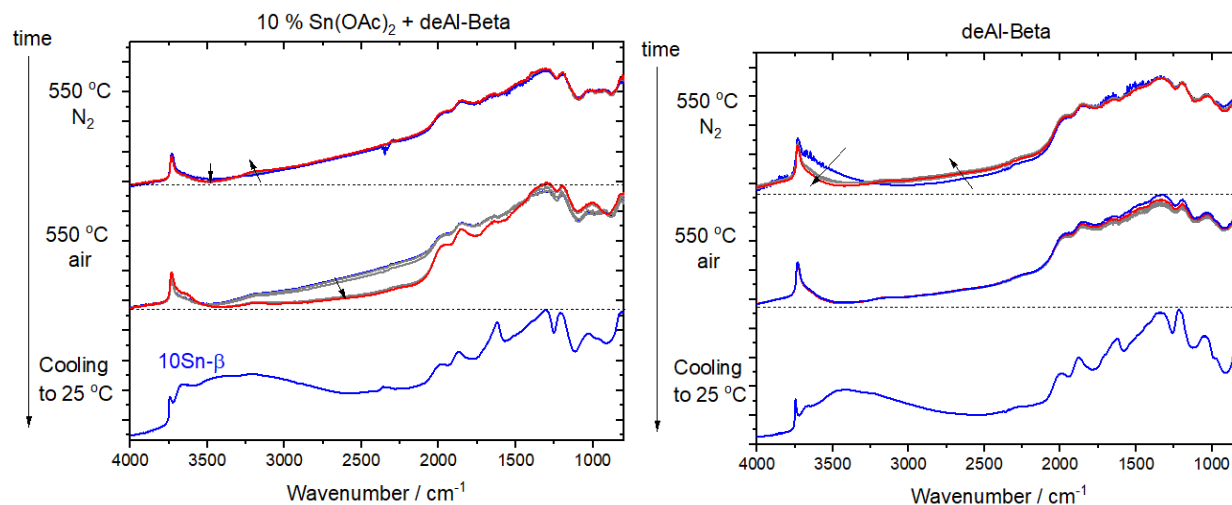


Figure 3.18. DRIFT comparison between $\text{Sn}(\text{OAc})_2/\text{deAl-Beta}$ and deAl-Beta alone during isotherms stages and cooled to room temperature following heat treatment.

To complement the DRIFTS studies, DRUV-Vis was performed during heat treatment of $\text{Sn}(\text{OAc})_2/\text{deAl-Beta}$, as shown in Figure 3.19. From this, it was found that only minor changes to the absorption spectra of the mixture occurred during the ramp stage and first isotherm in N_2 . However, a drastic decrease in intensity and an evident blue shift of the major absorption band was observed $\text{Sn}(\text{OAc})_2/\text{deAl-Beta}$ after the switch to air and the resulting 3 h isotherm. These observations strongly indicate major variations in Sn speciation occur during heat treatment, but only in the second part of the heat treatment, *i.e.*, upon moving from N_2 to air flow.

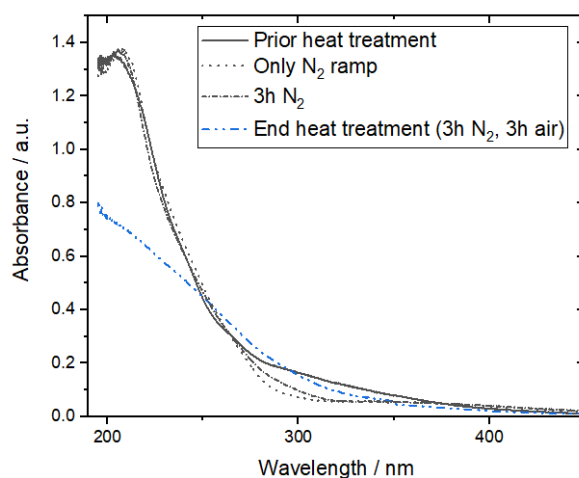


Figure 3.19. Stepwise DRUV-Vis analysis of $\text{Sn}(\text{OAc})_2/\text{deAl-Beta}$ mixture at different stages of the heat treatment protocol.

To complement these findings, an *in situ* experiment following the SSI of Sn was performed with X-ray Absorption Spectroscopy (XAS). As reference points for the normalised intensity, pure Sn(OAc)₂, the grinded sample, and the sample following the entire heat treatment protocol are also presented (Figure 3.20, Right). The catalyst used for XAS was Sn(OAc)₂/deAl-Beta with 10 wt. % Sn (*i.e.* 10Sn-Beta).

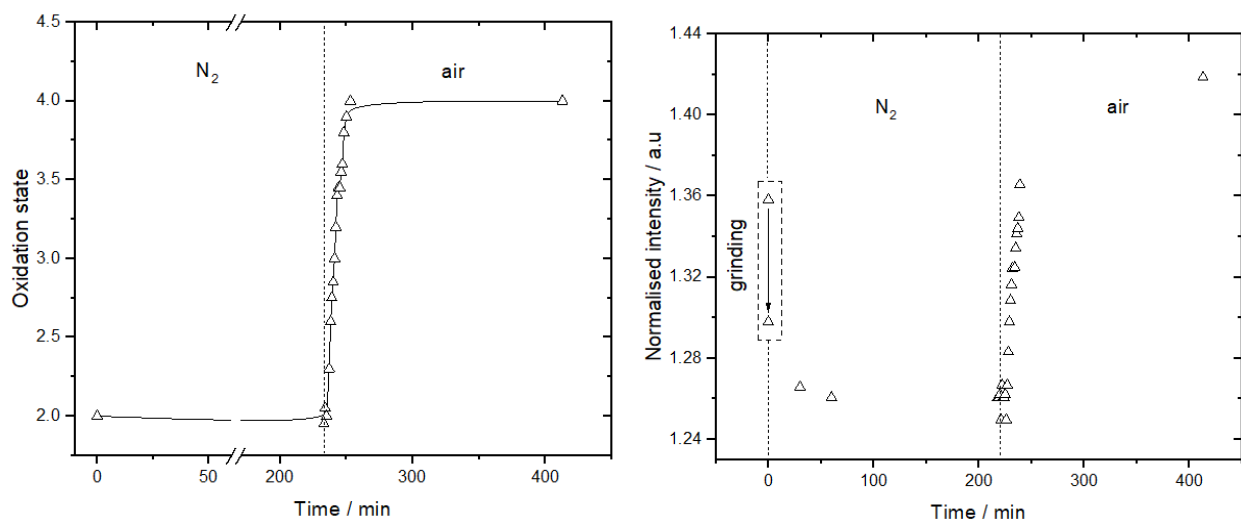


Figure 3.20. *In situ* XAS analysis of 10Sn-Beta synthesis. (Left) Oxidation state of Sn as a function of time. (Right) Position of the 1st derivative maxima (Normalised intensity) of Sn K edge XANES spectra.

However, the beamline only provided He as the inert gas. To ascertain that the change in the inert gas in the heat treatment did not overall affect the catalysts' compound evolution, textural properties, and/or activity, reference experiments (spectroscopic and catalytic) were performed on 10Sn-Beta and underwent the same screening as can be seen in Figures 3.21-3.23 and Table 3.1. Same catalytic activity was observed for samples prepared in He/air and N₂/air for the Meerwein–Ponndorf–Verley (MPV) transfer hydrogenation of cyclohexanone to cyclohexanol, demonstrating that other inert gases such as He can be implemented without having any contrasting changing.

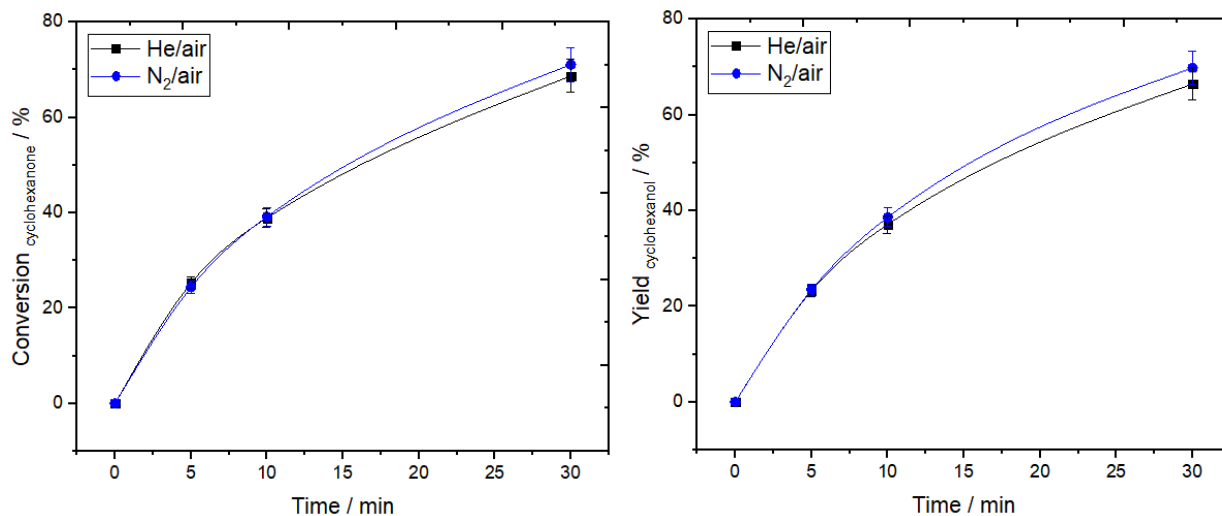


Figure 3.21. Comparison catalytic performances for Meerwein–Ponndorf–Verley reaction of cyclohexanone to cyclohexanol over 10Sn-Beta calcined using nitrogen flow and helium flow as inert gas. Reaction conditions: 0.2 M cyclohexanone and 0.01 M Biphenyl in 2-butanol, 373 K.

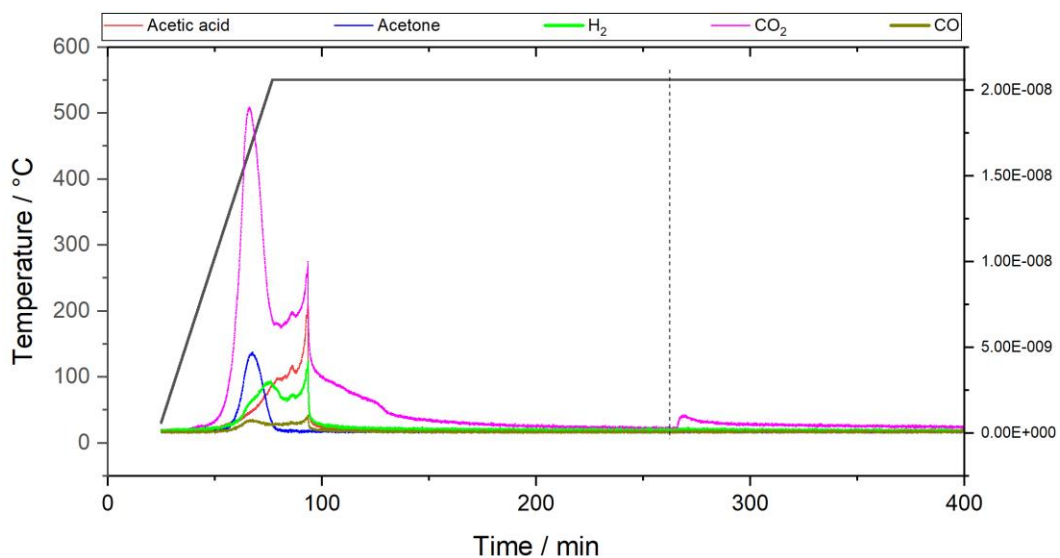


Figure 3.22. TPD-MS of 10Sn-Beta using helium as inert gas.

Table 3.1. Textural properties of Air and He 10Sn-Beta catalysts.

Catalyst	t-plot		External Surface area (m^3g^{-1})	DFT Method		
	Micropore volume (cm^3g^{-1})	Micropore area (m^3g^{-1})		Surface Area	Pore Volume	Surface Area
Air Sn-Beta	0.219	416	92	509	0.35	890
He Sn-Beta	0.207	396	94	490	0.34	874

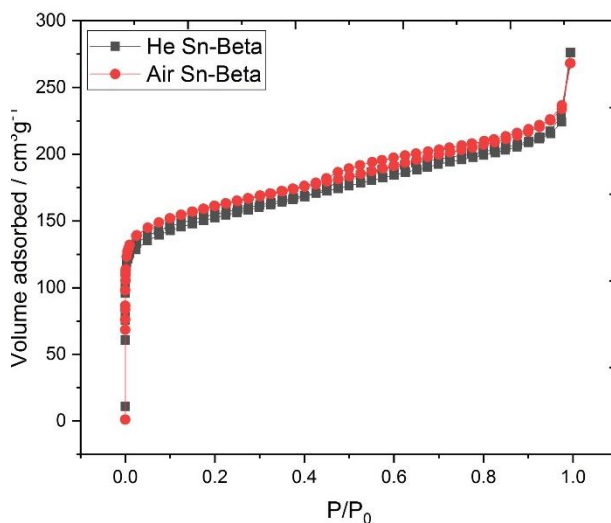


Figure 3.23. Nitrogen physisorption of He/air 10Sn-Beta catalysts.

Firstly, eventual changes within the near edge structure by X-ray Absorption Near Edge Structure (XANES) were investigated and the maximum of the first derivative of the XANES data was used to determine the position of the absorption edge. In accordance with previous findings (*i.e.* ^{119}Sn MAS DE CPMG NMR), grinding $\text{Sn}(\text{OAc})_2$ with deAl-Beta led to a slight shift in edge position, and a very small decrease in intensity. However, the edge position was still consistent with Sn^{2+} being the dominant species (Figure 3.7). Heat treatment of the sample under the X-ray beam was subsequently performed. To aid the understanding of the changes in the XANES spectra, the intensity and position of the 1st derivative maxima are plotted against time, allowing both the level of order (intensity) and the oxidation state (position) of Sn during the heat treatment to be monitored (Figure 3.20, Left). Notably, the edge position was transformed to an oxidation state value by comparison to authentic standards of SnO (+2) and SnO_2 (+4), which were observed at

29185 and 29190 eV, respectively.⁴³⁻⁴⁵ During the first stages of the heat treatment (ramp to 550 °C and 3 h isotherm in N₂), little change was observed to the Sn species despite the loss of the acetate ligands, which is in excellent accordance with DRUV-Vis and ¹¹⁹Sn MAS DE CPMG NMR analysis. Although there was a minor decrease in order during this period, as evidenced by the slight decrease in normalized intensity of the maxima of the first derivative (Figure 3.20, Right), Sn²⁺ was clearly still present throughout this process. However, dramatic changes to the XANES spectrum occurred upon switching the gas stream from the inert carrier to air. As can be seen in Figure 3.20 (Left), the introduction of air led to extremely rapid increases in both the order and the oxidation state of Sn. Indeed, within 60 minutes, the oxidation state of Sn rapidly increased from +2 to +4.

To gain further insight on how these changes correlate to the structure of the catalyst, and in particular the coordination environment of Sn, Extended X-ray Absorption Fine Structure (EXAFS) measurements were also performed. To simplify interpretation and the level of analysis required, focus was placed on the speciation of Sn just prior to, and following, the switch to air, where the major spectral changes were expected based on XANES and ¹¹⁹Sn MAS NMR spectroscopy. Figure 3.24 presents the magnitude of the k³-weighted Fourier transform of the EXAFS spectrum of the mixture in R-space. The first features present in the spectra (1-2 Å, peak maxima at 1.4 Å) can be assigned to Sn-O scattering interactions (Figure 3.24, Left), whilst Sn-Sn scattering indicative of clustered/extra-lattice Sn species can be identified by features between 3.0 and 4 Å (peak maxima at 2.8 Å) (Figure 3.24, Right), where it has been reported that bulk SnO and SnO₂ scattering are found at 2.21 and 2.052 Å, respectively.^{46,47} Prior to the introduction of air, only one major feature is observed at approximately 1.8 Å, indicative of Sn-O bonding. The Sn-O signal observed at this particular time is almost identical to that observed following the physical grinding stage, confirming the lack of major changes to the Sn sites during the ramp and first isotherm period in N₂. However, upon introduction of air into the system, a dramatic increase in the intensity of the first peak in the FT spectrum occurred, indicating either i) an increase in the number of Sn-O bonds, ii) an increase in the order/uniformity of the existing Sn-O bonds, or iii) a combination of both. Notably, this increase in intensity occurred over the same period of time as the oxidation state of Sn increases to +4. Over the course of 60 minutes, the first-shell oxygen distance (Sn-O) also shifts to 1.95 Å. Notably, this value is consistent with Sn atoms that are isomorphously substituted into the Beta framework, confirming that full isomorphous substitution

occurs at the same time as the Sn atoms are oxidised from +2 to +4.⁴⁶ At this stage, the Sn atoms remain tetrahedrally coordinated, due to their dehydrated nature at high temperature.

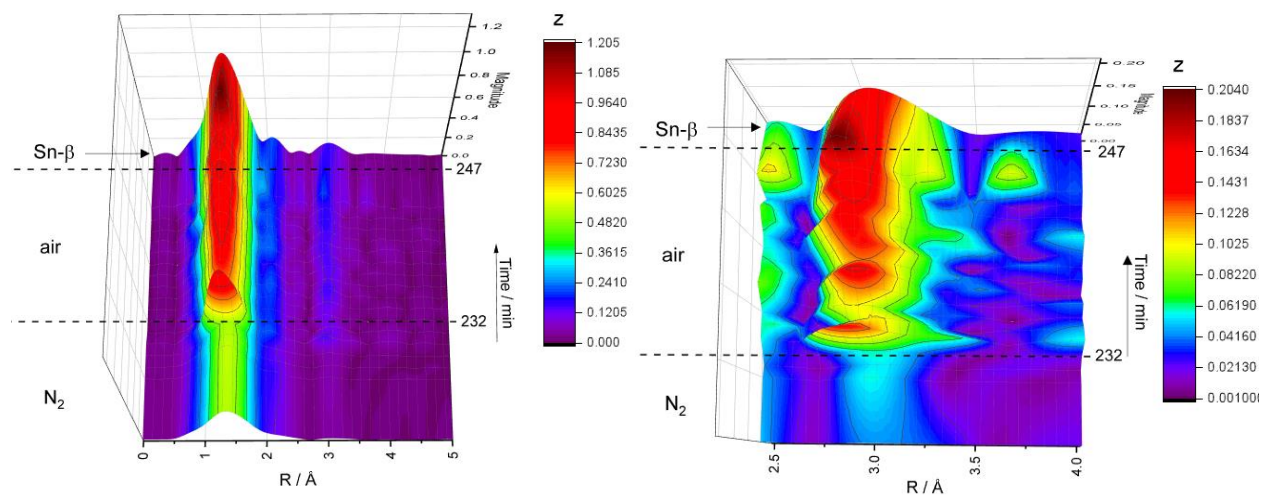


Figure 3.24. (Left) EXAFS 3D spectrum of the k^3 weighted FT of 10Sn-Beta calcination in R-space. (Right) EXAFS 3D spectrum of the k^3 weighted FT of 10Sn-Beta calcination in R-space with zoom on Sn-Sn cluster.

After the first 60 minutes of the isotherm in air, only minor additional changes were observed in the first-shell Sn-O feature, indicating that after the initial oxidation and incorporation of Sn, no major modifications to the Sn-O bonds were observed. However, changes in the second shell (Sn-Sn) features can be observed throughout the isotherm. As can be seen in Figure 3.24, immediately upon switching to air, the feature at approximately 3.2 Å increases at a similar rate to that of the 1.8 Å feature. The increase in this feature throughout the heat treatment protocol indicated some Sn-Sn formation occurs regardless of how long the heat treatment protocol is carried out for at these Sn loadings. However, the 3.7 Å feature characteristic of SnO₂ is not observed until extended parts of the air isotherm, suggesting that additional clustering to form extra-framework SnOx species is a secondary process during the synthesis.

Further elucidation of Sn incorporation into the zeolite lattice was achieved by ¹¹⁹Sn CPMG MAS NMR spectroscopy, performed in direct excitation (DE) mode.⁴⁸ Technical limitations prohibited analysis of the samples at true operational conditions, and hence, the heat treatment was terminated at various stages prior to removal of the sample and measurement by *ex situ* means. Catalysts were let to rest in the furnace after reaching the designated temperature until reaching room temperature to assure that no external air could influence in the possible formation of +4 Sn in the framework.

Consequently, all Sn resonances are characteristic of Sn samples in their hydrated state.^{1,49,50} ^{119}Sn MAS NMR spectra of $\text{Sn}(\text{OAc})_2/\text{deAl-Beta}$ obtained at different stages of the ramp only revealed minimal changes between 300-550 °C, showing -600 ppm species to still be the dominant resonance (Figure 3.25, Left). Switching to air showed an evident increase in intensity at -689 ppm, which could be related to an active Sn species, assigned in previous reports to hydrated Sn(IV) species incorporated on beta zeolites (Figure 3.25, Right).^{49,51} However, upon having the catalyst in isotherm in air, no further changes in terms of speciation were shown. This proved the long isotherm under air to be superfluous, resulting in an overall similar speciation and requiring only 60 minutes for oxidation to complete, as suggested by XAS.

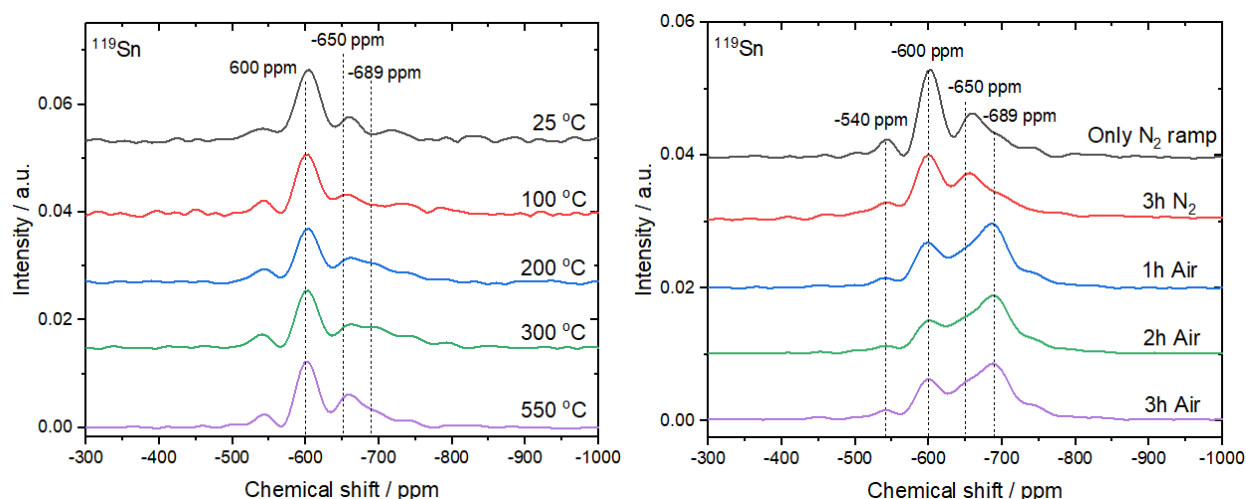


Figure 3.25. ^{119}Sn MAS DE CPMG NMR spectra of 10Sn-Beta (Left) at different stages of the ramp rate (in N_2) and (Right) different step of the isotherms.

Taken together, the UV-Vis, XANES, EXAFS and ^{119}Sn MAS DE CPMG NMR analyses all indicate that full isomorphous substitution of Sn into the framework of zeolite Beta, and its resulting oxidation to Lewis acidic Sn^{4+} only occurs upon introduction of air into the system. This oxidation is in line with what Sels *et al* have reported, demonstrating the oxidation of Sn^{+2} to Sn^{+4} in the same two-step heat treatment protocol via Mössbauer Spectroscopy.²⁹ However, unlike with calcining in pure air which showed to convert all Sn to +4 oxidation state, some Sn seems to maintain in +2 oxidation when carrying out N_2/air step (18 % Sn^{+2} / 82 % Sn^{+4} , which could partially represent the -600 ppm resonance in the ^{119}Sn NMR spectra. Another factor for which a

high amount of -600 ppm species is shown can be caused by the elevated wt. % of Sn(OAc)₂. Thus, a 1 wt. % Sn sample was subsequently studied to elucidate further on the SSI mechanism.

3.2.3 Increasing the relative proportion of active sites; spectroscopic analysis of 1Sn-Beta

As has been previously demonstrated,^{25,26} Sn-Beta catalysts possessing initial Sn loadings > 5 wt. % typically contain higher quantities of extra-framework SnO_x species. Although these species do not contribute to the catalytic performance of the material which results in an underestimation of the activity of the catalyst, they can also influence the spectroscopic signals generated, which may complicate mechanistic understanding of this system. Thus, key experiments described above were repeated for samples of using only 1 wt. % Sn, denoted 1Sn-Beta, using deAl-Beta as the zeolite parent. While lower metal loading catalysts are more challenging to study, these samples with a higher fraction of active to inactive sites evidently allows better evaluation of which of the processes occurring during SSI are most relevant to catalysis and active site formation. It is noted that recent studies have suggested that the turnover frequency of Sn in 1Sn-Beta is approximately 7-fold higher than that determined for 10Sn-Beta for continuous glucose to fructose isomerisation, and two-to-three fold for batch MPV transfer hydrogenation of cyclohexanone to cyclohexanol (2 wt. % vs. 10 wt. % Sn).^{25,26,52}

In situ TPD-MS analysis performed throughout the synthesis of 1Sn-Beta correlates well with the 10Sn-Beta, showing that most of the original acetate was released in the temperature range 300-550°C as CO₂, carbon monoxide, acetone, hydrogen, and small amounts of acetic acid (Figure 3.26), with an additional amount of CO₂ released when switching from N₂ to air flow. Analogously, DRIFT measurements performed on 1Sn-Beta prior to heat treatment revealed similar changes in the acetate coordination to the ones observed for the high loading sample (Figures 3.27).

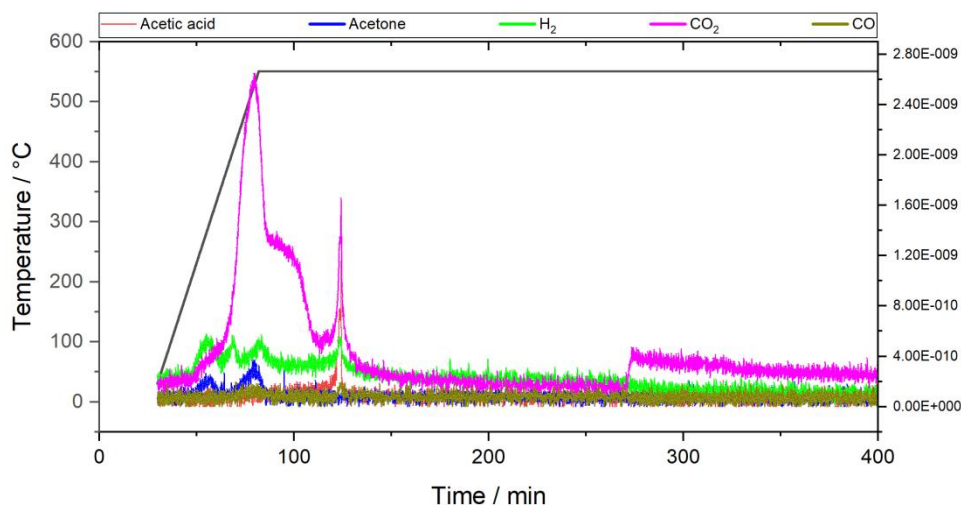


Figure 3.26. TPD-MS during calcination of $\text{Sn}(\text{OAc})_2/\text{deAl-Beta}$ mixture with 1 wt. % Sn loading.

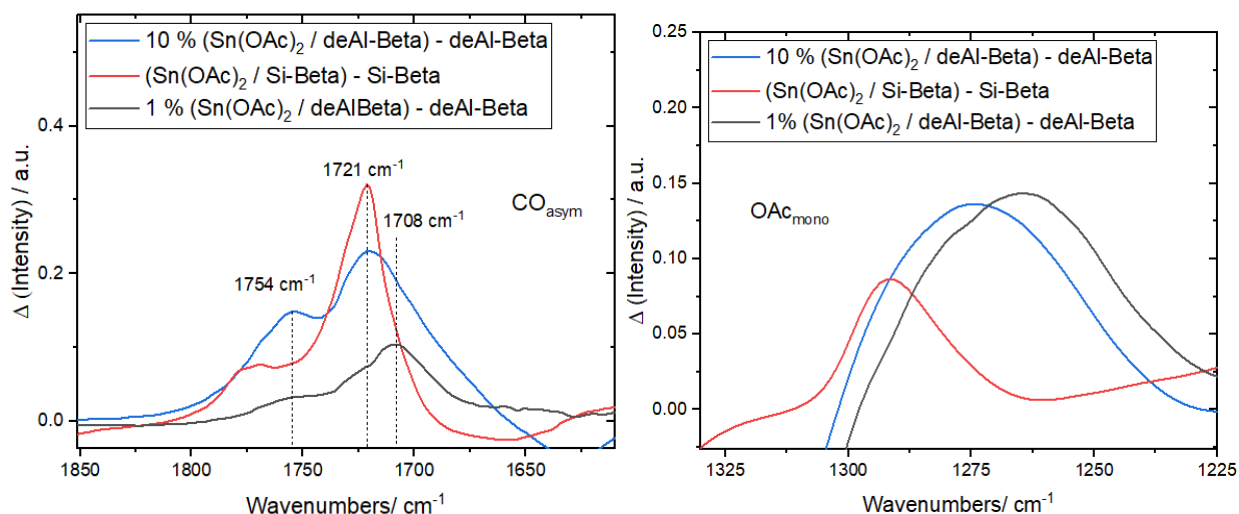


Figure 3.27. Differential FTIR spectra obtained through subtraction of i) $\text{Sn}(\text{OAc})_2/\text{deAl-Beta}$ mixture with 10 wt. % of Sn and deAl-Beta alone (blue line), ii) $\text{Sn}(\text{OAc})_2/\text{Si-Beta}$ mixture and Si-Beta alone (red line), and iii) $\text{Sn}(\text{OAc})_2/\text{deAl-Beta}$ mixture with 1 wt. % of Sn and deAl-Beta alone (Black line).

In situ DRIFT analysis performed throughout the ramping stage (Figure 3.28, Left, and Annex 3.4 for full spectra) was shown to indicate a greater level of clarity present in the 1 % Sn mixture in contrast to the 10 wt. % mixture. Upon heating the 1 % Sn mixture, fast decrease of the vibrational band at 1709 cm^{-1} , assigned to CO_{asym} stretching, was observed. This was accompanied by the formation of a band at 1751 cm^{-1} at 125°C , which disappeared at 375°C . These findings clearly

indicate changes of C=O coordination throughout the ramp, prior to full decomposition of the acetate groups at temperatures > 300 °C, comparable to previous observations reported for the 10 % Sn mixture (Figures 3.10 and 3.15). Notably, fast rehydration of the catalyst was again observed upon cooling the sample to room temperature following synthesis, which suggests the formation of hydrated Sn sites, as is shown in Figure 3.28 (Right).

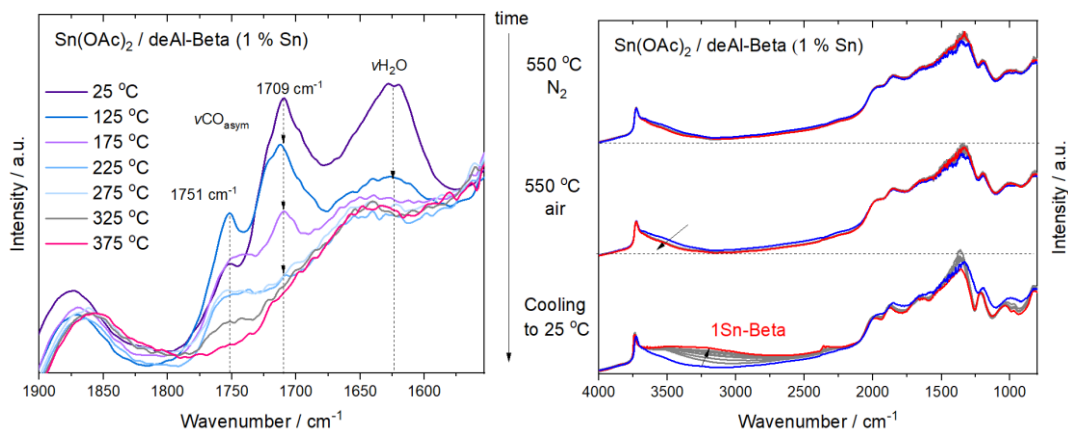


Figure 3.28. DRIFT spectra during heat treatment of $\text{Sn}(\text{OAc})_2/\text{deAl-Beta}$ mixture with 1 wt. % of Sn (Left) at different stages of the ramp rate in N_2 (zoom on CO_{asym} bands) and (Right) different steps of the isotherms and cooling to room temperature.

To investigate the evolution of the silanol sites, ^{29}Si MAS NMR analysis was also repeated at different stages of the ramp, as can be seen in Figure 3.29 (Left), revealing that despite a small decreasing of intensity observed between 100-300 °C, the majority of the silanol sites diminished in the range 300-550 °C in accordance with those findings reported in Figure 3.15, with a further reduction observed in the post synthetic sample. Following investigation of the acetate evolutions, focus was placed on the main changes in Sn speciation. Comparison between the ^{119}Sn MAS DE CPMG NMR spectra of 1Sn-Beta and 10Sn-Beta at the end of the ramp revealed clear similarities, confirming that only some Sn centres may be incorporated in the zeolite at this stage. Moreover, large formation of signal(s) in the region -650 – -750 ppm was observed on 1Sn-Beta sample, further suggesting hydrated species at -689/-703 ppm as active Sn sites (Figure 3.29, Right).

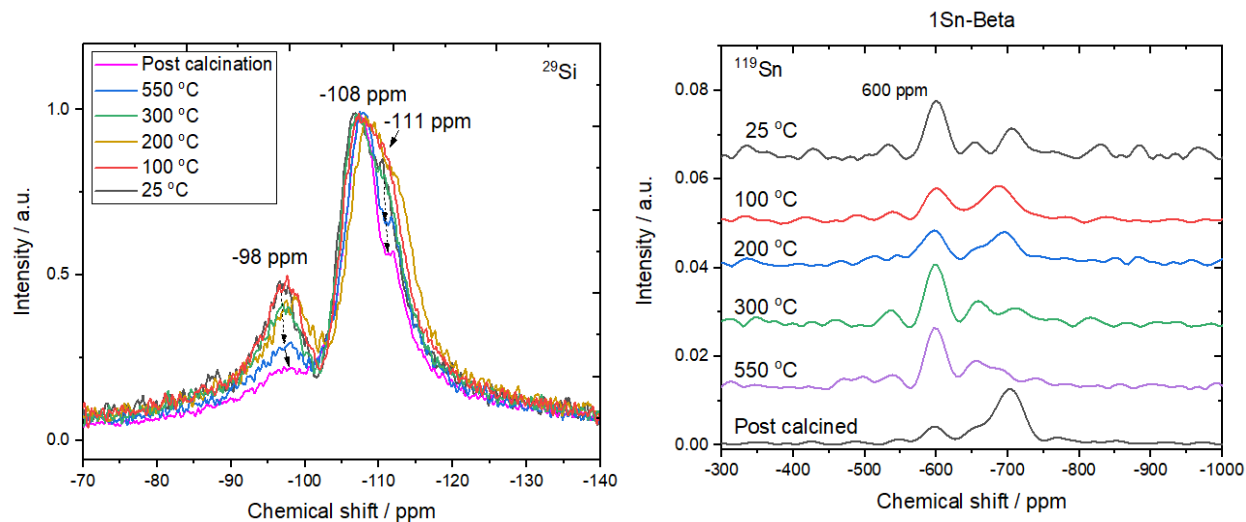


Figure 3.29. (Left) ^{29}Si DE MAS NMR spectra of 1Sn-Beta at different temperatures of the heat treatment protocol. (Right) ^{119}Sn MAS DE CPMG NMR spectra of 1Sn-Beta at different stages of the ramp rate and at following calcination (*i.e.* post calcined).

Key experiments repeated on 1Sn-Beta revealed that the main changes in both acetate evolution and Sn speciation previously observed for 10Sn-Beta are all essential to the synthesis of active Sn species. ^{29}Si - and ^{119}Sn -MAS NMR, along with TPD-MS, were shown to be consistent with the results obtained from 10Sn-Beta. DRIFT of 1Sn-Beta presented minor differences due to the better resolution of 1Sn-Beta, showing clear formation of acetic acid, confirming the key role it has for the synthesis of an active catalyst.

3.2.4 Application of mechanistic insight for catalyst design

Following preliminary understanding of the reaction mechanism(s) for Sn incorporation in deAl-Beta zeolites, this knowledge was used to focus on optimising the synthetic procedure of Sn-Beta. Despite possessing higher distribution of spectator sites compared to 1Sn-Beta, 10Sn-Beta was used as the study material for optimisation for two reasons. Firstly, its higher loading results in improved productivity, making it more favourable from an industrial perspective. Secondly, its higher ratio of spectator sites / active sites provides greater opportunity for improving the maximal performance of the catalyst. Based on spectroscopic data, two important key points were determined to be essential for an active catalyst: i) the use of a N_2 ramp, and ii) subsequent change

to air flow. However, given with previous data gathered (^{119}Sn MAS NMR and XAS), it was shown that it was not necessary for the air treatment isotherm to be that extensive (*i.e.* 3 hours), as it was traditionally done, demonstrating that an active catalyst can be created within 60 minutes. Therefore, to assess the kinetic impact on the different stages of the heat treatment, reactions using 10Sn-Beta samples were carried out and tested for batch MPV reaction of cyclohexanone to cyclohexanol using 2-butanol as a secondary alcohol and glucose to fructose isomerisation, reactions which are prevalent for the testing of Sn-Beta catalysts.^{5,53–56} Specifically, a set of Sn-Beta catalysts were prepared halting the standard heat treatment in different stages. Turnover frequency (TOF) was used to compare to observe the intrinsic activity of the catalysts.

Reducing the air isotherm to one hour, without modifying the initial N_2 step, resulted in no changes to the catalytic performances of Sn-Beta, resulting in a turnover frequency (TOF) of 191 h^{-1} , similar to other previously reported catalysts using Sn-Beta,⁵⁶ as can be observed in Figure 3.30, (full kinetic profiles shown in Figure 3.31), indicating that air isotherm steps longer than one hour are unnecessary. This is in line with the spectroscopic findings reported in the previous section (^{119}Sn NMR, XAS and TPD-MS). However, complete removal of the air isotherm step substantially decreases the performance of the catalyst, obtaining a TOF of only 140 h^{-1} (“3 h N_2 ”, Figure 3.30). Considering that most of the spectroscopic changes were detected throughout the ramping stage in N_2 , an additional sample was prepared and was halted straight after reaching $550 \text{ }^\circ\text{C}$, *i.e.* completely removing both isotherm stages (“only N_2 ramp”). As anticipated by the minor modifications highlighted by various spectroscopic analysis during the isotherm period in N_2 , this catalyst exhibited similar catalytic activity to the “3 h N_2 ” catalyst. Interestingly, a sample fully calcined in air was synthesised and tested for the model MPV reaction, revealing that replacing N_2 with air throughout the ramp stage leads to the formation of a catalyst with poorer catalytic performance than those prepared via conventional heat treatment (132 h^{-1} vs. 191 h^{-1} TOF for Sn-Beta in only air and conventional, respectively), potentially due to higher amounts of SnO_x formed on the catalyst (XRD and TPD-MS reported in Figures 3.32 and 3.33).

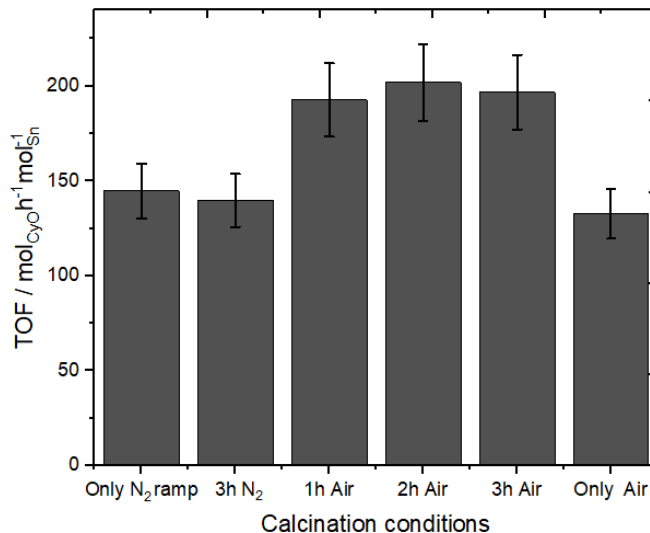


Figure 3.30. Initial TOF for MPV reaction of cyclohexanone to cyclohexanol using 10Sn-Beta catalysts calcined with different heating programs.

Combining together the spectroscopic data reported in previous sections with the experimental data collected on MPV reactions, it is evident that to maximise the rapidity of catalyst preparation the following hypothesis/conclusion can be made: i) heating the catalyst to 550 °C in an inert gas flow with a ramp rate of 10 °C/min is essential; ii) the first isotherm in nitrogen is superfluous; iii) switching to air at 550 °C is important to oxidise the Sn(II) to Sn(IV), and iv) air isotherm longer than one hour is unnecessary. Building on these findings, a new Sn-Beta material calcined under optimised conditions was prepared (ramp in nitrogen followed by one hour isotherm in air).

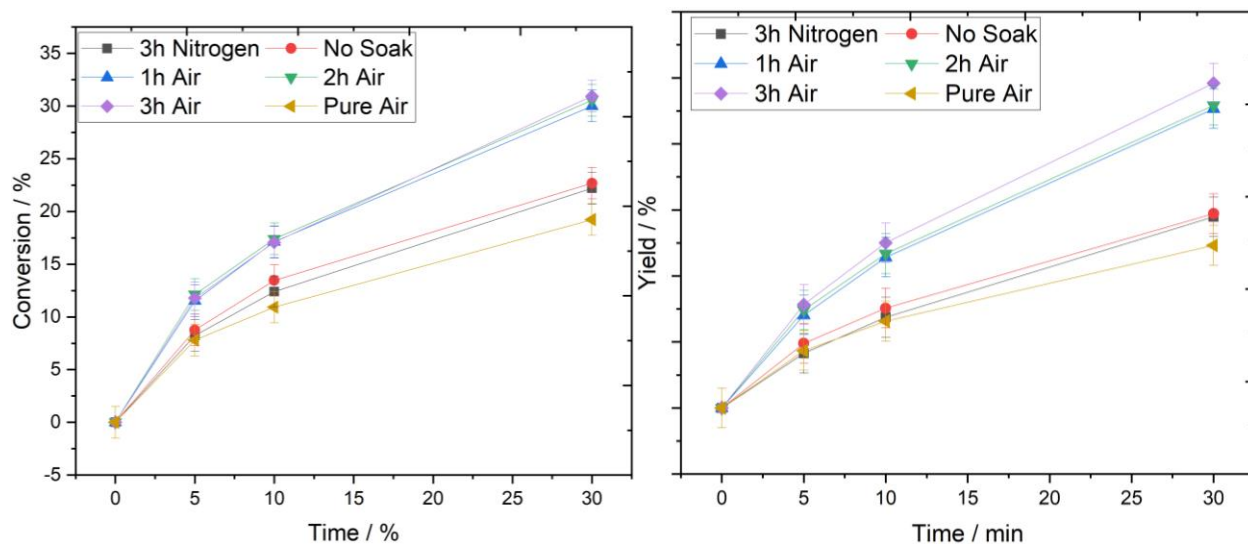


Figure 3.31 (Left) Conversion of cyclohexanone and (Right) yield of cyclohexanol over time for MPV reaction using 10Sn-Beta calcined with different heating programs. Reaction conditions: 0.2 M cyclohexanone and 0.01 M Biphenyl in 2-butanol, 373 K.

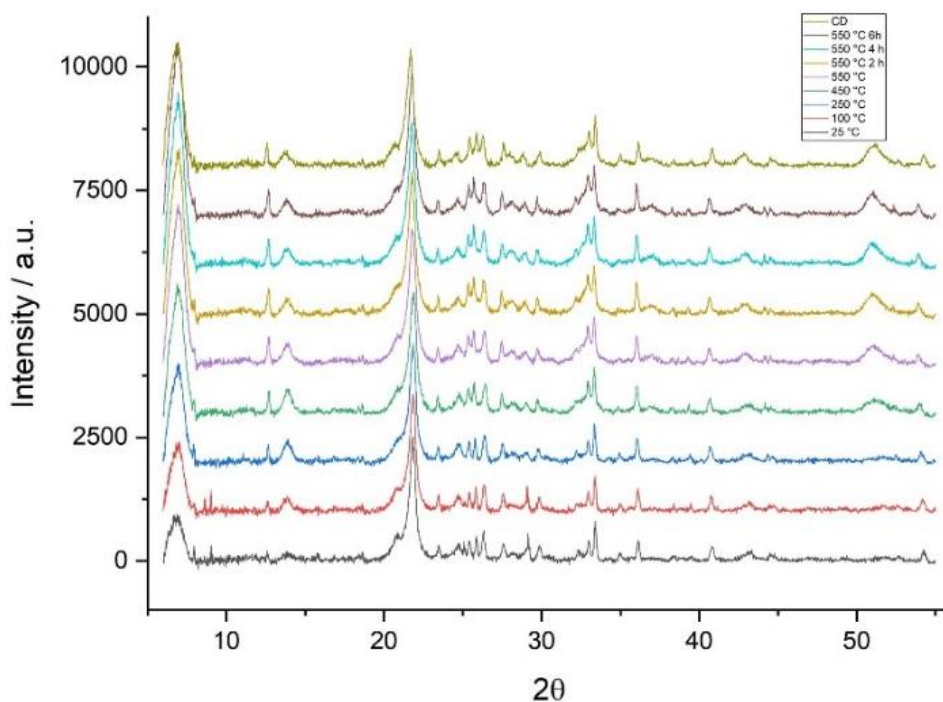


Figure 3.32. *In situ* XRD of 10Sn-Beta in only air. In situ experiments were conducted on an X'PertPRO diffractometer equipped with a CuK α radiation source using a ramp rate of 10 °C min⁻¹, and 10 mL min⁻¹ of N₂/air. Spectra were recorded in the 5-55 2θ range using a step size of 0.0167° and a time/step size of 40 s (total time per spectra = ~18 min).

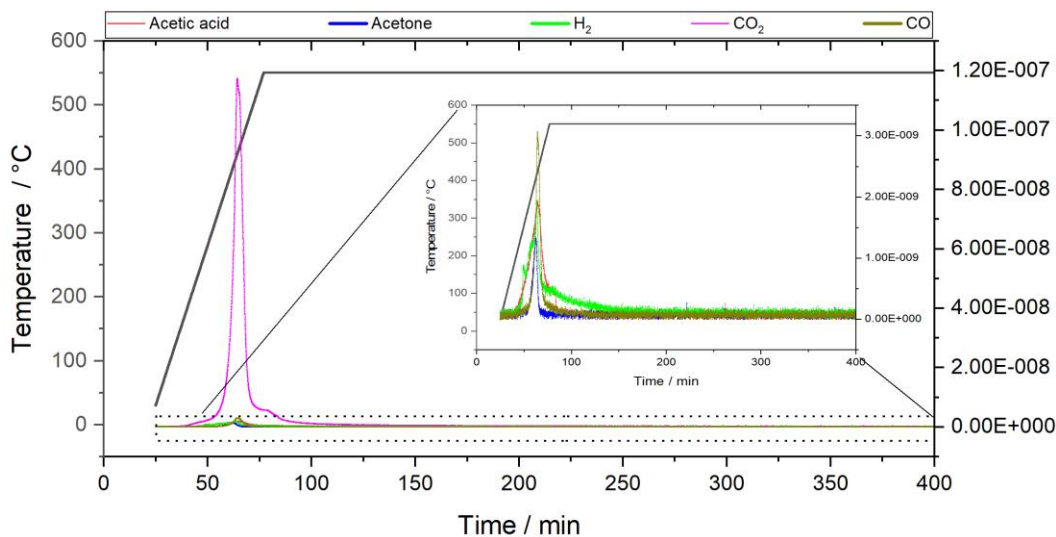


Figure 3.33. TPD-MS of 10Sn-Beta in only air. Inset. 10Sn-Beta without CO₂.

To investigate the general effect of the catalyst optimisation, regardless from one specific reaction, both Sn-Beta (0h, 1h) and the conventionally prepared Sn-Beta (3h, 3h) were employed for glucose isomerisation to fructose. Currently, glucose isomerisation has been receiving great attention from the scientific community due to the increasing demand for fructose as a building block for the synthesis of biobased chemicals and fuels in addition to its employment as a sweetener, and therefore, rapid synthesis of an active catalyst for glucose isomerisation to fructose is a challenge of fundamental societal relevance.^{57–59} When comparing the optimised catalyst to the conventional one, similar glucose conversion (X) and fructose yield (Y) were measured throughout the 30 minutes (Figure 3.30), with final conversions of 26 % and 23 % (3h, 3h and 0h, 3h, respectively) and yields of 13 % achieved on both catalysts (Figure 3.34). These values observed confirm identical (within margin of error) catalytic performances between the conventional catalyst and the new one, therefore, demonstrating successful synthesis of 10Sn-Beta *via* the optimised (rapid) synthesis protocol. Other than glucose and fructose, mannose yield was present at small percentages (*ca.* 1 %) throughout the reaction. Further loss of carbon balance is due to products that were not amenable to chromatographic analysis.

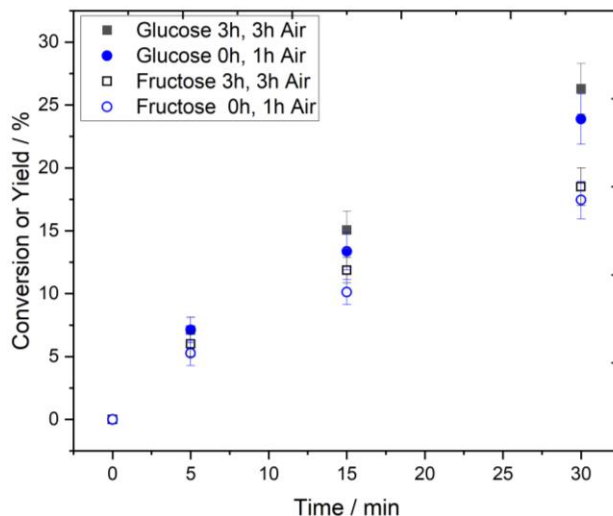


Figure 3.34. Glucose TOF for batch glucose isomerisation at 5 minutes over normal and optimised 10Sn-Beta. Experiments performed in 1 wt. % glucose in methanol solution using a 1:50 metal:glucose molar ratio at 110 °C. Reaction commenced after being submerged in the oil bath and left in isotherm for 10 minutes. Thereafter, stirring was carried out (750 rpm), commencing the reaction. Aliquots were extracted after prior cooling in an ice bath and centrifuged.

Further elucidation on the optimised catalyst was carried out with tests in glucose isomerisation under continuous flow (Figure 3.35). As with previous reactions, negligible changes with both glucose and fructose yields of the optimised catalyst was found to be unaffected, presenting a final conversion and fructose yields of ~ 12 % and 6 %, respectively. This implies that they both share similar fructose selectivity along with rate of deactivation, as is shown in the Levenspiel plot in Annex 3.5. Thus, it can be said that by omitting the isotherm step in inert gas flow as well as reducing the time in air by *ca.* 67 % resulted in no significant differences to catalytic activity, maintaining the catalysts typical space-time-yields and intrinsic activity. Same as batch glucose isomerisation, mannose was present at small percentages throughout the time on stream (*ca.* 2 %) and the loss of carbon balance was due to compounds not amenable to chromatographic analysis.

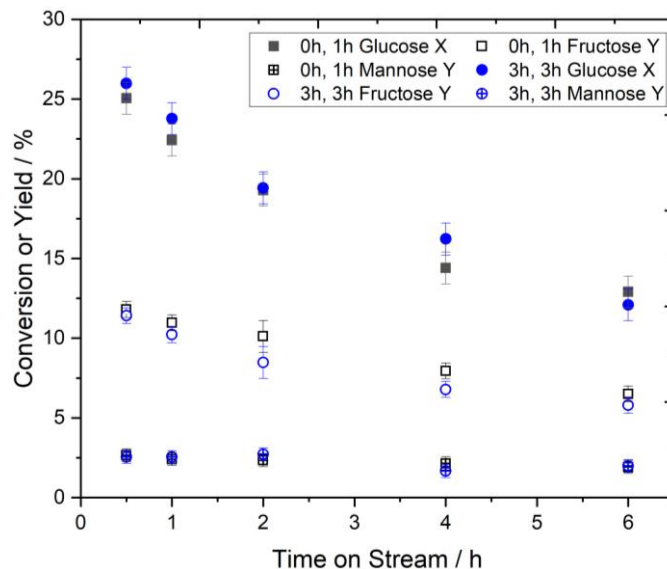


Figure 3.35. Continuous glucose isomerisation of optimized (0h, 1h) and normal (3h, 3h) 10Sn-Beta. Levenspiel plots for rate of deactivation can be found on Annex 3.5. Experiments performed in 1 wt. % glucose in methanol solution using 100 mg of catalyst at 110 °C at a flow rate of 1.5 mL min⁻¹.

3.3 Conclusions

Using a broad range of *in situ* and *ex situ* techniques, the key steps for successful incorporation of Sn in the lattice of dealuminate beta zeolite was investigated. Spectroscopic analysis of the standard synthetic protocol allowed us to both i) gain insights into the key mechanistic steps and ii) apply these findings to improve the synthesis protocol of Sn-Beta. In this study, it was identified that albeit not fully incorporated following the grinding step, heating Sn(OAc)₂/deAl-Beta mixture to 550 °C under inert gas flow is the key step to remove the acetates arising from Sn(OAc)₂, permitting Sn incorporation. However, this step is not sufficient to synthesise a Sn-Beta catalyst with optimised activity and replacing inert gas flow with air flow at high temperatures is required to oxidise the Sn species from an oxidation state of +2 to +4, permitting full incorporation of Sn in the lattice. Formation of the active site, proposed to be a Sn (IV) species resonating at -689 ppm, typically assigned to hydrated Sn centres, occurs during the first hour from the introduction of air in the calcination furnace, indicating completion of the synthesis. Building on these findings, successful preparation of Sn-Beta can be achieved in a total of only two hours was demonstrated (in addition to cooling time). Catalytic analysis of the optimised Sn-Beta for MPV reaction of cyclohexanone to cyclohexanol and glucose isomerisation to fructose revealed identical catalytic

performance between the Sn-Beta prepared via a designed protocol and the standard heat treatment, confirming the efficiency of the rapid protocol.

3.4. References

1. Padovan, D., Botti, L. & Hammond, C. Active Site Hydration Governs the Stability of Sn-Beta during Continuous Glucose Conversion. *ACS Catal.* **8**, 7131–7140 (2018).
2. Hammond, C. & Tarantino, G. Switching off H₂O₂ decomposition during TS-1 catalysed epoxidation via post-synthetic active site modification. *Catalysts* **5**, 2309–2323 (2015).
3. Hammond, C. *et al.* Direct catalytic conversion of methane to methanol in an aqueous medium by using copper-promoted Fe-ZSM-5. *Angew. Chemie - Int. Ed.* **51**, 5129–5133 (2012).
4. Otomo, R., Tatsumi, T. & Yokoi, T. Beta zeolite: a universally applicable catalyst for the conversion of various types of saccharides into furfurals. *Catal. Sci. Technol.* **5**, 4001–4007 (2015).
5. Corma, A., Domine, M. E., Nemeth, L. & Valencia, S. Al-free Sn-Beta zeolite as a catalyst for the selective reduction of carbonyl compounds (Meerwein-Ponndorf-Verley Reaction). *J. Am. Chem. Soc.* **124**, 3194–3195 (2002).
6. Jennings, J. A., Parkin, S., Munson, E., Delaney, S. P., Calahan, J. L., Isaacs, M., Hong, K. & Crocker, M. Regioselective Baeyer-Villiger oxidation of lignin model compounds with tin beta zeolite catalyst and hydrogen peroxide. *RSC Adv.* **7**, 25987–25997 (2017).
7. Xu, H., Wang, X., Ji, P., Wu, H., Guan, Y. & Wu, P. Hydrothermal synthesis of Sn-Beta zeolites in F⁻-free medium. *Inorg. Chem. Front.* **5**, 2763–2771 (2018).
8. Nemeth, L., Moscoso, J., Erdman, N., Bare, S. R., Oroskar, A., Kelly, S. D., Corma, A., Valencia, S. & Renz, M. Synthesis and characterization of Sn-Beta as a selective oxidation catalyst. in *Recent Advances in the Science and Technology of Zeolites and Related Materials* (eds. van Steen, E., Claeys, M. & Callanan, L. H. B. T.-S. in S. S. and C.) vol. 154 2626–2631 (Elsevier, 2004).
9. Van Der Graaff, W. N. P., Li, G., Mezari, B., Pidko, E. A. & Hensen, E. J. M. Synthesis of Sn-Beta with Exclusive and High Framework Sn Content. *ChemCatChem* **7**, 1152–1160 (2015).
10. Corma, A., Nemeth, L. T., Renz, M. & Valencia, S. Sn-zeolite beta as a heterogeneous chemoselective catalyst for Baeyer-Villiger oxidations. *Nature* **412**, 423–425 (2001).
11. Gounder, R. & Davis, M. E. Beyond shape selective catalysis with zeolites: Hydrophobic void spaces in zeolites enable catalysis in liquid water. *AIChE J.* **59**, 3349–3358 (2013).
12. Eom, I. Y., Lee, S., Hwang, S. Y. & Choi, M. Versatile post-synthetic Sn incorporation into hierarchically porous BEA zeolite for glucose isomerization in 1-butanol. *Microporous Mesoporous Mater.* **307**, 110524 (2020).
13. Serrano, D. P., Van Grieken, R., Sánchez, P., Sanz, R. & Rodríguez, L. Crystallization mechanism of all-silica zeolite beta in fluoride medium. *Microporous Mesoporous Mater.* **46**, 35–46 (2001).
14. Wolf, P., Valla, M., Núñez-Zarur, F., Comas-Vives, A., Rossini, A. J., Firth, C., Kallas, H., Lesage, A., Emsley, L., Copéret, C. & Hermans, I. Correlating Synthetic Methods,

- Morphology, Atomic-Level Structure, and Catalytic Activity of Sn- β Catalysts. *ACS Catal.* **6**, 4047–4063 (2016).
15. Tolborg, S., Katerinopoulou, A., Falcone, D. D., Sádaba, I., Osmundsen, C. M., Davis, R. J., Taarning, E., Fristrup, P. & Holm, M. S. Incorporation of tin affects crystallization, morphology, and crystal composition of Sn-Beta. *J. Mater. Chem. A* **2**, 20252–20262 (2014).
 16. Joshi, H., Ochoa-Hernández, C., Nürenberg, E., Kang, L., Wang, F. R., Weidenthaler, C., Schmidt, W. & Schüth, F. Insights into the mechanochemical synthesis of Sn- β : Solid-state metal incorporation in beta zeolite. *Microporous Mesoporous Mater.* **309**, (2020).
 17. Tang, B., Dai, W., Wu, G., Guan, N., Li, L. & Hunger, M. Improved postsynthesis strategy to Sn-beta zeolites as lewis acid catalysts for the ring-opening hydration of epoxides. *ACS Catal.* **4**, 2801–2810 (2014).
 18. Dapsens, P. Y., Mondelli, C. & Pérez-Ramírez, J. Design of Lewis-acid centres in zeolitic matrices for the conversion of renewables. *Chem. Soc. Rev.* **44**, 7025–7043 (2015).
 19. Dijkmans, J., Dusselier, M., Janssens, W., Trekels, M., Vantomme, A., Breynaert, E., Kirschhock, C. & Sels, B. F. An Inner-/Outer-Sphere Stabilized Sn Active Site in β -Zeolite: Spectroscopic Evidence and Kinetic Consequences. *ACS Catal.* **6**, 31–46 (2016).
 20. Li, P., Liu, G., Wu, H., Liu, Y., Jiang, J. G. & Wu, P. Postsynthesis and selective oxidation properties of nanosized Sn-beta zeolite. *J. Phys. Chem. C* **115**, 3663–3670 (2011).
 21. Cho, H. J., Gould, N. S., Vattipalli, V., Sabnis, S., Chaikittisilp, W., Okubo, T., Xu, B. & Fan, W. Fabrication of hierarchical Lewis acid Sn-BEA with tunable hydrophobicity for cellulosic sugar isomerization. *Microporous Mesoporous Mater.* **278**, 387–396 (2019).
 22. Bregante, D. T., Tan, J. Z., Sutrisno, A. & Flaherty, D. W. Heteroatom substituted zeolite FAU with ultralow Al contents for liquid-phase oxidation catalysis. *Catal. Sci. Technol.* **10**, 635–647 (2020).
 23. Hammond, C., Conrad, S. & Hermans, I. Simple and scalable preparation of highly active lewis acidic Sn- β . *Angew. Chemie - Int. Ed.* **51**, 11736–11739 (2012).
 24. Wolf, P., Hammond, C., Conrad, S. & Hermans, I. Post-synthetic preparation of Sn-, Ti- and Zr-beta: A facile route to water tolerant, highly active Lewis acidic zeolites. *Dalt. Trans.* **43**, 4514–4519 (2014).
 25. Botti, L., Navar, R., Tolborg, S., Martinez-Espin, J. S., Padovan, D., Taarning, E. & Hammond, C. Influence of Composition and Preparation Method on the Continuous Performance of Sn-Beta for Glucose-Fructose Isomerisation. *Top. Catal.* **0**, 0 (2018).
 26. Hammond, C., Padovan, D., Al-Nayili, A., Wells, P. P., Gibson, E. K. & Dimitratos, N. Identification of Active and Spectator Sn Sites in Sn- β Following Solid-State Stannation, and Consequences for Lewis Acid Catalysis. *ChemCatChem* **7**, 3322–3331 (2015).
 27. Nakai, M., Miyake, K., Inoue, R., Ono, K., Al Jabri, H., Hirota, Y., Uchida, Y., Miyamoto, M. & Nishiyama, N. Synthesis of high silica *BEA type ferrisilicate (Fe-Beta) by dry gel conversion method using dealuminated zeolites and its catalytic performance on acetone to olefins (ATO) reaction. *Microporous Mesoporous Mater.* **273**, 189–195 (2019).
 28. Wang, J., Jaenicke, S. & Chuah, G. K. Zirconium-Beta zeolite as a robust catalyst for the transformation of levulinic acid to γ -valerolactone via Meerwein-Ponndorf-Verley reduction. *RSC Adv.* **4**, 13481–13489 (2014).

29. Peeters, E., Pomalaza, G., Khalil, I., Dettaille, A., Debecker, D. P., Douvalis, A. P., Dusselier, M. & Sels, B. F. Highly Dispersed Sn-beta Zeolites as Active Catalysts for Baeyer–Villiger Oxidation: The Role of Mobile, In Situ Sn(II)O Species in Solid-State Stannation. *ACS Catal.* 5984–5998 (2021) doi:10.1021/acscatal.1c00435.
30. Groenewold, G. S., de Jong, W. A., Oomens, J. & Van Stipdonk, M. J. Variable Denticity in Carboxylate Binding to the Uranyl Coordination Complexes. *J. Am. Soc. Mass Spectrom.* **21**, 719–727 (2010).
31. Zeleňák, V., Vargová, Z. & Györyová, K. Correlation of infrared spectra of zinc(II) carboxylates with their structures. *Spectrochim. Acta - Part A Mol. Biomol. Spectrosc.* **66**, 262–272 (2007).
32. Palacios, E. G., Juárez-López, G. & Monhemius, A. J. Infrared spectroscopy of metal carboxylates: II. Analysis of Fe(III), Ni and Zn carboxylate solutions. *Hydrometallurgy* **72**, 139–148 (2004).
33. Stafeeva, V. S., Mitiaev, A. S., Abakumov, A. M., Tsirlin, A. A., Makarevich, A. M. & Antipov, E. V. Crystal structure and chemical bonding in tin(II) acetate. *Polyhedron* **26**, 5365–5369 (2007).
34. Hao, W., Zhang, W., Guo, Z., Ma, J. & Li, R. Mesoporous beta zeolite catalysts for benzylation of naphthalene: Effect of pore structure and acidity. *Catalysts* **8**, (2018).
35. Kuzume, A., Ozawa, M., Tang, Y., Yamada, Y., Haruta, N. & Yamamoto, K. Ultrahigh sensitive Raman spectroscopy for subnanoscience: Direct observation of tin oxide clusters. *Sci. Adv.* **5**, 1–8 (2019).
36. Arai, T. & Kishi, A. The effect of humidity on thermal process of zinc acetate. *Thermochim. Acta* **400**, 175–185 (2003).
37. Donaldson, J. D., Moser, W. & Simpson, W. B. 1147. Tin(II) acetates. *J. Chem. Soc.* 5942 (1964) doi:10.1039/jr9640005942.
38. Wright, P. A., Zhou, W., Pérez-Pariente, J. & Arranz, M. Direct observation of growth defects in zeolite beta. *J. Am. Chem. Soc.* **127**, 494–495 (2005).
39. Zhu, Z., Xu, H., Jiang, J., Wu, H. & Wu, P. Hydrophobic Nanosized All-Silica Beta Zeolite: Efficient Synthesis and Adsorption Application. *ACS Appl. Mater. Interfaces* **9**, 27273–27283 (2017).
40. Cambor, M. A., Corma, A. & Valencia, S. Synthesis in fluoride media and characterisation of aluminosilicate zeolite beta. *J. Mater. Chem.* **8**, 2137–2145 (1998).
41. Zhang, W.-H., Lu, J., Han, B., Li, M., Xiu, J., Ying, P. & Li, C. Direct Synthesis and Characterization of Titanium-Substituted Mesoporous Molecular Sieve SBA-15. *Chem. Mater.* **14**, 3413–3421 (2002).
42. Courtney, T. D., Chang, C. C., Gorte, R. J., Lobo, R. F., Fan, W. & Nikolakis, V. Effect of water treatment on Sn-BEA zeolite: Origin of 960 cm⁻¹ FTIR peak. *Microporous Mesoporous Mater.* **210**, 69–76 (2015).
43. Farges, F., Linnen, R. L. & Brown, G. E. Redox and speciation of tin in hydrous silicate glasses: A comparison with Nb, Ta, Mo and W. *Can. Mineral.* **44**, 795–810 (2006).
44. Park, J.-W. & Park, C.-M. A Fundamental Understanding of Li Insertion/Extraction Behaviors in SnO and SnO₂. *J. Electrochem. Soc.* **162**, A2811–A2816 (2015).

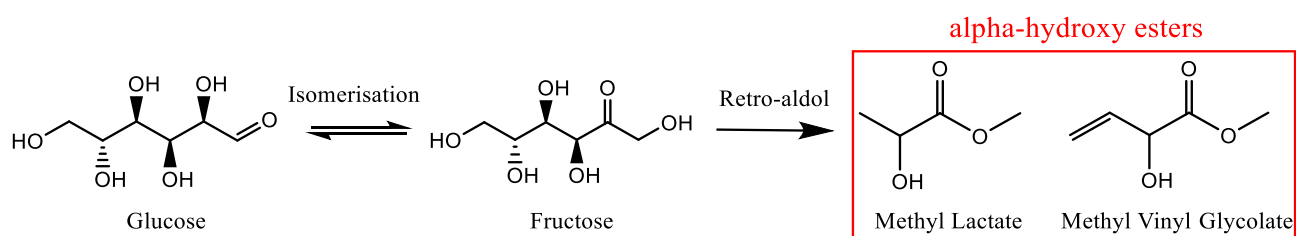
45. Murata, N., Suzuki, T., Kobayashi, M., Togoh, F. & Asakura, K. Characterization of Pt-doped SnO₂ catalyst for a high-performance micro gas sensor. *Phys. Chem. Chem. Phys.* **15**, 17938–17946 (2013).
46. Grandjean, D., Benfield, R. E., Nayral, C., Maisonnat, A. & Chaudret, B. EXAFS and XANES study of a pure and Pd doped novel Sn/SnO_x nanomaterial. *J. Phys. Chem. B* **108**, 8876–8887 (2004).
47. Bare, S. R., Kelly, S. D., Sinkler, W., Low, J. J., Modica, F. S., Valencia, S., Corma, A., Nemeth, L. T., R. Bare, S., D. Kelly, S., Sinkler, W., J. Low, J., S. Modica, F., Valencia, S., Corma, A. & T. Nemeth, L. Uniform catalytic site in Sn-β-zeolite determined using X-ray absorption fine structure. *J. Am. Chem. Soc.* **127**, 12924–12932 (2005).
48. Kolyagin, Y. G., Yakimov, A. V., Tolborg, S., Vennestrøm, P. N. R. & Ivanova, I. I. Application of ¹¹⁹Sn CPMG MAS NMR for Fast Characterization of Sn Sites in Zeolites with Natural ¹¹⁹Sn Isotope Abundance. *J. Phys. Chem. Lett.* **7**, 1249–1253 (2016).
49. Hwang, S. J., Gounder, R., Bhawe, Y., Orazov, M., Bermejo-Deval, R. & Davis, M. E. Solid State NMR Characterization of Sn-Beta Zeolites that Catalyze Glucose Isomerization and Epimerization. *Top. Catal.* **58**, 435–440 (2015).
50. Dai, W., Lei, Q., Wu, G., Guan, N., Hunger, M. & Li, L. Spectroscopic Signature of Lewis Acidic Framework and Extraframework Sn Sites in Beta Zeolites. *ACS Catal.* **10**, 14135–14146 (2020).
51. Bermejo-Deval, R. *et al.* Metalloenzyme-like catalyzed isomerizations of sugars by Lewis acid zeolites. *Proc. Natl. Acad. Sci.* **109**, 9727–9732 (2012).
52. Botti, L., Padovan, D., Navar, R., Tolborg, S., Martinez-Espin, J. S. & Hammond, C. Thermal Regeneration of Sn-Containing Silicates and Consequences for Biomass Upgrading: From Regeneration to Preactivation. *ACS Catal.* **10**, 11545–11555 (2020).
53. Gounder, R. & Davis, M. E. Monosaccharide and disaccharide isomerization over Lewis acid sites in hydrophobic and hydrophilic molecular sieves. *J. Catal.* **308**, 176–188 (2013).
54. Yang, G., Pidko, E. A. & Hensen, E. J. M. The mechanism of glucose isomerization to fructose over Sn-BEA zeolite: A periodic density functional theory study. *ChemSusChem* **6**, 1688–1696 (2013).
55. Boronat, M., Corma, A. & Renz, M. Mechanism of the Meerwein - Ponndorf - Verley - Oppenauer (MPVO) redox equilibrium on Sn- and Zr - Beta zeolite catalysts. *J. Phys. Chem. B* **110**, 21168–21174 (2006).
56. Moliner, M., Roman-Leshkov, Y. & Davis, M. E. Tin-containing zeolites are highly active catalysts for the isomerization of glucose in water. *Proc. Natl. Acad. Sci.* **107**, 6164–6168 (2010).
57. Marianou, A. A., Michailof, C. M., Ipsakis, D. K., Karakoulia, S. A., Kalogiannis, K. G., Yiannoulakis, H., Triantafyllidis, K. S. & Lappas, A. A. Isomerization of Glucose into Fructose over Natural and Synthetic MgO Catalysts. *ACS Sustain. Chem. Eng.* **6**, 16459–16470 (2018).
58. Li, H., Yang, S., Saravanamurugan, S. & Riisager, A. Glucose Isomerization by Enzymes and Chemo-catalysts: Status and Current Advances. *ACS Catal.* **7**, 3010–3029 (2017).

59. Bermejo-Deval, R., Orazov, M., Gounder, R., Hwang, S. J. & Davis, M. E. Active sites in Sn-beta for glucose isomerization to fructose and epimerization to mannose. *ACS Catal.* **4**, 2288–2297 (2014).

Chapter 4. A greener approach to solid-state incorporation: kinetic evaluation of different heteroatom-derived Sn-beta zeolites

4.1 Introduction

Lewis acidic zeolites have emerged as state-of-the-art catalysts for the conversion of biomass to commodity chemicals over the past decade, due to their high levels of activity and selectivity. Zeolites are crystalline microporous materials which can exhibit a wide array of catalytic properties depending on their precise composition (choice of metal, metal loading) and topology.¹⁻⁴ In the context of biomass conversion, the most notable Lewis acidic zeolite is the stannosilicate catalyst Sn-Beta. Sn-Beta is a highly siliceous zeolite within which small amounts of Lewis acidic Sn(IV) atoms are isomorphously substituted into the three-dimensional lattice. The presence of isolated Sn(IV) atoms has been shown to endow the material with discrete levels of Lewis acidity, suitable for the conversion of biomass into various bio-based compounds of industrial interest.⁵⁻⁷ Methyl lactate (ML)⁸ and methyl vinyl glycolate (MVG)⁹, for instance, are the main α -hydroxy esters that can be gathered by the cleavage of glucose when catalysed by Sn-Beta (Scheme 4.1). These compounds are highly sought-after due to their application as monomers for synthesis of bioplastics or as precursor for surfactant production.



Scheme 4.1. Sn-Beta catalysed conversion of glucose to ML and MVG in methanol.

The synthesis of Lewis acidic zeolites, and particularly Sn-Beta, can be achieved by two generalised approaches. The first involves conventional hydrothermal synthesis (bottom-up),

during which an appropriate metal precursor (such as SnCl_4) is added to the synthesis gel, resulting in direct incorporation of the metal into the lattice during crystallisation at elevated temperature and pressure. Alternatively, Sn-Beta can be synthesised by post-synthetic treatment of an existing zeolite (top-down). In such cases, a previously-prepared zeolite is pre-treated to create vacant lattice sites,^{10,11} into which Sn can be incorporated in a subsequent synthetic step.¹² The advantages of such a top-down approach (also known as ‘demetallation-remetallation’) include the avoidance of long crystallisation times, and high degrees of synthetic flexibility in terms of choice of metal and ultimate metal loading.^{13–16} Amongst top-down methods, Solid-State Incorporation (SSI) is an attractive method in which the desired heteroatom is introduced into the vacant tetrahedral framework sites (*vide infra*) by a combination of mechanochemistry and thermal treatment, thereby avoiding the generation of aqueous metal streams.^{17,18}

A common step in all demetallation-remetallation strategies is the preparation of a zeolite containing vacant lattice sites suitable for hosting the desired Lewis acidic heteroatom. This is typically achieved by pre-treating a parent zeolite material at elevated temperature and at concentrated acidic conditions, resulting in the removal of an original heteroatom.^{17,19–22} These harsh conditions represent an important obstacle from an environmental and economic standpoint in the zeolite synthesis process. In fact, the presence of strongly acidic solutions results in the need for acid-resistant reactors and infrastructure, which negatively impacts the economic balance of the process. Furthermore, the acidic effluents require adequate neutralisation prior to disposal, increasing the variable costs in downstream processing alongside generating liquid waste that may be harmful to the environment.

In previous demetallation-remetallation studies, aluminosilicates have almost exclusively been employed as the parent zeolite, primarily due to their commercial availability and the ease of incorporating Al into the lattice of several zeolite structures. However, a variety of other metal-containing zeolites could also act as parent materials for the preparation of post-synthetic Sn-Beta. These include zeolites containing B, Fe and Ga, amongst others, as these heteroatoms are also known to be prone to demetallation at appropriate conditions. However, to the best of our knowledge, no study has investigated the catalytic properties of otherwise-analogous Sn-Beta samples prepared from hydrothermally synthesized zeolite parents containing different original heteroatoms, even though such an approach could provide access to final zeolite materials

exhibiting different levels of performance, and a large discrepancy between the ease of demetallation exists between these different zeolite parents. In particular, B-derived zeolites have been shown to possess the ability to be demetallated at very mild conditions, since boron is primarily trigonally coordinated and is thus susceptible to nucleophilic water attack.^{23–25}

As such, the aim of this study is to investigate the kinetic properties of samples of Sn-Beta samples prepared by SSI starting from analogous hydrothermally synthesised Al-, B-, Fe-, and Ga-Beta zeolites, to determine the impact of using different heteroatom-containing zeolites as parent materials for top-down Sn-Beta synthesis. The performances of the resulting materials are evaluated by investigating the continuous conversion of glucose to α -hydroxy ester compounds (ML and MVG), allowing the activity, selectivity, and stability of the post-synthetic catalysts to be determined.

4.2 Results and discussion

4.2.1 Catalyst synthesis and characterisation

Four analogous Beta zeolites were first prepared by hydrothermal synthesis according to established procedures.²⁶ Within this series, a different metal was incorporated as the heteroatom of each material. Specifically, Al-, B-, Ga- and Fe-Beta zeolites were prepared at a target Si/M molar ratio of 200. Additionally, two metal precursors (Al-, B-) were chosen as candidates to evaluate the impact of initial heteroatom loading in the parent zeolite, and hence, were also prepared at a target Si/M molar ratio of 100.

To determine if all parent Beta zeolites were successfully synthesised, X-ray Diffraction (XRD) patterns were recorded for each sample following removal of the residual Structure Directing Agent (SDA) by calcination. As can be seen (Figure 4.1), XRD patterns of the hydrothermally synthesized Beta zeolites were indistinguishable and were identical in terms of crystallinity, confirming successful synthesis of the Beta framework regardless of the choice of starting heteroatom and metal loading.

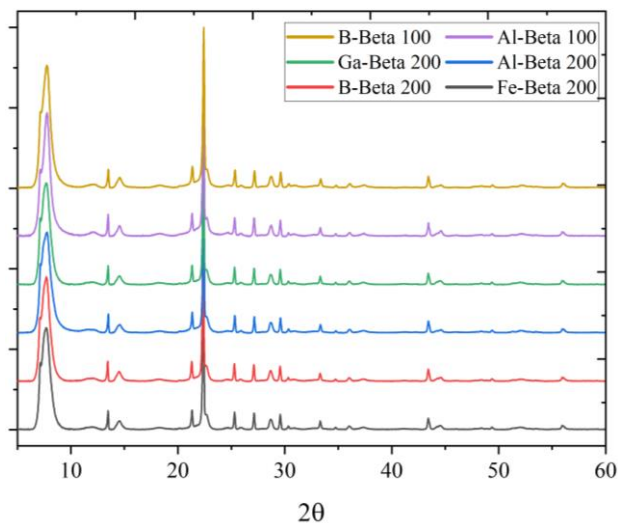


Figure 4.1. X-Ray Diffraction patterns of the hydrothermally synthesized M-beta zeolites.

To further evaluate the properties of each zeolite, Diffuse Reflectance Infrared Fourier Transform Spectroscopy (DRIFTS) was conducted (Figure 4.2 and Table 4.1). All synthesised zeolites presented vibrations typical of the Beta framework.^{27,28} However, both B-Beta zeolites gave rise to additional vibrations at ca. 910-950 and 3734 cm^{-1} indicative of stretching vibrations of Si-O belonging to uncoupled SiO_4 tetrahedra²⁹ and of internal Si-OH groups present at framework defects, respectively.³⁰ While other zeolites presented either one of the vibrations or the other, as shown in Figure 4.2, only in the B-Beta zeolites were both of these aforementioned vibrations present. Al-Beta 100 was interestingly the only zeolite to not present any of these vibrations.

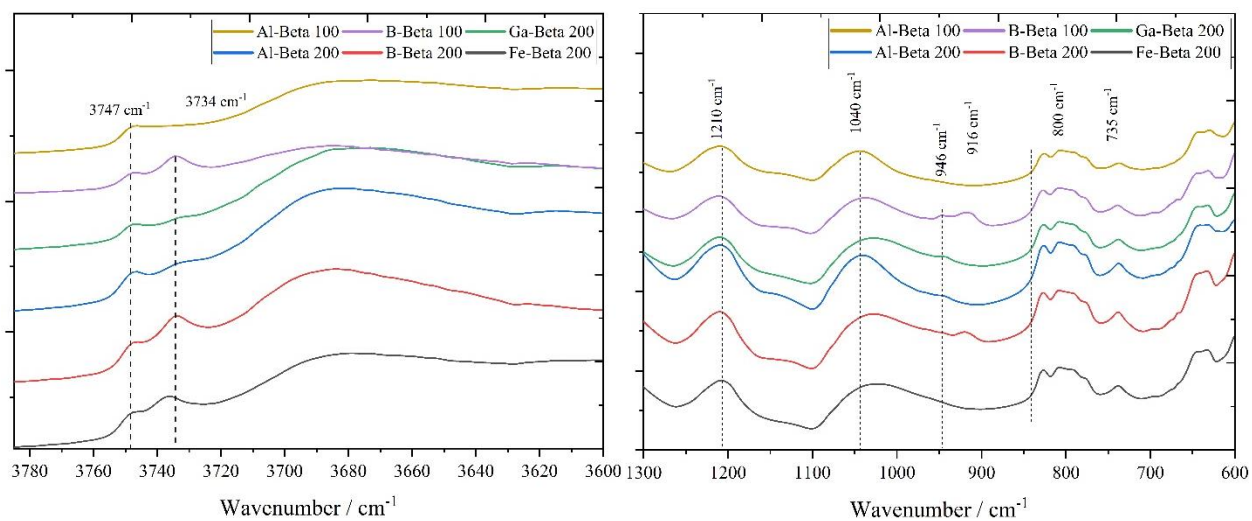


Figure 4.2 DRIFTS spectra of 100 and 200 Si/M ratio parent betas.

Table 4.1. Principal modes and assignments of hydrothermal M-Beta zeolites.

Zeolite	Assignment (cm ⁻¹)						
	$\nu_{\text{O-T-O}}^{\text{Int.}}$ T ^a	$\nu_{(\text{s}) \text{O-T-O}}^{\text{Ext.}}$ O ^b	ν_{SiO_4} (UC) ^c	$\nu_{\text{O-T-O}}^{\text{Int.}}$ O ^d	$\nu_{(\text{as}) \text{O-T-O}}^{\text{Ext.}}$ O ^e	$\nu_{\text{SiOH}}^{\text{Int.}}$ f	$\nu_{\text{SiOH}}^{\text{Term.}}$ h
Al-Beta 100	736	~800	-	1042	1208	-	3748
B-Beta 100	737	~800	916 948	1040	1209	3734	3747
Ga-Beta 200	736	~800	942	1029	1209	-	3748
Al-Beta 200	737	~800	941	1039	1208	-	3747
B-Beta 200	736	~800	917	1033	1208	3733	3747
Fe-Beta 200	736	~800	-	1031	1207	3735	3748

^a Intertetrahedral O-T-O.

^b Symmetric external O-T-O.

^c Vibrations of Si-O belonging to uncoupled SiO₄ tetrahedra.

^d Symmetric internal O-T-O.

^e Asymmetric external O-T-O.

^f Internal Si-OH groups present at framework defects.

^h Terminal Si-OH groups.

To determine the impact of choice of metal on zeolite morphology, Scanning Electron Microscopy (SEM) was performed for the Si/M=200 zeolites. As can be seen in Figure 4.3, all four samples were of comparable morphology and size, and possessed the typical trigonal bipyramidal structure of the Beta zeolite when synthesised in fluoride media.³¹

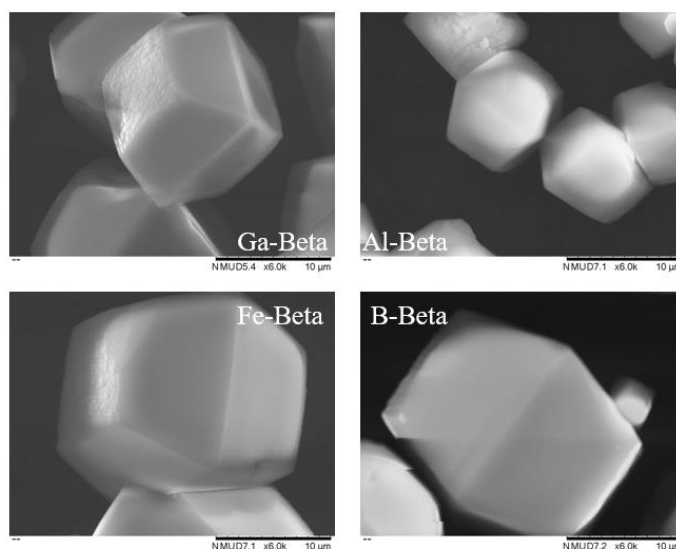


Figure 4.3. SEM images of the hydrothermally synthesised 1Sn-Beta_{M200} zeolites .

Nitrogen physisorption measurements and Inductively Coupled Plasma Mass Spectroscopy (ICP-MS) analyses were also in line with previous studies of Beta zeolites (Table 4.2). All isotherms were typical of microporous zeolites, exhibiting mainly type I character (Figure 4.4), but did present some hysteresis in the higher P/P_0 range. The presence of some mesoporosity was confirmed both by Non-linear Density Functional Theory (NLDFT) pore size distribution, and the t-plot method, as shown in Table 1. All samples presented comparable BET surface areas (S_{BET}) and micropore volumes (V_{pore}), irrespective of the original choice of metal (Table 2). Elemental analysis ICP-MS showed that all parent zeolites contained the anticipated loading of heteroatoms, corresponding to a Si/M molar ratio of 200, with the exception of Ga-Beta, which showed a lower Si/M ratio (152), indicating a higher-than-anticipated concentration of Ga in the zeolitic framework. Taken together, XRD, DRIFTS, N_2 physisorption, SEM and ICP-MS confirm that all zeolites were successfully synthesised, and possessed comparable porosity, topology, and composition, making them suitable parent materials for SSI.

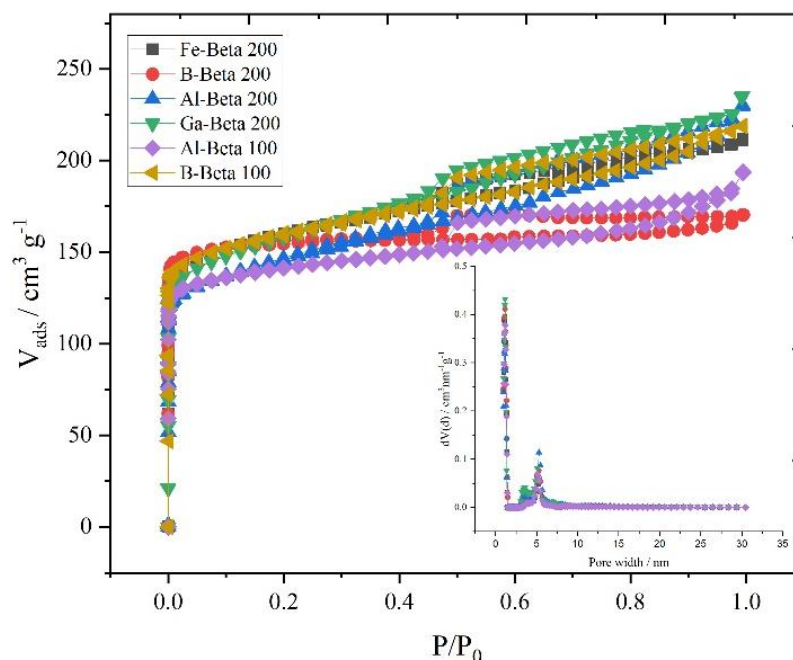


Figure 4.4. Nitrogen sorption isotherm and pore size distribution using DFT model (inset) of parent M-Beta zeolites.

Table 4.2. Elemental and textural characteristics of the hydrothermally synthesised metal Betas and subsequent demetallation. All textural data was performed on the parent metal Betas whereas elemental analysis was performed for both parent and post-demetallation.

Catalyst	Si/M ^a	DeM Si/M ^a	S _{BET} ^b (m ² g ⁻¹)	S _{meso/ext} ^c (m ² g ⁻¹)	V _{pore} ^c (cm ³ g ⁻¹)	V _{micro} ^d (cm ³ g ⁻¹)
Fe-Beta 200	207	—	501	59	0.32	0.23
Ga-Beta 200	152	—	504	83	0.34	0.22
Al-Beta 200	220	—	463	87	0.34	0.20
B-Beta 200	204	—	468	13	0.32	0.22
Al-Beta 100	116	—	453	46	0.34	0.21
B-Beta 100	107	—	499	65	0.33	0.22

^a Measured by ICP-MS analysis

^b Calculated using BET method.

^c Calculated using t-plot method.

^d Calculated from total pore volume.

Following successful synthesis, all parental zeolites were demetallated in order to generate the vacant framework sites required for incorporation of Sn.¹² Although some of the materials can be readily demetallated at mild conditions (particularly B-Beta, which is known to be hydrolytically unstable)^{25,32,33}, for comparative purposes all parent zeolites described in Table 4.1 were demetallated by treatment in HNO₃ according to previous studies (13M HNO₃, 100 °C, 20 h).¹⁹ ICP-MS confirmed the successful extraction of all the original heteroatom content in each sample (Table 4.2) without major changes to the overall crystallinity of the material.

Following successful demetallation, SSI of Sn was undertaken. The synthesis involved mechanochemical treatment of the demetallated zeolites with the appropriate quantity of tin (II) acetate to yield a catalyst with a final metal loading of 1 wt. % Sn, prior to heat treatment at 550 °C for a total of 1 h (ramp in N₂, 1 h air). Final post-synthetic catalysts were labelled as 1Sn-Beta_MX, where M is the metal incorporated and the X value represents the original Si/M molar ratio of the material. An XRD pattern of the final post-synthetic zeolite showed no changes to the overall crystallinity of the material, as is shown in Figure 4.5.

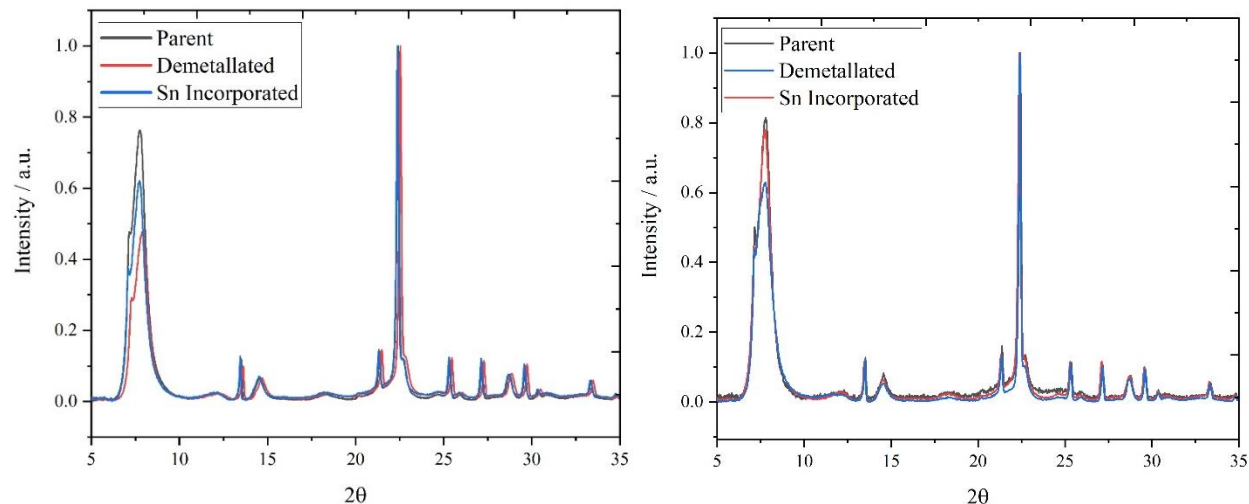


Figure 4.5. Examples of X-Ray Diffraction patterns changes of calcined parent, demetallated, and SSI Sn-Beta of B-Beta zeolite (left) and Al-Beta (Right) .

To provide further insight as to their respective Sn speciation, ^{119}Sn Magic Angle Spinning Nuclear Magnetic Resonance using the Carr-Purcell-Meiboom-Gill echo train acquisition method (^{119}Sn MAS CPMG NMR) was performed. Spectra were measured in Direct Excitation (DE) mode with a relaxation time sufficient to fully relax all the Sn species in a quantitative manner ($t_1 = 135$ s). Samples were compared to a sample of 1Sn-Beta prepared from a commercially available aluminosilicate (ZeolystTM, Si/M = 19), labelled as 1Sn-Beta_{COM19}, which we have extensively characterised over recent years.^{13,34–37}

^{119}Sn DE CPMG MAS NMR samples exhibited resonances at -600 ppm, characteristic of extra-framework SnOx species, as shown in Figure 4.6. It is notable that all samples possessed higher quantities of extra-framework Sn than 1Sn-Beta_{COM19}, indicating SSI to be less successful for the parental materials made by the fluoride-route synthesis. This could be due to i) the lower Si/M ratio of the commercial material resulting in a greater number of vacant framework sites, ii) to the much larger crystallites generated by fluoride media preparation aiding clustering of Sn on the external regions of the material, and/or iii) differences in the chemical properties of the crystallites (hydrophobicity), impacting the incorporation mechanism. Interestingly, out of the hydrothermally synthesised Beta zeolites, the degallinated analogue exhibited a lower quantity of SnOx species. This could result from the initial material having a higher amount of Ga in the zeolite (Table 4.2),

and, as a result, to the material having more vacant framework sites available following demetallation for Sn to incorporate itself more readily.

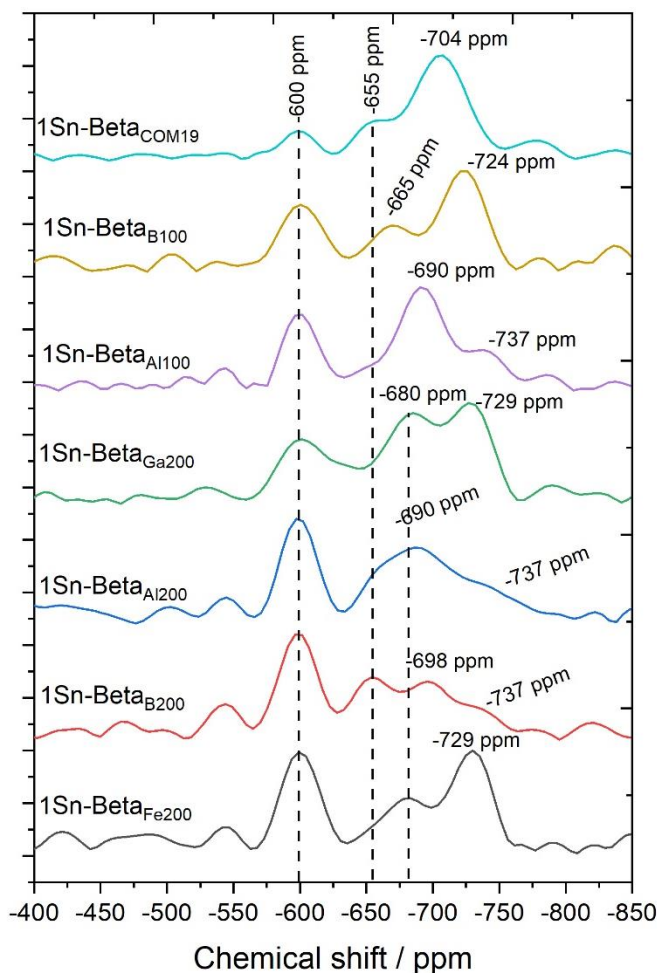


Figure 4.6. ^{119}Sn DE CPMG MAS NMR spectra of all post-synthetic 1Sn-Beta_M zeolites and 1Sn-Beta_{COM19}. Further characterisation details reported in experimental section.

Besides extra-framework SnO_x species, a variety of Sn species that resonate in the range of -650 to -737 ppm were also detected in the analysed samples. These resonances can be attributed to isomorphously substituted Sn-atoms in the zeolitic framework in a hydrated state.^{38,39} Although the materials were synthesized with the same amount of tin precursor, a wide array of species were detected by ^{119}Sn DE CPMG MAS NMR. All samples exhibited resonances attributable to isomorphously-substituted Sn species.³⁷ However, the chemical shift of these varied widely (-730, -700, -680 and -650 ppm) based on the choice of metal and the original Si/M ratio of the material

(Al- and B-derived betas) (Figure 4.7). Unfortunately, the consequences of the Sn chemical shift from a chemical prospective is still not fully understood and the scientific community is still divided on this matter.^{40–43} However, it is commonly accepted that the different chemical shifts in this region are attributed to different Sn(IV) sites which could indicate: i) Sn incorporated in different T-sites of the zeolitic framework; ii) presence of open or closed sites, and; iii) innate zeolitic structure derived from using OH⁻ or F⁻ ions. The plethora of Sn-speciation gathered from these analyses showed how different heteroatom precursors can allow different Sn-site formations, which may be of consequence to kinetic performance.

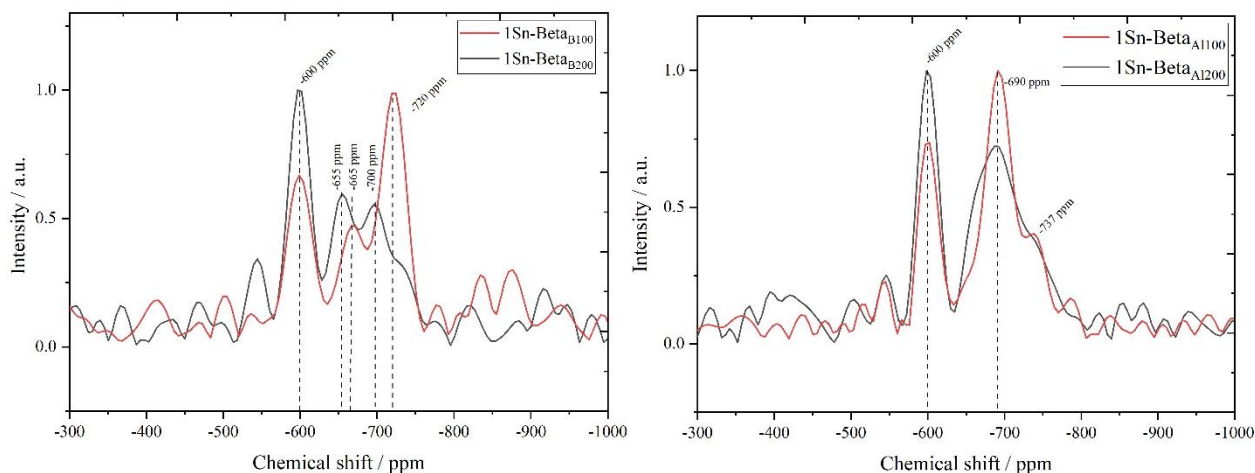


Figure 4.7. ¹¹⁹Sn De CPMG MAS NMR spectra of 1Sn-Beta 100 and 200 for boron (left) and aluminium (right).

4.2.2 Kinetic evaluation of synthesised catalyst materials

4.2.2.1 Retro-aldol fragmentation

To evaluate the performance of the post-synthetic catalysts, the post-synthetic 1Sn-Beta_M series were first screened for activity for the conversion of glucose to α -hydroxy esters (MVG and ML) *via* retro-aldol fragmentation. The samples generated from the hydrothermally synthesised parents were also compared to 1Sn-Beta_{COM19} (preparation steps are detailed in Chapter 2 – Demetallation and SSI), which has been used in our previous studies, to provide context to the experimental trends. Initial experiments were performed at established literature conditions, using a feed of 1

wt. % glucose in methanol and a reaction temperature of 160 °C, and initially undertaken for a period of two hours of operation to gain preliminary insight into the performance of each sample.

The overall carbon balance for the continuous conversion of glucose to α -hydroxy esters gathered at the second hour of time on stream was calculated, as shown in Figure 4.8. All the samples were active for the conversion of glucose, resulting in the production of ML, MVG, fructose and mannose. In line with previous studies, all samples resulted in the formation of by-products not amenable to chromatographic detection, as evidenced by the decrease in carbon balance observed in each reaction.

All the Sn-Beta zeolites synthesised by means of fluoride-obtained precursors presented an improvement in carbon balance, surpassing 1Sn-Beta_{COM19} when it came to its overall carbon balance, which was approximately 70-80 % for the Sn-Beta_M series, and 48 % for the latter. All 1Sn-Beta_M samples were shown to be active and had similar trends in product distribution, with retro-aldol products (ML and MVG) dominating the carbon balance. However, some differences in overall yield and selectivity were detected within the 1Sn-Beta_M series. 1Sn-Beta_{B200} exhibited slightly higher carbon balance due to its enhanced yields of α -hydroxy esters (above 70%), whereas the remaining catalysts exhibited α -hydroxy ester yields between 35-60 %. Interestingly, the overall carbon balance was higher for the samples with an original Si/M of 200 than 100, for both the boron and aluminium parent zeolites. This may indicate a role in product distribution not only in terms of the choice of metal precursors, but also the amount of metal initially incorporated and its number of defect sites.

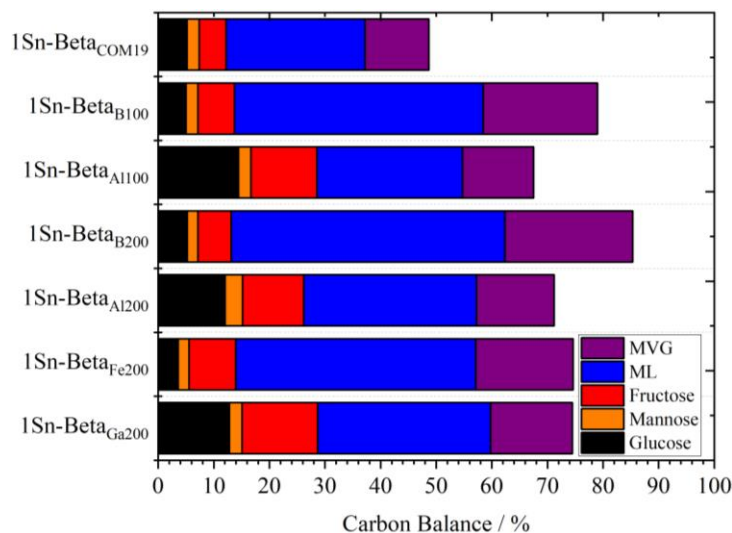


Figure 4.8. Carbon balance and product distribution in post-synthetic zeolites for methyl lactate reaction. Percentages obtained in the second hour or time of maximum methyl lactate obtained. Reaction conditions: 1 wt. % glucose in methanol, 1 mL min⁻¹ flow rate, 100 mg, 160 °C, aliquot obtained in the second hour. Further details reported in kinetic studies.

To acquire a more comprehensive evaluation of the overall catalytic performance and stability of the catalysts, glucose upgrading at 160 °C was performed in continuous flow for approximately 72 h on stream (Figure 4.9). We note that the operational conditions were tuned so that the quantity of substrate converted was sub-maximal at the initial hours of the reaction, thereby allowing intrinsic stability to be evaluated.^{44,45}

Figure 4.9 presents the time on stream data for each catalyst at identical conditions. As can be seen, all catalysts broadly exhibited similar trends during continuous operation, showing a steep deactivation in conversion in the first 20 hours of reaction (from *ca.* 95 % to 50 % conversion), which slightly stabilised thereafter. The loss of activity over the initial reaction period was accompanied by corresponding decreases to the yields of the desired retro-aldol products. Fructose yields increased in this timeframe due to the monosaccharide being an intermediate product in the reaction, and after the first 20 hours of time on stream, fructose became the main reaction product in all cases. However, although all the catalysts showed relatively similar trends kinetically, indicating that the choice of starting heteroatom for the Beta zeolite did not overly affect the performance of the catalyst, more detailed analysis of the time on stream data revealed that the

choice of preparation methodology and starting heteroatom did result in some differences to the activity, selectivity, and stability of the catalyst.

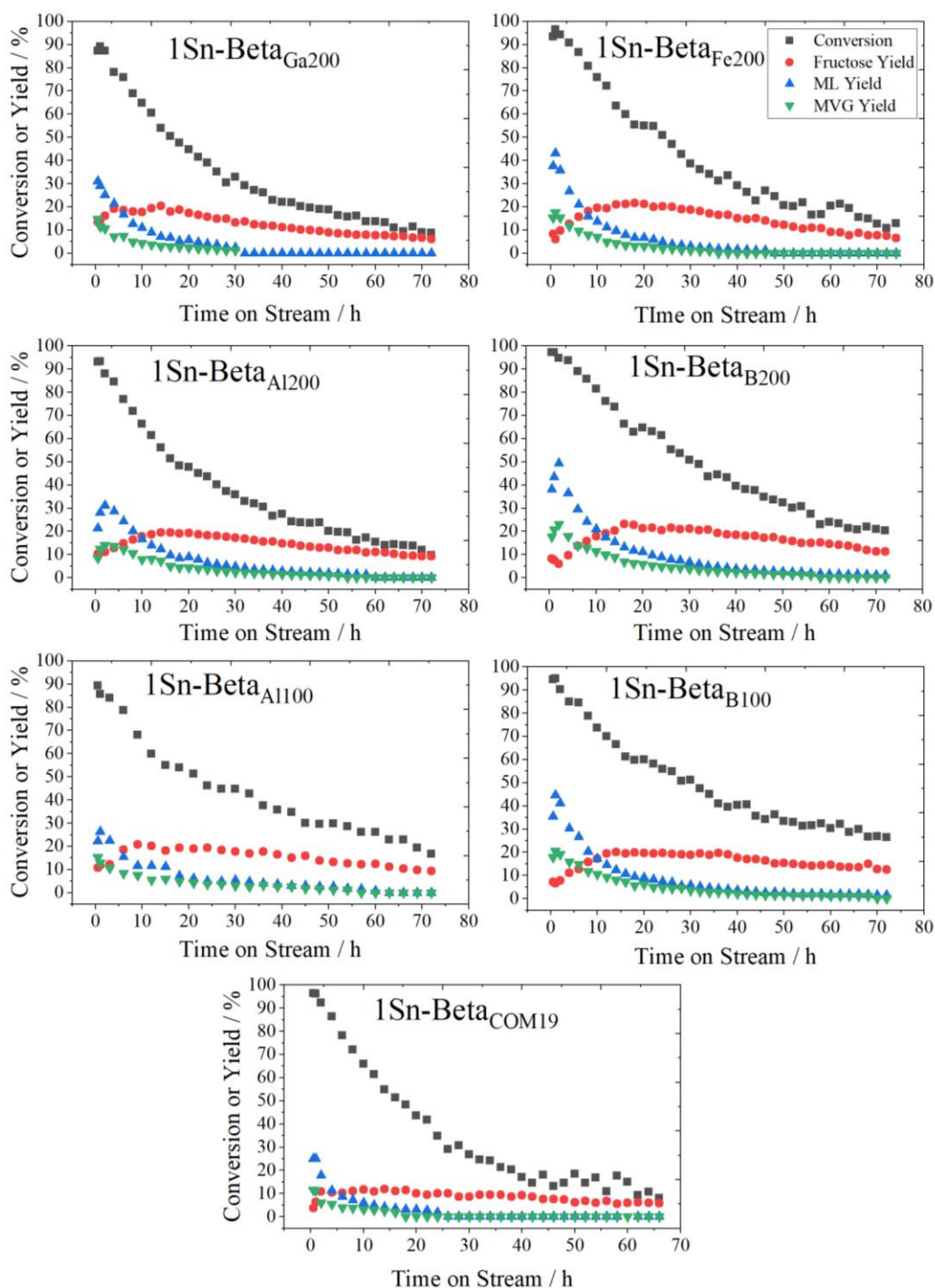


Figure 4.9. Methyl lactate production reaction in continuous flow 1Sn-Beta_{MX} and 1Sn-Beta_{COM19}. Reaction conditions: 1 wt. % glucose in methanol, 1 mL min⁻¹ flow rate, 100 mg, 160 °C. Further details reported in experimental section.

The choice of preparation and starting heteroatom also impacted the selectivity performance of the catalyst. In Figure 4.10, conversion vs. α -hydroxy ester (ML and MVG) selectivity plot is shown. This figure provided a comparison in selectivity at the same rate of conversion for the analysed materials, showing which catalyst possessed higher selectivity towards the desired α -hydroxy esters. Of the catalysts investigated, the ones obtained by means of fluoride-synthesis with Al- and B- as starting heteroatoms showed the best selectivity in terms of α -hydroxy esters, with a selectivity value of approximately 50 % obtained at 80 % substrate conversion. Interestingly, 1Sn-Beta_{COM19} showed much lower selectivity, displaying only 17 % selectivity to the desired esters at 80% conversion, similar selectivity to previously reported reactions.³⁷ Other reports have shown stable activity, with yields within the range of 30-40 % over 400 h using a trickle bed with a flow of 0.85 mL min⁻¹.⁴⁶ 1Sn-Beta_{Al100}, however, showed an unusually low selectivity in contrast to its other 1Sn-Beta_{Al200} analogue. This suggests how the catalyst synthesised by the commercial precursor is prone to catalyse different reactions pathways which are not easily detectable by common chromatographic analysis. Low selectivity can be attributed to various 4+2 carbons (erythrose and glycoaldehyde) or other trioses obtained during the retro-adol fragmentation (*e.g.*, dihydroxyacetone, pyruvaldehyde) as well as furanics (5-HMF)

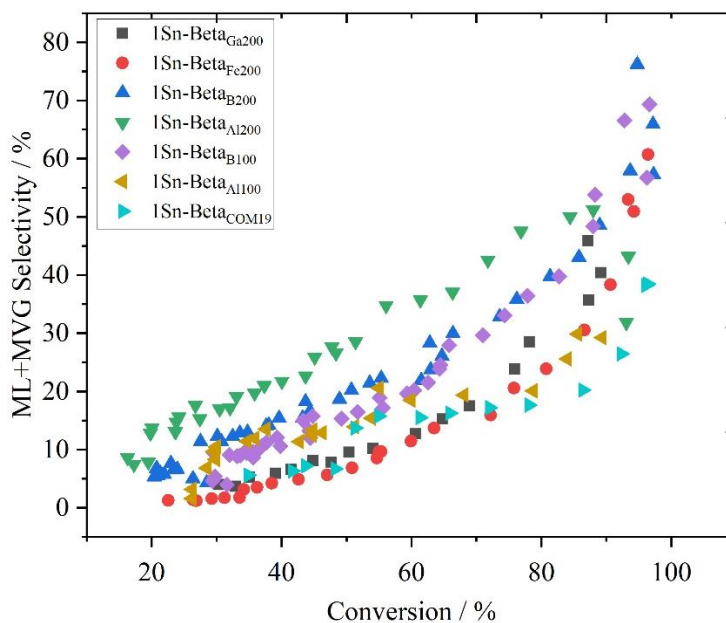


Figure 4.10. Glucose conversion vs. ML+MVG selectivity plot of 1Sn-Beta_{MX} and 1Sn-Beta_{COM19}. Reaction conditions: 1 wt. % glucose in methanol, 1 mL min⁻¹ flow rate, 100 mg, 160 °C. Further details reported in experimental section.

Firstly, analysis of the time on stream data for 1Sn-Beta_{COM19} revealed that the commercially-derived catalyst showed slightly steeper deactivation in the first 20 hours of the reaction (Figure 4.11), meaning that a slight advantage is retained from a stability perspective using a fluoride media-synthesized precursor. To further probe the effect of deactivation, kinetic data was converted to the Levenspiel function to calculate the rate of deactivation in each experiment (k_d), as shown in Figure 4.12 (left). Overall, 1Sn-Beta_{COM19} was shown to have the highest k_d (0.048 h^{-1}) compared to the fluoride mediated synthesised catalysts, indicative of a faster rate of deactivation, showing a *ca.* 60 % higher rate of deactivation.

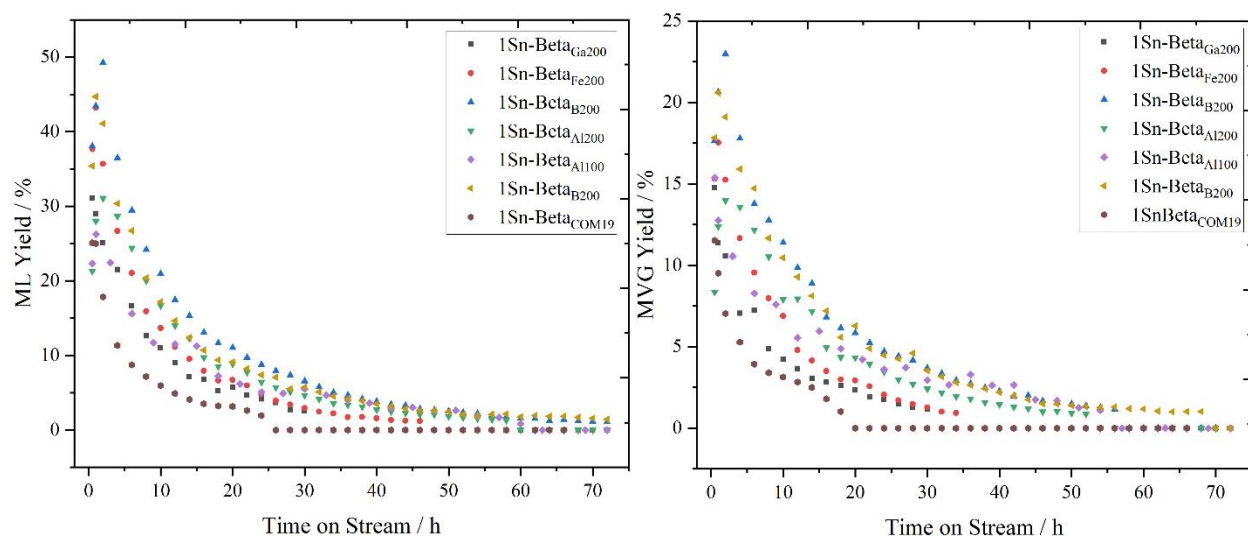


Figure 4.11. Methyl lactate (left) and methyl vinyl glycolate (right) yields for catalysts tested.

Comparable analysis of the fluoride-media catalysts also demonstrated some small differences in stability between the catalyst. For example, 1Sn-Beta_{B100} and 1Sn-Beta_{Al100} presented k_d 's of 0.0284 and 0.0299 h^{-1} , respectively. Furthermore, the remaining Si/M = 200 analogues presented a relatively similar k_d within the range of 0.037 - 0.041 h^{-1} .

To supplement and elucidate the kinetics of deactivation, relative performance *versus* time on stream of the catalysts is shown in Figure 4.12 (right). Relative performance demonstrated an evident advantage in terms of catalytic activity for the 1Sn-Beta_{BX} catalysts throughout the time on stream.

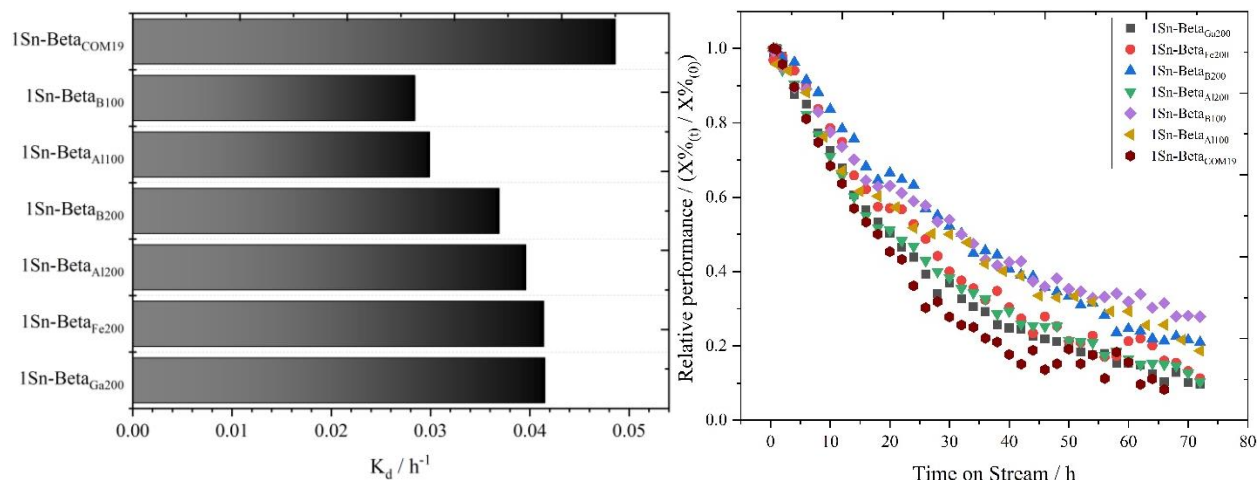


Figure 4.12. Conversion k_d (left) and relative catalytic activity (right) of 1Sn-BetaMX catalysts over time on stream. Reaction conditions: 1 wt. % glucose in methanol, 1 mL min⁻¹ flow rate, 100 mg, 160 °C.

Additionally, a comparison in productivity (g_{ML+MVG}/g_{catalyst}⁻¹ h⁻¹) in α -hydroxy-esters amongst the catalysts obtained by the fluoride-synthesised precursors was calculated. The higher α -hydroxy ester selectivity of 1Sn-Beta_{B200} coupled with its slightly lower rate of deactivation resulted in this catalyst presenting a higher productivity per gram of catalyst towards α -hydroxy-esters (ML and MVG, Figure 4.13). Therefore, this material not only offers the possibility of employing a simpler demetallation procedure, but it delivers slightly better performance in this process.

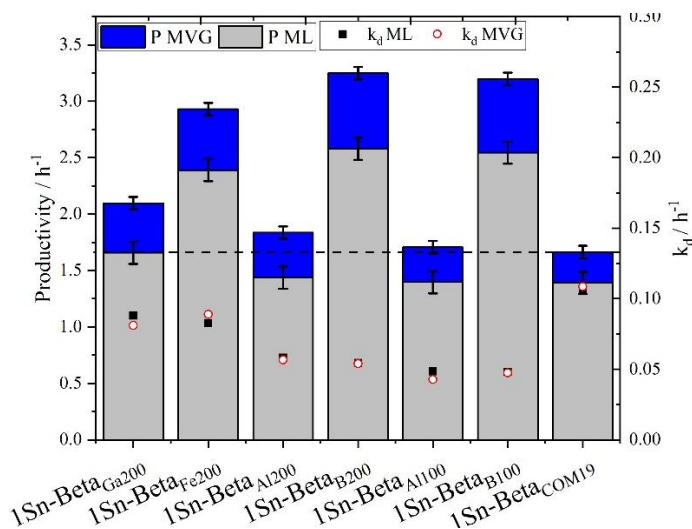


Figure 4.13. Maximum productivity comparison of ML and MVG per gram of catalyst and glucose conversion k_d . Calculations based on the highest yield of respective products (*ca.* 2 h). Dashed line reference to the maximum productivity of 1Sn-Beta_{COM19}. Reaction conditions: 1 wt. % glucose in methanol, 1 mL min⁻¹ flow rate, 100 mg, 160 °C.

4.2.2.2 Effect of water and alkali on kinetic performance

The previous section demonstrated how improvement to the activity (productivity), selectivity and stability of post-synthetic Sn-Beta could be achieved by varying the choice of heteroatom and heteroatom loading in the parent M-Beta zeolite. On a balance of these activity indicators,⁴⁵ the best performance was achieved for Sn-Beta materials prepared from parental borosilicate Beta zeolite (1Sn-Beta_{B200}). However, at the conditions described above, the overall performance yield of retro-aldol products (ML and MVG) obtained from 1Sn-Beta_{B200} in terms of yield of desired retro-aldol products was limited to approximately 50 % at maximal conversion. Although these initial yields are comparable to previous reports addressing the catalytic conversion of glucose to α -hydroxy ester compounds (although in batch),⁴⁷⁻⁵⁰ the selectivity and the lifetime of 1Sn-Beta_{B200} towards the production of the retro-aldol products (ML and MVG) should be improved.

Towards this, previous studies in the literature have shown how a slight change to the reaction conditions can improve the performance of Sn-Beta for the retro-aldol fragmentation of glucose to α -hydroxy ester compounds. In particular, alkali metal chlorides and carbonates have been shown to increase methyl lactate selectivity during the retro-aldol fragmentation of glucose by a pronounced level.⁵¹ Of the alkali salts, potassium salts, such as potassium chloride (KCl), has been shown to be an activity promoter for retro-aldol cleavage reactions, primarily effective in the increase of substrate conversion.^{52,53} In addition, it has been shown that an increase in the stability of the process can be achieved by adding small amounts (1-10 % w/w) of water to the sugar/MeOH feed, by mitigating deactivation under continuous flow reactions.³⁷

Hence, to gauge the potential of these materials with these activity promoters, the retro-aldol fragmentation of glucose over was carried out with the addition of KCl (0.335 mol) directly to the feed solution, rather than being incorporated in the zeolite, along with minuscule amount of water (1:99 H₂O:MeOH v/v). Concentrations used were based on recent studies where addition of water content from 0 % to 1 wt. % was shown to increase the TOF by more than double in contrast to methanol,⁵⁴ whereas high concentrations of alkali have the susceptibility of deactivating all Sn-Beta pathways.⁵² For these final studies, 1Sn-Beta_{B200} was used as catalyst, and its performance was compared to 1Sn-Beta_{COM19} following similar perturbation with water and alkali.

As shown in Figure 4.14, a considerable increase in yield, selectivity, and stability for both catalysts was achieved following addition of applying alkali and water, increasing initial ML

production to ca. 60 and 66 % for 1Sn-Beta_{COM19} and 1Sn-Beta_{B200}, respectively (Figure 4.14, C). The stabilising effect of water instead aided in drastically improving the stability of these materials towards retro-aldol products; in fact, in these kinetic conditions ML and MVG were the main products of reactions for up to 70 hours of time on stream maintaining a yield of 30% towards α -hydroxy-esters.⁵³

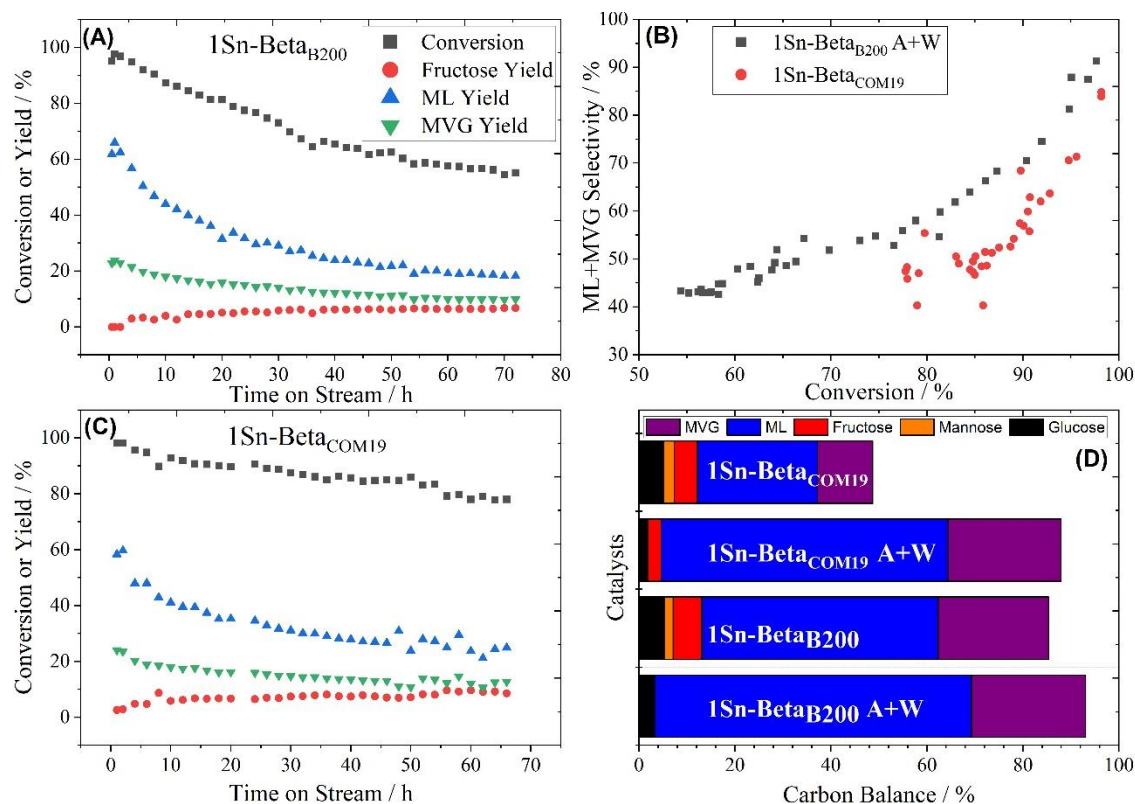


Figure 4.14. Retro-aldol fragmentation of glucose in the presence of water and alkali for 1Sn-Beta_{B200} (A) and 1Sn-Beta_{COM19} (C). Conversion vs. ML+MVG selectivity (B) and initial carbon balance comparison of original ML fragmentation and ML fragmentation using alkali and water (D). Reaction conditions: 160 °C, 20 bar, 1% glucose, solvent: 99% methanol/water (99:1 v/v %) with 50 mg KCl (0.335 mmol) per 2 L of solution, 1 mL/min flow rate per 100 mg of catalyst.

Interestingly, a slightly different response to alkali and water was detected by 1Sn-Beta_{B200} and 1Sn-Beta_{COM19}. Both the catalysts showed an increase in selectivity in the presence of water and alkali, which led to yields in α -hydroxy-esters above 85% for both the materials, in contrast to yields in the region of 50-60 % in the absence of water and alkali. Although both catalysts resulted

in higher yields following addition of water and alkali, Figure 4.14B shows that the selectivity in α -hydroxy-esters at the same rate of conversion was higher for 1Sn-Beta_{B200} throughout the entire reaction. This indicated that a greater quantity of substrate was converted into undesired products throughout the whole reaction with 1Sn-Beta_{COM19}, leading to a loss of valuable substrate that could otherwise have been recycled post reaction. In contrast, the stability of the material over 72 hours of time on stream followed a different trend. In fact, 1Sn-Beta_{B200} experienced a loss of 40% activity over 72 hours of time on stream, whereas the 1Sn-Beta_{COM19} experienced only a loss of 20% of the starting activity. This indicates that the beneficial role played by small quantities of water in this catalytic system is less pronounced for 1Sn-Beta_{B200} than 1Sn-Beta_{COM19}, which likely arises from differences in their hydrophilic properties impacting the uptake of water by the catalyst. Based on this observation, water sorption analysis was conducted on the aforementioned catalysts tested to determine their hydrophobicity.^{55,56,57} As shown in Figure 4.15, water uptake was notably higher in the commercial hydroxide synthesised Beta zeolite compared to the fluoride synthesised zeolites. The decrease in water sorption for the synthesised catalysts is likely a by-product of the fluoride anions present during synthesis, which normally result in the formation of larger, more hydrophobic crystals of micrometre size, which can create diffusional constraints on diffusing molecules and hinder uptake of polar sorbates. F⁻ mineralisers serve as a compensator for the organic structure-directing agent (OSDA) (e.g. tetraethylammonium TEA⁺) and remain occluded within the zeolite, mitigating defect sites to maintain charge neutrality. OH⁻ mineralisers, on the other hand, form framework SiO⁻ defects to compensate TEA⁺ cations which become Si-OH after removing the OSDA.^{55,58,59} The higher hydrophilicity of 1Sn-Beta_{COM19} is likely why the addition of water is more beneficial to this catalyst than to 1Sn-Beta_{B200}. We note that 1Sn-Beta_{B200} showed a higher-than-usual water uptake compared to the as synthesised (defect-free) zeolite synthesised in fluoride media, which is almost certainly due to the initial demetallation procedure creating defect sites, thereby increasing the overall hydrophilicity of the material. This likely account for the slight increase in stability⁴³

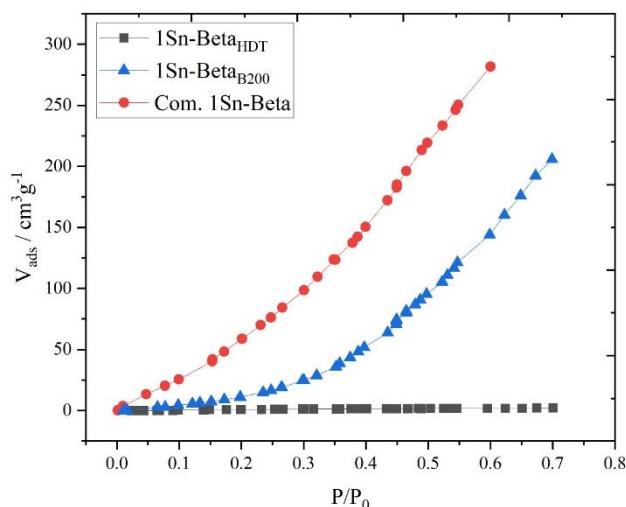


Figure 4.15. Water sorption of catalysts 1Sn-Beta_{COM19} and 1Sn-Beta_{B200}, as well as a hydrothermally synthesised 1Sn-Beta_{HDT}.

4.2.2.3 Low temperature glucose isomerisation

Furthermore, to elucidate more on the differences in catalytic activity of these zeolites, glucose isomerisation was conducted using the six demetallated Sn-Betas where reactions were conducted at the same time length (72 h). All reactions seemingly had relatively similar initial conversion and fructose yield (Figure 4.16), however, there were slight differences in terms of stability, where 1Sn-Beta_{B200} appeared to be the superior for both glucose and fructose, as shown in their respective deactivation constants (K_d) in Figure 4.17 (left).

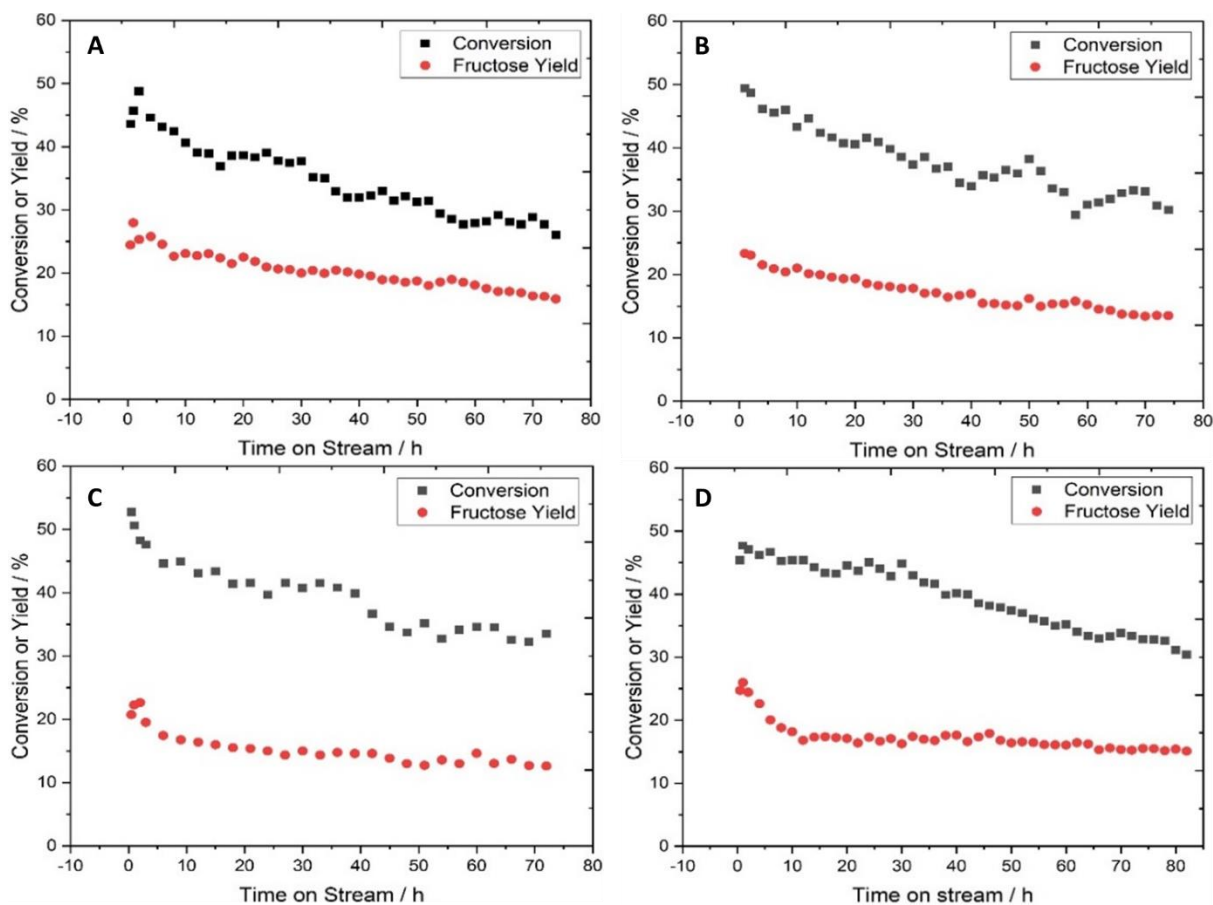


Figure 4.16. Glucose isomerization in continuous flow for 1Sn-Beta_{Ga200} (A), 1Sn-Beta_{Fe200} (B), 1Sn-Beta_{Al200} (C), and 1Sn-Beta_{Ga200} (D). Reaction conditions: 110 °C, 10 bar, 1% glucose, solvent: 99% methanol, 0.65 mL/min flow rate per 100 mg of catalyst.

Regarding the selectivity towards fructose (Figure 4.17, right), 1Sn-Beta_{Ga200} showed higher selectivity than its three other counterparts. It, however, showed a faster rate of deactivate (0.0091 h^{-1}). 1Sn-Beta_{B200} and 1Sn-Beta_{Fe200} had comparable selectivity percentages whereas DeAl Sn-Beta was the lowest of the four. Interestingly, most k_d comparisons showed that glucose was deactivating faster than the drop in glucose. This can imply that while fructose yield is relatively stable, there are other short-lived side reactions that glucose is undergoing in the initial stages. These reactions finish in the first hours, lowering the glucose conversion, hence, simulating a decrease in deactivation when these side reactions have ended, when in fact it is stabilising its conversion and selectivity in the later stages, producing only fructose. Taking into consideration all the parameters ($\text{TOF}_{\text{Glu/Fru}}$, K_d , selectivity), 1Sn-Beta_{B200} had the better performance overall.

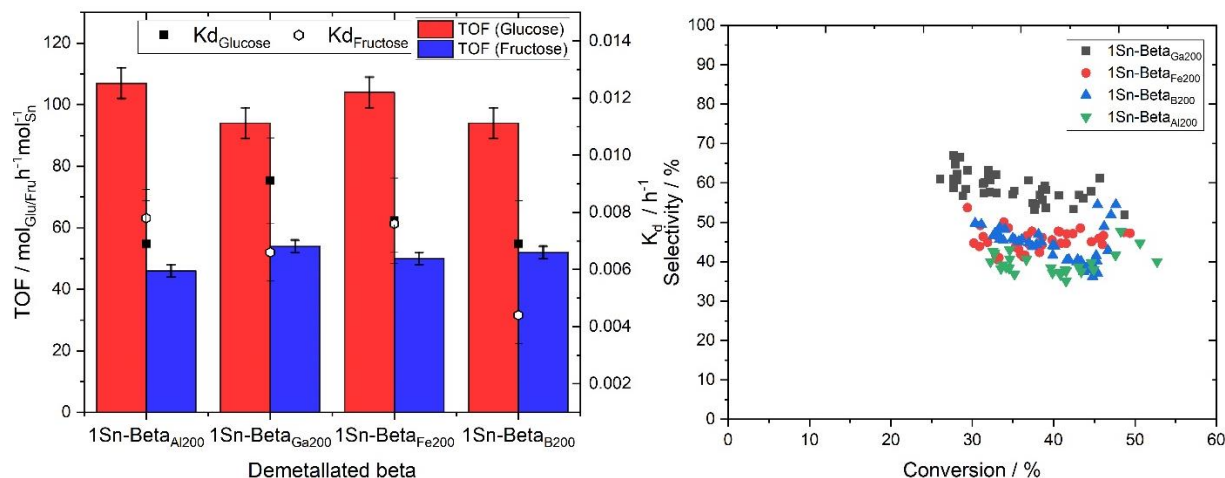


Figure 4.17. Initial TOF (*ca.* 2 h) vs. k_d Glu/Fru of the 200 Si/M beta zeolites (left) and their conversion v. selectivity (right) for glucose isomerization. Reaction conditions: 110 °C, 10 bar, 1% glucose, solvent: 99% methanol, 0.65 mL/min flow rate per 100 mg of catalyst.

As for the preceding reaction, 100 Si/M treated Sn-betas were tested and compared with their 200 Si/M counterparts. When it came to kinetic performance, the catalysts appear to have benefitted in different ways from utilizing more of their initial metal to strip, as can be seen in Figure 18. With an excessive number of sites available for tin to migrate to, seeing as how the wt. % in use for these experiments is 1 wt. %, the metal is able to find a more thermodynamically stable T-site in which to incorporate itself, which can potentially enhance performance or its stability. In the case of 1Sn-Beta_{B100}, however, while not showing any improvement in terms of its conversion, it showed clearly a higher activity as well as stability.

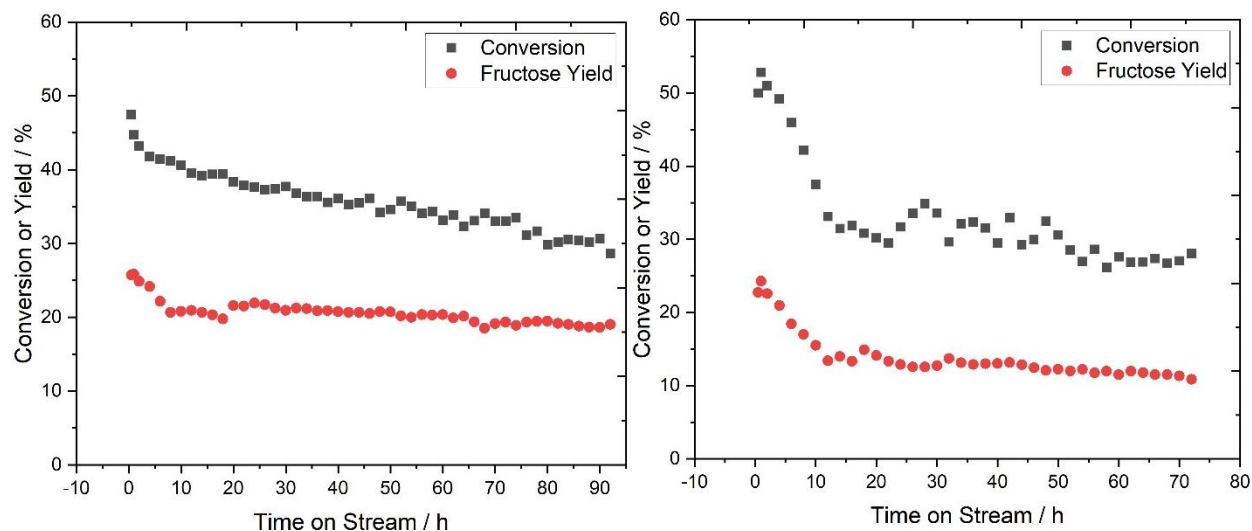


Figure 4.18. Glucose isomerization reaction in continuous flow for 100 Si/M ratio 1Sn-Beta_{B100} (left) and 1Sn-Beta_{A1100}. Reaction conditions: 110 °C, 10 bar, 1% glucose, solvent: 99% methanol, 0.65 mL/min flow rate per 100 mg of catalyst.

1Sn-Beta_{A1100} on the other hand, started relatively equal to its 200 analogue. However, in the first hours it had a sudden decrease on both conversion and yield, having a toll on its overall deactivation rate for both the substrate and product (Figure 4.19, Left). For both B ratios, similar initial TOF for glucose conversion and fructose yield can be seen (Figure 4.19, Left). Despite this, 1Sn-Beta_{B100} had a higher stabilizing point in its fructose yield, *ca.* 20% for 1Sn-Beta_{B100} and *ca.* 15% for 1Sn-Beta_{B200}, improving the catalysts overall selectivity towards this product (Figure 4.19, Right).

Looking towards the catalysts k_d , 1Sn-Beta_{A1100} strangely did not result benefitted from having more vacant sites. While the initial TOF of both 1Sn-Beta_{A1} were similar, the 100 analogue suffered deactivation-wise. This is mainly due to the behaviour of the initial hours, where its trend was precipitous compared to 1Sn-Beta_{B100}. 1Sn-Beta_{B100} additionally showed a considerable improvement in both glucose and fructose k_d , (0.005 and 0.0025 h⁻¹, respectively) compared to 1Sn-Beta_{B200} (0.0079 and 0.0044 h⁻¹, respectively).

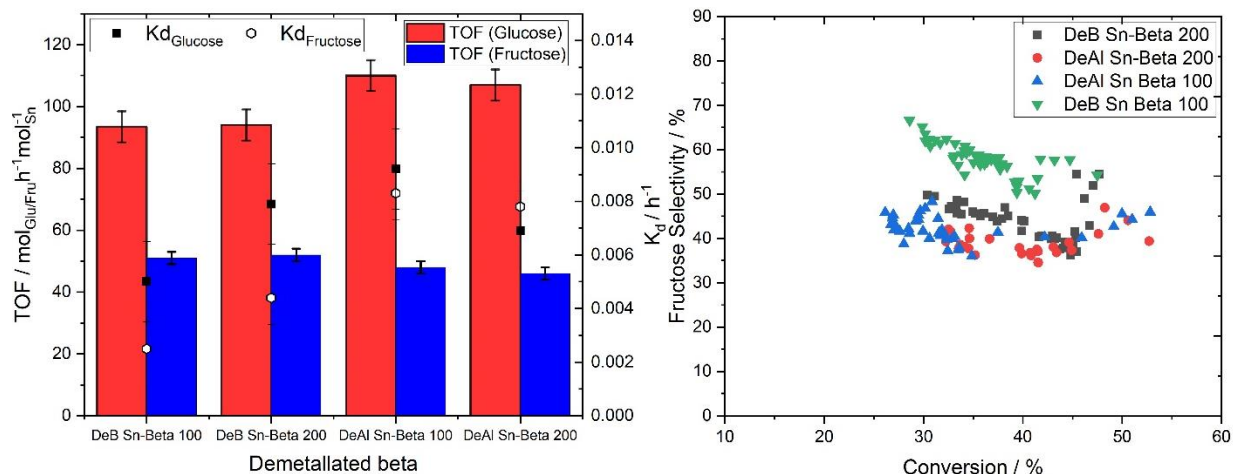


Figure 4.19. Initial TOF v. k_d Glu/Fru of the 100 and 200 Si/M analogues of 1Sn-Beta_B and 1Sn-Beta_{Al} catalysts (left) and their conversion v. selectivity (right) for glucose isomerization.

A proposed theory as to why the deboronated has a slightly more enhanced performance than its counterparts can be due to the T-site placement of boron in the zeolitic framework. The boron species seemingly take place always in “diagonal” sites. Korányi et al⁶⁰ have shown that boron incorporates typically in pairs in the membered rings (MR). While boron is in pairs in the frameworks, metals such as aluminium are not necessarily shown to have this characteristic, showing that there are typically more lone Al atoms than paired ones within a MR.^{60,61} Given the importance of the crystallographic T-sites, this mono- or double isomorphous substitution can greatly determine the kinetic potential of a material; with a double substitution. It has been shown that it has a greater Lewis acidity than having the same two species isolated from one another.⁶² This is one of the main reasons as to why Sn has a higher activity in sugar conversion than other metals such as zirconia and titanium, which are not necessarily stable for double lattice substitution.

In Figure 4.20 we can see the BEA framework where we observe the T2 site, which is considered the most overall T-site in this zeolite. This T-site, along with T1, conform part of the 4-MR in the beta zeolite, secondary building unit in which the boron atom has a preferential substitution.

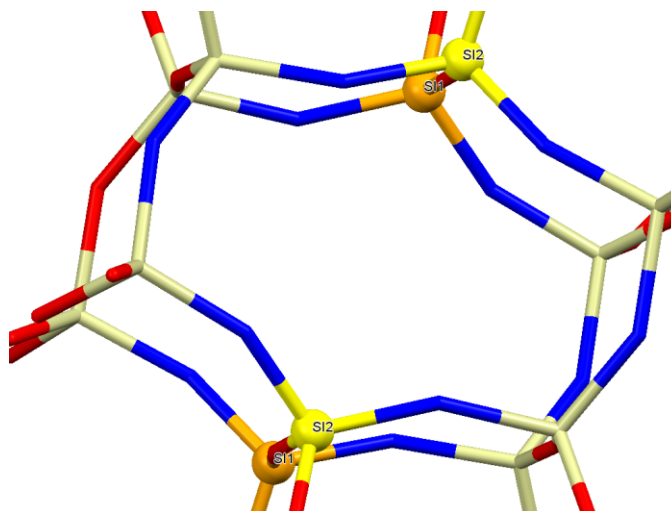


Figure 4.20 Visual representation of T1 and T2 sites of beta zeolite showing a double lattice substitution. Blue coloured bonds show the 6-MR.

4.3 Conclusions

This study focuses on how the choice of starting zeolite material impacts the preparation and performance of post-synthetic Sn-Beta catalysts prepared by Solid State Incorporation. In particular, four different metal-incorporated Beta zeolites (M-Betas, M= Ga-, Fe-, B-, Al-) were explored as parent materials for the top-down synthesis of Sn-Beta via demetallation-remetallation, and their ultimate performances were explored for the retro-aldol fragmentation of glucose to α -hydroxy ester compounds methyl lactate and methyl vinyl glycolate. ^{119}Sn MAS DE CPMG NMR, alongside XRD, IR and porosimetry analysis, demonstrated the successful synthesis of Sn-Beta in all cases, albeit with a wide array of different isomorphously-substituted Sn species being present in each sample.

The kinetic performance of each catalyst was evaluated in continuous flow, and revealed that all the synthesised materials were active for this reaction, and hence, that different metal precursors can be employed as starting materials for the synthesis of Sn-Beta by SSI. The catalyst synthesised from the B-Beta starting material shows the best performance in term of productivity in α -hydroxy-esters, in particular following the addition of alkali additives to the reaction feed.

Based on these findings, we can conclude that B-derived zeolites are a feasible alternative to Al-containing zeolites for Solid State Incorporation. This finding may be advantageous in the long term, since the hydrolytically unstable nature of borosilicate zeolites may prove to be easier to demetallated than their aluminosilicate analogues.

4.4 References

1. Pachamuthu, M. P., Shanthi, K., Luque, R. & Ramanathan, A. SnTUD-1: A solid acid catalyst for three component coupling reactions at room temperature. *Green Chem.* **15**, 2158–2166 (2013).
2. Corma, A., Domine, M. E., Nemeth, L. & Valencia, S. Al-free Sn-Beta zeolite as a catalyst for the selective reduction of carbonyl compounds (Meerwein-Ponndorf-Verley Reaction). *J. Am. Chem. Soc.* **124**, 3194–3195 (2002).
3. Takahara, I., Saito, M., Inaba, M. & Murata, K. Dehydration of ethanol into ethylene over solid acid catalysts. *Catal. Letters* **105**, 249–252 (2005).
4. Esteban, J., Yustos, P. & Ladero, M. Catalytic processes from biomass-derived hexoses and pentoses: A recent literature overview. *Catalysts* **8**, 1–39 (2018).
5. Li, Y. P., Head-Gordon, M. & Bell, A. T. Analysis of the reaction mechanism and catalytic activity of metal-substituted beta zeolite for the isomerization of glucose to fructose. *ACS Catal.* **4**, 1537–1545 (2014).
6. Moliner, M., Roman-Leshkov, Y. & Davis, M. E. Tin-containing zeolites are highly active catalysts for the isomerization of glucose in water. *Proc. Natl. Acad. Sci.* **107**, 6164–6168 (2010).
7. Zhang, J. *et al.* Hierarchical Sn-Beta Zeolite Catalyst for the Conversion of Sugars to Alkyl Lactates. *ACS Sustain. Chem. Eng.* **5**, 3123–3131 (2017).
8. Yang, X. *et al.* Synthesis of Sn-Containing Nanosized Beta Zeolite As Efficient Catalyst for Transformation of Glucose to Methyl Lactate. *ACS Sustain. Chem. Eng.* **6**, 8256–8265 (2018).
9. De Clercq, R. *et al.* Confinement Effects in Lewis Acid-Catalyzed Sugar Conversion: Steering Toward Functional Polyester Building Blocks. *ACS Catal.* **5**, 5803–5811 (2015).
10. Pérez-Ramírez, J. *et al.* Evolution of isomorphously substituted iron zeolites during activation: Comparison of Fe-beta and Fe-ZSM-5. *J. Catal.* **232**, 318–334 (2005).
11. Müller, M., Harvey, G. & Prins, R. Comparison of the dealumination of zeolites beta, mordenite, ZSM-5 and ferrierite by thermal treatment, leaching with oxalic acid and treatment with SiCl₄ by ¹H, ²⁹Si and ²⁷Al MAS NMR. *Microporous Mesoporous Mater.* **34**, 135–147 (2000).
12. Wolf, P., Hammond, C., Conrad, S. & Hermans, I. Post-synthetic preparation of Sn-, Ti- and Zr-beta: A facile route to water tolerant, highly active Lewis acidic zeolites. *Dalt. Trans.* **43**, 4514–4519 (2014).
13. Botti, L. *et al.* Influence of Composition and Preparation Method on the Continuous Performance of Sn-Beta for Glucose-Fructose Isomerisation. *Top. Catal.* **62**, 1178–1191 (2019).

14. Losch, P. *et al.* Mesoporous ZSM-5 zeolites in acid catalysis: Top-down vs. bottom-up approach. *Catalysts* **7**, (2017).
15. Tang, B. *et al.* Mesoporous Zr-Beta zeolites prepared by a post-synthetic strategy as a robust Lewis acid catalyst for the ring-opening aminolysis of epoxides. *Green Chem.* **17**, 1744–1755 (2015).
16. Tang, B. *et al.* A procedure for the preparation of Ti-Beta zeolites for catalytic epoxidation with hydrogen peroxide. *Green Chem.* **16**, 2281–2291 (2014).
17. van der Graaff, W. N. P. *et al.* Deactivation of Sn-Beta during carbohydrate conversion. *Appl. Catal. A Gen.* **564**, 113–122 (2018).
18. Kucherov, A. V. & Slinkin, A. A. Solid-state reaction as a way to transition metal cation introduction into high-silica zeolites. *J. Mol. Catal.* **90**, 323–354 (1994).
19. Hammond, C., Conrad, S. & Hermans, I. Simple and scalable preparation of highly active lewis acidic Sn- β . *Angew. Chemie - Int. Ed.* **51**, 11736–11739 (2012).
20. Van Bokhoven, J. A., Koningsberger, D. C., Kunkeler, P., Van Bekkum, H. & Kentgens, A. P. M. Stepwise dealumination of zeolite Beta at specific T-sites observed with ^{27}Al MAS and ^{27}Al MQ MAS NMR. *J. Am. Chem. Soc.* **122**, 12842–12847 (2000).
21. Escola, J. M. *et al.* Synthesis of hierarchical Beta zeolite with uniform mesopores: Effect on its catalytic activity for veratrole acylation. *Catal. Today* **304**, 89–96 (2018).
22. Zhu, Z., Xu, H., Jiang, J., Guan, Y. & Wu, P. Sn-Beta zeolite derived from a precursor synthesized via an organotemplate-free route as efficient Lewis acid catalyst. *Appl. Catal. A Gen.* **556**, 52–63 (2018).
23. Koller, H. *et al.* Post-Synthesis Conversion of Borosilicate Zeolite Beta to an Aluminosilicate with Isolated Acid Sites: A Quantitative Distance Analysis by Solid-State NMR. *J. Phys. Chem. C* **120**, 9811–9820 (2016).
24. Ranoux, A., Djanashvili, K., Arends, I. W. C. E. & Hanefeld, U. B-TUD-1: A versatile mesoporous catalyst. *RSC Adv.* **3**, 21524–21534 (2013).
25. de Ruiter, R., Kentgens, A. P. M., Grootendorst, J., Jansen, J. C. & van Bekkum, H. Calcination and deboronation of [B]-MFI single crystals. *Zeolites* **13**, 128–138 (1993).
26. Tolborg, S. *et al.* Incorporation of tin affects crystallization, morphology, and crystal composition of Sn-Beta. *J. Mater. Chem. A* **2**, 20252–20262 (2014).
27. Flanigen, E. M., Khatami, H. & Szymanski, H. A. Infrared Structural Studies of Zeolite Frameworks. in *Molecular Sieve Zeolites-I* **101**, 16–201 (AMERICAN CHEMICAL SOCIETY, 1974).
28. Tomlinson, S. R., McGown, T., Schlup, J. R. & Anthony, J. L. Infrared Spectroscopic Characterization of CIT-6 and a Family of *BEA Zeolites. *Int. J. Spectrosc.* **2013**, 1–7 (2013).
29. Chalupka, K. *et al.* Dealuminated Beta Zeolite Modified by Alkaline Earth Metals. *J. Chem.* **2018**, (2018).
30. Kiricsi, I. *et al.* Progress toward understanding zeolite β acidity: An IR and ^{27}Al NMR spectroscopic study. *J. Phys. Chem.* **98**, 4627–4634 (1994).
31. Xia, Q. H., Song, J., Kawi, S. & Li, L. L. Characterization and morphological control of β zeolite synthesized in a fluoride medium. *Stud. Surf. Sci. Catal.* **154 A**, 195–202 (2004).
32. Tong, H. T. T. & Koller, H. Control of Al for B framework substitution in zeolite Beta by counterions. *Microporous Mesoporous Mater.* **148**, 80–87 (2012).
33. Hamoudi, S., Larachi, F. & Sayari, A. Synthesis and characterization of titanium-substituted large pore SSZ-42 zeolite. *Catal. Letters* **77**, 227–231 (2001).

34. Kolyagin, Y. G., Yakimov, A. V., Tolborg, S., Vennestrøm, P. N. R. & Ivanova, I. I. Application of ^{119}Sn CPMG MAS NMR for Fast Characterization of Sn Sites in Zeolites with Natural ^{119}Sn Isotope Abundance. *J. Phys. Chem. Lett.* **7**, 1249–1253 (2016).
35. Bermejo-Deval, R., Gounder, R. & Davis, M. E. Framework and extraframework tin sites in zeolite beta react glucose differently. *ACS Catal.* **2**, 2705–2713 (2012).
36. Padovan, D., Botti, L. & Hammond, C. Active Site Hydration Governs the Stability of Sn-Beta during Continuous Glucose Conversion. *ACS Catal.* **8**, 7131–7140 (2018).
37. Wolf, P. *et al.* Correlating Synthetic Methods, Morphology, Atomic-Level Structure, and Catalytic Activity of Sn- β Catalysts. *ACS Catal.* **6**, 4047–4063 (2016).
38. Hwang, S. J. *et al.* Solid State NMR Characterization of Sn-Beta Zeolites that Catalyze Glucose Isomerization and Epimerization. *Top. Catal.* **58**, 435–440 (2015).
39. Kolyagin, Y. G., Yakimov, A. V., Tolborg, S., Vennestrøm, P. N. R. & Ivanova, I. I. Direct Observation of Tin in Different T-Sites of Sn-BEA by One- and Two-Dimensional ^{119}Sn MAS NMR Spectroscopy. *J. Phys. Chem. Lett.* **9**, 3738–3743 (2018).
40. Corma, A., Nemeth, L. T., Renz, M. & Valencia, S. Sn-zeolite beta as a heterogeneous chemoselective catalyst for Baeyer-Villiger oxidations. *Nature* **412**, 423–425 (2001).
41. Scott, S. L. A Matter of Life(time) and Death. *ACS Catal.* **8**, 8597–8599 (2018).
42. Hammond, C. Intensification studies of heterogeneous catalysts: Probing and overcoming catalyst deactivation during liquid phase operation. *Green Chem.* **19**, 2711–2728 (2017).
43. Tolborg, S. *et al.* Tin-containing Silicates: Alkali Salts Improve Methyl Lactate Yield from Sugars. doi:10.1002/cssc.201403057
44. Elliot, S. G., Tolborg, S., Madsen, R., Taarning, E. & Meier, S. Effects of Alkali-Metal Ions and Counter Ions in Sn-Beta-Catalyzed Carbohydrate Conversion. *ChemSusChem* **11**, 1198–1203 (2018).
45. Elliot, S. G. *et al.* Stoichiometric active site modification observed by alkali ion titrations of Sn-Beta. *Catal. Sci. Technol.* **9**, 4339–4346 (2019).
46. Padovan, D. *et al.* Overcoming catalyst deactivation during the continuous conversion of sugars to chemicals: Maximising the performance of Sn-Beta with a little drop of water. *React. Chem. Eng.* **3**, 155–163 (2018).
47. Vega-Vila, J. C., Harris, J. W. & Gounder, R. Controlled insertion of tin atoms into zeolite framework vacancies and consequences for glucose isomerization catalysis. *J. Catal.* **344**, 108–120 (2016).
48. Humplik, T., Raj, R., Maroo, S. C., Laoui, T. & Wang, E. N. Effect of hydrophilic defects on water transport in MFI zeolites. *Langmuir* **30**, 6446–6453 (2014).
49. Zhu, Z., Xu, H., Jiang, J., Wu, H. & Wu, P. Hydrophobic Nanosized All-Silica Beta Zeolite: Efficient Synthesis and Adsorption Application. *ACS Appl. Mater. Interfaces* **9**, 27273–27283 (2017).
50. Gounder, R. & Davis, M. E. Beyond shape selective catalysis with zeolites: Hydrophobic void spaces in zeolites enable catalysis in liquid water. *AIChE J.* **59**, 3349–3358 (2013).
51. Fickel, D. W., Shough, A. M., Doren, D. J. & Lobo, R. F. High-temperature dehydrogenation of defective silicalites. *Microporous Mesoporous Mater.* **129**, 156–163 (2010).
52. Korányi, T. I. & Nagy, J. B. Distribution of aluminum in different periodical building units of MOR and BEA zeolites. *J. Phys. Chem. B* **109**, 15791–15797 (2005).
53. Korányi, T. I., Föttinger, K., Vinek, H. & Nagy, J. B. Characterization of aluminium siting in MOR and BEA zeolites by ^{27}Al , ^{29}Si NMR and FTIR spectroscopy. in *Molecular*

- Sieves: From Basic Research to Industrial Applications* (eds. Čejka, J., Žilková, N. & Nachtigall, P. B. T.-S. in S. S. and C.) **158**, 765–772 (Elsevier, 2005).
54. Yang, G., Pidko, E. A. & Hensen, E. J. M. Structure, stability, and lewis acidity of mono and double Ti, Zr, and Sn framework substitutions in BEA zeolites: A periodic density functional theory study. *J. Phys. Chem. C* **117**, 3976–3986 (2013).

Chapter 5. Tailoring of beta zeolites with post-synthetic modifications using pore-directing agents for sugar valorisation

5.1 Introduction

Conventional zeolites are microporous heterogeneous materials, which comprise of 8 to 12 membered rings (MR) pore channels. Due to their capability of incorporating a variety of metal heteroatoms, these inorganic solids have been used in a plethora of catalytic processes, such as Baeyer-Villiger oxidation (BVO),¹ dehydrogenation,² catalytic reduction of NO_x,³ and many more.⁴⁻⁶ Despite the wide applications that these materials have, they can also suffer from diffusion limitations due to their previously mentioned microporous nature.⁷ This limitation can also negatively affect the catalysts' lifetime, due to the material being more prone to pore fouling, or may result in the catalyst exhibiting no activity whatsoever substrate due to steric hindrances.⁸

Hierarchical zeolites consist in the creation of mesopores or macropores in an already microporous zeolite, giving the material a bimodal distribution of pore sizes. Hence, they theoretically maintain the benefits of the microporous active site environment (*e.g.*, high activity and shape selectivity), whilst offering improved mass transfer properties. Such hierarchical zeolites can be prepared in several ways. Some procedures involve in creating these mesopores during the synthesis (bottom-up) of the zeolite, such as carbon-,⁹ cellulose-,¹⁰ or CaCO₃-templating.¹¹ Post-synthetic treatments (top-down) such as demetallation (dealumination, desilication) involve leaching with highly acidic or basic solutions. Desilication, for instance, is created by partial dissolution of the zeolite framework using an alkaline solution, whereas to remove aluminium from the framework (Figure 5.1) requires use of an acidic medium.^{12,13} Advantages of the top-down approach are the relative ease of performing it, the high reproducibility and the fact it is more cost-effective than any of the bottom-up approaches.⁷

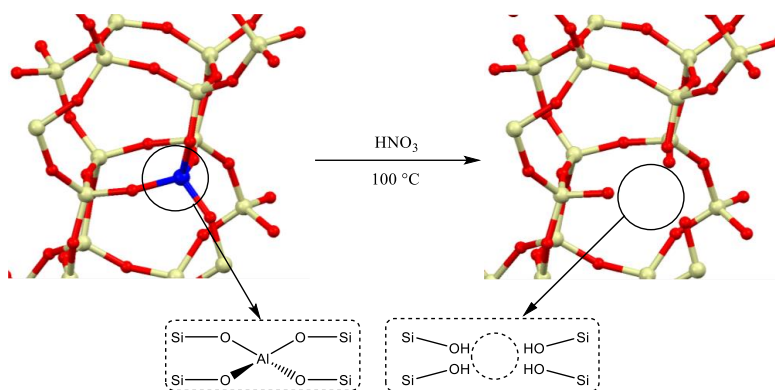


Figure 5.1. Dealumination of zeolite framework.

Desilication procedures can also be accompanied by the insertion of a mesoporegens as a pore-directing agent (PDA).^{9,14} This can aid in the procedure by mitigating a high degree of silicon dissolution, preventing the zeolitic structure from collapsing, as well as creating a more uniform distribution of mesopores. Typical PDAs consist of cationic surfactants (tetraalkylammoniums – typically 10 to 20 carbon atoms), anionic surfactants (*e.g.*, hexadecanesulfonic acid)¹⁵ and non-ionic surfactants (amines). One of the most used and studied consist of cetyltrimethylammonium (CTA⁺), which is also applied in the formation of various other zeolite materials.^{16,17} These PDA form micelles which are adhered to the framework while undergoing base leaching, protecting vicinal silicon groups, as shown in Figure 5.2.

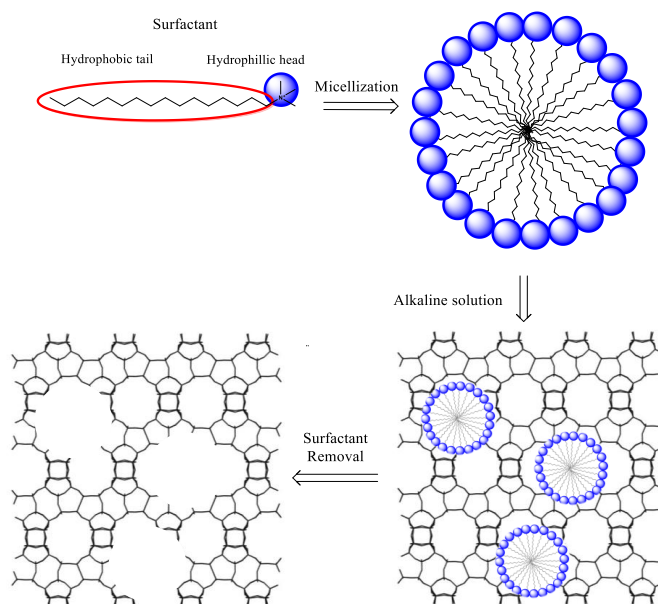


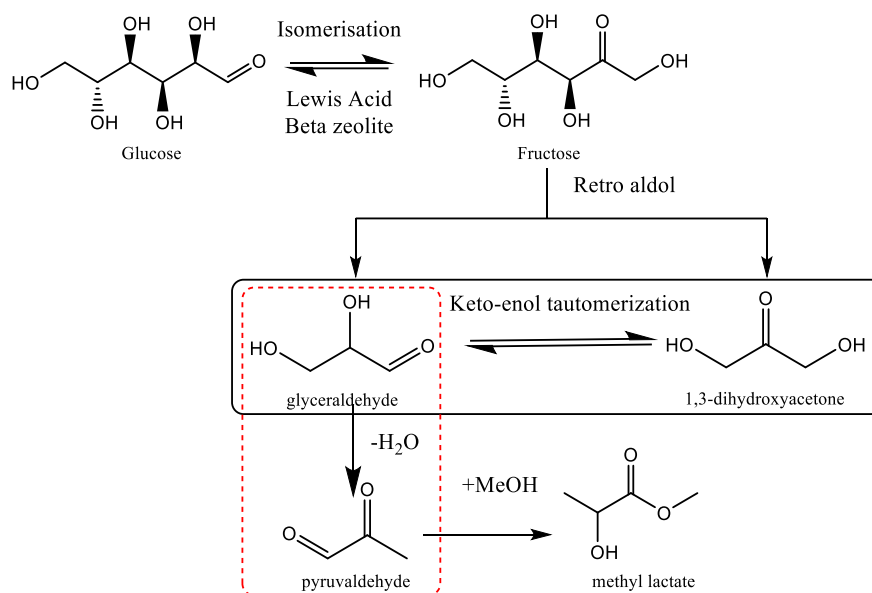
Figure 5.2. Use of PDA for base leaching.

Desilication has been typically carried out for hydroxide-assisted (OH^- as mineralising agent) zeolites.^{18–21} Nevertheless, unlike OH^- -assisted zeolites, zeolites made in fluoride (F^-) media may afford the incorporation of different heteroatoms other than silicon and aluminium into the framework.²² The use of F^- as a mineralising agent, however, comes with setbacks. F^- anions typically work at low pH (*ca.* 5) which favours slow growth.²³ This suppression of the nucleation step increases the crystal size of the zeolite to micron-sized levels.^{24–26} This increase in crystal size can create diffusional limitations, making smaller crystal size catalysts more favourable to reduce mass transfer resistance.^{27–30} The incorporation of heteroatoms along with the introduction of mesoporous in the zeolite can potentially lead to catalytically more active zeolites along with eliminating said mass transfer limitations.^{33–35} Herein, post-synthetic treatment of fluoride-mediated zeolites will be carried out to test the effectiveness on these particular zeolites.

The creation of hierarchical zeolites has been shown to offer improved rates of deactivation,³⁶ having shown improvements in hydrodesulfurization reactions,³⁷ and has been gaining attention for their application in catalytic cracking systems, where coking is known to be a prevalent form of deactivation.^{38–40} Incorporation of a wide array of heteroatoms have further given these hierarchical zeolites a broader substrate applicability, such as glucose isomerisation,⁴¹ propane dehydrogenation,⁴² olefin hydroisomerisation,⁴³ or Meerwein-Ponndorf-Verley (MPV) reduction reactions.³⁵ Moreover, this incorporation has as well as shown improved yields over a plethora of reactions when compared to their conventional microporous analogues.^{44,45} Indeed, the creation of additional porosity has been demonstrated to provide outstanding benefits in terms of kinetic activity and has opened the possibilities of carrying out inconceivable reactions if one were to apply conventional microporous zeolites.

Of particular interest is the hierarchical Sn-Beta zeolite, which has gained a lot of attention. Out of the plethora of reactions that have been carried out with this catalyst, glucose retro-aldol fragmentation to methyl lactate, has gained a lot of attention (Scheme 5.2). Xu *et al* reported higher yields of methyl lactate with hierarchical Sn-Beta (58 % ML yield) made *via* hydrothermal post-synthesis method than with the conventional fluoride media synthesised Sn-Beta (42 % ML yield).⁴⁶ Li *et al* showed that an improvement of mass transfer, hydrophobicity, and Lewis acidity are advantageous for high yielding of methyl lactate with glucose as a substrate.⁴⁷ Other methods that have been done to improve rate of deactivation and/or activity/selectivity for these α -hydroxy

esters (methyl lactate, methyl vinyl glycolate) is the addition of small quantities of water (up to 10 % v/v), presenting higher degrees of stability and reactivity.⁴⁸ Given the versatility of Sn-Beta as a Lewis acid catalyst, it can potentially provide good performance for a plethora of mono- and disaccharides for methyl lactate production.



Scheme 5.1. Pathway for glucose to methyl lactate *via* retro-aldol fragmentation using Lewis acid catalysts.

Authors have reported the susceptibility of fouling for this particular reaction using catalysts such as Sn-Beta, in both water and methanol.^{49,50} Therefore, glucose retro-aldol fragmentation was chosen as the reaction study to assess the stability and reactivity potential when implementing hierarchically ordered mesopores in F⁻-assisted zeolites. Furthermore, two other heteroatoms – Hf and Zr, (along with Sn) will be used as precursors to synthesise fluoride-assisted Hf-Beta and Zr-Beta, respectively (named M-Beta-F). Hf-Beta has been recently reported to be a highly active and selective zeolite for glucose conversion at high temperatures (140 °C) in continuous flow.⁵¹ Zr-Beta has been shown to have potential for glucose isomerisation, presenting the lowest activation barrier alongside Sn.^{52,53} Furthermore, the preparation of mesoporous Zr-Betas has been reported using different methods such as: DeSi-DeAl-dry impregnation using Cp₂ZrCl₂ (Bis(cyclopentadienyl) Zr(IV) chloride),⁵⁴ and DeSi+PDA (C10-C16)-DeAl + Zr(IV) oxychloride octahydrate.⁵⁵ To date, no information for mesoporous Hf-Beta or any other framework has been

reported. Prior to this, initial tests were also carried out using a commercial Beta zeolite by incorporating Sn into the framework using various temperatures for the desilication step to assess the degree of mesopore formation.

5.2. Results and discussion

5.2.1. Zeolite characterisation

Firstly, the three commercial hierarchical Sn-Betas prepared from commercial Al-Beta were characterised. As can be seen in Figure 5.3, Sn-beta zeolites derived from commercial zeolites did not show any detrimental effect in regard to their crystallinity after hierarchical modification, according to the X-ray diffraction patterns (XRD). No beta zeolites showed any major degradation with a small exception to 85CTA-NaOH which presented a slightly lower intensity in intensity in comparison with the other two treatments in the 7.2° peak.

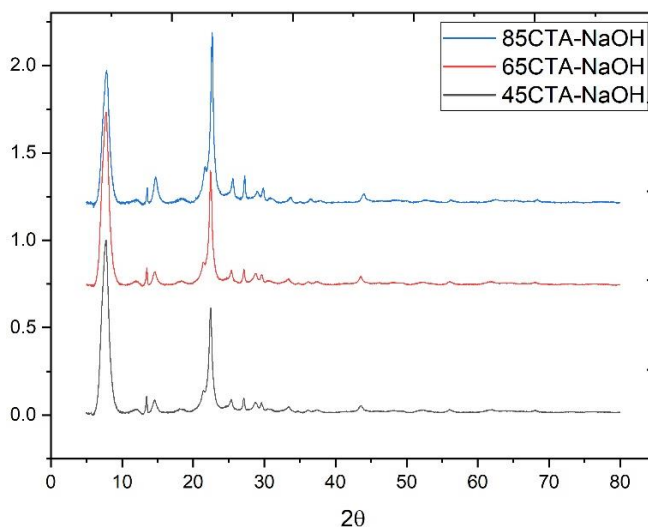


Figure 5.3. X-ray diffraction patterns of post-treated commercial zeolites.

Unlike XRD, N_2 physisorption provided further data and the influence of both the temperature as well as the effect of using PDA as a mesoporegen. As is shown in Figure 5.4, all zeolites present similar isotherms, albeit a difference in their respective specific surface areas (SSA) as well as having hysteresis, indicative of mesopore formation. Seemingly, the application of higher temperature when under alkaline leaching increases the SSA. This increase, however, does not

affect the pore size distribution (PSD) of the resulting leaching, which can be attributed to the use of PDA.

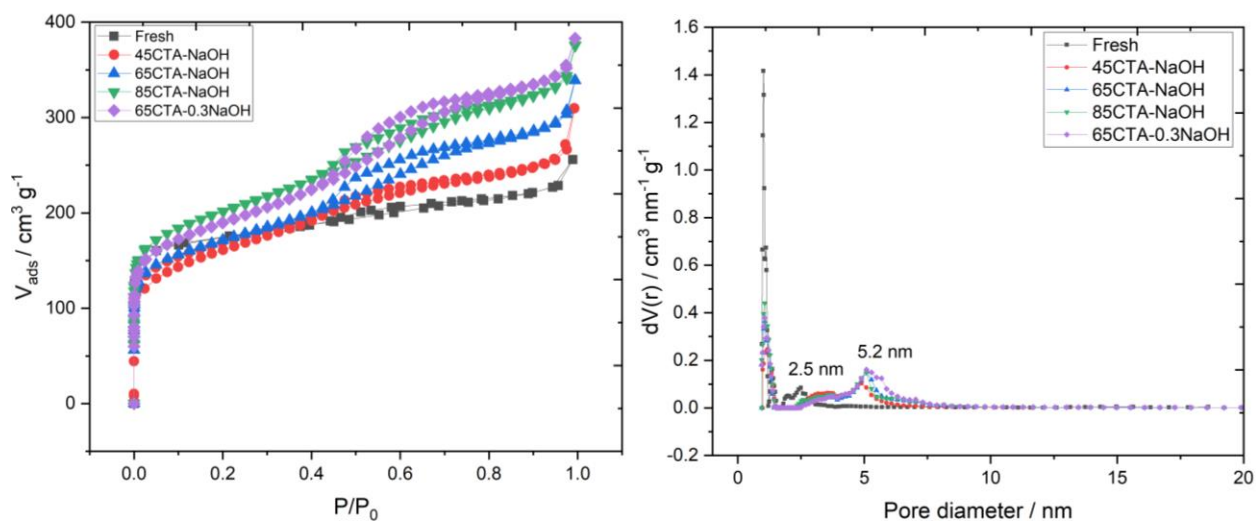


Figure 5.4. Nitrogen physisorption isotherms (Left) and Non-local Density Function Theory (NLDFT) PSD (Right) of the desilicated post-synthetic Sn-Beta.

Table 5.1 provides further information into the influence of the varying temperature had on zeolites. Interestingly, the zeolites presented an increase in virtually all parameters as the temperature was increased. This applies to also the micropore volume, having a value of $0.186 \text{ cm}^3 \text{ g}^{-1}$, $0.223 \text{ cm}^3 \text{ g}^{-1}$, and $0.27 \text{ cm}^3 \text{ g}^{-1}$, for 45CTA-NaOH, 65CTA-NaOH, and 85CTA-NaOH, respectively. BET surface area also increased with a higher temperature, having an area of $661 \text{ cm}^2 \text{ g}^{-1}$ for 85CTA-NaOH in contrast to $556 \text{ cm}^2 \text{ g}^{-1}$ for 45CTA-NaOH. DFT calculations were also compared and the discrepancy between them appeared to be larger. In particular, clearer differences in micropore ($> 2 \text{ nm}$) mesopore ($2 - 50 \text{ nm}$) volumes could be observed, which showed a higher amount of mesopores in the zeolites following desilication: $0.2562 \text{ cm}^3 \text{ g}^{-1}$, $0.2973 \text{ cm}^3 \text{ g}^{-1}$, and $0.32394 \text{ cm}^3 \text{ g}^{-1}$ for 45-, 65-, and 85CTA-NaOH zeolites, respectively.

Table 5.1. Textural data on desilicated Sn-Beta zeolites.

Catalyst	t-plot			BET		NLDFT		
	Micropore volume (cm ³ g ⁻¹)	Micropore area (m ² g ⁻¹)	External Surface area (m ² g ⁻¹)	Surface Area	Pore Volume	Surface Area	Micropore volume	Mesopore Volume
Fresh	0.219	416	92	509.	0.35	890	0.18525	0.21226
45CTA-NaOH	0.186	393	162	556	0.402	763	0.1309	0.2562
65CTA-NaOH	0.223	395	167	562	0.454	826	0.1447	0.2973
85CTA-NaOH	0.27	487	174	661	0.508	953	0.1725	0.3239
65CTA-0.3NaOH	0.245	421	205	627	0.526	883	0.14886	0.3654

Additionally, another treatment was done using a 0.3 M NaOH solution at 65 °C (65CTA-0.3NaOH) to evaluate the effect of using a higher concentration of alkaline media. While comparing 65CTA-0.3NaOH to 65CTA-NaOH, the former continued to have an incremental effect in all its textural properties. However, when comparing it to 85CTA-NaOH, it proved to have only higher mesopore volume (0.3654 cm³ g⁻¹ and 0.3239 cm³ g⁻¹ for 65CTA-0.3NaOH and 85CTA-NaOH, respectively) to and external surface area. By applying a higher concentration of NaOH, the leaching provided more amounts of mesoporosity at the expense of losing microporosity, whereas temperature seems to have a relatively proportional increase to all of the zeolite's textural properties. While there may be a limit to the application of temperature or concentration due to the catalyst degradation, this could aid with the tuning of higher mesopore zeolites while maintaining a sufficient amount of microporosity in the framework.

To visualise the physical changes to the catalysts, transmission electron microscopy was performed on the 45CTA-NaOH catalyst. As can be seen in Figure 5.5, 45CTA-NaOH Sn-Beta is shown to have clear degradation, particularly in the surface of the zeolite crystallite.

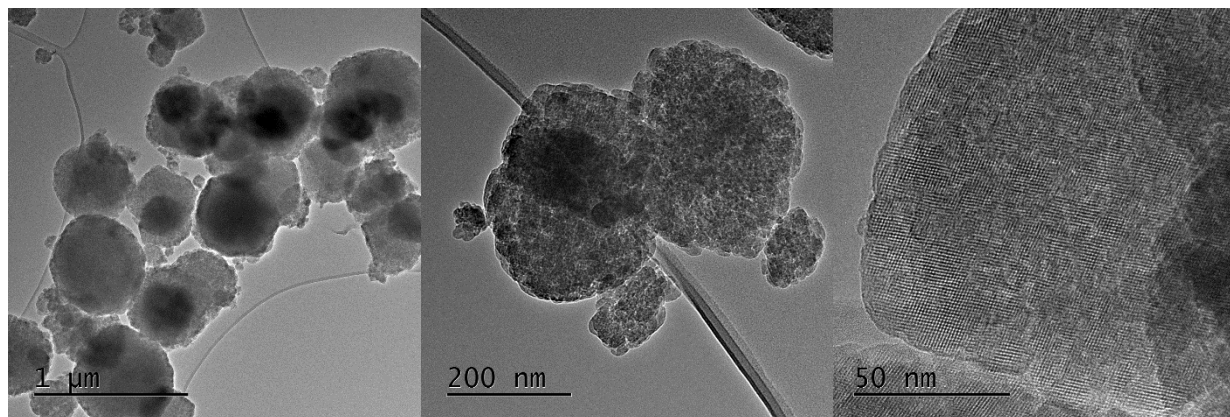


Figure 5.5. TEM of 45CTA-NaOH Sn-Beta at 8,000x (left), 30,000x (middle), and 150,000x (right) magnification.

To further assess the degradation, TEM of 85CTA-NaOH was carried out (Figure 6.6) Whilst external surface areas seem relatively similar (162 and $174 \text{ m}^3 \text{ g}^{-1}$ for 45CTA-NaOH and 85CTA-NaOH, respectively), 85CTA-NaOH was shown to have a more severe degradation in the external area of the crystals. Although the premise for the implementation of desilication is to generate mesopore channels to hinder any mass transfer constraints, degradation with higher temperatures could possibly aid in the increase of micropore area and volume.

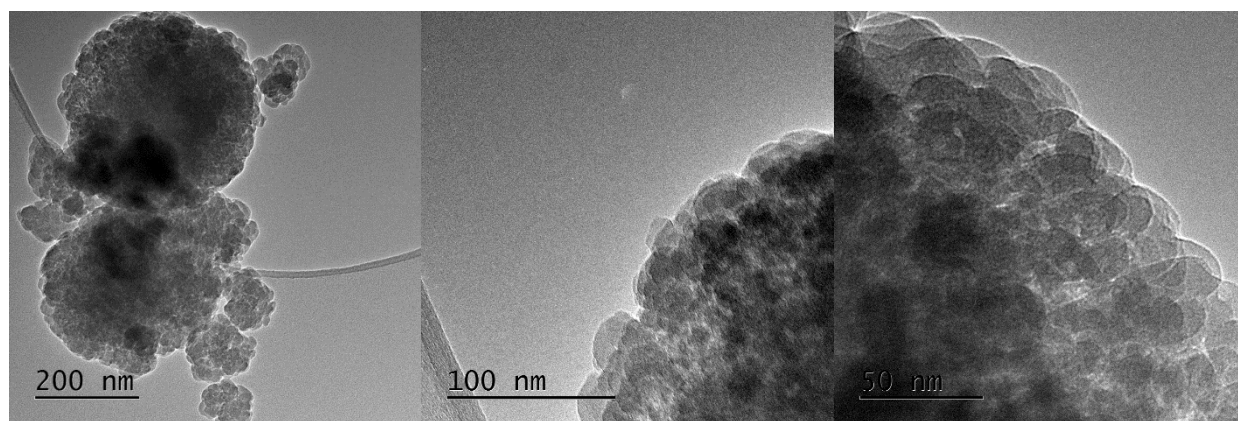


Figure 5.6. TEM of 85CTA-NaOH Sn-Beta at 25,000x (left), 80,000x (middle), 120,000x (right) magnification.

5.2.2. Catalytic tests of the hierarchical Sn-Beta samples.

Methyl lactate production from glucose (Scheme 5.1, *vide supra*) under continuous flow was used as the system for these zeolites to evaluate the stability of these zeolites. A normal post-synthetic (SSI *via* only dealumination) Sn-Beta named PS Sn-Beta (created using procedure in Section 2.3.2.1) was also tested as a benchmark to gauge the effect of the alkaline-treated zeolites. 65CTA-

NaOH and 85CTA-NaOH were chosen as the catalysts for this reaction study, to observe if there existed any beneficial effects with higher degree of degradation as evidenced by TEM from 85CTA-NaOH. As can be seen in Figure 5.7 (left), a great improvement with respect to the conversion over time on stream can be observed, showing a glucose conversion of 53 % and 63 % for 65CTA-NaOH and 85CTA-NaOH, respectively, in contrast to 17 % conversion obtained from PS Sn-Beta. To further assess the stability of the catalysts, rates of deactivation (k_d) were plotted using the Levenspiel function.^{56,57} k_d presented in Figure 5.7 (right) show a significantly lower for both of the hierarchical zeolites, having values of 0.0365 and 0.0374 h^{-1} for 65CTA-NaOH and 85CTA-NaOH, respectively. PS Sn-Beta, on the other hand, presented a k_d with almost double the value, having 0.0685 h^{-1} . Whilst there was an improvement from the alkaline-treated to the normal post-synthetic Sn-Beta, the variances of k_d between both temperatures were minimal.

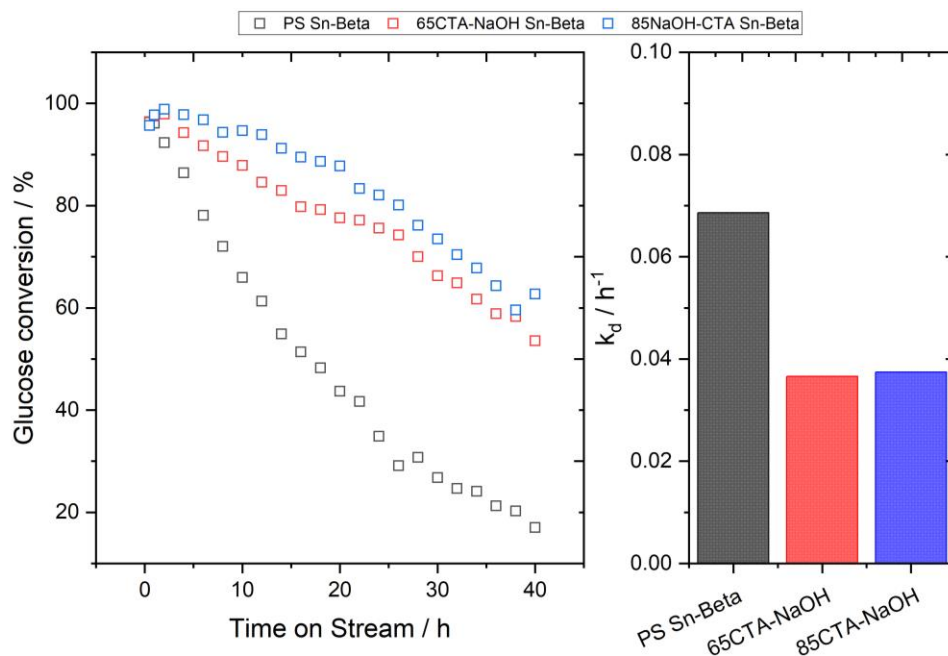


Figure 5.7. Catalytic conversion of glucose to methyl lactate *via* retro-aldol fragmentation using various post-synthetic catalysts: (left) glucose conversion and (right) glucose k_d plotted by the Levenspiel method. Reaction conditions: 1 wt. % glucose in methanol, 1 mL min^{-1} flow rate, 100 mg, 160 $^{\circ}\text{C}$.

As can be seen in Figure 5.8, fructose (left) and methyl lactate (right) yields are shown. As with the improvement in stability shown for glucose conversion, ML yield appeared to benefit substantially. Methyl lactate yield showed a higher activity for both hierarchical catalysts, yielding *ca.* 35 % higher initial ML yield (32.5 %) than the conventional PS Sn-Beta (25 %). Whilst PS Sn-

Beta would not show any yield after 26 h, both hierarchical catalysts continued to produce after 40 h, with an average of 2.5 % methyl lactate yield. Unlike the ML production, fructose yields appeared to have minor changes (10.8 % fructose yield for 65CTA-NaOH) or relatively similar yields (in the case of 85CTA-NaOH vs. PS Sn-Beta fructose yield – 9.6 %). This minor change in fructose accompanied by the increase in ML yield is beneficial due to fructose being an intermediate to ML, implies that the increase in activity/stability is not necessarily improving secondary or intermediate reactions but rather ML production overall. This could indicate even if the main factor of deactivation can be mitigated by creating mesopores, this does not necessarily implicate a better reactivity towards materials which were previously able to catalyse.

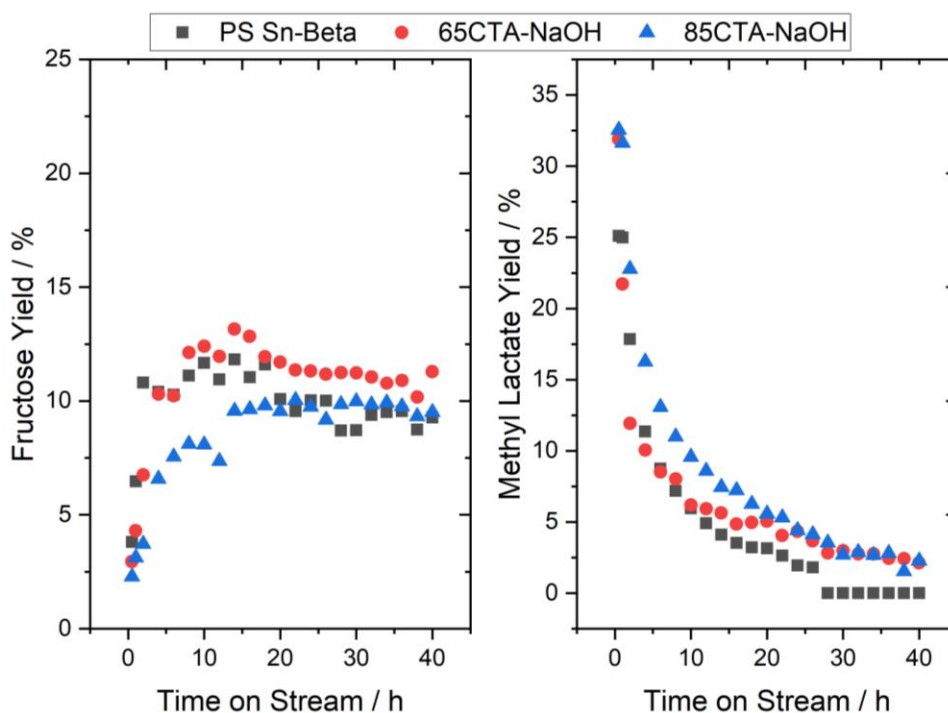


Figure 5.8. Fructose (left) and methyl lactate (right) yield of glucose retro-aldol fragmentation. Reaction conditions: 1 wt. % glucose in methanol, 1 mL min⁻¹ flow rate, 100 mg catalyst, 160 °C.

Glucose conversion *vs.* selectivity presented at Figure 5.9 showed similar trends for fructose selectivity (Figure 6.9 – left). However, methyl lactate was shown to have higher selectivity on similar conversion rates when compared to both hierarchical catalysts. This is to be expected given the abrupt drop in glucose conversion that PS Sn-Beta exhibits throughout the time on stream.

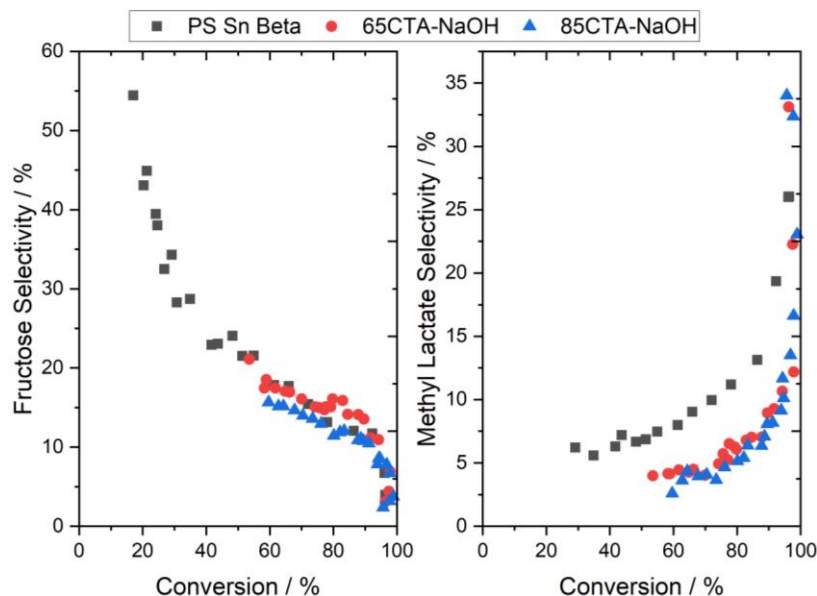


Figure 5.9 Glucose conversion vs. fructose (left) and methyl lactate (right) selectivities.

Despite the lower methyl selectivity obtained from the hierarchical Sn-Beta catalysts, overall carbon balance with respect to glucose conversion presented similar trends and percentages (Figure 5.10). This could indicate that the creation of bimodal catalysts did not create any additional reaction pathways, and hence, was simply an overall improvement stability-wise.

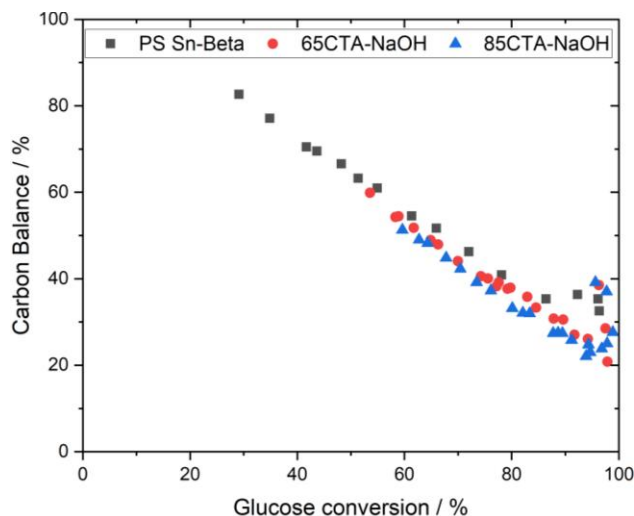


Figure 5.10. Glucose conversion vs. Carbon balance of the three catalysts. Glucose, fructose, and methyl lactate were considered for the overall carbon balance.

The creation of mesopores for Sn-Beta was shown to improve drastically the initial ML yield. Accompanied with this newfound increase in stability could be pivotal for future studies in gauging their potential for the production of α -hydroxy esters. As has been discussed previously, the addition of water can potentially further increase the stability in this system.⁴⁸ Furthermore, the addition of alkali salts (*i.e.*, KCl, K₂CO₃) at small concentrations to increase methyl lactate selectivity has been reported to work for both fluoride-assisted as well as post-synthetic catalysts.^{58,59} Moreover, this has the advantage of suppressing alkyl glycoside formation, for the case of K₂CO₃.⁶⁰ Thus, the creation of mesopores resulted to be beneficial in regards to the catalysts' stability while not hindering or decreasing activity in any way. Furthermore, addition of activity promoters such as alkali salts and/or water could further increase the activity and selectivity to a higher degree given its newfound bimodal pore size.

5.2.3. Catalytic tests of the desilicated, fluoride-synthesised Hf-, Zr-, and Sn-Beta zeolites

To further assess the desilication procedure, desilication studies were focused on three different metal betas synthesised using fluoride as a mineraliser, in contrast to the commercial zeolites previously tested which are synthesised using hydroxide as a mineraliser. Due to the higher activity obtainable by fluoride-synthesised zeolites, application of slight desilication can potentially decrease their rate of deactivation on processes whose main form of deactivation consists of coking.

While temperature did indeed change the textural properties when catalysts underwent desilication, no drastic change in terms of activity, selectivity and overall carbon balance was observed from 65CTA-NaOH and 85CTA-NaOH. Therefore, the same desilication procedure was carried out using only 65 °C to the fluoride-assisted zeolites and were subsequently tested. Another desilication treatment involving solely 0.2 M NaOH was also performed to observe the effect of degradation.

As can be seen in Figure 5.11, desilication on all zeolites were unsuccessful. All zeolites resulted in complete degradation of the crystal structure after undergoing desilication, showing complete amorphisation in all catalysts done with pure NaOH as is shown by the absence of the peaks that represent a Beta zeolite (*i.e.*, 2θ of ca. 7.9° and 22.6°).^{61,62} Despite the degradation of the

zeolites, Sn-Beta-F presented traces of the Beta zeolite, albeit still mainly amorphous, showing diffractions at 7.9 and 22.6 2θ . Pérez-Ramírez *et al* reported the interaction of various tetraalkylammonium cations (TAA) under alkaline conditions, working as a pore-growth moderator as well as providing protection from complete zeolite dissolution.⁶³

Possible reasons for the complete dissolution of the M-Beta-F zeolites are: 1) while Al helps by hindering Si leaching, this does not necessarily apply for other types of heteroatoms (Hf, Zr, Sn) as is evidenced by the difference in degradation while having similar Si/M ratios; 2) due to the defect-free nature, silicon leaching, even under mild conditions, can cause a total collapse of the structural framework.¹²

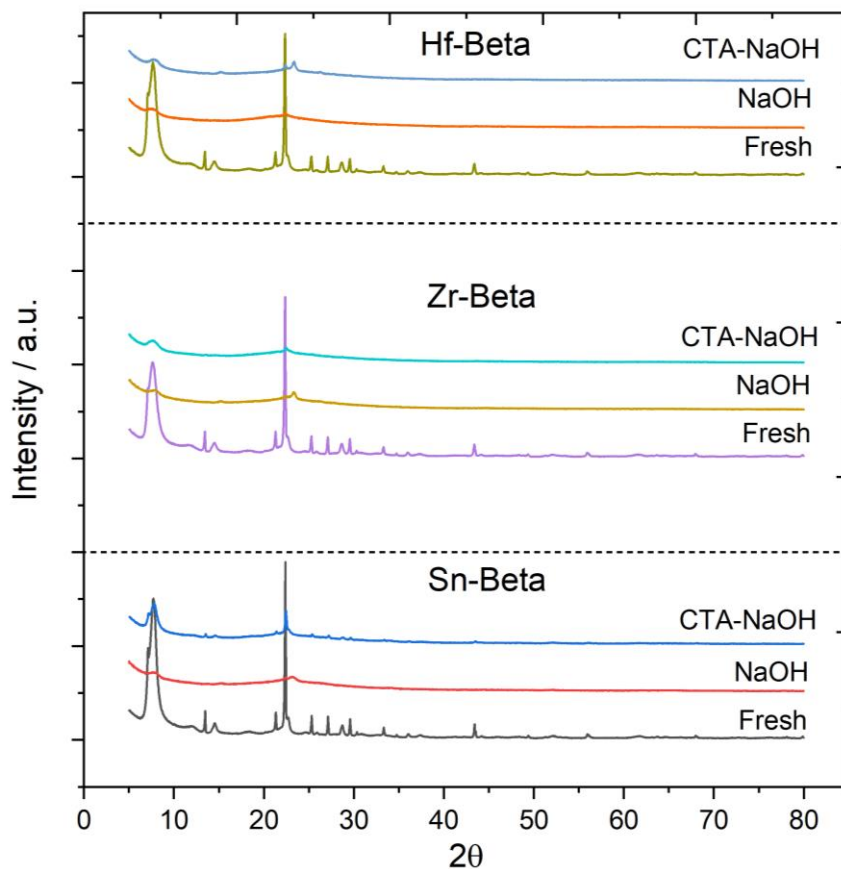


Figure 5.11. XRD patterns of fresh and desilicated (with and without PDA) of Zr-, Hf-, and Sn-Beta zeolites.

In lieu of kinetic information from desilicated Sn-Beta from fluoride media, fresh Sn-Beta-F was compared with the 85CTA-NaOH Sn-Beta (Figure 5.12). Interestingly, the desilicated zeolite, despite being synthesised in hydroxide media, presented a higher stability conversion-wise than Sn-Beta synthesised with fluoride as a mineraliser. It did, nevertheless, lack in kinetic activity, as is demonstrated by a lower fructose yield.

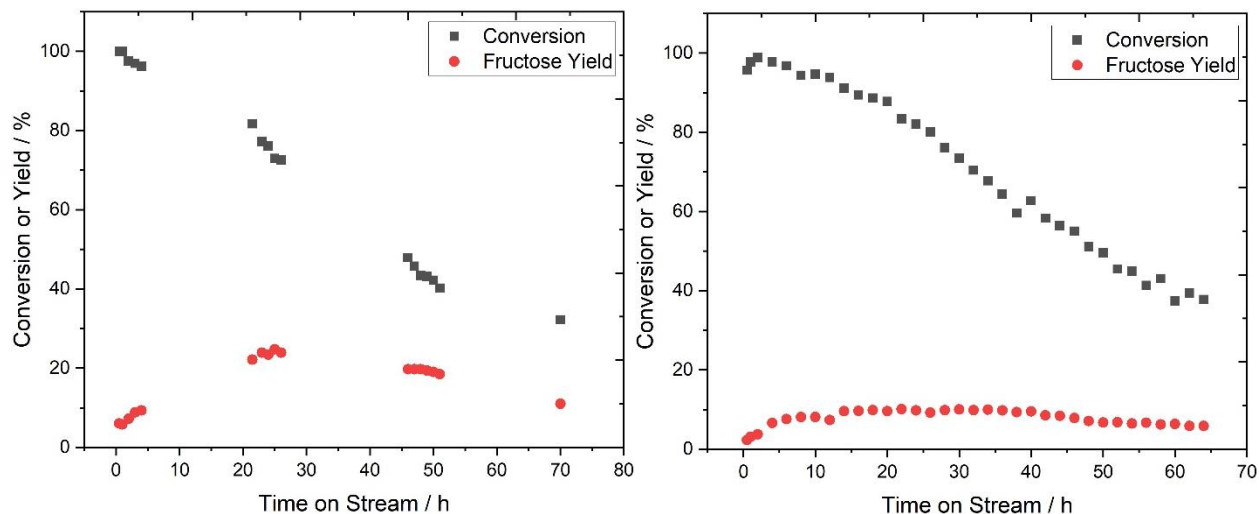


Figure 5.12. Catalytic conversion of glucose at high temperature, showing fructose yields using Sn-Beta-F (Left) and with 85CTA-NaOH Sn-Beta (Right). Reaction conditions: 1 wt. % glucose in methanol, 1 mL min⁻¹ flow rate, 100 mg of catalyst at 160 °C.

Desilication tests conducted with a milder treatment were also carried out (0.1 M NaOH + 0.2 M CTABr, 30 °C, 30 min); despite decreasing the concentration of the alkali, no activity was shown when testing the catalyst, indicating a complete dissolution even with the modified desilication.

One of the probable reasons for the hydrothermal dissolution caused by desilication is due to the low amount of M which could help in the mitigation of silicon leaching.⁶⁴ Nevertheless, Pérez-Ramírez *et al* have reported the desilication of Beta zeolites synthesised in fluoride media using Al as the metal a low Si/Al ratio of 35.¹² Despite having an elevated Al content in the zeolite, uncontrolled dissolution occurred due to the low stability of framework Al in Beta zeolites. In conventional (hydroxide-assisted) aluminosilicate zeolites, for instance (Figure 5.13), having a

lower Si/Al ratio mitigates the OH^- attack. High Si/Al ratios, on the other hand, typically undergo uncontrolled silicon extraction, resulting in amorphisation of the framework due to the ease of Si-O-Si leaching using OH^- .^{19,65} Thus, it can be concluded that while a high metal content can provide some protection to the catalyst when undergoing alkaline leaching, the innate defect-free fluoride zeolite will inevitably suffer substantial framework degradation.

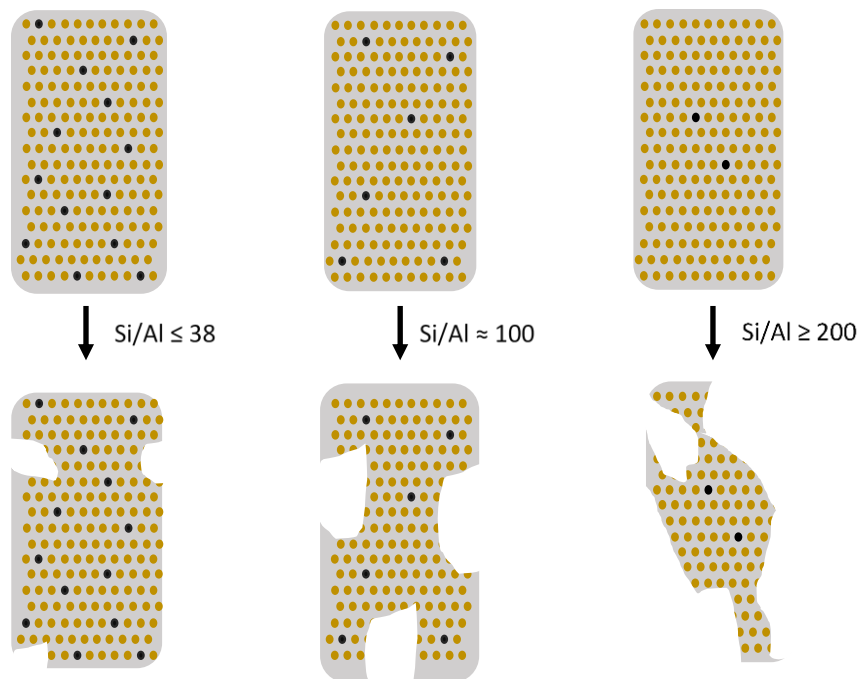


Figure 5.13. Schematic of desilication degree according to Si/Al ratio.

5.3 Conclusion

Commercial aluminosilicate beta zeolite was used as a testing material to tailor the effect of temperature when undergoing desilication. When applied to high temperature glucose valorisation, catalyst stability improved significantly, presenting an initial 35 % higher ML yield than the conventional PS catalyst. Desilication was also implemented into fluoride synthesised zeolites (Hf-, Zr-, and Sn-Beta). However, all zeolites synthesised with fluoride anions underwent complete degradation, with and without the use of a PDA. This could be due to the type of metal incorporated, which does not have the same hindering effect that Al has, the low quantity of said metal ($\text{Si/M} =$

200) or due to the zeolite's defect-free structure, which makes it prone to full dissolution even if partial leaching was performed. Overall, the use of desilication for the creation of mesopores is not applicable in fluoride synthesised zeolites in the typical conditions that are used for the hydroxide synthesised zeolites and further studies would need to be done to ascertain the applicability of alkaline leaching. However, when carried out on materials suitable for desilication, there is a substantial increase in stability, activity, and selectivity in contrast to the conventional untreated material.

5.4 References

1. Jennings, J. A., Parkin, S., Munson, E., Delaney, S. P., Calahan, J. L., Isaacs, M., Hong, K. & Crocker, M. Regioselective Baeyer-Villiger oxidation of lignin model compounds with tin beta zeolite catalyst and hydrogen peroxide. *RSC Adv.* **7**, 25987–25997 (2017).
2. Nakai, M., Miyake, K., Inoue, R., Ono, K., Al Jabri, H., Hirota, Y., Uchida, Y., Tanaka, S., Miyamoto, M., Oumi, Y., Kong, C. Y. & Nishiyama, N. Dehydrogenation of propane over high silica *BEA type gallosilicate (Ga-Beta). *Catal. Sci. Technol.* **9**, 6234–6239 (2019).
3. Xia, Y., Zhan, W., Guo, Y., Guo, Y. & Lu, G. Fe-Beta zeolite for selective catalytic reduction of NO_x with NH₃: Influence of Fe content. *Cuihua Xuebao/Chinese J. Catal.* **37**, 2069–2078 (2016).
4. Wang, C., Zheng, M., Li, X., Li, X. & Zhang, T. Catalytic conversion of ethanol into butadiene over high performance LiZnHf-MFI zeolite nanosheets. *Green Chem.* **21**, 1006–1010 (2019).
5. Htay, M. M. & Oo, M. M. Preparation of Zeolite Y Catalyst for Petroleum Cracking. *World Acad. Sci. Eng. Technol.* **24**, 114–120 (2008).
6. Uysal, B. & Buyuktas, B. S. Chemoselective reduction of aldehydes and ketones to alcohols using boron tri-isopropoxide, B(O-*i*-Pr)₃ and boron tri-secondary butoxide, B(O-*s*-Bu)₃ as catalysts. *Arkivoc* **2007**, 134 (2007).
7. Fernandez, S., Ostraat, M. L., Lawrence, J. A. & Zhang, K. Tailoring the hierarchical architecture of beta zeolites using base leaching and pore-directing agents. *Microporous Mesoporous Mater.* **263**, 201–209 (2018).
8. Kawai, T. & Tsutsumi, K. Adsorption characteristics of surfactants and phenol on modified zeolites from their aqueous solutions. *Colloid Polym. Sci.* **273**, 787–792 (1995).
9. Zhu, K., Egeblad, K. & Christensen, C. H. *Tailoring the porosity of hierarchical zeolites by carbon-templating. Studies in Surface Science and Catalysis* vol. 174 (Elsevier B.V., 2008).
10. Sabarish, R. & Unnikrishnan, G. Synthesis, characterization and catalytic activity of hierarchical ZSM-5 templated by carboxymethyl cellulose. *Powder Technol.* **320**, 412–419 (2017).
11. Zhu, H., Liu, Z., Wang, Y., Kong, D., Yuan, X. & Xie, Z. Nanosized CaCO₃ as hard template for creation of intracrystal pores within silicalite-1 crystal. *Chem. Mater.* **20**, 1134–1139 (2008).

12. Groen, J. C., Abelló, S., Villaescusa, L. A. & Pérez-Ramírez, J. Mesoporous beta zeolite obtained by desilication. *Microporous Mesoporous Mater.* **114**, 93–102 (2008).
13. Li, K., Valla, J. & Garcia-Martinez, J. Realizing the commercial potential of hierarchical zeolites: New opportunities in catalytic cracking. *ChemCatChem* **6**, 46–66 (2014).
14. Sammoury, H., Toufaily, J., Cherry, K., Hamieh, T., Pouilloux, Y. & Pinard, L. Impact of desilication of *BEA zeolites on the catalytic performance in hydroisomerization of n-C10. *Appl. Catal. A Gen.* **551**, 1–12 (2018).
15. Sabarish, R. & Unnikrishnan, G. A novel anionic surfactant as template for the development of hierarchical ZSM-5 zeolite and its catalytic performance. *J. Porous Mater.* **27**, 691–700 (2020).
16. Verboekend, D., Vilé, G. & Pérez-Ramírez, J. Mesopore formation in usy and beta zeolites by base leaching: Selection criteria and optimization of pore-directing agents. *Cryst. Growth Des.* **12**, 3123–3132 (2012).
17. Meng, L., Mezari, B., Goesten, M. G. & Hensen, E. J. M. One-Step Synthesis of Hierarchical ZSM-5 Using Cetyltrimethylammonium as Mesoporegen and Structure-Directing Agent. *Chem. Mater.* **29**, 4091–4096 (2017).
18. Sammoury, H., Toufaily, J., Cherry, K., Hamieh, T., Pouilloux, Y. & Pinard, L. Desilication of *BEA zeolites using different alkaline media: Impact on catalytic cracking of n-hexane. *Microporous Mesoporous Mater.* **267**, 150–163 (2018).
19. Sadowska, K., Góra-Marek, K., Drozdek, M., Kuśtrowski, P., Datka, J., Martinez Triguero, J. & Rey, F. Desilication of highly siliceous zeolite ZSM-5 with NaOH and NaOH/tetrabutylamine hydroxide. *Microporous Mesoporous Mater.* **168**, 195–205 (2013).
20. Hasan, Z., Jun, J. W., Kim, C. U., Jeong, K. E., Jeong, S. Y. & Jung, S. H. Desilication of ZSM-5 zeolites for mesoporosity development using microwave irradiation. *Mater. Res. Bull.* **61**, 469–474 (2015).
21. Sousa, L. V., Silva, A. O. S., Silva, B. J. B., Quintela, P. H. L., Barbosa, C. B. M., Fréty, R. & Pacheco, J. G. A. Preparation of zeolite P by desilication and recrystallization of zeolites ZSM-22 and ZSM-35. *Mater. Lett.* **217**, 259–262 (2018).
22. Cambor, M. A., Corma, A. & Valencia, S. Synthesis in fluoride media and characterisation of aluminosilicate zeolite beta. *J. Mater. Chem.* **8**, 2137–2145 (1998).
23. Möller, K. & Bein, T. Mesoporosity – a new dimension for zeolites. *Chem. Soc. Rev.* **42**, 3689–3707 (2013).
24. Louis, B. & Kiwi-Minsker, L. Synthesis of ZSM-5 zeolite in fluoride media: An innovative approach to tailor both crystal size and acidity. *Microporous Mesoporous Mater.* **74**, 171–178 (2004).
25. Grand, J., Awala, H. & Mintova, S. Mechanism of zeolites crystal growth: New findings and open questions. *CrystEngComm* **18**, 650–664 (2016).
26. Serrano, D. P., Van Grieken, R., Sánchez, P., Sanz, R. & Rodríguez, L. Crystallization mechanism of all-silica zeolite beta in fluoride medium. *Microporous Mesoporous Mater.* **46**, 35–46 (2001).
27. Xue, T., Wang, Y. M. & He, M. Y. Synthesis of ultra-high-silica ZSM-5 zeolites with tunable crystal sizes. *Solid State Sci.* **14**, 409–418 (2012).

28. Davis, M. E. Ordered porous materials for emerging applications. *Nature* **417**, 813–821 (2002).
29. Cheng, X., Wang, X. & Long, H. Transalkylation of benzene with 1,2,4-trimethylbenzene over nanosized ZSM-5. *Microporous Mesoporous Mater.* **119**, 171–175 (2009).
30. Xu, X., Zhang, Y., Li, X., Xia, X., Jiang, H. & Toghan, A. Comparative study on the catalytic behaviors of zeolites with different diffusion limitation in ethane aromatization. *Microporous Mesoporous Mater.* **315**, 110926 (2021).
31. Lopez-Orozco, S., Inayat, A., Schwab, A., Selvam, T. & Schwieger, W. Zeolitic materials with hierarchical porous structures. *Adv. Mater.* **23**, 2602–2615 (2011).
32. Zhang, X., Liu, D., Xu, D., Asahina, S., Cychosz, K. A., Agrawal, K. V., Al Wahedi, Y., Bhan, A., Al Hashimi, S., Terasaki, O., Thommes, M. & Tsapatsis, M. Synthesis of self-pillared zeolite nanosheets by repetitive branching. *Science (80-.)*. **336**, 1684–1687 (2012).
33. Al-Nayili, A., Yakabi, K. & Hammond, C. Hierarchically porous BEA stannosilicates as unique catalysts for bulky ketone conversion and continuous operation. *J. Mater. Chem. A* **4**, 1373–1382 (2016).
34. Srivastava, R., Choi, M. & Ryoo, R. Mesoporous materials with zeolite framework: Remarkable effect of the hierarchical structure for retardation of catalyst deactivation. *Chem. Commun.* **41**, 4489–4491 (2006).
35. Wang, Y., Lancelot, C., Lamonier, C., Yang, M., Sun, Y., Morin, J. C. & Rives, A. Restraining deactivation of hierarchical zeolite supported NiW catalysts in the HDS of thiophene. *RSC Adv.* **5**, 74150–74158 (2015).
36. Liu, B., Xie, K., Oh, S. C., Sun, D., Fang, Y. & Xi, H. Direct synthesis of hierarchical USY zeolite for retardation of catalyst deactivation. *Chem. Eng. Sci.* **153**, 374–381 (2016).
37. Talebian-Kiakalaieh, A. & Tarighi, S. Synthesis of hierarchical Y and ZSM-5 zeolites using post-treatment approach to maximize catalytic cracking performance. *J. Ind. Eng. Chem.* **88**, 167–177 (2020).
38. Zhao, J., Wang, G., Qin, L., Li, H., Chen, Y. & Liu, B. Synthesis and catalytic cracking performance of mesoporous zeolite y. *Catal. Commun.* **73**, 98–102 (2016).
39. Cho, H. J., Gould, N. S., Vattipalli, V., Sabnis, S., Chaikittisilp, W., Okubo, T., Xu, B. & Fan, W. Fabrication of hierarchical Lewis acid Sn-BEA with tunable hydrophobicity for cellulosic sugar isomerization. *Microporous Mesoporous Mater.* **278**, 387–396 (2019).
40. Kim, W. G., So, J., Choi, S. W., Liu, Y., Dixit, R. S., Sievers, C., Sholl, D. S., Nair, S. & Jones, C. W. Hierarchical Ga-MFI Catalysts for Propane Dehydrogenation. *Chem. Mater.* **29**, 7213–7222 (2017).
41. Pan, T., Wu, Z. & Zhou, K. In Situ Incorporation of Zn into Hierarchical ZSM-5 Zeolites for Olefin Hydroisomerization. *Ind. Eng. Chem. Res.* **59**, 12371–12380 (2020).
42. Kustova, M. Y., Rasmussen, S. B., Kustov, A. L. & Christensen, C. H. Direct NO decomposition over conventional and mesoporous Cu-ZSM-5 and Cu-ZSM-11 catalysts: Improved performance with hierarchical zeolites. *Appl. Catal. B Environ.* **67**, 60–67 (2006).
43. Bonilla, A., Baudouin, D. & Pérez-Ramírez, J. Desilication of ferrierite zeolite for porosity generation and improved effectiveness in polyethylene pyrolysis. *J. Catal.* **265**, 170–180 (2009).

44. Yang, X., Bian, J., Huang, J., Xin, W., Lu, T., Chen, C., Su, Y., Zhou, L., Wang, F. & Xu, J. Fluoride-free and low concentration template synthesis of hierarchical Sn-Beta zeolites: Efficient catalysts for conversion of glucose to alkyl lactate. *Green Chem.* **19**, 692–701 (2017).
45. Tang, B., Li, S., Song, W. C., Yang, E. C., Zhao, X. J., Guan, N. & Li, L. Fabrication of Hierarchical Sn-Beta Zeolite as Efficient Catalyst for Conversion of Cellulosic Sugar to Methyl Lactate. *ACS Sustain. Chem. Eng.* **8**, 3796–3808 (2020).
46. Padovan, D., Tolborg, S., Botti, L., Taarning, E., Sádaba, I. & Hammond, C. Overcoming catalyst deactivation during the continuous conversion of sugars to chemicals: Maximising the performance of Sn-Beta with a little drop of water. *React. Chem. Eng.* **3**, 155–163 (2018).
47. Lari, G. M., Dapsens, P. Y., Scholz, D., Mitchell, S., Mondelli, C. & Pérez-Ramírez, J. Deactivation mechanisms of tin-zeolites in biomass conversions. *Green Chem.* **18**, 1249–1260 (2016).
48. Zhang, Y., Luo, H., Zhao, X., Zhu, L., Miao, G., Wang, H., Li, S. & Kong, L. Continuous Conversion of Glucose into Methyl Lactate over the Sn-Beta Zeolite: Catalytic Performance and Activity Insight. *Ind. Eng. Chem. Res.* **59**, 17365–17372 (2020).
49. Botti, L., Kondrat, S. A., Navar, R., Padovan, D., Martinez-Espin, J. S., Meier, S. & Hammond, C. Solvent-Activated Hafnium-Containing Zeolites Enable Selective and Continuous Glucose–Fructose Isomerisation. *Angew. Chemie - Int. Ed.* **59**, 20017–20023 (2020).
50. Li, Y. P., Head-Gordon, M. & Bell, A. T. Analysis of the reaction mechanism and catalytic activity of metal-substituted beta zeolite for the isomerization of glucose to fructose. *ACS Catal.* **4**, 1537–1545 (2014).
51. Luo, H. Y., Lewis, J. D. & Román-Leshkov, Y. Lewis Acid Zeolites for Biomass Conversion: Perspectives and Challenges on Reactivity, Synthesis, and Stability. *Annu. Rev. Chem. Biomol. Eng.* **7**, 663–692 (2016).
52. Tang, B., Dai, W., Sun, X., Wu, G., Guan, N., Hunger, M. & Li, L. Mesoporous Zr-Beta zeolites prepared by a post-synthetic strategy as a robust Lewis acid catalyst for the ring-opening aminolysis of epoxides. *Green Chem.* **17**, 1744–1755 (2015).
53. Yang, G., Wang, L. & Jiang, H. Preparation of β zeolite with intracrystalline mesoporosity via surfactant -templating strategy and its application in ethanol-acetaldehyde to butadiene. *Microporous Mesoporous Mater.* **316**, 110949 (2021).
54. Levenspiel, O. Chemical Reaction Engineering. *Ind. Eng. Chem. Res.* **38**, 4140–4143 (1999).
55. Levenspiel, O. *Chemical reaction engineering*. (Wiley, 1998). doi:10.1002/aic.690190143.
56. Tolborg, S., Súdaba, I., Osmundsen, C. M., Frstrup, P., Holm, M. S. & Taarning, E. Tin-containing Silicates: Alkali Salts Improve Methyl Lactate Yield from Sugars. *ChemSusChem* **8**, 613–617 (2015).
57. Elliot, S. G., Tosi, I., Meier, S., Martinez-Espin, J. S., Tolborg, S. & Taarning, E. Stoichiometric active site modification observed by alkali ion titrations of Sn-Beta. *Catal. Sci. Technol.* **9**, 4339–4346 (2019).

58. Elliot, S. G., Tolborg, S., Madsen, R., Taarning, E. & Meier, S. Effects of Alkali-Metal Ions and Counter Ions in Sn-Beta-Catalyzed Carbohydrate Conversion. *ChemSusChem* **11**, 1198–1203 (2018).
59. Hajjar, R., Millot, Y., Man, P. P., Che, M. & Dzwigaj, S. Two kinds of framework Al sites studied in BEA zeolite by X-ray diffraction, Fourier Transform Infrared spectroscopy, NMR techniques, and V probe. *J. Phys. Chem. C* **112**, 20167–20175 (2008).
60. Yang, X., Liu, Y., Li, X., Ren, J., Zhou, L., Lu, T. & Su, Y. Synthesis of Sn-Containing Nanosized Beta Zeolite As Efficient Catalyst for Transformation of Glucose to Methyl Lactate. *ACS Sustain. Chem. Eng.* **6**, 8256–8265 (2018).
61. Pérez-Ramírez, J., Verboekend, D., Bonilla, A. & Abelló, S. Zeolite catalysts with tunable hierarchy factor by pore-growth moderators. *Adv. Funct. Mater.* **19**, 3972–3979 (2009).
62. Rac, V., Rakíc, V., Miladinović, Z., Stošić, D. & Auroux, A. Influence of the desilication process on the acidity of HZSM-5 zeolite. *Thermochim. Acta* **567**, 73–78 (2013).
63. Verboekend, D. & Pérez-Ramírez, J. Desilication mechanism revisited: Highly mesoporous all-silica zeolites enabled through pore-directing agents. *Chem. - A Eur. J.* **17**, 1137–1147 (2011).

Chapter 6. Polar solvent stability of UiO-66 metal organic framework and its application for lactose valorisation under continuous flow

6.1 Introduction

The depletion of non-renewable resources such as fossil feedstock as well as the transition towards greener, more sustainable processes has been a focal point over the last decades. In this respect, the valorisation of renewable feedstock (*e.g.*, cellulose, starch, algae) to important commodity chemicals at scalable and continuous processing conditions has become increasingly important. Amongst potential heterogeneous catalysts, Sn-Beta has proven to be effective for the valorisation of various carbohydrates in continuous flow and is known to catalyse different reactions such as isomerisation,^{1,2} and dehydration,³ due to its tuneable acidic properties. While offering a more flexible applicability on account of the capability to endow the solid with different metal clusters, they are more environmentally friendly than homogeneous analogues.⁴⁻⁶ Heterogeneous catalysts also offer higher potential than homogeneous catalysts for process intensification due to their ability to be re-used,⁷⁻⁹ or continuously used,¹⁰ for substantial periods of time. Nevertheless, applicability of these catalysts in larger-scale operations can be hampered, whether it is due to the laborious procedure to obtain these catalysts or due to the chemicals required to undergo the synthesis. Hazardous reactants such as, hydrofluoric acid make fluoride-mediated catalysts unattractive to scale-up. As such, the search for new heterogeneous catalysts with interesting activities and good stability remains an important challenge.

Amongst heterogeneous catalysts, metal organic frameworks (MOFs) are of interest due to their high surface areas,^{11,12} tuneable activities,¹³⁻¹⁵ and the ability to insert a variety of metal centres.¹⁶⁻¹⁸ These heterogeneous catalysts are organic-inorganic hybrid crystalline materials which are formed by reticular synthesis.¹⁹ These porous materials are constructed with a secondary building metal unit (SBU) as an organic linker and a metal ion cluster. Although thousands of MOFs have been synthesised, a relatively few amount of these have been investigated as catalysts.²⁰⁻²³ Of the MOFs, one of particular interest is the UiO-66 (Figure 6.1).²⁴ This MOF has been reported to

possess high degrees of water stability, along with Lewis acidity. UiO-66 is typically made up of $[\text{Zr}_6\text{O}_4(\text{OH})_4]$ clusters with terephthalic acid (H_2BDC) as linker, resulting in the formation of UiO-66(Zr)-H. Its structure is characteristic for having a pore size of 6 Å along with tetrahedral and octahedral cavities of 7.4 and 8.4 Å, respectively.^{25,26} Among its uses, UiO-66(Zr)-H and its modified analogues have been applied for gas²⁷ and energy storage,^{28,29} gas separations³⁰ and for catalytic processes.^{31–33} Along with being thermally stable up until 300 °C, the most intriguing property is its reported water stability among other commonly used solvents.^{34,35}

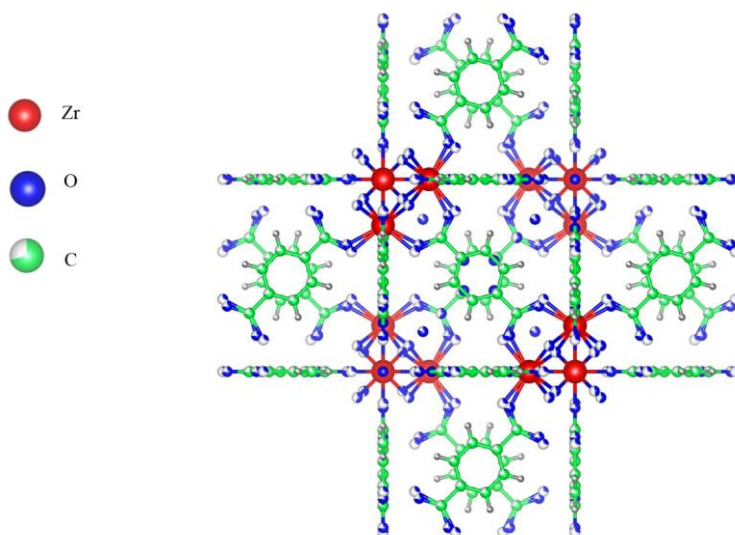


Figure 6.1. A visual representation of the UiO-66(Zr)-H MOF.

Due to the possibility of incorporating various metals (i.e. Zr, Hf, Ce) and linkers (i.e. H_2BDC , NH_2BDC , BDC-COOH etc.) into the MOF framework, these solids have been used on a wide array of kinetic reactions, such as in the glycerol acetylation,³³ glucose isomerization³⁶ and dehydration of glucose to 5-hydroxymethylfurfural (HMF).³¹ Due to the bigger channels available in this MOF, its potential to valorise bulkier substrates such as disaccharides with more ease, and can become an attractive application for these types of sugars.

However, although UiO-66(Zr)-H has been reported to possess good tolerance to water, its stability under true operational conditions (temperature, pressure, continuous), particularly as a function of catalytic reaction and choice of solvent, has not yet been explored. Moreover, their use as catalysts for biomass conversion processes is also relatively unexplored. This chapter presents a study

focused on the catalytic conversion of lactose to lactulose over UiO-66(Zr) MOFs. The solvents chosen for lactose isomerisation were based on solvothermal stability tests conducted by Justyna Minkiewicz³⁷ at continuous processing conditions, and preliminary kinetic details describing the activity and performance of these materials for this reaction are presented.

6.2 Results and discussion

6.2.1 MOF synthesis and characterisation

UiO-66(Zr)-H, as well as an amino-functionalised MOF (UiO-66(Zr)-NH₂) were synthesised by Justyna Minkiewicz. To verify the successful synthesis of the MOFs, powder X-ray diffraction (XRD) tests were carried out. Diffraction patterns of both untreated MOFs presented high crystallinity (Figure 6.2) and were consistent with previously reported XRD of this framework. No impurity or secondary phases were detected, and the most intense peaks were observed at 2θ values of 7.5° and 8.6° , which correspond to the (111) and (200) crystal planes, respectively.^{24,35} These findings, along with Scanning Electron Microscopy (SEM) images (Appendix 6.1, images obtained by Justyna Minkiewicz) indicate that the synthesis of UiO-66(Zr)-H and UiO-66(Zr)-NH₂ resulted in highly crystalline and uniform MOF structures.

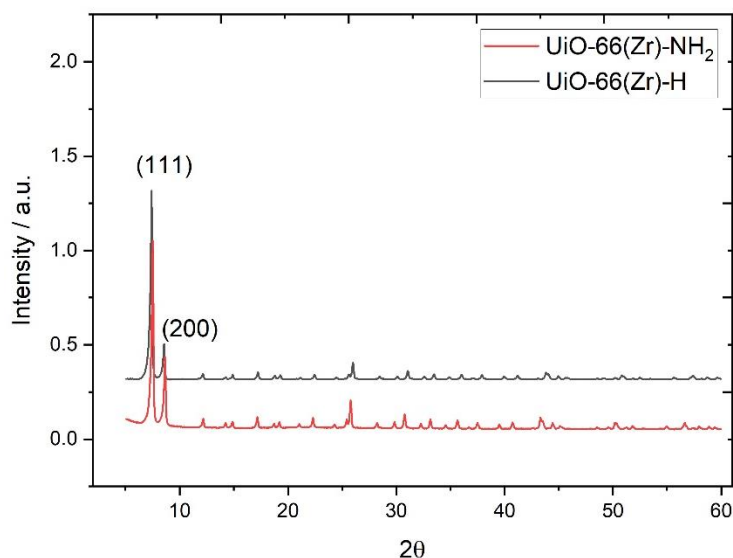


Figure 6.2. XRD spectra of untreated UiO-66(Zr)-H and UiO-66(Zr)-NH₂.

Nitrogen physisorption showed a significant change between both MOFs specific surface areas (SSA); while both presented a type I isotherm, their specific surface areas varied quite significantly, with UiO-66(Zr)-H having the higher SSA. Pore structure parameters can be seen in Appendix 6.2 and Table 6.1. As can be seen from Table 6.1, an inferior SSA was observed for the UiO-66(Zr)-NH₂ MOF (939 m² g⁻¹) compared to UiO-66(Zr)-H (1242 m² g⁻¹), which are in line with previously reported literature³⁸ Furthermore, the micropore volume showed a slightly higher amount for UiO-66(Zr)-NH₂ (0.504 cm³ g⁻¹) in comparison to UiO-66(Zr)-H (0.615 cm³ g⁻¹). These differences in area can be attributed due to the different number of linker defects as well as the available free space and increased overall weight of the UiO-66(Zr)-NH₂ MOF.^{38,39}

Table 6.1. Textural and pore size data of UiO-66(Zr)-H and -NH₂ MOFs.

Sample	Surface area (m ² g ⁻¹) ^a	Pore size (nm) ^b	V _{micro} (cm ³ g ⁻¹) ^b
UiO-66(Zr)-H	1242	1.98	0.615
UiO-66(Zr)-NH₂	939	2.14	0.504

^a Specific surface area obtained from BET.

^b Single point adsorption total pore volume of pores at P/P₀= 0.98.

UV-Vis analysis was performed to elucidate more on the speciation of Zr on both samples, as shown in Figure 6.3. In both UiO-66(Zr) structures, UV-Vis spectra presented peaks at 232 nm and 259 nm which are attributed to absorption of Zr-O oxo-clusters.⁴⁰ For UiO-66(Zr)-H, the terephthalate linker is attributed by the band shown at 285 nm and a shoulder at 300 nm, as reported by Roeffaers *et al.*⁴¹ It was observed that the H₂BDC linker showed no absorption in the visible region. However, unlike UiO-66(Zr)-H, UiO-66(Zr)-NH₂ sample presented two broad peaks which spanned between 350-450 nm; this is due to the nitrogen lone pairs ability to resonate through the benzene raising the energy required for the ligand-to-metal charge transfer (LMCT).⁴²

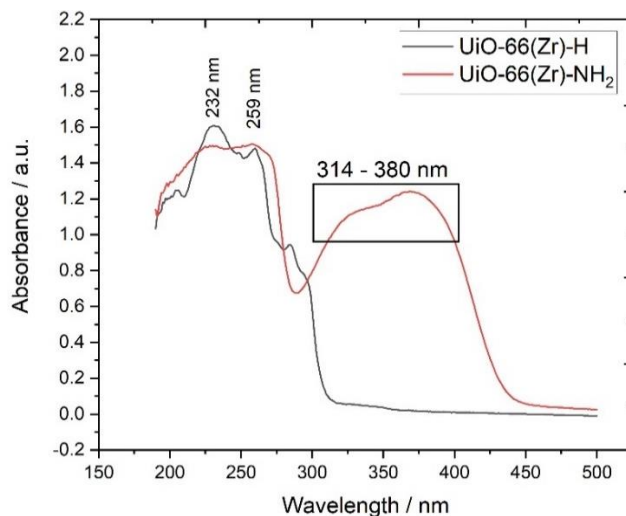


Figure 6.3. UV-Vis spectra of UiO-66(Zr)-H and UiO-66(Zr)-NH₂.

DRIFT spectra of UiO-66(Zr)-H and UiO-66(Zr)-NH₂ were also recorded, as illustrated in Figure 6.4. Whilst both spectra possessed similarities in the fingerprint region, clear distinctive features were observed, specifically at 3349 and 3465 cm⁻¹, which can be attributed to N-H stretches. Other peaks observed are 3676 cm⁻¹ and 1504 cm⁻¹, which are attributed to the bonding hydroxyl group $\nu(\text{Zr-O-H})$ and C=C stretching vibration of the phenyl ring, respectively; symmetric and asymmetric $\nu(-\text{COO})$ groups can be observed at 1451 cm⁻¹ and 1605 cm⁻¹, respectively. Symmetric and asymmetric vibrations of the aliphatic and aromatic modes can be accredited to the peaks at *ca.* 2800-3100 cm⁻¹. Other than the typical peaks observed from the MOFs, residual DMF from the synthesis could also be identified by the sharp peak at 1660-1675 cm⁻¹.

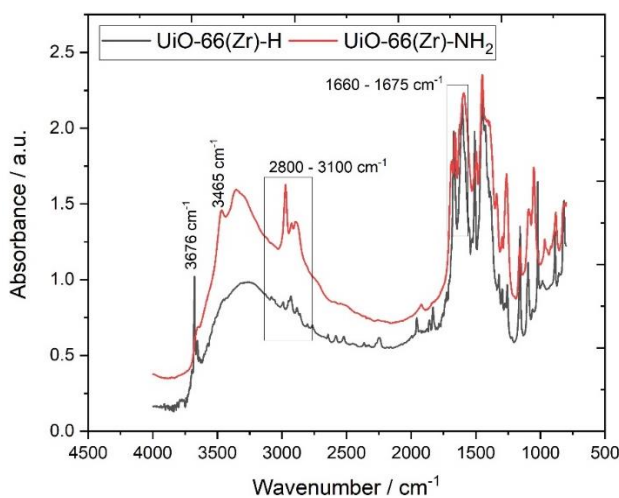


Figure 6.4. DRIFT spectra of UiO-66(Zr)-H and UiO-66(Zr)-NH₂.

The acidic properties of MOFs are known to be influenced by the choice of metal and linker, and can strongly impact ultimate catalytic performance. These properties can be elucidated by means of NH₃-Temperature Programmed Desorption studies, as demonstrated in the recent work by Minkiewicz.³⁷ As demonstrated in this recent study³⁷ (reproduced for ease of reviewing in Appendix 6.10 and Appendix 6.11), NH₃-TPD of UiO-66(Zr)-H displayed a peak at 270 °C, attributed to medium acid sites. UiO-66(Zr)-NH₂, on the other hand, showed three peaks: one weak (216 °C) and medium acid site 310 °C. For these MOFs, it has been reported that temperatures within the range of 250-300 °C, the frameworks inorganic [Zr₆O₄(OH)₄]¹²⁺ cluster undergo dehydroxylation,²⁴ modifying the metal unit to a Zr₆O₆ inner cluster, signalling that these peaks are mainly attributed to Lewis acids.⁴⁴ Peaks at elevated temperatures (+350 °C) have also been attributed to the degradation of both frameworks, albeit at a lower temperature for UiO-66(Zr)-NH₂ (387 °C) than for UiO-66(Zr)-H (*ca.* 500 °C).⁴⁵ This is in line with the signal observed for both MOFs without the sorption of NH₃. Whilst at elevated temperatures UiO-66 MOFs typically undergo degradation, NH₃ desorption was still present at 405 and 417 °C for UiO-66(Zr)-H and UiO-66(Zr)-NH₂, respectively. This can be possibly due to the available Zr metal sites which could form Zr-NH₃ complexes, despite the MOF structure degrading, leaving only the Zr oxo-clusters.¹⁸

6.2.2 Solvothermal stability studies of UiO-66(Zr)-H

Having characterised the textural properties of the untreated MOFs, solvothermal stability (STS) tests were subsequently conducted to ascertain the suitability of UiO-66(Zr)-H and UiO-66(Zr)-NH₂ for biomass conversion processes in the condensed phase. Solvothermal stability tests consist in the use of solvents under designated pressure and temperature to subsequently evaluate crystallinity, textural characteristics, and overall stability under that solvent. Due to the prevalence of methanol as a solvent during various biomass processing reactions,⁴⁶⁻⁴⁹ STS tests were performed with methanol as well as water. Given that methanol is considered unfavourable due to its toxicity, ethanol was also evaluated. STS measurements, along with their subsequent characterizations were carried out by Justyna Minkiewicz.³⁷ For ease of reviewing, this data has been provided by the previous author in the appendix, and the main conclusions of this previous study have been summarised in the following paragraph. STS tests were undertaken on 200 ± 10

mg of each material for a total of 120 h at 110 °C (10 bar) in a flow of the appropriate solvent at 0.3 mL min⁻¹.

Solvothermal-treated MOFs with water and ethanol studies showed negligible changes in their crystallinity and maintained their original crystalline phase even under high temperature and pressure for UiO-66(Zr)-H (120 h, 110 °C) (Appendix 6.7, inset). The methanol-treated MOFs, on the other hand, showed severe detrimental effect in terms of the framework crystallinity. Other than having a great loss of its crystallinity, additional peaks were observed, creating new, unknown phases. For UiO-66(Zr)-H, only one additional peak at 7.8 2 θ arose whereas for UiO-66(Zr)-NH₂ gave rise to three new peaks (7.8, 8.9, 9.5 2 θ). In conclusion, using methanol under these conditions was shown to have a severe detrimental effect on the overall structure, damaging the structure, as can be clearly seen in Appendices 6.7 and 6.8. It is important to note that while reactions using methanol have been carried out, they consisted in batch reactions,³⁶ which can drastically change the behaviour of the catalyst such as its stability from continuous flow reactions.

Nitrogen physisorption studies presented in Appendix 6.8 showed a significant change in the SSA of both MOFs following STS testing. Whilst both untreated MOFs originally presented different SSA, both MOFs interestingly exhibited the same trends in how their areas became modified upon STS treatment. In both cases, SSA was found to increase upon treatment in ethanol, with an increase to 2270 m² g⁻¹ for UiO-66(Zr)-H, and to 1841 m² g⁻¹ for UiO-66(Zr)-NH₂, a 42.5 % and 49 % increase in SSA, respectively. Water interestingly showed a 25% increase for both MOFs, with UiO-66(Zr)-H increasing from 1593 to 1991 m² g⁻¹, and UiO-66(Zr)-NH₂ from 1235 to 1647 m² g⁻¹. Methanol post-treated samples, however, not only showed the lowest SSA, but were the only samples to show hysteresis, which can be attributed to the presence of mesoporosity. This presence was corroborated by NLDFT PSD of the samples (Appendix 6.9), giving rise to pore diameters of 5.3 and 5.1 nm for UiO-66(Zr)-H and UiO-66(Zr)-NH₂, respectively. This formation of mesopores from the methanol treated sample can also be appreciated in Appendix 6.10, showing a decrease in the microporous volume from UiO-66(Zr)-H and UiO-66(Zr)-NH₂ with a V_{micro} of 0.229 cm³ g⁻¹, and 0.096 cm³ g⁻¹, respectively, which can indicate the partial collapsing of the MOF.

The UV-Vis spectra for the post-treated samples are shown in Appendix 6.11. It was observed that the 285 nm band, attributed to the terephthalate linker, lost some absorbance after treating UiO-

66(Zr)-H sample in methanol and water.⁴¹ Treatment in ethanol resulted in no change to the spectrum of the untreated catalyst sample. Some broadening of the 233 and 262 nm bands was observed following treatment in methanol and ethanol, which could indicate a modification in the Zr-O oxo clusters. This could be due to a change in the O-NH₂ complexation caused by the polar solvents. With the polar solvents occluding within the MOF, changes in their stretching vibration can be limited, hence, creating these distinct bathochromic shifts.⁵⁰

UiO-66(Zr)-NH₂ also showed physical changes in the colour of the MOF after STS. This is caused due to the shifts of the amino functionalization group responsible for providing the colour of the MOF. These variations could also indicate modifications in the electronic band structure around the band gap after applying different polar solvents.⁵¹ As can be seen in Appendix 6.12, every STS treatment had a distinct colour after drying the sample at 110 °C, where the methanol-treated MOF had a brighter yellow colour; the ethanol-treated sample showed a yellow-brown colour; and lastly, the water-treated sample had the most drastic change out of the three, with a light brown colour. UiO-66(Zr)-H, due to the absence of any peaks close to the visible range, did not present any physical changes in its hue.

Solid-State Magic Angle Spinning Nuclear Magnetic Resonance (SS MAS-NMR) analysis was studies provided information of the solvent's effect on the carbon speciation (Appendix 6.13). Prior to MAS NMR analysis, samples were placed in an oven at 110 °C to remove any excess solvent. Solid state ¹³C Cross-polarization (CP) MAS-NMR for UiO-66(Zr)-H showed three distinct peaks: at 172 ppm, attributed to the carboxylic group carbon atoms, 138 ppm to the quaternary carbon atoms, and 130 ppm which consists of -CH groups. In both frameworks, but primarily in UiO-66(Zr)-NH₂, residual dimethylformamide (DMF) from the synthesis preparation could be detected in the untreated samples (28, 34, and 161 ppm). In addition to possessing the three previously mentioned peaks from the UiO-66(Zr)-H, three additional peaks were detected for UiO-66(Zr)-NH₂. 149 ppm is attributed to the C atom attached to the functionalized amino whilst the 116 and 122 ppm signals arise from the surrounding carbon atoms of the amino-attached carbon.⁵¹ In the methanol-treated STS UiO-66(Zr)-NH₂, there was a significant decrease of intensity on the carboxylic resonance (~170 ppm); additional peaks could also be seen within the range of 45-60 ppm, which can be attributed to the methanol used for STS treatment.⁵² Nandy *et*

al reported that methanol absorption at higher frequencies (Appendix 6.12, Right) can be attributed mainly to in-pore methanol whereas ex-pore methanol corresponds to lower frequency. Given the higher intensity shown mainly for in-pore methanol, this could indicate that after subsequent removal of the solvents at elevated temperatures, methanol remained occluded within the framework.

Moreover, in all STS treatments for UiO-66(Zr)-NH₂, the 122 ppm peak disappears. This signal can be attributed to the surrounding carbon atoms of the amino-attached carbon, indicating they could have been damaged during the STS. Small resonances at 30 and 39 ppm can be observed for all post-treated samples with the exception of the MeOH-treated MOFs, due to the higher degree of degradation. These peaks could possibly indicate dangling -R₃CH₃ or R₂CH₂NH₂ groups caused by the solvents, for UiO-66(Zr)-H and UiO-66(Zr)-NH₂, respectively. This could possibly indicate a reasoning as to the increase of SSA in the MOFs after STS (Appendix 6.8), undergoing a similar procedure as to dealumination/desilication of zeolites.

Marreiros *et al.* have shown its post-synthetic linker exchange (PSE), step to exchange the MOF with a differently functionalized analogue without losing its crystallinity, using solvents such as methanol for both the terephthalate and 2-aminoterephthalate linkers.⁵³ This has shown to provide stability of dangling linkers as well as their creation.⁵⁴ For this experiment, however, strong resonances were detected in NMR for their STS, regardless of them being washed prior to their study,

From the data gathered in this recent study, it has been concluded that out of the three solvents tested for STS testing, methanol was the only solvent to have shown any negative effects towards the crystalline structure of the MOF, reducing its crystallinity and its total surface area whilst creating mesopores, as a result of damage to the building units by affecting the terephthalate linker. In contrast, excellent stability was observed when STS treatments were performed in water or ethanol, indicating these to be more suitable solvents for catalytic studies.

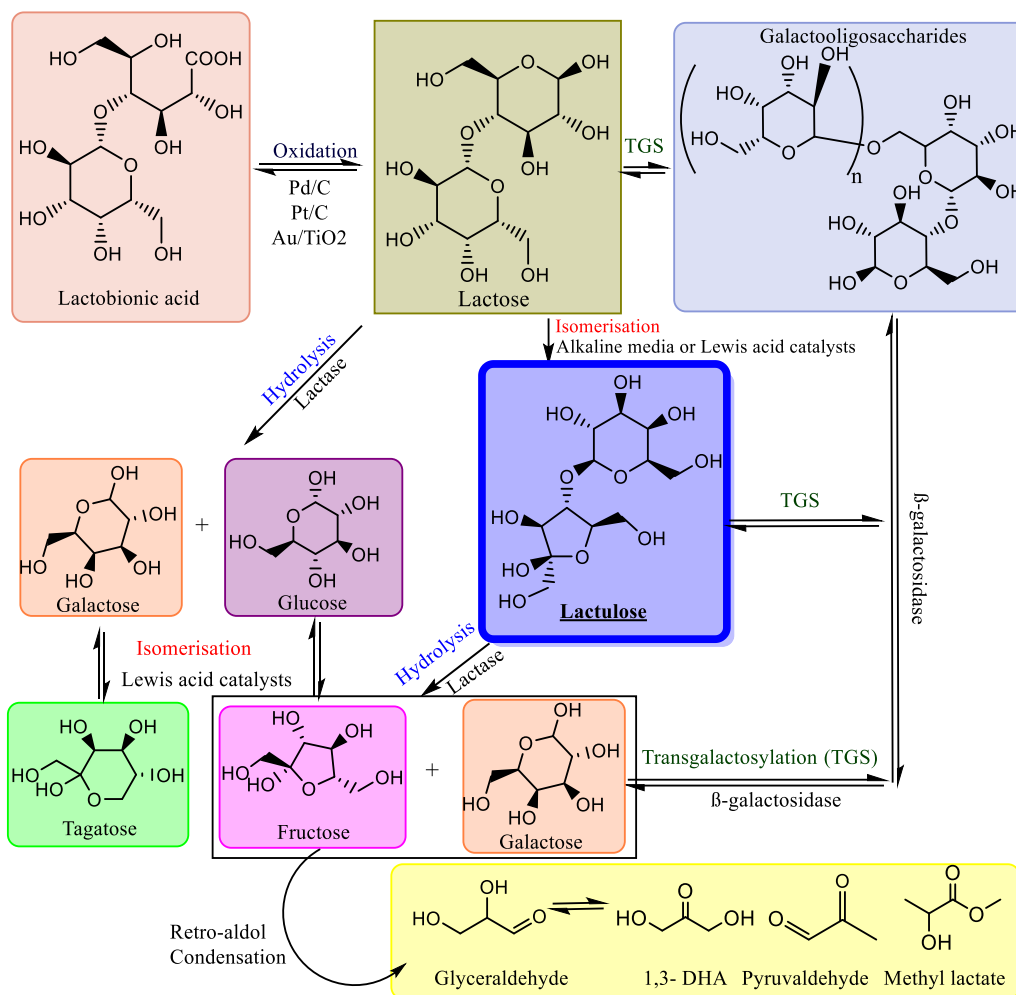
6.2.3. Kinetic studies of MOF for lactose isomerisation

Having known the implications and the influence of the solvothermal stability studies as performed by Minkiewicz³⁷, to probe and understand the kinetic performance of UiO-66(Zr), instead of conventional glucose isomerisation, liquid phase isomerisation of lactose to lactulose was investigated. Lactose was chosen based on its kinetically analogous similarities to glucose,

additionally to allow the probing of the channels for potential bulky substrate upgrading. For these studies, water and ethanol were chosen as reaction solvents, due to the better compatibility of the MOFs in these solvents as evidenced by the STS studies. Furthermore, reactions were performed in continuous flow, which in addition to providing several advantages with regards to process intensification, also provide more rigorous evaluation of catalyst stability.

Lactulose is a non-absorbable disaccharide made up of galactose and fructose monomers linked through β -1,4-glycosidic bond, which can be obtained from lactose, a disaccharide commonly found in milk and whey. This synthetic sugar is mainly used for pharmaceutical and nutraceutical purposes, as well as in the food industry. It is mainly used to reduce blood ammonia concentrations in the treatment of hepatic encephalopathy,⁵⁵ and as a laxative for constipation. Due to its prebiotic properties, it can also promote healthy gastrointestinal tract bacteria like bifidobacterial and lactobacilli,⁵⁶ which help digestion and stave off harmful bacteria like salmonella.⁵⁷ Lactulose has also gained more interest as a precursor along with lactose to make galactooligosaccharides (GOS) via transgalactosylation, which also have prebiotic effects,⁵⁸⁻⁶⁰ and have been shown to have benefits with colorectal cancer (CRC).^{61,62} The global lactulose market was valued between \$180-190 million USD in 2010,⁶³ with an estimated global production of 42,000 tons per year. With an abundance of uses that promote health benefits, the lactulose market is expected to increase growth within the forthcoming years.

Lactulose can also be used as a precursor to produce equimolar amounts of galactose and fructose *via* hydrolysis using β -galactosidase, as shown in Scheme 6.1.⁶⁴ This pathway can offer a distinctive alternative to obtain fructose and fructose-derived compounds to the typical glucose isomerisation route (glyceraldehyde, 1,3 dihydroxyacetone, pyruvaldehyde, methyl lactate, and methyl vinyl glycolate)⁶⁵ which may allow both lactose and whey waste to also be employed more usefully, further promoting sustainable waste management and a circular economy. From the galactose moiety, it is also possible to produce tagatose, a reducing sugar that is generally recognized as a safe product (GRAS) and is used a nutritional sweetener with low caloric value, *via* isomerisation with a Lewis acid catalyst.



Scheme 6.1. Schematic representation of the reaction pathways of lactose.

Industrially, lactulose is achieved by isomerization via the Lobry de Bruyn-Alberda van Ekenstein (LA) rearrangement,⁶⁶ isomerising the glucose moiety of lactose to fructose mainly using homogeneous alkaline media. Typical catalysts used for this process include hydroxides^{67,68}, boric acid,⁶⁹ carbonates⁷⁰ and aluminates.⁷¹ Other present works involving lactose upgrading are lactose electroisomerisation carried out by Aider and Karim,⁷² which involved using a cation exchange (RuO₂-IrO₂-TiO₂ electrode) and anion exchange (stainless steel electrode) membrane with K₂SO₄ as the electrolyte at various currents. Although effective, there are several downsides when employing the former catalysts. These include the requirement of expensive and challenging separation procedures when employing alkali salts, which are usually achieved by electrolysis or ion-exchange resins. Another key disadvantage is the catalytic degradation of lactose that can occur at elevated temperatures in the presence of alkali compounds, which makes the use of higher

temperatures impossible, negatively impacting reactor productivity and limiting the thermodynamic equilibrium yields that are achievable. The utilisation of homogeneous additives, along with the purification of lactulose from the by-products produced in these cases, can make downstream processing operationally expensive and unattractive.

At this time, no literature exists regarding the isomerisation of lactose to lactulose with any MOF under the continuous regime. However, given the promising stability of UiO-66(Zr) at high temperature and pressure in continuous flow, the MOFs were tested for lactose isomerisation at continuous processing conditions. The use of a higher reaction temperature (160 °C) was deliberately chosen, as elevated temperature permits the stability of the catalysts to be probed in a more intense manner, and such elevated temperature operation cannot be achieved by the state of the art approaches due to the degrading effects in alkaline solution.

Lactose is typically composed from two anomers (α - and β -lactose), each of which has different levels of solubility in various solvents, with α -lactose tending to be the less soluble of the two.^{73,74} These solubilities are an important factor when it comes to working with alcoholic solvents given that at even low relative wt.% of the substrate, lactose does not solubilize effectively with polar solvents other than water. As such, the poor solubility of lactose in the alcohol (0.07 g L⁻¹ at 22 °C) prohibited the use of pure ethanol as the solvent for lactose isomerisation.⁷⁵

Due to limited previous work, initial experiments on lactose isomerization were carried out in pure water. Additionally, given the prevalent application of methanol as a medium for sugar isomerization – albeit to the detriment of catalyst stability during glucose isomerisation - ethanol was used as a potential substitute, given its promising results, stability-wise.^{75–78} Ethanol is hypothesized to act similar to methanol, increasing sugar conversion due to the higher solvation (higher solvent uptake) of the zeolite's hydrophobic pores.⁷⁹ However, due to the low solubility of lactose in pure alcohol, reactions using binary mixtures of ethanol and water were carried out.

Prior to lactose isomerization tests using the aforementioned MOFs, a hydrothermally synthesised Sn-Beta (1 wt. % Sn) in fluoride media was tested in continuous flow at 160 °C at 0.4 mL min⁻¹. However, no lactulose nor any other side-products were observed throughout the reaction. While there have been reports on Sn-Beta⁸⁰ and other zeolites such as a hierarchical⁸¹ and self-pillared MFI nanosheets⁸², these mentioned reactions were carried out in batch. This lack of contact time with the substrate in continuous flow for bulkier sugars can possibly diminish any Sn-substrate

interaction due to steric hindrances whereas with batch reactions it is much easier for the sugars to react with surface Sn atoms available.

As can be seen in Figure 6.5, reactions took place using pure water as solvent, and three binary mixtures of EtOH:H₂O. Firstly, in pure water as solvent, both MOFs presented slight differences in lactulose yield, with UiO-66(Zr)-H being the higher-active MOF, averaging *ca* 9 % lactulose yield throughout the 72 h period. For UiO-66(Zr)-NH₂, although lactulose yield was shown to be higher than the UiO-66(Zr)-H (10 %), it steadily decreased within the first hours, showing discreet signs of deactivation throughout the run, averaging a 5.6 % lactulose yield within the final hours.

Reactions done in a 50:50 EtOH:H₂O binary mixture with UiO-66(Zr)-H showed no signs of deactivation and presented a higher lactulose yield (15 %) than its preceding reaction that was done solely in water. UiO-66(Zr)-NH₂ showed a high initial lactulose yield similar to UiO-66(Zr)-H, seemingly benefiting from having ethanol in the feed. However, lactulose yield showed an abrupt drop within the first hours, having an average yield of *ca.* 10 % throughout the time on stream, showing overall a lower activity than UiO-66(Zr)-H just as the reaction with solely water.

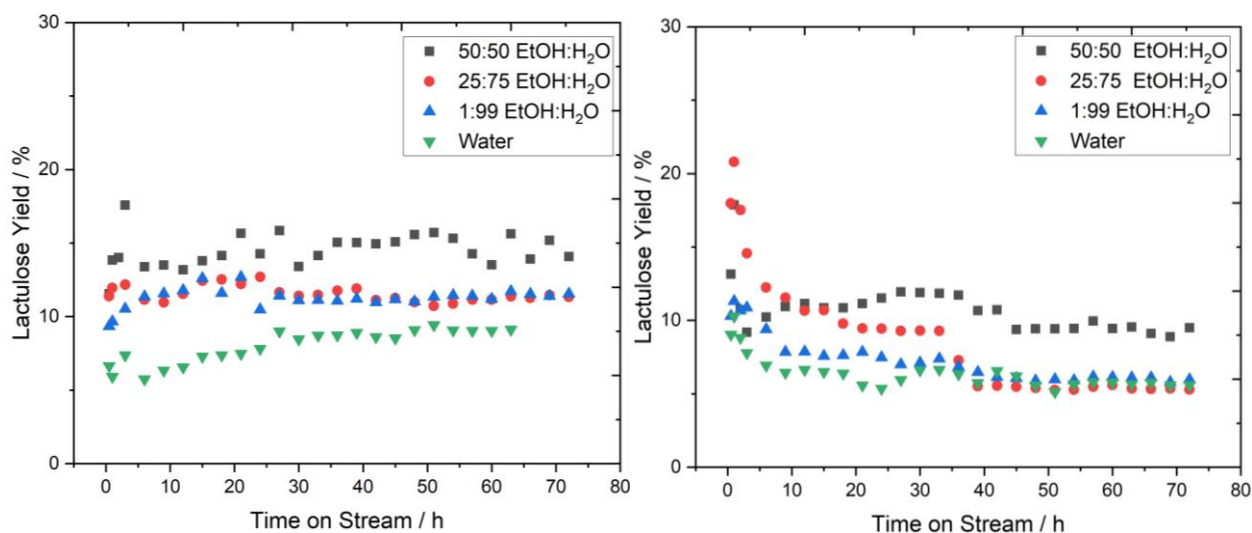


Figure 6.5. Lactulose yield for UiO-66(Zr)-H (left) and UiO-66(Zr)-NH₂ (right) in water and different EtOH:H₂O ratios. Reaction conditions: 160 °C, 18 bar, 1 wt.% lactose in water, flow rate of 0.4 mL min⁻¹, 100 mg of catalyst.

To further probe the effects of ethanol and its influence on the kinetic activity, two additional EtOH:H₂O ratios were carried out: 25:75 and 1:99 EtOH:H₂O; these were compared with the previous two reactions. As its preceding reactions, for UiO-66(Zr)-H, 25:75 and 1:99 EtOH:H₂O

ratio reactions were stable throughout the 72 h period and showed no signs of deactivation. Both reactions also presented relatively identical yields ($\sim 11\%$). Reactions for UiO-66(Zr)-NH₂, on the other hand, revealed similar tendencies when it came to performance and deactivation. Unlike the UiO-66(Zr)-H, reactions using 1:99 and 25:75 EtOH:H₂O did not exhibit similar activity, as is shown in Figure 6.6 (right). The 25:75 EtOH:H₂O mixture presented a high initial lactulose yield followed by a steep decline, similar to the 50:50 EtOH:H₂O mixture. Looking further into the yield, we can see that unlike UiO-66(Zr)-H, there is no clear difference after 72 h in the reaction, obtaining similar yields (5.6 %) in all mixtures excluding the 50:50 EtOH:H₂O mixture, which can clearly indicate that a higher ethanol content is beneficial for kinetic activity in this system.

To elucidate further, a lactose conversion vs. lactulose selectivity graph was plotted to determine if there existed any trend to selectivity with the change in alcohol content. As can be seen in Figure 6.6 (Left), UiO-66(Zr)-H presented two distinguishable regimes of selectivity in accordance with the EtOH:H₂O ratio; the 50:50 EtOH:H₂O mixture was found to be not only the most active, but most selective as well, showing higher selectivity at overlapping conversions with higher ethanol. This was followed by the remaining two EtOH:H₂O ratios (25:75 and 1:99), which presented similar selectivity along with kinetic activity. Lastly was water, being the least selectivity as well as active.

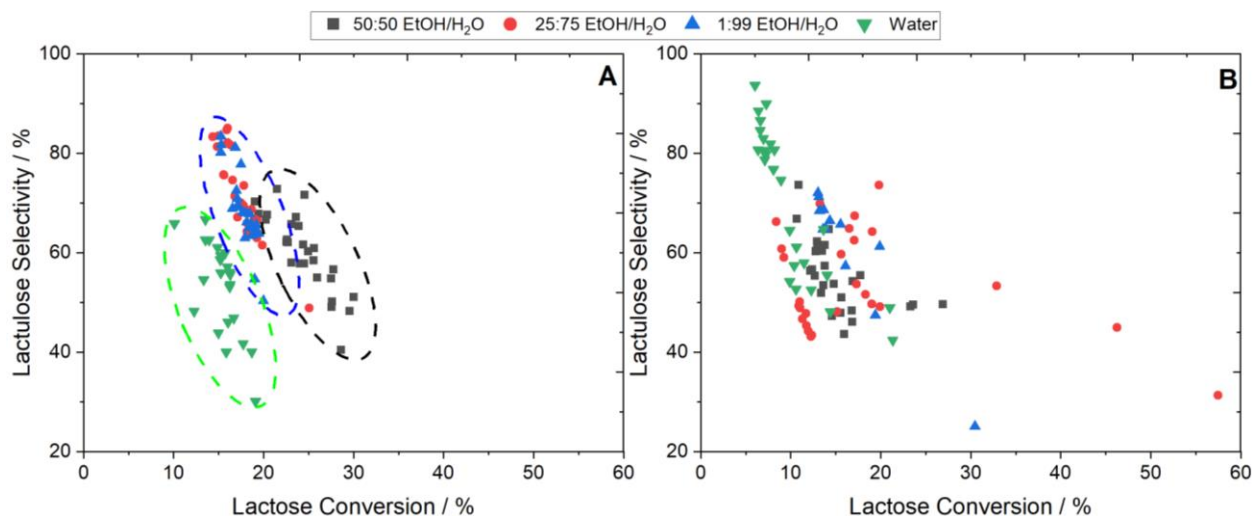


Figure 6.6. Lactose conversion vs. lactulose selectivity of UiO-66(Zr)-H (left) UiO-66(Zr)-NH₂ (right) in water and different EtOH:H₂O ratios. Reaction conditions: 160 °C, 18 bar, 1 wt.% lactose in water, flow rate of 0.4 mL min⁻¹, 100 mg of catalyst.

UiO-66(Zr)-NH₂, on the other hand, presented contrasting trends regarding its lactulose selectivity when compared to UiO-66(Zr)-H. Along with having overall lower selectivity for all ratios at overlapping conversion, UiO-66(Zr)-NH₂ did not seem to have distinctive separation in selectivity performance as observed for UiO-66(Zr)-H (Figure 6.6, Right) when using different binary mixtures and water. However, the 50:50 mixture was still overall the most selective with the remaining mixtures and water falling in line with one another. This could indicate the positive influence ethanol can have at higher concentration for activity as well as selectivity, showing a positive effect in both MOFs.

Whilst there was clearly distinct activity amongst the reactions with different binary mixtures, the overall carbon balance with respect to lactose conversion had similar trends for both MOFs regardless of the mixture (Figure 6.7). This sudden drop in selectivity can indicate that other reaction pathways are more favourable with UiO-66(Zr)-NH₂. A possible product which can be created is epilactose (galactose-mannose moieties), achieved by epimerisation of the glucose moiety, or simply complete degradation of the substrate.⁸³ Owing to the absence of monosaccharides (glucose, fructose, galactose, tagatose), hydrolysis of the disaccharides (lactose and lactulose) is not considered to be responsible for the drop in carbon balance nor any retro-aldol fragmentation products such as methyl lactate or methyl vinyl glycolate.

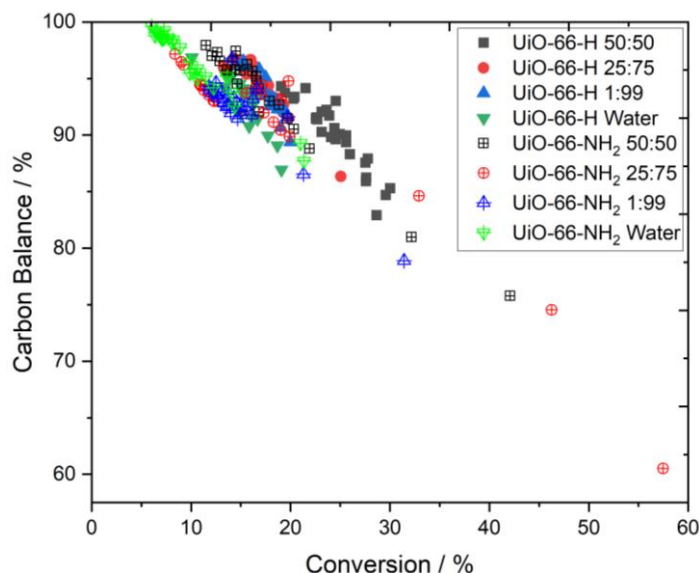


Figure 6.7 Lactose conversion vs. carbon balance of UiO-66(Zr)-H and UiO-66(Zr)-NH₂ in binary mixtures and water.

However, when it came to their productivity, there was an increase shown for UiO-66(Zr)-H when it came to higher ethanol content (Figure 6.8), unlike with UiO-66(Zr)-NH₂, which did not show a clear trend in productivity. This increase in productivity with higher ethanol content can also mutually benefit lactulose purification/separation from lactose due to the differences in solubility of both disaccharides. The use of supercritical fluid,⁸⁴ solid-phase,⁸⁵ and pressurized liquid extraction⁸⁶ for lactulose separation have been reported using binary mixtures of ethanol and water, obtaining lactulose purities of up to 95 %.

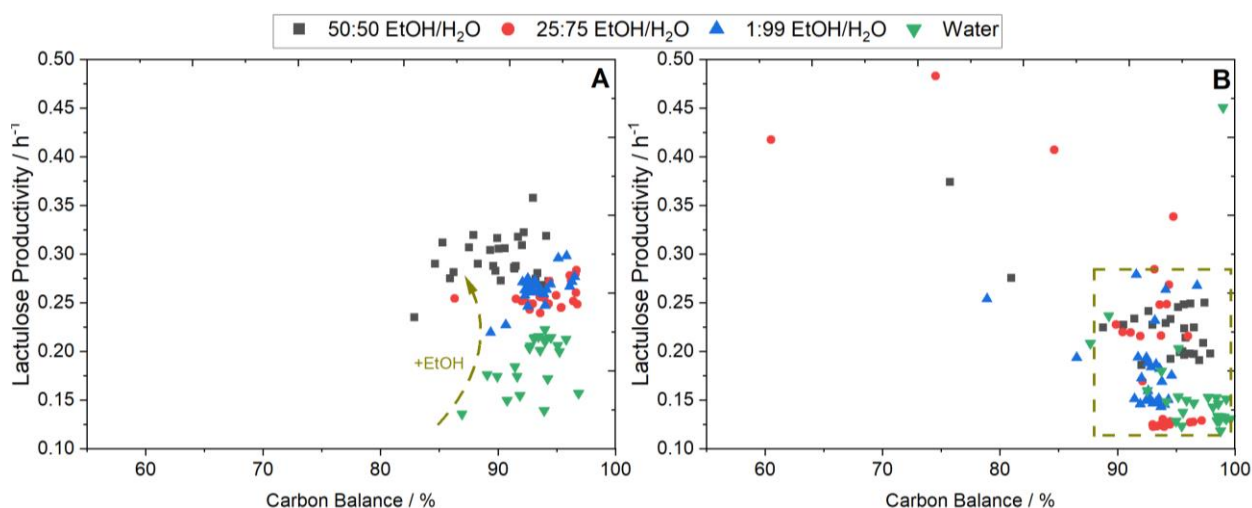
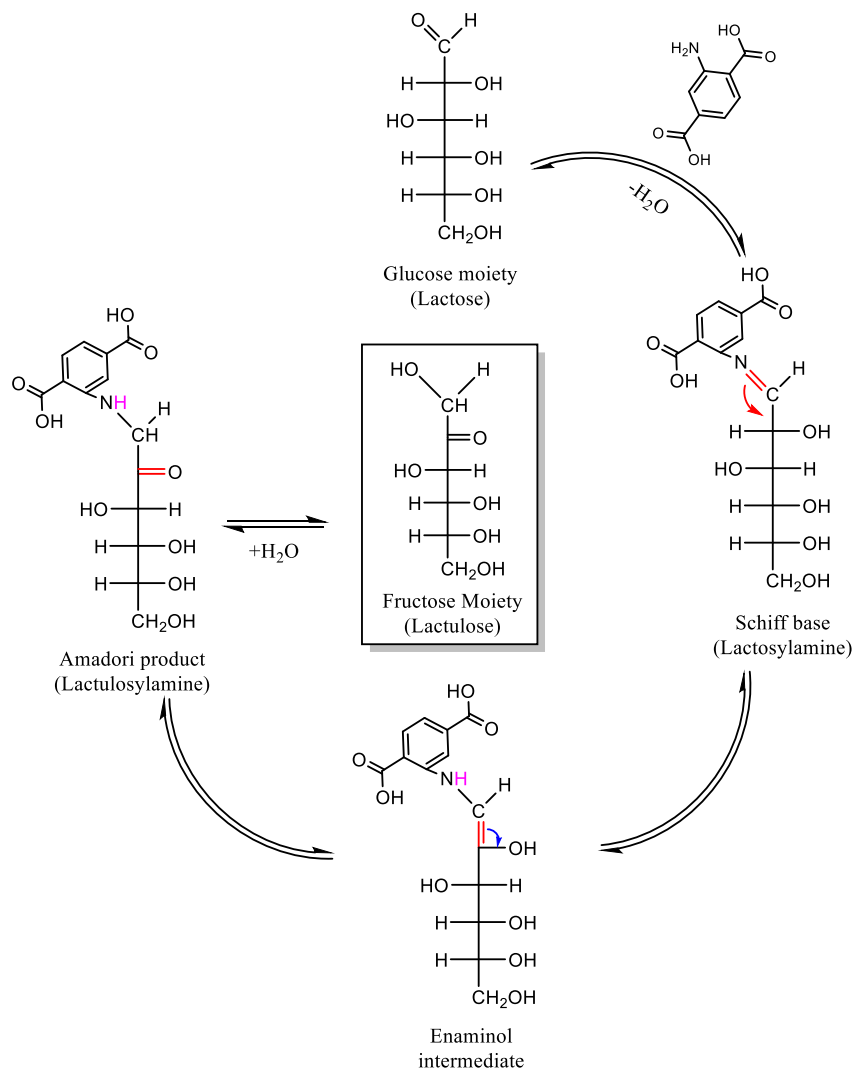


Figure 6.8. Carbon balance vs. lactulose productivity of UiO-66(Zr)-H (left) and UiO-66(Zr)-NH₂ (right) in binary mixtures and water.

This high initial conversion that is presented only in the UiO-66(Zr)-NH₂ could indicate that the amino functional group serves a role when it comes to converting lactose. Other than the 1,2-hydride shift that could be expected from the Zr metal, the -NH₂ group could aid in the production of lactulose via the Maillard reaction,^{63,87} as is shown in Scheme 6.2. The chemical reaction between the -NH₂ group in the aminoterephthalic acid and the glucose moiety forms a Schiff base (secondary imine) to form the lactosylamine.⁸⁸ The lactosylamine undergoes an Amadori rearrangement, forming a 1-amino-deoxy-ketose (lactulosylamine), which can be hydrated to remove the amino group, forming lactulose. This, along with the isomerisation reactions from the Zr metal cluster, could be working in tandem, thus the reason as to its high conversion. Nevertheless, due to the conditions of the reaction system that was used, this high conversion is

short-lived. Furthermore, the colour of UiO-66(Zr)-NH₂ post-reaction can also be seen in Figure 6.10. This dark brown colour can also be attributed to the Maillard reaction, which provides the browning of foods.



Scheme 6.2. Proposed mechanism of lactose isomerisation with the amino group from 2-aminoterephthalic acid.



Figure 6.9. UiO-66(Zr)-NH₂ after lactose isomerisation reaction with 50:50 EtOH:H₂O solution.

6.3 Conclusions

STS tests using three different polar solvents (MeOH, EtOH, H₂O) were performed for UiO-66(Zr)-H and UiO-66(Zr)-NH₂ to determine their overall effectiveness as catalysts under true operational conditions in continuous flow. While EtOH- and H₂O-treated MOFs seemed to provide a beneficial effect in the MOFs, increasing their SSA while not affecting its crystallinity, MeOH-treated MOFs showed severe degradation in their crystallinity as well as the creation of new phases and pore sizes. Based on the findings of STS testing, preliminary kinetic studies were performed focusing on lactose isomerisation as a model reaction for biomass upgrading using water, and different mixtures of EtOH:H₂O. During these studies it was found that the application of these MOFs in continuous flow proved to be a stable catalyst under long periods in all the solutions used. Whilst reactions in water were successful, isomerisation benefitted both kinetically and selectivity-wise with the presence of ethanol in the mixture, even when adding a small quantity (1:99 EtOH:H₂O) in the solution. This (1:99 EtOH:H₂O) interestingly showed the same result at 25:75 EtOH:H₂O mixture and only improved at the higher 50:50 ratio, which can indicate that ethanol concentration requires a certain threshold to improve the catalytic activity or that water can have a slight negative impact in the activity at high (>50 %) concentrations. This, however, did not present itself when tested on UiO-66(Zr)-NH₂, and only showed a higher production of lactulose at 50:50 EtOH:H₂O ratio. This novel usage of this MOF can open a variety of reactions regarding different disaccharides or other bulkier substrates in continuous flow and more importantly, straying away from the use of methanol and facilitate the scale-up of the reaction, a commonly

used solvent for sugar valorisation. Additionally, the conditions that were implemented give optimistic results towards the use of these materials in a practical, industrial setting for these substrates.

6.4 References

1. Graça, I., Bacariza, M. C., Fernandes, A. & Chadwick, D. Desilicated NaY zeolites impregnated with magnesium as catalysts for glucose isomerisation into fructose. *Appl. Catal. B Environ.* **224**, 660–670 (2018).
2. Lari, G. M., Dapsens, P. Y., Scholz, D., Mitchell, S., Mondelli, C. & Pérez-Ramírez, J. Deactivation mechanisms of tin-zeolites in biomass conversions. *Green Chem.* **18**, 1249–1260 (2016).
3. Takahara, I., Saito, M., Inaba, M. & Murata, K. Dehydration of ethanol into ethylene over solid acid catalysts. *Catal. Letters* **105**, 249–252 (2005).
4. Kim, J., Park, W. & Ryoo, R. Surfactant-directed zeolite nanosheets: A high-performance catalyst for gas-phase beckmann rearrangement. *ACS Catal.* **1**, 337–341 (2011).
5. Pérez-Ramírez, J., Verboekend, D., Bonilla, A. & Abelló, S. Zeolite catalysts with tunable hierarchy factor by pore-growth moderators. *Adv. Funct. Mater.* **19**, 3972–3979 (2009).
6. Koller, H., Senapati, S., Ren, J., Uesbeck, T., Siozios, V., Hunger, M. & Lobo, R. F. Post-Synthesis Conversion of Borosilicate Zeolite Beta to an Aluminosilicate with Isolated Acid Sites: A Quantitative Distance Analysis by Solid-State NMR. *J. Phys. Chem. C* **120**, 9811–9820 (2016).
7. Padovan, D., Parsons, C., Simplicio Grasina, M. & Hammond, C. Intensification and deactivation of Sn-beta investigated in the continuous regime. *Green Chem.* **18**, 5041–5049 (2016).
8. Oozeerally, R., Burnett, D. L., Chamberlain, T. W., Walton, R. I. & Degirmenci, V. Exceptionally Efficient and Recyclable Heterogeneous Metal–Organic Framework Catalyst for Glucose Isomerization in Water. *ChemCatChem* **10**, 706–709 (2018).
9. Yuthalekha, T., Wattanakit, C., Warakulwit, C., Wannapakdee, W., Rodponthukwaji, K., Witoon, T. & Limtrakul, J. Hierarchical FAU-type zeolite nanosheets as green and sustainable catalysts for benzylation of toluene. *J. Clean. Prod.* **142**, 1244–1251 (2017).
10. Botti, L., Navar, R., Tolborg, S., Martinez-Espin, J. S., Padovan, D., Taarning, E. & Hammond, C. Influence of Composition and Preparation Method on the Continuous Performance of Sn-Beta for Glucose-Fructose Isomerisation. *Top. Catal.* **0**, 0 (2018).
11. Farha, O. K., Eryazici, I., Jeong, N. C., Hauser, B. G., Wilmer, C. E., Sarjeant, A. A., Snurr, R. Q., Nguyen, S. T., Yazaydin, A. Ö. & Hupp, J. T. Metal-organic framework materials with ultrahigh surface areas: Is the sky the limit? *J. Am. Chem. Soc.* **134**, 15016–15021 (2012).
12. Martin, R. L. & Haranczyk, M. Exploring frontiers of high surface area metal–organic frameworks. *Chem. Sci.* **4**, 1781–1785 (2013).
13. Qin, L. & Zheng, H. G. Structures and applications of metal-organic frameworks featuring metal clusters. *CrystEngComm* **19**, 745–757 (2017).
14. Dhakshinamoorthy, A., Asiri, A. M. & Garcia, H. Tuneable nature of metal organic frameworks as heterogeneous solid catalysts for alcohol oxidation. *Chem. Commun.* **53**, 10851–10869 (2017).

15. Moreno, J. M., Veltý, A., Díaz, U. & Corma, A. Synthesis of 2D and 3D MOFs with tuneable Lewis acidity from preformed 1D hybrid sub-domains. *Chem. Sci.* **10**, 2053–2066 (2019).
16. Jacobsen, J., Ienco, A., D'Amato, R., Costantino, F. & Stock, N. The chemistry of Ce-based metal-organic frameworks. *Dalt. Trans.* **49**, 16551–16586 (2020).
17. He, T., Xu, X., Ni, B., Wang, H., Long, Y., Hu, W. & Wang, X. Fast and scalable synthesis of uniform zirconium-, hafnium-based metal-organic framework nanocrystals †. **9**, (2017).
18. Decoste, J. B., Peterson, G. W., Schindler, B. J., Killops, K. L., Browe, M. A. & Mahle, J. J. The effect of water adsorption on the structure of the carboxylate containing metal-organic frameworks Cu-BTC, Mg-MOF-74, and UiO-66. *J. Mater. Chem. A* **1**, 11922–11932 (2013).
19. Furukawa, H., Cordova, K. E., O'Keeffe, M. & Yaghi, O. M. The chemistry and applications of metal-organic frameworks. *Science (80-.)*. **341**, (2013).
20. Kuo, C. H., Tang, Y., Chou, L. Y., Sneed, B. T., Brodsky, C. N., Zhao, Z. & Tsung, C. K. Yolk-shell nanocrystal@ZIF-8 nanostructures for gas-phase heterogeneous catalysis with selectivity control. *J. Am. Chem. Soc.* **134**, 14345–14348 (2012).
21. Brozek, C. K. & Dincă, M. Ti³⁺-, V^{2+/3+}-, Cr^{2+/3+}-, Mn²⁺-, and Fe²⁺-substituted MOF-5 and redox reactivity in Cr- and Fe-MOF-5. *J. Am. Chem. Soc.* **135**, 12886–12891 (2013).
22. Fan, S., Dong, W., Huang, X., Gao, H., Wang, J., Jin, Z., Tang, J. & Wang, G. In Situ-Induced Synthesis of Magnetic Cu-CuFe₂O₄@HKUST-1 Heterostructures with Enhanced Catalytic Performance for Selective Aerobic Benzylic C-H Oxidation. *ACS Catal.* **7**, 243–249 (2017).
23. Smolders, S., Lomachenko, K. A., Bueken, B., Struyf, A., Bugaev, A. L., Atzori, C., Stock, N., Lamberti, C., Roeffaers, M. B. J. & De Vos, D. E. Unravelling the Redox-catalytic Behavior of Ce⁴⁺ Metal-Organic Frameworks by X-ray Absorption Spectroscopy. *ChemPhysChem* **19**, 373–378 (2018).
24. Cavka, J. H., Jakobsen, S., Olsbye, U., Guillou, N., Lamberti, C., Bordiga, S. & Lillerud, K. P. A new zirconium inorganic building brick forming metal organic frameworks with exceptional stability. *J. Am. Chem. Soc.* **130**, 13850–13851 (2008).
25. Furukawa, H., Gándara, F., Zhang, Y. B., Jiang, J., Queen, W. L., Hudson, M. R. & Yaghi, O. M. Water adsorption in porous metal-organic frameworks and related materials. *J. Am. Chem. Soc.* **136**, 4369–4381 (2014).
26. Peterson, G. W., Moon, S. Y., Wagner, G. W., Hall, M. G., Decoste, J. B., Hupp, J. T. & Farha, O. K. Tailoring the Pore Size and Functionality of UiO-Type Metal-Organic Frameworks for Optimal Nerve Agent Destruction. *Inorg. Chem.* **54**, 9684–9686 (2015).
27. Connolly, B. M., Aragonés-Anglada, M., Gandara-Loe, J., Danaf, N. A., Lamb, D. C., Mehta, J. P., Vulpe, D., Wuttke, S., Silvestre-Albero, J., Moghadam, P. Z., Wheatley, A. E. H. & Fairen-Jimenez, D. Tuning porosity in macroscopic monolithic metal-organic frameworks for exceptional natural gas storage. *Nat. Commun.* **10**, 1–11 (2019).
28. Wang, Q. & Tang, S. Energy storage analysis of CO₂ in MOF-74 and UiO-66 nanoparticles: A molecular simulation study. *Int. J. Mod. Phys. B* 229–234 (2019) doi:10.1142/S0217979219501960.

29. Zhou, Y., Li, Q. & Wang, Q. Energy storage analysis of UiO-66 and water mixed nanofluids: An experimental and theoretical study. *Energies* **12**, 1–9 (2019).
30. Castarlenas, S., Téllez, C. & Coronas, J. Gas separation with mixed matrix membranes obtained from MOF UiO-66-graphite oxide hybrids. *J. Memb. Sci.* **526**, 205–211 (2017).
31. Gong, J., Katz, M. J. & Kerton, F. M. Catalytic conversion of glucose to 5-hydroxymethylfurfural using zirconium-containing metal-organic frameworks using microwave heating. *RSC Adv.* **8**, 31618–31627 (2018).
32. Fang, Y., Ma, Y., Zheng, M., Yang, P., Asiri, A. M. & Wang, X. Metal-organic frameworks for solar energy conversion by photoredox catalysis. *Coord. Chem. Rev.* **373**, 83–115 (2018).
33. Bakuru, V. R., Churipard, S. R., Maradur, S. P. & Kalidindi, S. B. Exploring the Brønsted acidity of UiO-66 (Zr, Ce, Hf) metal-organic frameworks for efficient solketal synthesis from glycerol acetalization. *Dalt. Trans.* **48**, 843–847 (2019).
34. Ma, D., Han, G., Peh, S. B. & Chen, S. B. Water-Stable Metal-Organic Framework UiO-66 for Performance Enhancement of Forward Osmosis Membranes. *Ind. Eng. Chem. Res.* **56**, 12773–12782 (2017).
35. Liu, X., Demir, N. K., Wu, Z. & Li, K. Highly Water-Stable Zirconium Metal-Organic Framework UiO-66 Membranes Supported on Alumina Hollow Fibers for Desalination. *J. Am. Chem. Soc.* **137**, 6999–7002 (2015).
36. de Mello, M. D. & Tsapatsis, M. Selective Glucose-to-Fructose Isomerization over Modified Zirconium UiO-66 in Alcohol Media. *ChemCatChem* **10**, 2417–2423 (2018).
37. Minkiewicz, J. Published Thesis. (Cardiff University, 2021).
38. Kandiah, M., Nilsen, M. H., Usseglio, S., Jakobsen, S., Olsbye, U., Tilset, M., Larabi, C., Quadrelli, E. A., Bonino, F. & Lillerud, K. P. Synthesis and stability of tagged UiO-66 Zr-MOFs. *Chem. Mater.* **22**, 6632–6640 (2010).
39. Waitschat, S., Fröhlich, D., Reinsch, H., Terraschke, H., Lomachenko, K. A., Lamberti, C., Kummer, H., Helling, T., Baumgartner, M., Henninger, S. & Stock, N. Synthesis of M-UiO-66 (M = Zr, Ce or Hf) employing 2,5-pyridinedicarboxylic acid as a linker: Defect chemistry, framework hydrophilisation and sorption properties. *Dalt. Trans.* **47**, 1062–1070 (2018).
40. Sun, D., Liu, W., Qiu, M., Zhang, Y. & Li, Z. Introduction of a mediator for enhancing photocatalytic performance via post-synthetic metal exchange in metal-organic frameworks (MOFs). *Chem. Commun.* **51**, 2056–2059 (2015).
41. Laurier, K. G. M., Fron, E., Atienzar, P., Kennes, K., Garcia, H., Van Der Auweraer, M., De Vos, D. E., Hofkens, J. & Roeyffers, M. B. J. Delayed electron-hole pair recombination in iron(iii)-oxo metal-organic frameworks. *Phys. Chem. Chem. Phys.* **16**, 5044–5047 (2014).
42. Nasalevich, M. A., Van Der Veen, M., Kapteijn, F. & Gascon, J. Metal-organic frameworks as heterogeneous photocatalysts: Advantages and challenges. *CrystEngComm* **16**, 4919–4926 (2014).
43. Zhang, K. D., Tsai, F. C., Ma, N., Xia, Y., Liu, H. L., Zhan, X. Q., Yu, X. Y., Zeng, X. Z., Jiang, T., Shi, D. & Chang, C. J. Adsorption behavior of high stable Zr-Based MOFs for the removal of acid organic dye from water. *Materials (Basel)*. **10**, 1–4 (2017).

44. Zhou, F., Lu, N., Fan, B., Wang, H. & Li, R. Zirconium-containing UiO-66 as an efficient and reusable catalyst for transesterification of triglyceride with methanol. *J. Energy Chem.* **25**, 874–879 (2016).
45. Mounfield, W. P., Taborga Claire, M., Agrawal, P. K., Jones, C. W. & Walton, K. S. Synergistic Effect of Mixed Oxide on the Adsorption of Ammonia with Metal-Organic Frameworks. *Ind. Eng. Chem. Res.* **55**, 6492–6500 (2016).
46. Bermejo-Deval, R., Gounder, R. & Davis, M. E. Framework and extraframework tin sites in zeolite beta react glucose differently. *ACS Catal.* **2**, 2705–2713 (2012).
47. Hwang, S. J., Gounder, R., Bhawe, Y., Orazov, M., Bermejo-Deval, R. & Davis, M. E. Solid State NMR Characterization of Sn-Beta Zeolites that Catalyze Glucose Isomerization and Epimerization. *Top. Catal.* **58**, 435–440 (2015).
48. Parker, J. & Novakovic, K. The effect of using a methanol–water solvent mixture on pH oscillations in the palladium-catalyzed phenylacetylene oxidative carbonylation reaction. *React. Kinet. Mech. Catal.* **123**, 113–124 (2018).
49. Paquin, F., Rivnay, J., Salleo, A., Stingelin, N. & Silva, C. Multi-phase semicrystalline microstructures drive exciton dissociation in neat plastic semiconductors. *J. Mater. Chem. C* **3**, 10715–10722 (2015).
50. Hendrickx, K., Vanpoucke, D. E. P., Leus, K., Lejaeghere, K., Van Yperen-De Deyne, A., Van Speybroeck, V., Van Der Voort, P. & Hemelsoet, K. Understanding Intrinsic Light Absorption Properties of UiO-66 Frameworks: A Combined Theoretical and Experimental Study. *Inorg. Chem.* **54**, 10701–10710 (2015).
51. Devautour-Vinot, S., Maurin, G., Serre, C., Horcajada, P., Paula Da Cunha, D., Guillerm, V., De Souza Costa, E., Taulelle, F. & Martineau, C. Structure and dynamics of the functionalized MOF type UiO-66(Zr): NMR and dielectric relaxation spectroscopies coupled with DFT calculations. *Chem. Mater.* **24**, 2168–2177 (2012).
52. Nandy, A., Forse, A. C., Witherspoon, V. J. & Reimer, J. A. NMR Spectroscopy Reveals Adsorbate Binding Sites in the Metal-Organic Framework UiO-66(Zr). *J. Phys. Chem. C* **122**, 8295–8305 (2018).
53. Marreiros, J., Caratelli, C., Hajek, J., Krajnc, A., Fleury, G., Bueken, B., De Vos, D. E., Mali, G., Roeffaers, M. B. J., Van Speybroeck, V. & Ameloot, R. Active Role of Methanol in Post-Synthetic Linker Exchange in the Metal-Organic Framework UiO-66. *Chem. Mater.* **31**, 1359–1369 (2019).
54. Kim, M., Cahill, J. F., Su, Y., Prather, K. A. & Cohen, S. M. Postsynthetic ligand exchange as a route to functionalization of ‘inert’ metal-organic frameworks. *Chem. Sci.* **3**, 126–130 (2012).
55. Weber, F. L. Lactulose and combination therapy of hepatic encephalopathy: The role of the intestinal microflora. *Dig. Dis.* **14**, 53–63 (1996).
56. Aider, M. & Halleux, D. de. Isomerization of lactose and lactulose production: review. *Trends Food Sci. Technol.* **18**, 356–364 (2007).
57. Ankenbauer-Perkins, K. *Small Animal Clinical Pharmacology. Australian Veterinary Journal* vol. 80 (Elsevier Ltd, 2002).

58. Sabater, C., Fara, A., Palacios, J., Corzo, N., Requena, T., Montilla, A. & Zárata, G. Synthesis of prebiotic galactooligosaccharides from lactose and lactulose by dairy propionibacteria. *Food Microbiol.* **77**, 93–105 (2019).
59. Adamczak, M., Charubin, D. & Bednarski, W. Influence of reaction medium composition on enzymatic synthesis of galactooligosaccharides and lactulose from lactose concentrates prepared from whey permeate. *Chem. Pap.* **63**, 111–116 (2009).
60. Marín-Manzano, M. C., Abecia, L., Hernández-Hernández, O., Sanz, M. L., Montilla, A., Olano, A., Rubio, L. A., Moreno, F. J. & Clemente, A. Galacto-oligosaccharides derived from lactulose exert a selective stimulation on the growth of bifidobacterium animalis in the large intestine of growing rats. *J. Agric. Food Chem.* **61**, 7560–7567 (2013).
61. Fernández, J., Moreno, F. J., Olano, A., Clemente, A., Villar, C. J. & Lombó, F. A galacto-oligosaccharides preparation derived from lactulose protects against colorectal cancer development in an animal model. *Front. Microbiol.* **9**, 1–14 (2018).
62. Bruno-Barcena, J. M. & Azcarate-Peril, M. A. Galacto-oligosaccharides and colorectal cancer: Feeding our intestinal probiome. *J. Funct. Foods* **12**, 92–108 (2015).
63. Paterson, A. H. J. & Kellam, S. J. *Transformation of lactose for value-added ingredients. Dairy-Derived Ingredients: Food and Nutraceutical Uses* (Woodhead Publishing Limited, 2009). doi:10.1533/9781845697198.3.625.
64. Marconi, E., Messia, M. C., Amine, A., Moscone, D., Vernazza, F., Stocchi, F. & Palleschi, G. Heat-treated milk differentiation by a sensitive lactulose assay. *Food Chem.* **84**, 447–450 (2004).
65. Díez-Municio, M., Herrero, M., Olano, A. & Moreno, F. J. Synthesis of novel bioactive lactose-derived oligosaccharides by microbial glycoside hydrolases. *Microb. Biotechnol.* **7**, 315–331 (2014).
66. Silvério, S. C., Macedo, E. A., Teixeira, J. A. & Rodrigues, L. R. Biocatalytic Approaches Using Lactulose: End Product Compared with Substrate. *Compr. Rev. Food Sci. Food Saf.* **15**, 878–896 (2016).
67. Montgomery, E. M. Relations between rotatory power and structure in the sugar group. XXVII. Synthesis of a new disaccharide ketose (lactulose) from lactose. *J. Am. Chem. Soc.* **52**, 2101–2106 (1930).
68. Tariq, N. The Chemical Isomerization of Lactose to Lactulose by Using Sodium Hydroxide as Batch Reaction The Chemical Isomerization of Lactose to Lactulose by Using Sodium Hydroxide as Batch Reaction. (2018).
69. Kozempel, M. & Kurantz, M. The isomerization kinetics of lactose to lactulose in the presence of borate. *J. Chem. Technol. Biotechnol.* **59**, 25–29 (1994).
70. Seo, Y. H., Park, G. W. & Han, J. I. Efficient lactulose production from cheese whey using sodium carbonate. *Food Chem.* **173**, 1167–1171 (2015).
71. Wang, M., Gasmalla, M. A. A., Admassu Tessema, H., Hua, X. & Yang, R. Lactulose production from efficient isomerization of lactose catalyzed by recyclable sodium aluminate. *Food Chem.* **233**, 151–158 (2017).
72. Karim, A. & Aider, M. Sustainable Electroisomerization of Lactose into Lactulose and Comparison with the Chemical Isomerization at Equivalent Solution Alkalinity. *ACS Omega* **5**, 2318–2333 (2020).

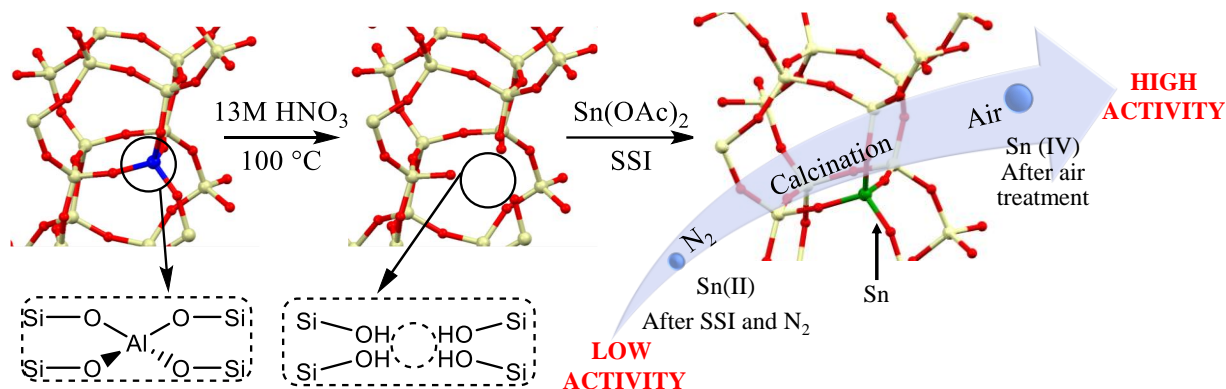
73. Majd, F. & Nickerson, T. A. Effect of Alcohols on Lactose Solubility. *J. Dairy Sci.* **59**, 1025–1032 (1976).
74. Altamimi, M. J., Wolff, K., Nokhodchi, A., Martin, G. P. & Royall, P. G. Variability in the α and β anomer content of commercially available lactose. *Int. J. Pharm.* **555**, 237–249 (2019).
75. Montañés, F., Olano, A., Ibáñez, E. & Fornari, T. Modeling solubilities of sugars in alcohols based on original experimental data. *AIChE J.* **53**, 2411–2418 (2007).
76. Gounder, R. & Davis, M. E. Titanium-beta zeolites catalyze the stereospecific isomerization of d -glucose to l -sorbose via intramolecular C5-C1 hydride shift. *ACS Catal.* **3**, 1469–1476 (2013).
77. Bermejo-Deval, R., Orazov, M., Gounder, R., Hwang, S. J. & Davis, M. E. Active sites in Sn-beta for glucose isomerization to fructose and epimerization to mannose. *ACS Catal.* **4**, 2288–2297 (2014).
78. Botti, L., Padovan, D., Navar, R., Tolborg, S., Martinez-Espin, J. S. & Hammond, C. Thermal Regeneration of Sn-Containing Silicates and Consequences for Biomass Upgrading: From Regeneration to Preactivation. *ACS Catal.* **10**, 11545–11555 (2020).
79. Christianson, J. R., Caratzoulas, S. & Vlachos, D. G. Computational Insight into the Effect of Sn-Beta Na Exchange and Solvent on Glucose Isomerization and Epimerization. *ACS Catal.* **5**, 5256–5263 (2015).
80. Gounder, R. & Davis, M. E. Monosaccharide and disaccharide isomerization over Lewis acid sites in hydrophobic and hydrophilic molecular sieves. *J. Catal.* **308**, 176–188 (2013).
81. Dapsens, P. Y., Mondelli, C., Jagielski, J., Hauert, R. & Pérez-Ramírez, J. Hierarchical Sn-MFI zeolites prepared by facile top-down methods for sugar isomerisation. *Catal. Sci. Technol.* **4**, 2302–2311 (2014).
82. Ren, L., Guo, Q., Kumar, P., Orazov, M., Xu, D., Alhassan, S. M., Mkhoyan, K. A., Davis, M. E. & Tsapatsis, M. Self-Pillared, Single-Unit-Cell Sn-MFI Zeolite Nanosheets and Their Use for Glucose and Lactose Isomerization. *Angew. Chemie - Int. Ed.* **54**, 10848–10851 (2015).
83. Seki, N. & Saito, H. Lactose as a source for lactulose and other functional lactose derivatives. *Int. Dairy J.* **22**, 110–115 (2012).
84. Montañés, F., Fornari, T., Martín-Álvarez, P. J., Montilla, A., Corzo, N., Olano, A. & Ibáñez, E. Selective fractionation of disaccharide mixtures by supercritical CO₂ with ethanol as co-solvent. *J. Supercrit. Fluids* **41**, 61–67 (2007).
85. Brereton, K. R. & Green, D. B. Isolation of saccharides in dairy and soy products by solid-phase extraction coupled with analysis by ligand-exchange chromatography. *Talanta* **100**, 384–390 (2012).
86. Ruiz-Matute, A. I., Sanz, M. L., Corzo, N., Martín-Álvarez, P. J., Ibáñez, E., Martínez-Castro, I. & Olano, A. Purification of lactulose from mixtures with lactose using pressurized liquid extraction with ethanol-water at different temperatures. *J. Agric. Food Chem.* **55**, 3346–3350 (2007).
87. Smit, G. *Dairy processing - Improving Quality*. (Woodhead Publishing Limited, 316AD).
88. Adachi, S. & Patton, S. Presence and Significance of Lactulose in Milk Products: A Review. *J. Dairy Sci.* **44**, 1375–1393 (1961).

Chapter 7. Conclusions and pertaining challenges

7.1 Final conclusions

Over the last two decades, Lewis acid catalysts, in particular Sn-Beta, have been meticulously studied given their promising potential for biomass valorisation. Whilst possessing high catalytic activity, Sn-Beta has still not reached industrial feasibility. This is due to the difficult synthesis procedure, requiring vast amounts of time even for low wt. % (<2 wt. %) of Sn. Furthermore, hydrothermal synthesis of Sn-Beta also requires the use of fluoride anions as a mineraliser rather than hydroxide. This route is not only environmentally unfriendly but creates micron-sized crystals, leading to intracrystalline diffusion limitations.¹ Hence, various methods of zeolite synthesis, both bottom-up and top-down, have been carried out to tailor the synthesis of Sn-Beta, whether it be to reduce the crystal sizes,² avoid the use of fluoride as a mineraliser,³ or to increase the overall Sn content in the zeolite.⁴

Top-down synthesis of Sn-Beta via mechanochemical grinding has been thoroughly studied to assess the evolution of the Sn precursor (Sn(II) acetate) and how it interacts with a dealuminated beta zeolite and Si-Beta (*i.e.*, no silanol nests). The importance of silanol nests was necessary to obtain a highly active catalyst along with a two-step heat treatment protocol of inert atmosphere (N₂ or He) and air afterwards. The most interesting aspect that was observed via the spectroscopic data was the superfluous isotherm step in the inert gas flow as well as the extended air isotherm. This data provided a substantial optimization of the heat treatment, with no negative impact whatsoever in regard to the intrinsic activity nor the stability of the final catalyst. This optimization can make the application of SSI an even more attractive alternative for this particular catalyst, cutting unnecessary energy costs. However, there exist limitations when taking the SSI approach. As has been shown previously, the formation of Sn spectator sites occurs when incorporating at Sn content of 5 wt. % and higher, which consequently exhibit lower TOF values.^{4,5}



Scheme 7.1. SSI using two-step (inert and air flow) heat treatment.

Seeing the potential of SSI when applying it to the conventional (and commercial) Al-Beta, another point of interest lied in the application of using hydrothermally-synthesised parent zeolites with different heteroatoms (B, Ga, Fe, Al) to subsequently remove and incorporate Sn. Here, fluoride as the mineraliser was used to assure the incorporation of the heteroatoms. It was found that the different heteroatoms were shown to have some differences when it came to kinetic activity, but the difference was more apparent in their rate of deactivation as evidenced by their stability during the retro-aldol fragmentation of glucose. B-Beta as initial parent zeolite for SSI was shown to have promising results for retro-aldol fragmentation, presenting the highest yields for α -hydroxy esters. To check how effective this change in heteroatoms really was, these catalysts were further tested with low temperature glucose isomerisation, during which it demonstrated a more evident improvement in activity to the other catalysts, presenting higher yields as well as a better rate of deactivation. This increase in stability and/or activity can be due to how the order of the silanol nests are after demetallation. Using Al and B siting with SS-NMR,⁶ it has been reported that when B is incorporated, they are incorporated in diagonal pairs, while Al is typically incorporated as a lone atom. Sn has been reported to increase in Lewis acidity when there exists a double isomorphous substitution (*i.e.* two Sn in the 4-MR instead of one), which can possibly indicate the increase in activity for glucose isomerisation.^{7,8} Although this increase in activity (*i.e.* yield) is not as evident for the high temperature retro-aldol fragmentation, this might suggest that this increase in activity does not necessarily apply to all systems, where reaction temperature can potentially influence the performance of these diagonal Sn pairs. The use of B may also present a greener solution as an alternative to the heteroatom of choice for SSI due to the ease of removing this

heteroatom from the zeolitic framework, seeing as how it has been shown that B can be removed under mild conditions using water instead of the highly concentrated HNO_3 that is typically required for the demetallation of conventional Al-Beta zeolites.

In chapter 5, an alternative class of porous heterogeneous catalysts was explored. Specifically, metal-organic frameworks containing Zr ions were explored as catalysts. UiO-66(Zr)-H and its amino-functionalised analogue UiO-66(Zr)- NH_2 were tested on the same reactor systems for sugar valorisation. Given the high stability that these MOFs reportedly possess, they seemed to have potential to carry out similar reactions as zeolites, given that they have isolated Lewis acid metal centres. Given that the MOFs possess larger channels than conventional zeolites, lactose, a disaccharide, was used as the precursor to gauge the activity and stability of the MOFs. Initially, to investigate whether there were issues concerning the stability of the materials in solvent media, the MOFs were tested under three different polar solvents, *i.e.* water, methanol, and ethanol. These were carried out at reaction conditions similar to the glucose isomerisation reaction. These solvents were chosen given their extensive use as solvents for sugar isomerisation. Methanol was shown to have a detrimental effect on the crystallinity and overall structure of the MOF whereas ethanol and water showed no negative outcome. One property that was modified, however, was their surface area, as determined by BET and NLDFT. In particular, a flow of the polar solvents (water and ethanol) was found to increase the surface area by a substantial amount after solvothermal treatment. With this, ethanol and water were chosen for the subsequent reactions of lactose. In view of the stability obtained from prior data, a higher degree to the reaction conditions was opted for the conversion of lactose to lactulose. One problem that was encountered was the solubility of lactose in pure alcohol, especially ethanol. Thus, binary mixtures of ethanol and water were used to carry out the reaction. All reactions performed in binary mixtures as well as water were shown to be active for lactose isomerisation and presented high stability, maintaining similar lactulose yields for 72 h. Ethanol seemingly played an important role when it came to increasing the activity, even when only small amounts were added (1 % EtOH v/v in water), for both MOFs, increasing lactulose productivity up by *ca.* 55 % (0.18 h^{-1} and 0.28^{-1} for H_2O and 1:99 EtOH: H_2O , respectively). UiO-66(Zr)- NH_2 presented kinetic differences in comparison to UiO-66(Zr)-H, particularly at the initial stages, showing an elevated conversion of lactose of up to 58 %. This was attributed to the amino group, which has been demonstrated to aid lactose in undergoing an Amadori rearrangement forming firstly a lactosylamine, and subsequently lactulosylamine. This

lactulosylamine is rehydrated to create the fructose moiety from the lactulose. Although this MOF was shown to have initially elevated conversion rates, it is relatively brief. This was attributed to possible usage of the amino groups, hence, no possibility of undergoing this secondary reaction. Nevertheless, the use of UiO-66(Zr) was found to be successful at reaction conditions similar to that of zeolites that we have previously reported.

Lastly, in chapter 6, a study was carried out for hierarchical zeolites using a pore-directing agent (PDA). Zeolites, whilst predominantly microporous in nature, have the ability to be treated to create a bimodal porosity (*i.e.*, micro-mesopores, micro-macro). The creation of these additional pores of different sizes can provide the zeolite to have enhanced properties such as an improvement in rate of deactivation, diffusion of bulkier substrates, and overall changes in selectivity. Desilication studies for the creation of hierarchical zeolites were initially studied using commercial zeolites (Zeolyst – Si/Al = 19) applying mixture of CTABr (0.2 M) as the PDA and NaOH (0.2 M) at different temperatures to assess their respective textural modifications. Both micropore and mesopore volume and areas were shown to increase with respect to the increase in temperature, as confirmed by NLDFT and the t-plot method. Application of a higher concentration of alkali (0.3 M) resulted in an overall increase in the micro-meso structural properties (area/volume), indicating that improvement of the zeolites textural properties were possible even at higher OH⁻ concentration, provided that a PDA was also present. The use of PDA did show the uniformity of the secondary pores, with a slight rise in the peak when using 0.3 M, which could be due to the elevated degradation, and hence, more susceptibility of pore creation. Activity and stability were shown to drastically improve over glucose retro-aldol fragmentation when using the hierarchical catalysts, showing a 40 % initial increase in methyl lactate (ML) yield than the post-synthetic Sn-Beta. ML over time was improved as well, as it still produced product after 40 h of time on stream whereas the conventional post-synthetic catalysts ceased to produce ML after *ca.* 25 h. Nevertheless, the creation of hierarchical zeolites over fluoride-assisted zeolites did not show any fruitful results. When applying desilication on the catalysts, even with the use of a PDA, it was found that their crystallinity was severely affected. Various reasons for this observation were considered, including the possibilities that; the different heteroatoms (*i.e.* Sn, Hf, Zr) may not protect the lattice as well as Al when undergoing desilication, ii) if the use of heteroatom does not play a key role for protection, the high Si/M molar ratio can be a key factor in the catalysts amorphization; or iii) due

to the defect-free nature of the catalysts, a total collapse can give rise when performing any sort of silicon leaching, even if mild.

7.2 Pertaining challenges

Whilst a thorough study was carried out for the SSI of Sn-Beta was carried out and provides a fundamental reasoning to the incorporation mechanism, additional studies can further complement the holistic view of this mechanistic study:

- 1) Implementing the same mechanism for another framework (*i.e.* MFI, TUD-1). Would the difference in zeolite channels influence the ease of incorporation and/or would SSI be more easily applicable in a zeolite with mesopores?
- 2) Mechanistic study utilising different Sn precursors such as Sn(IV) acetate, Sn(II) chloride, Sn(IV) chloride, Sn(II) oxalate, Sn(II) sulphate, etc. Studies involving these different precursors could lead to helpful answers involving the requirements to what is needed for an active catalyst: would the use Sn(IV) acetate require only the nitrogen step, seeing as how it is already in a +4 oxidation state, or would be it more inefficient, further emphasising the importance of the two-step protocol of nitrogen/air. Is there a specific reason as to why acetate has been universally used for SSI? What kinetic differences would there exist if one would use a different Sn precursor? Does the evolution of the acetate group (in the case of Sn(II) acetate) influence the adequate incorporation to create an active catalyst, or would any derivative (*i.e.* sulphate, oxalate, chloride) suffice? This can be in combination with the first bullet point, particularly for zeolites with mesoporosity, which can effectively null any steric hindrances from the Sn precursor.
- 3) Applying the SSI for different target metals, such as Hf-, Zr-, or possibly trivalent metals such (Ga, Fe). This could show provide vital information of the transferability of the mechanism or a newfound mechanistic study which would imply that the study is mainly Sn (or even Sn(II) acetate) specific.

Given the results obtained from SSI, a crucial role which could provide a greener synthesis to the overall scheme of this route, is the substitution of Al for another more easily extractable heteroatom while inhibiting similar (or better) catalytic activity, which Chapter 4 provides. One thing to note is that while better, all the zeolites were synthesised under fluoride medium. This can be enough

to reconsider the use of the zeolite for any commercial use. Thus, tests using a hydroxide-assisted synthesis for B-Beta should be an imperative step for the catalyst to be more feasible in an industrial scope. Similar to the previous points (1), one challenge can consist in the exploration of different frameworks for the substitution of the initial heteroatom with Sn. This could possibly be more easily achievable due to the absence of requiring fluoride as a mineraliser, hence, a greener alternative to create B-derived zeolites for subsequent demetallation-remetallation.

Valorisation of disaccharides (or other bulky substrates) using metal-organic frameworks under continuous flow reactors is a relatively new area of catalysis. Although it was shown that they have potential for biomass upgrading in the continuous regime, more studies are still necessary to adequately assess these heterogeneous catalysts which can compete with conventionally-used/studied catalysts (*i.e.*, zeolites). Furthermore, more reactions can be explored in which hierarchical zeolites have been used, such as MPV reduction of cyclododecanone, a sterically-challenging substrate for conventional microporous zeolites.⁹ This reaction could be possible due to the good stability observed in ethanol in contrast with methanol, which can indicate that with a higher carbon chain, the more stable the solvent with the MOF. Other points of interest are long, time on stream stability of the MOFs. The MOFs were shown to be highly stable over 72 h, which can be considered apposite for reactions such as these. Nevertheless, to assess the potential of activity as well as stability, longer time on stream reaction is needed.

Although desilication on fluoride-assisted zeolites was found unsuccessful, this provided important insight regarding the degree of degradation. Sn-Beta-F was found to be the least affected catalyst, crystallinity-wise, albeit not by much. This can indicate influence of initial heteroatom and their degrees of protecting the adjacent or nearby silicon atoms from being leached. Possible methods of improving, or better yet, successfully creating a hierarchical catalyst from a fluoride-assisted zeolite, consist in synthesising a lower Si/M catalyst. This, however, can be considered a difficult task for heteroatoms that have been previously used (Sn, Hf, Zr) for the Beta framework. Therefore, to conclusively ascertain the desilication effect on defect-free zeolites, a Sn-MFI with a Si/Sn ratio of 33 can be used as a catalyst for this subsequent procedure, in this case, with fluoride anions.¹⁰

To conclude, this thesis work provides research on mechanistic studies of the conventional Sn-Beta zeolite and an optimisation of the heat treatment protocol, which has never been thoroughly

explored. Studies that show potential heteroatoms other than Al atoms for the SSI protocol to provide a greener catalyst synthesis. A prospective substitute for bulky substrate upgrading, MOFs, and their surprising stability in similar reaction conditions as the ones carried out for zeolites. And finally, an attempt into creating hierarchical catalysts with fluoride-assisted zeolites. Together, these findings contribute to the body of work surrounding the use of Lewis acidic for continuous flow liquid-phase reactions.

7.3. References

1. Hammond, C., Conrad, S. & Hermans, I. Simple and scalable preparation of highly active lewis acidic Sn- β . *Angew. Chemie - Int. Ed.* **51**, 11736–11739 (2012).
2. Yang, X., Liu, Y., Li, X., Ren, J., Zhou, L., Lu, T. & Su, Y. Synthesis of Sn-Containing Nanosized Beta Zeolite As Efficient Catalyst for Transformation of Glucose to Methyl Lactate. *ACS Sustain. Chem. Eng.* **6**, 8256–8265 (2018).
3. Yang, X., Bian, J., Huang, J., Xin, W., Lu, T., Chen, C., Su, Y., Zhou, L., Wang, F. & Xu, J. Fluoride-free and low concentration template synthesis of hierarchical Sn-Beta zeolites: Efficient catalysts for conversion of glucose to alkyl lactate. *Green Chem.* **19**, 692–701 (2017).
4. Botti, L., Navar, R., Tolborg, S., Martinez-Espin, J. S., Padovan, D., Taarning, E. & Hammond, C. Influence of Composition and Preparation Method on the Continuous Performance of Sn-Beta for Glucose-Fructose Isomerisation. *Top. Catal.* **0**, 0 (2018).
5. Hammond, C., Padovan, D., Al-Nayili, A., Wells, P. P., Gibson, E. K. & Dimitratos, N. Identification of Active and Spectator Sn Sites in Sn- β Following Solid-State Stannation, and Consequences for Lewis Acid Catalysis. *ChemCatChem* **7**, 3322–3331 (2015).
6. Bodart, P., Nagy, J. B., Debras, G., Gabelica, Z. & Jacobs, P. A. Aluminum siting in mordenite and dealumination mechanism. *J. Phys. Chem.* **90**, 5183–5190 (1986).
7. Korányi, T. I. & Nagy, J. B. Distribution of aluminum in different periodical building units of MOR and BEA zeolites. *J. Phys. Chem. B* **109**, 15791–15797 (2005).
8. Korányi, T. I. & Nagy, J. B. Distribution of aluminum and boron in the periodical building units of boron-containing β zeolites. *J. Phys. Chem. B* **110**, 14728–14735 (2006).
9. Al-Nayili, A., Yakabi, K. & Hammond, C. Hierarchically porous BEA stannosilicates as unique catalysts for bulky ketone conversion and continuous operation. *J. Mater. Chem. A* **4**, 1373–1382 (2016).
10. Peng, Y., Peng, H., Liu, W., Xu, X., Liu, Y., Wang, C., Hao, M., Ren, F., Li, Y. & Wang, X. Sn-MFI as active, sulphur and water tolerant catalysts for selective reduction of NO_x. *RSC Adv.* **5**, 42789–42797 (2015).

Appendix

Chapter 3 Appendix

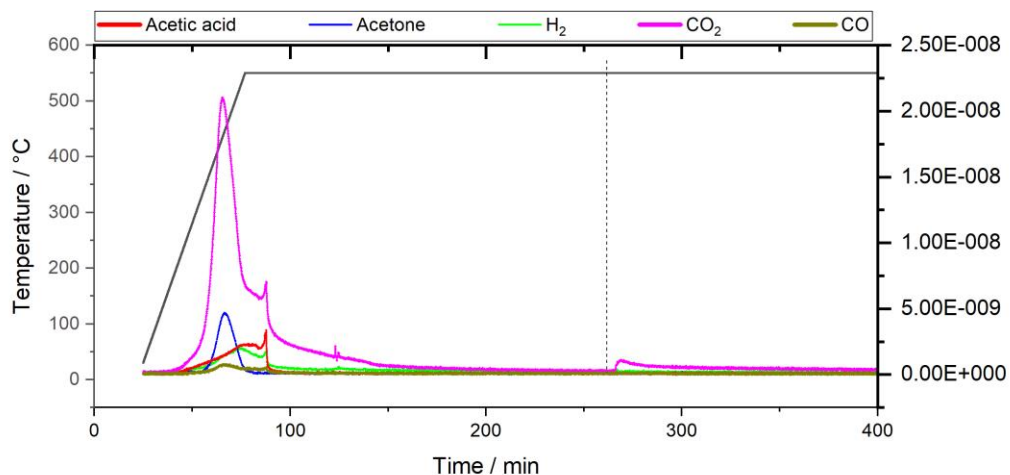
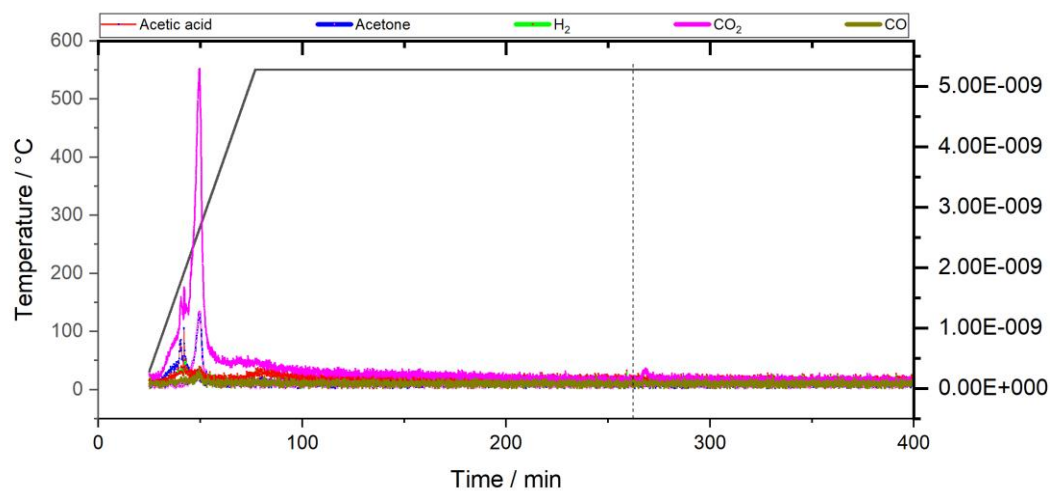
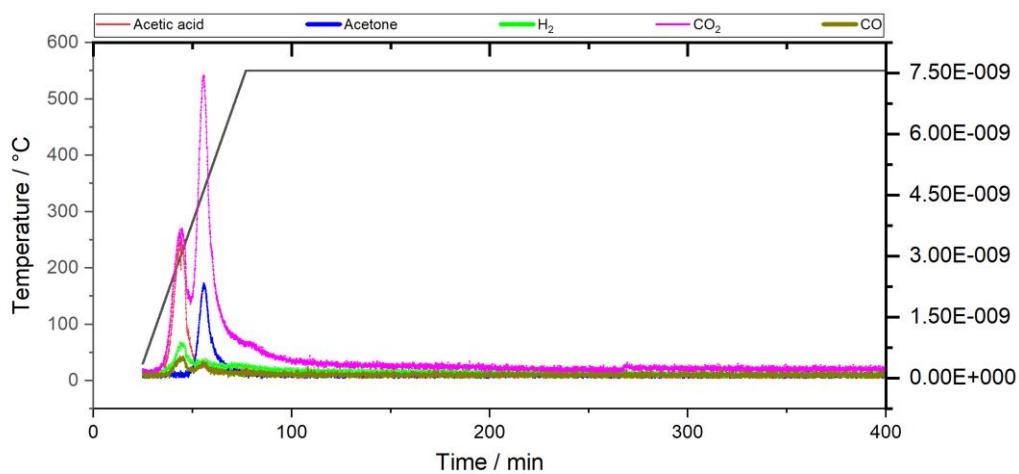
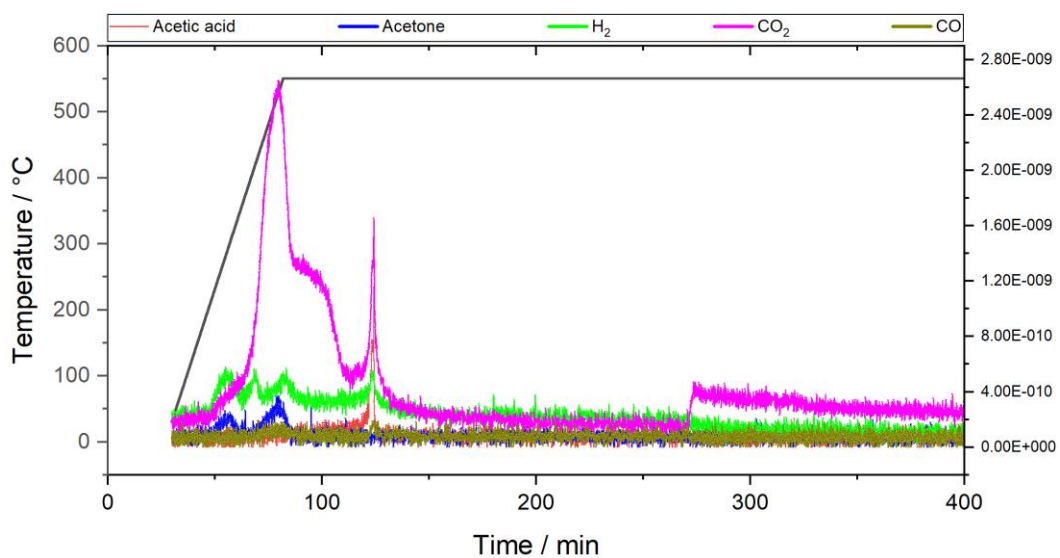
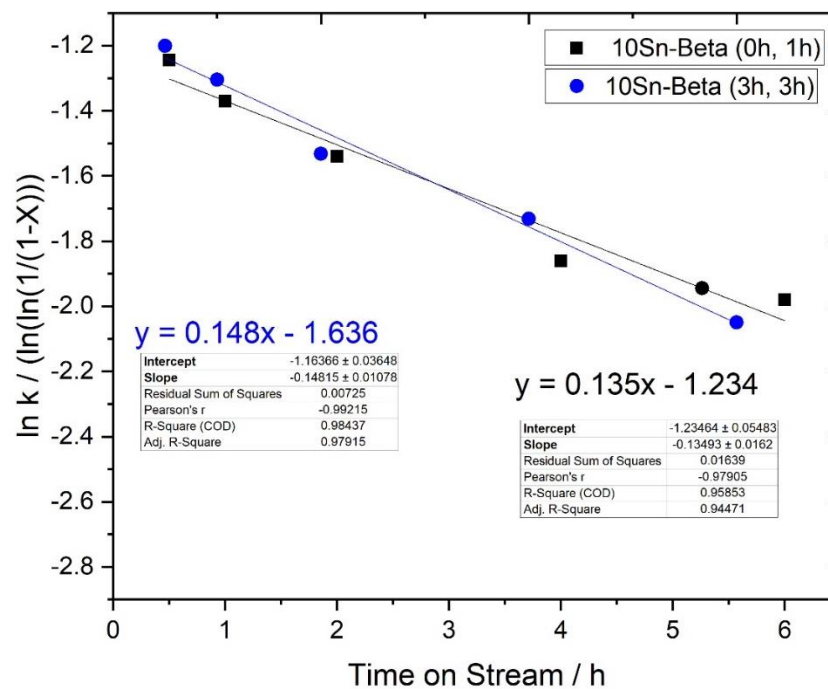


Figure 3.1. TPD-MS during calcination of $\text{Sn}(\text{OAc})_2/\text{deAl-Beta}$ mixture with 10 wt. % Sn loading.



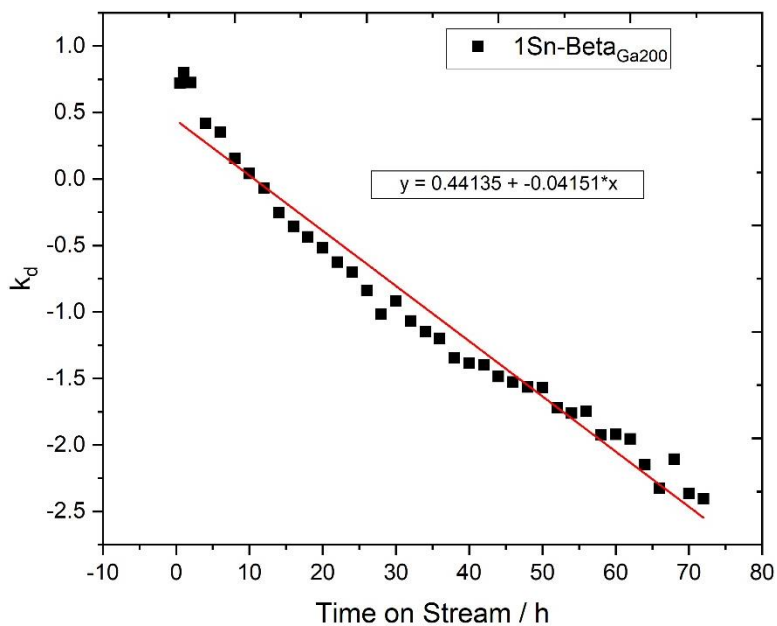
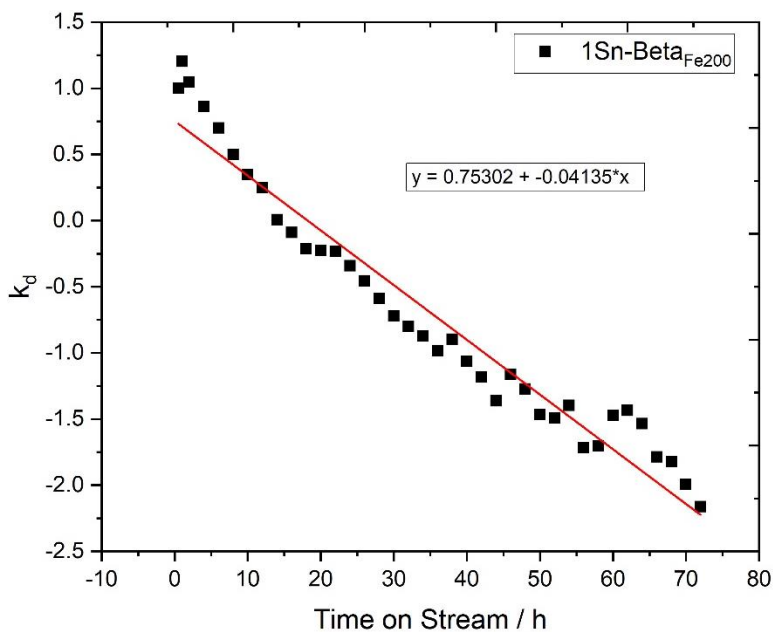
Appendix 3.2. Full TPD-MS of pure $\text{Sn}(\text{OAc})_2$.

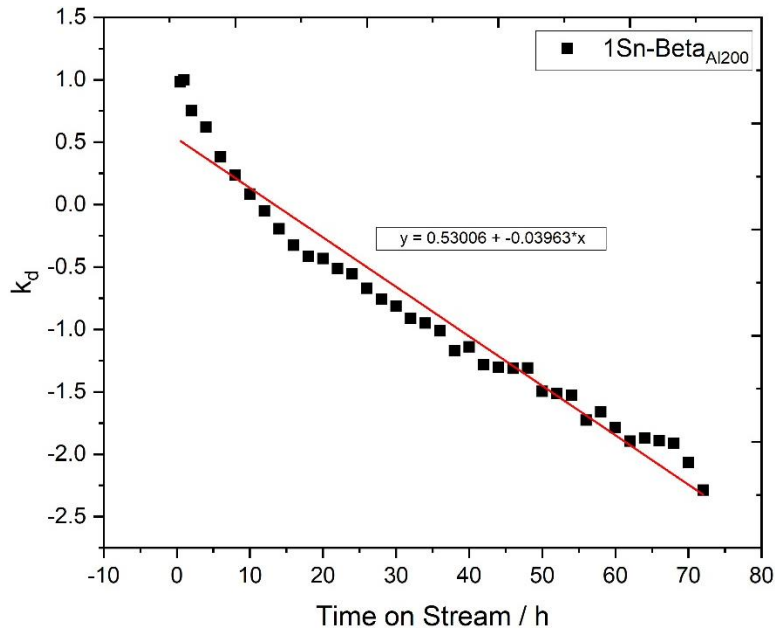
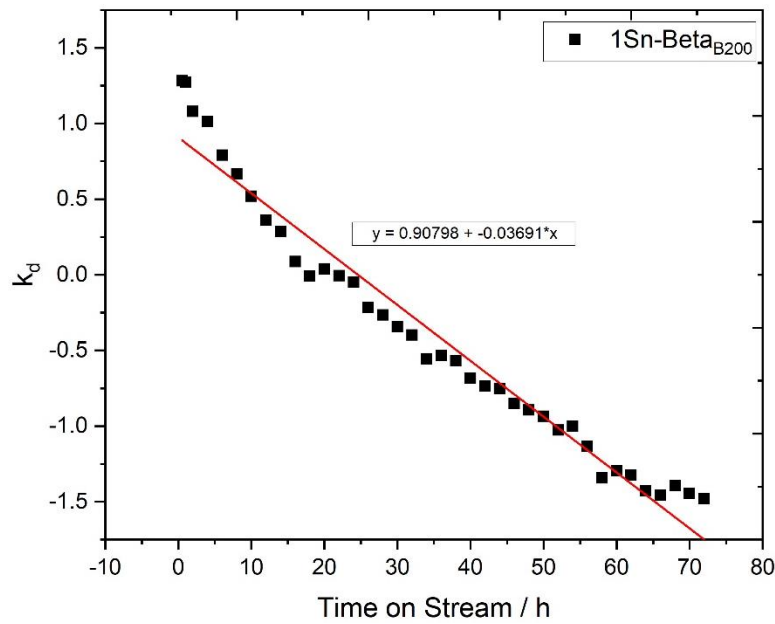
Appendix 3.3. Full TPD-MS of Sn(OAc)₂/Si-Beta mixture.Appendix 3.4 TPD-MS during calcination of Sn(OAc)₂/deAl-Beta mixture with 1 wt. % Sn loading.

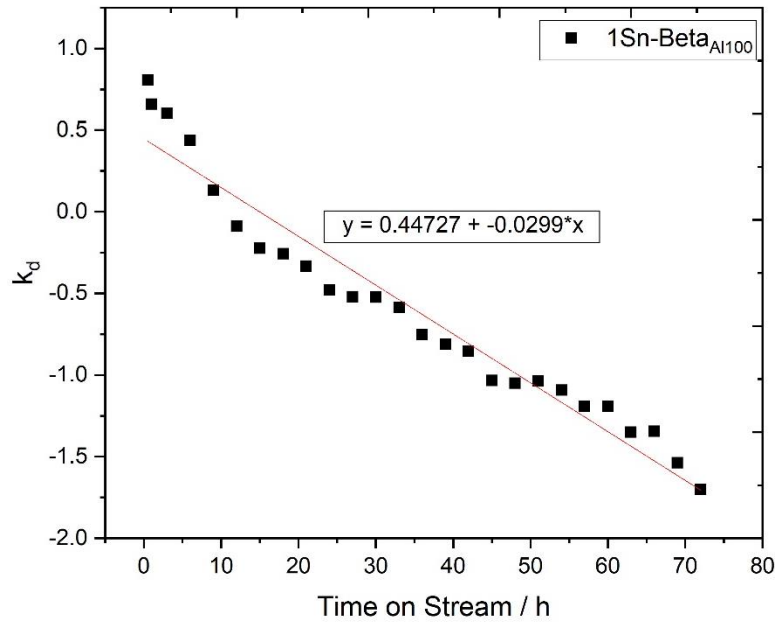
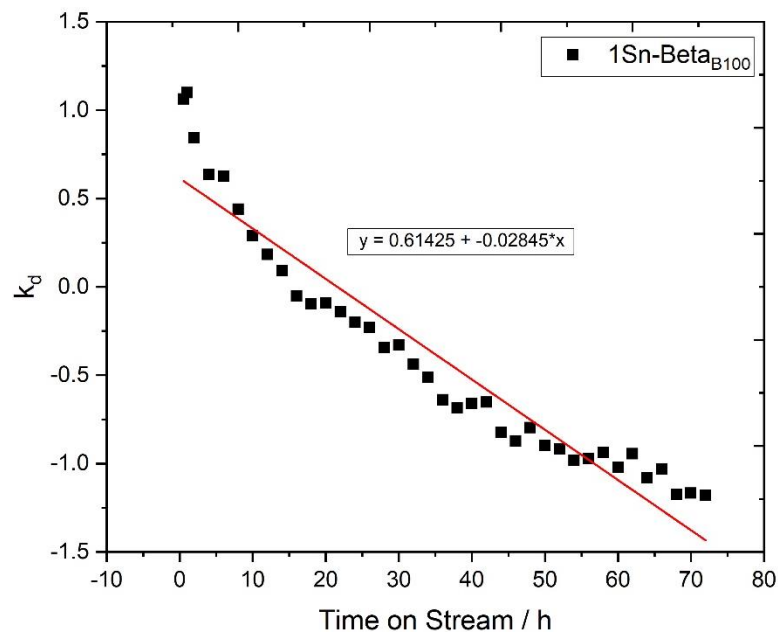


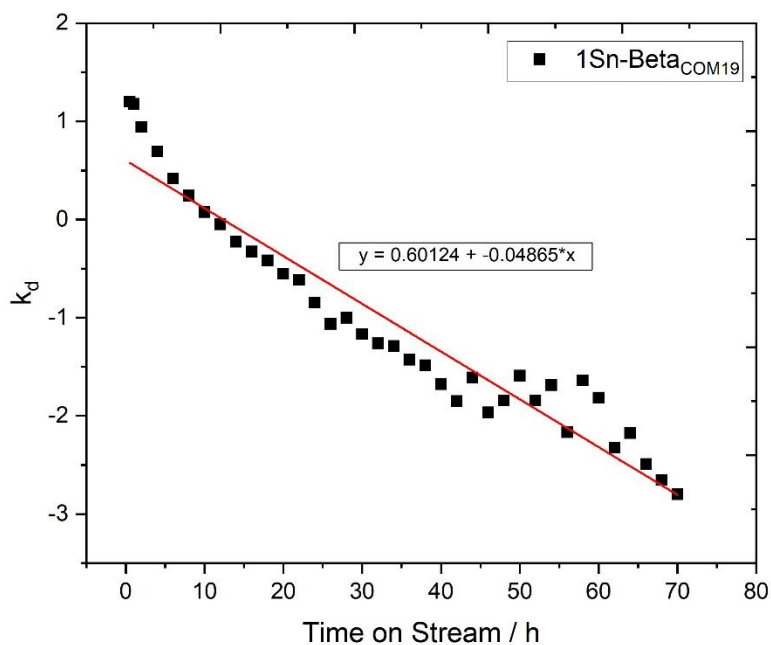
Appendix 3.5 Levenspiel plots to obtain glucose rate of deactivation (k_d) for optimised (0h N₂, 1h air isotherm) and normal (3h N₂, 3h air isotherm) 10Sn-Beta. Experiments performed in 1 wt. % glucose in methanol solution using 100 mg of catalyst at 110 °C at a flow rate of 1.5 mL min⁻¹.

Chapter 4 Appendix

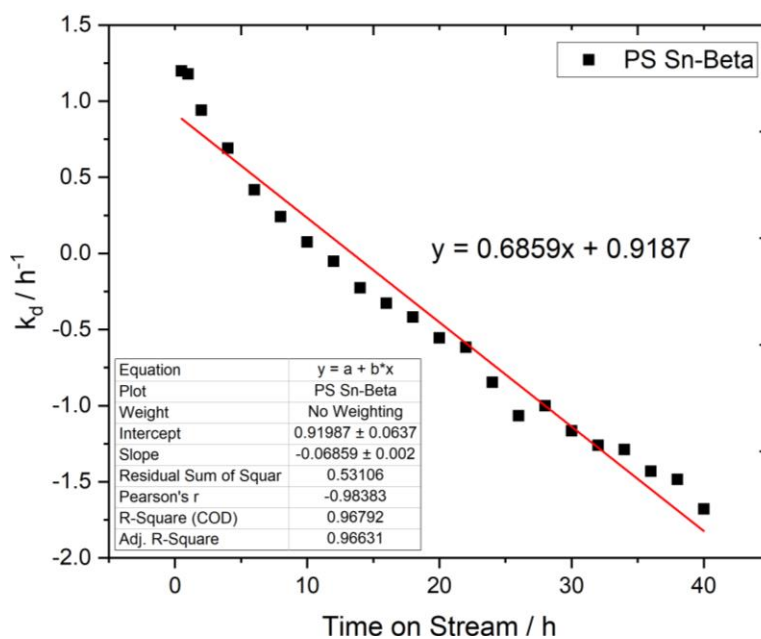
Appendix 4.1. k_d plot of 1Sn-Beta_{Ga200}.Appendix 4.2. k_d plot of 1Sn-Beta_{Fe200}.

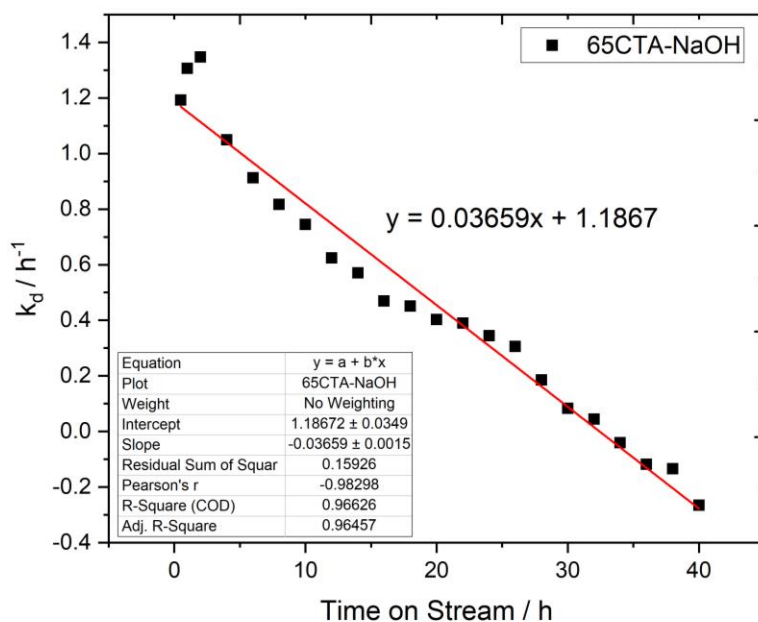
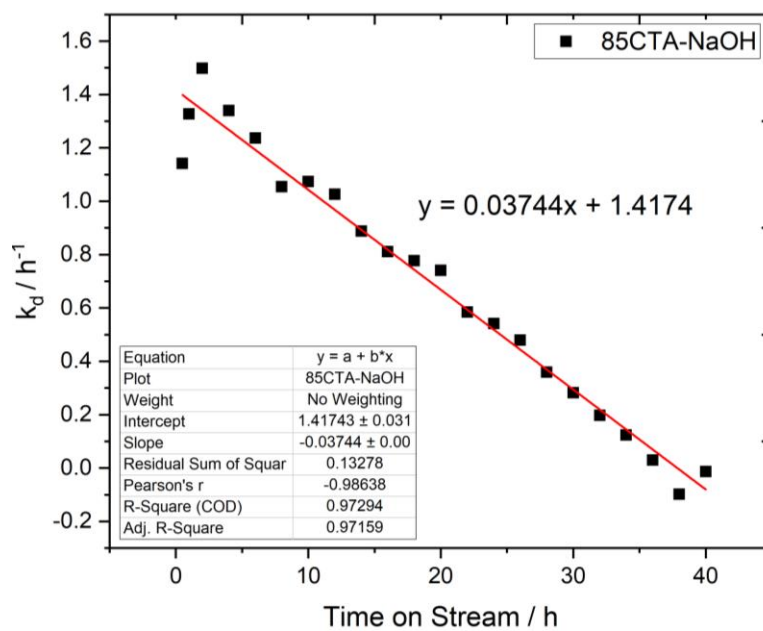
Appendix 4.3. k_d plot of $1\text{Sn-Beta}_{\text{Al200}}$.Appendix 4.4. k_d plot of $1\text{Sn-Beta}_{\text{B200}}$.

Appendix 4.5. k_d plot of 1Sn-Beta_{Al100}.Appendix 4.6. k_d plot of 1Sn-Beta_{B100}.

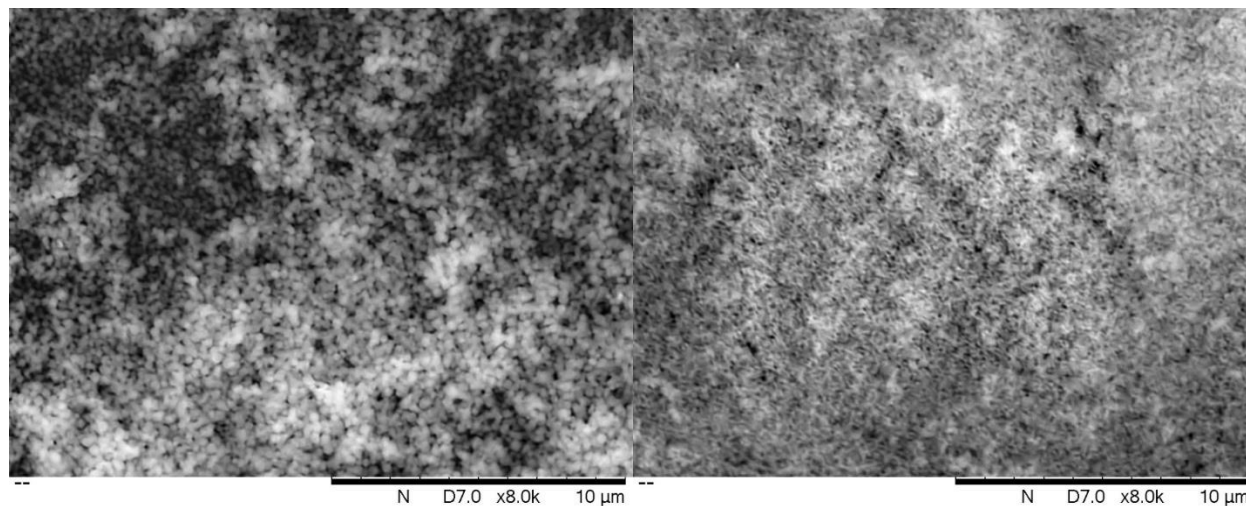
Appendix 4.7. k_d plot of 1Sn-Beta_{COM19}.

Chapter 5 Appendix

Appendix 5.1. k_d plot of post-synthetic (PS) Sn-Beta catalyst.

Appendix 5.2. k_d plot of 65CTA-NaOH Sn-Beta catalyst.Appendix 5.3. k_d plot of 85CTA-NaOH Sn-Beta catalyst.

Chapter 6 Appendix

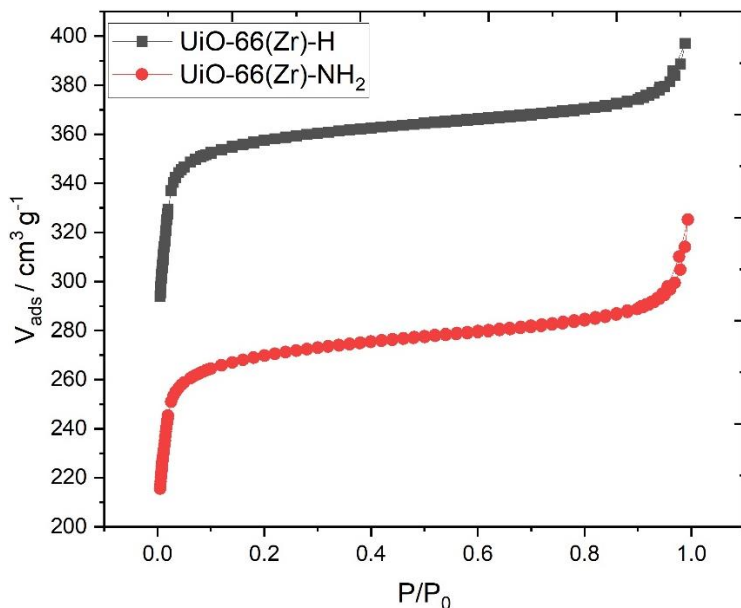
Appendix 6.1. SEM of UiO-66(Zr)-H (Left) UiO-66(Zr)-NH₂ (Right).Appendix 6.2. Textural and pore size data of UiO-66(Zr)-H and -NH₂ MOFs.

Sample	Surface area (m ² g ⁻¹) ^a	V _t (cm ³ g ⁻¹) ^b	V _{micro} (cm ³ g ⁻¹) ^c
UiO-66(Zr)-H	1593	0.544	0.459
UiO-66(Zr)-NH₂	1235	0.562	0.325

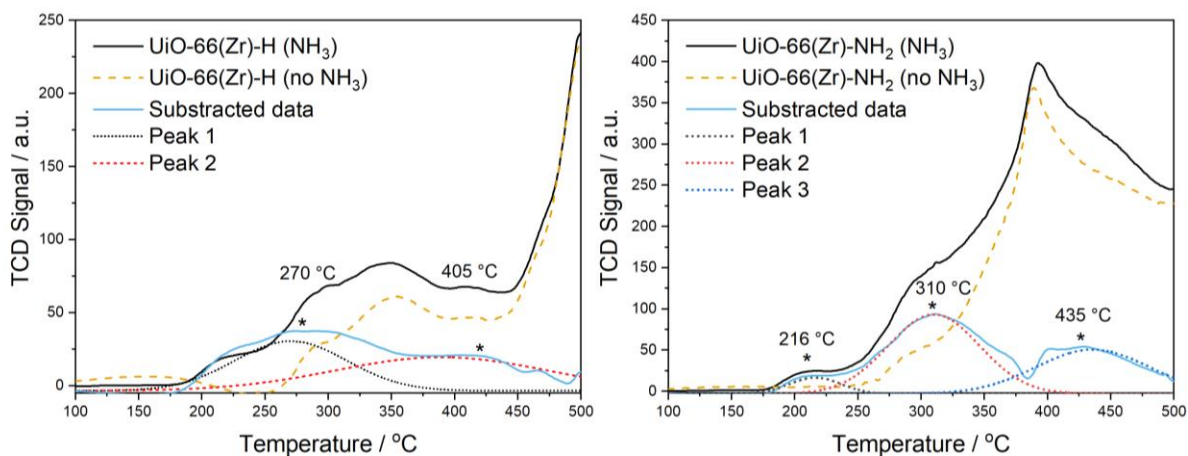
^a Specific surface area obtained from NLDFT.

^b Total pore volume.

^c Micropore volume from NLDFT.



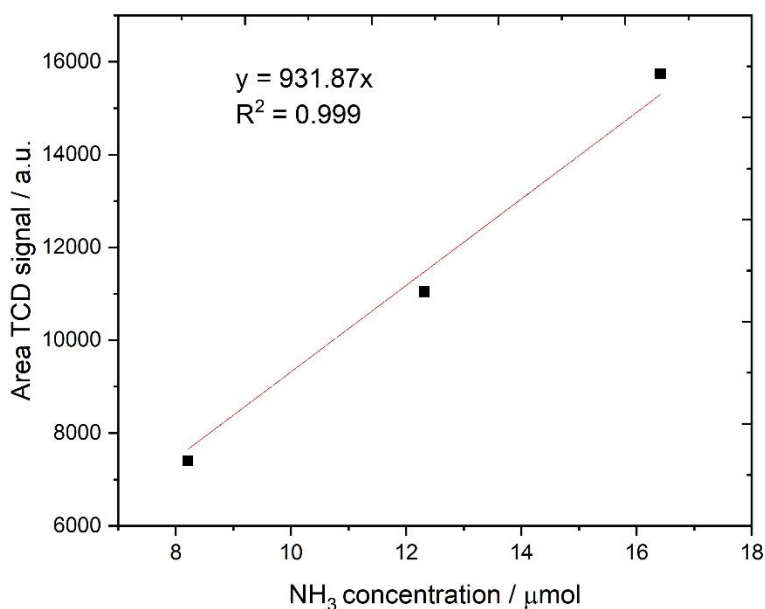
Appendix 6.3. Isotherm (left) and NLDFT pore size distribution (right) of UiO-66(Zr)-H and -NH₂ MOFs and DFT PSD.



Appendix 6.4. NH₃-TPD of fresh UiO-66(Zr)-H (Left) and UiO-66(Zr)-NH₂ (Right). Dashed lines indicate blank experiments where no NH₃ is adsorbed, and TCD signal is caused by degradation of the MOFs.

Appendix 6.5. Acidity of the untreated MOFs. Acidity values were obtained and calculated *via* NH₃ (10 % in Ar) calibration acquired in different flows (volume) to obtain their respective TCD signals and subsequently applied the ideal gas law equation to acquire the NH₃ concentration (moles) for each respective flow. Calibration curve and formula applied can be found in appendix 6.6.

Sample and temperature	Peak area	Acidity $\mu\text{mol g}^{-1}$
UiO-66(Zr)-H		
270 °C	3779	73.73
389 °C	4815	93.94
UiO-66(Zr)-NH₂		
216 °C	996	12.72
310 °C	8708	111.24
435 °C	6012	76.80

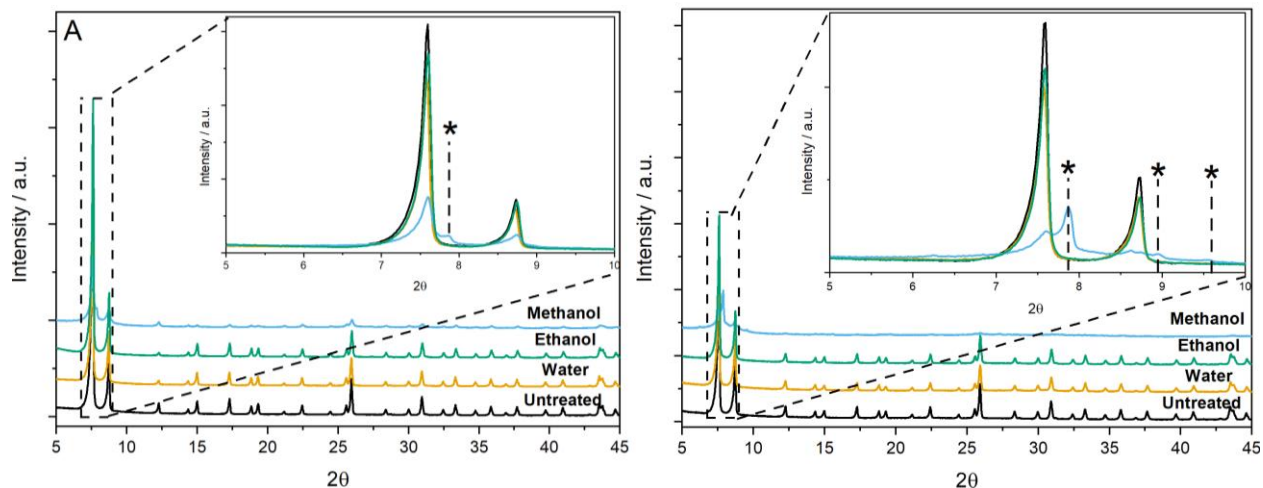


Appendix 6.6. NH₃ calibration curve.

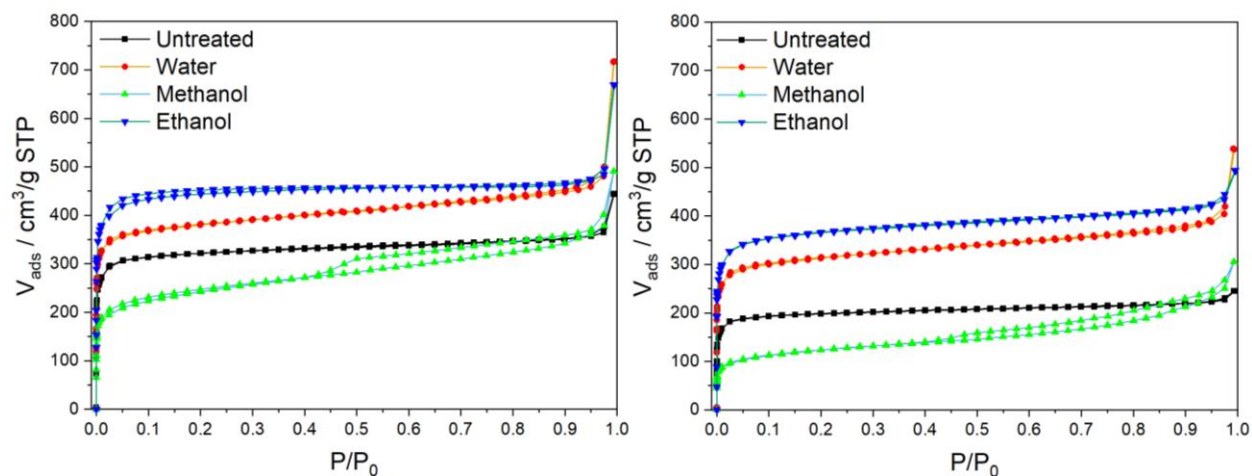
Flow rates used: 0.2, 0.3, 0.4 mL

With ideal gas law formula (using 0.2 mL as example):

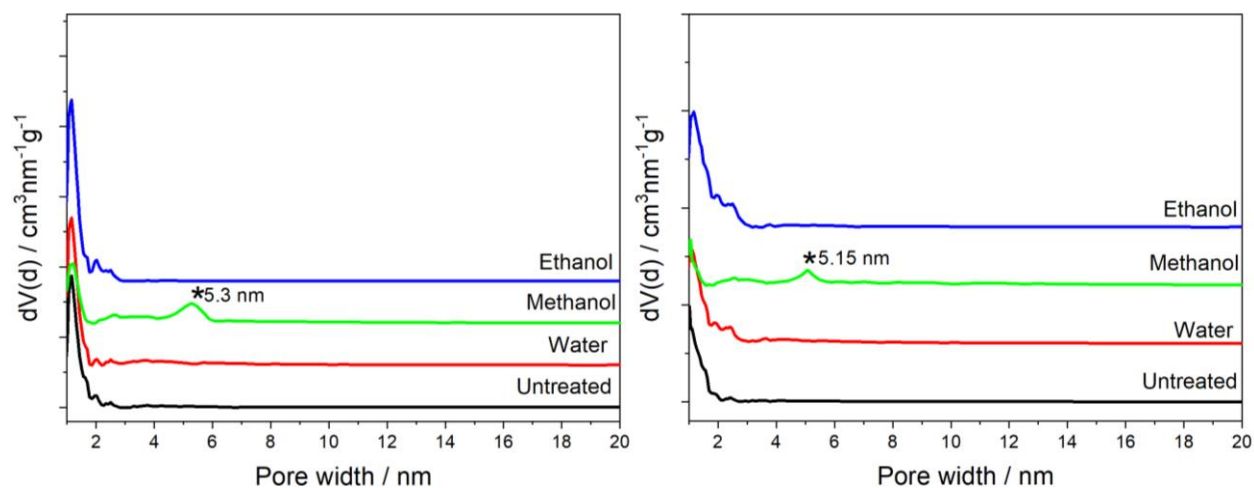
$$n = \frac{PV}{RT} = \frac{1 \text{ atm} * 0.0002 \text{ L}}{0.0821 \frac{\text{L} * \text{atm}}{\text{mol K}} * 298 \text{ K}} = 8.17 \times 10^{-6} \text{ mol} = 8.17 \mu\text{mol}$$



Appendix 6.7. XRD spectra of UiO-66(Zr)-H (left) and UiO-66(Zr)-NH₂ (right) prior to and following STS treatment. Inset: XRD spectra range between 5-10 2θ showing the rise of a new peak. Zoomed-in spectra in the range of 5-10° 2θ show the drastic decrease in intensity of peaks as well as the appearance of a new peak for the methanol-treated MOFs.



Appendix 6.8. Nitrogen adsorption isotherms of UiO-66(Zr)-H (left) and UiO-66(Zr)-NH₂ (right) for untreated and post-treated samples.



Appendix 6.9. DFT differential pore size distribution of UiO-66(Zr)-H (left) and UiO-66(Zr)-NH₂ (right) for untreated and post-treated samples.

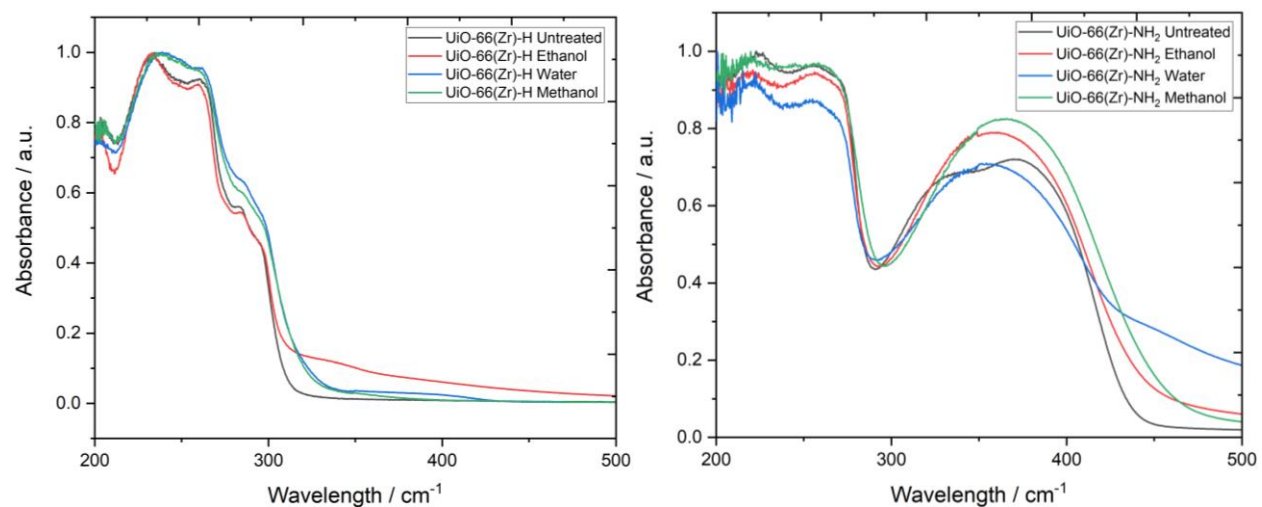
Appendix 6.10. Textural properties of UiO-66(Zr)-H and UiO-66(Zr)-NH₂.

Sample	Surface area (m ² g ⁻¹) ^a	V _t (cm ³ g ⁻¹) ^b	V _{micro} (cm ³ g ⁻¹) ^c
UiO-66(Zr)-H	1593	0.544	0.459
Water	1991	0.728	0.512
Ethanol	2270	0.719	0.623
Methanol	1179	0.587	0.229
UiO-66(Zr)-NH₂	1235	0.562	0.325
Water	1647	0.615	0.394
Ethanol	1841	0.651	0.472
Methanol	592	0.393	0.096

^a Specific surface area obtained from NLDFT.

^b Total pore volume.

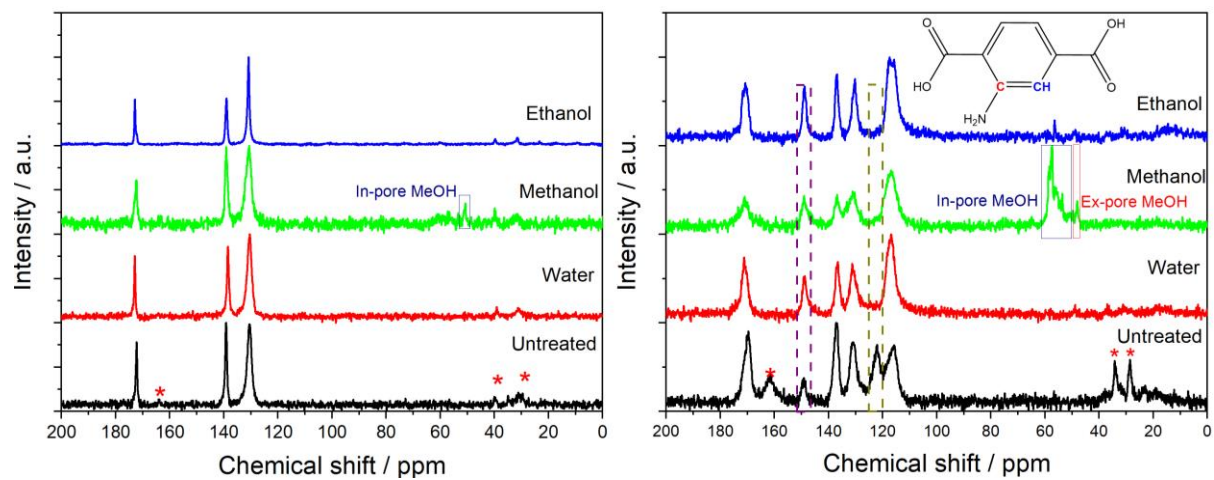
^c Micropore volume obtained from NLDFT.



Appendix 6.11. UV-Vis spectra of UiO-66(Zr)-H (left) and UiO-66(Zr)-NH₂ (right).



Appendix 6.12. UiO-66(Zr)-NH₂ MOFs before (fresh, A) and after undergoing STS with methanol (B), ethanol (C), and water (D) solvents. Images obtained from post-STs reactions carried out by Justyna Minkiewicz.



Appendix 6.13. ^{13}C CP-MAS NMR of UiO-66-H (left) and UiO-66-NH₂ (right). Red asterisks indicate residual DMF.